6-14-2012

# Carbon Nanostructure Based Electrodes for High Efficiency Dye Sensitize Solar Cell

Santanu Das
*Florida International University*, sdas001@fiu.edu

**DOI:** 10.25148/etd.FI12073001

FLORIDA INTERNATIONAL UNIVERSITY

Miami, Florida

# CARBON NANOSTRUCTURE BASED ELECTRODES FOR HIGH EFFICIENCY DYE SENSITIZED SOLAR CELL

A dissertation submitted in partial fulfillment of the

requirements for the degree of

DOCTOR OF PHILOSOPHY

in

MATERIALS SCIENCE AND ENGINEERING

by

Santanu Das

2012

To: Dean Amir Mirmiran
College of Engineering and Computing

This dissertation, written by Santanu Das, and entitled Carbon Nanostructure Based Electrodes for High Efficiency Dye Sensitize Solar Cell, having been approved in respect to style and intellectual content, is referred to you for judgment.

We have read this dissertation and recommend that it be approved.

_____
Norman D. H. Munroe

_____
Jiuhua Chen

_____
Nezih Pala

_____
Wonbong Choi, Major Professor

Date of Defense: June 14, 2012

The dissertation of Santanu Das is approved.

_____
Dean Amir Mirmiran
College of Engineering and Computing

_____
Dean Lakshmi N. Reddi
University Graduate School

Florida International University, 2012

DEDICATED

TO

MY BELOVED MOTHER

LATE SMT. NARAYANI DAS

ACKNOWLEDGMENTS

First and foremost I express my sincerest gratitude to my supervisor, Prof. Wonbong Choi, who has encouraged me throughout my dissertation with his patience and knowledge whilst allowing me the room to work in my own way. Prof. Choi led me towards an exciting area of my career with his insights and suggestions that helped to shape my research skills. I am extremely grateful to Prof. Choi for providing me opportunities during my studies at Florida International University (FIU) with all moral and financial support. I would also like to express my sincere gratitude to my dissertation committee members, Dr. Jiuhua Chen, Dr. Norman D. H. Munroe and Dr. Nezih Pala for their continuous support, encouragement and discussion whenever required.

I wish to express my warm and sincere thanks to Prof. Arvind Agarwal, Department of Mechanical and Materials Engineering (MME), FIU who helped me all the way during the DYF fellowship from FIU graduate school for doctoral studies and was always available when I needed some research related discussion with him.

I am very much obliged and grateful to Prof. Cesar Levy, Chairperson and Graduate Program Director, Department of Mechanical and Materials Engineering, FIU for all his kind help and support for getting graduate school fellowships during my dissertation period.

My Special thanks and gratitude are also go to Prof. Saxena, Director, CESMEC, FIU for extending the Raman spectroscopy facility for my PhD research. I would also like to convey thanks to Dr. Durygin, Dr. Drozd, Ross and Ali for all their support during my Raman experiments at CESMEC.

I am highly indebted to Prof. Y. S Kang and his Postdoctoral researcher Dr. P. Sudhagar at Hanyang University, Seoul, South Korea for collaborating with me for my experiments and research. This thesis would not have been possible without helps and supports from them.

Special thanks go to my friends and lab members and staff at Advanced Materials Engineering Research Institute (AMERI) who helped me throughout my research and study at FIU. Many thanks go to Dr. Raghunandan Seelaboyina, Dr. Harindra Vedala, Dr. Ved Verma, and Dr. Jun Hwang for introducing me to various CVD, nanofabrication and electrical measurement techniques during the early stage of my experiments at FIU. I am also thankful to Dr. K. Balani, Dr. Bakshi, Dr. Keshari, Dr. I. Lahiri, Dr. D. Lahiri, Dr. S. Hwang, Mustafa Karabiyik for their helpful discussion and Mr. Neal Ricks for his teaching and training to use clean room facility at AMERI. I would also thanks to my colleagues Chiwon, Sara, Divya for helping me in some of my experiments.

I gratefully acknowledge the financial support from Doctoral Evidence Assistantships and Dissertation Year Fellowship (DYF) program at Graduate School, FIU during my dissertation period at FIU.

I would also like to convey my heartfelt thanks to Prof. Arindam Chowdhury, Dr. Goutam Mandal, Dr. Sudheesh and Sushant for their constant support and encouragements during my PhD dissertation period at FIU.

Parents are God on the earth and I am sincerely expressing my gratitude to my parents for all they have been to me and without them I could not have been traversed this distance in my life. Finally, I am expressing my deepest gratitude to my friends, and other family members for their endless support, courage and love. I do highly

acknowledge the help of my brother Mr. Avijit Roy who always feel proud of me and supports at his best for all my pursuits.

ABSTRACT OF THE DISSERTATION

CARBON NANOSTRUCTURE BASED ELECTRODES FOR HIGH EFFICIENCY DYE SENSITIZED SOLAR CELL

by

Santanu Das

Florida International University, 2012

Miami, Florida

Professor Wonbong Choi, Major Professor

Synthesis and functionalization of large-area graphene and its structural, electrical and electrochemical properties has been investigated. First, the graphene films, grown by thermal chemical vapor deposition (CVD), contain three to five atomic layers of graphene, as confirmed by Raman spectroscopy and high-resolution transmission electron microscopy. Furthermore, the graphene film is treated with $CF_4$ reactive-ion plasma to dope fluorine ions into graphene lattice as confirmed by X-ray photoelectron spectroscopy (XPS) and UV-photoemission spectroscopy (UPS). Electrochemical characterization reveals that the catalytic activity of graphene for iodine reduction enhanced with increasing plasma treatment time, which is attributed to increase in catalytic sites of graphene for charge transfer. The fluorinated graphene is characterized as a counter-electrode (CE) in a dye-sensitized solar cell (DSSC) which shows ~ 2.56% photon to electron conversion efficiency with ~11 $mAcm^{-2}$ current density. Second, the large scale graphene film is covalently functionalized with $HNO_3$ for high efficiency electro-catalytic electrode for DSSC. The XPS and UPS confirm the covalent attachment of C-OH, C(O)OH and $NO_3^-$ moieties with carbon atoms through $sp^2$-$sp^3$ hybridization

and Fermi level shift of graphene occurs under different doping concentrations, respectively. Finally, CoS-implanted graphene (G-CoS) film was prepared using CVD followed by SILAR method. The G-CoS electro-catalytic electrodes are characterized in a DSSC CE and is found to be highly electro-catalytic towards iodine reduction with low charge transfer resistance ($R_{ct}$ ~5.05 $\Omega cm^2$) and high exchange current density ($J_0$~2.50 $mAcm^{-2}$). The improved performance compared to the pristine graphene is attributed to the increased number of active catalytic sites of G-CoS and highly conducting path of graphene.

We also studied the synthesis and characterization of graphene-carbon nanotube (CNT) hybrid film consisting of graphene supported by vertical CNTs on a Si substrate. The hybrid film is inverted and transferred to flexible substrates for its application in flexible electronics, demonstrating a distinguishable variation of electrical conductivity for both tension and compression. Furthermore, both turn-on field and total emission current was found to depend strongly on the bending radius of the film and were found to vary in ranges of 0.8 – 3.1 V/μm and 4.2 – 0.4 mA, respectively.

TABLE OF CONTENTS

LIST OF TABLES

LIST OF FIGURES

CHAPRER 1

# INTRODUCTION

## 1.1. Overview of Carbon Nanomaterials

Now a day, nanomaterials and nanotechnology creates innumerable research interests in the field of materials science towards a goal to develop low power miniaturized devices with enhanced performance for future generation ultra-fast electronics[1]. One nanometer is defined as one hundredth ($10^{-3}$) of a micrometer ($10^{-6}$ meter) or one billionth ($10^{-9}$) of a meter whereas nanotechnology involve the science and engineering with the materials dimensions belong to the category in the ranges from sub nanometers (Angstrom, Å) to several hundreds of nanometers. This scientific domain includes design, fabrication and application of nanomaterials of nanostructures, and the fundamental meaning of the relationships between physical properties and material dimensions.

Recently, carbon nanomaterials create unprecedented attention in academics and industries to be used as a next generation electronic and photonic material[2-6]. The basic building blocks of all the carbon nanostructures are single graphitic layer which is covalently functionalized $sp^2$ bonded carbon atoms exist in a hexagonal honeycomb lattice which forms 3D bulk graphite, when the layers of single honeycomb graphitic lattices are stacked and bounded by a weak Vander wall force. The single graphite layer, when forms sphere is well known as 0-dimensonal fullerene or bulkyball, when rolled up with respect to its axis forms 1-dimensional cylindrical structure, very known as carbon nanotube (CNT) for past two decades and when it exhibit the planner 2D structure with one to couple of layers stacked to each other called graphene[7].

Among all the carbon nanomaterials CNT and graphene exhibits high conductivity[8, 9], ballistic charge transport[10, 11], high charge carrier mobility[10, 12], good mechanical[13] and thermal properties[14] which are ideal for applications in electronics and photonics. Apart from their applications in electronics and photonics, these $sp^2$ bonded graphitic allotropes (CNT and graphene) are also possesses high surface area, high electro catalytically active and chemically inert, hence could be applied in a vast number of electro-catalytically active devices for energy harvesting and storage[15-19]. On the other hand, graphene, a newly invented two-dimensional carbon allotropes has ignited an exponentially increasing publications in the research communities, particularly towards a goal to incorporate it into future nano-scale devices.

Owing to their remarkable electronic, mechanical and thermal properties, CNT and graphene has been projected for potential applications in transistors, integrated electronic circuits, super-capacitors, solar cells and batteries[19, 20]. Recently, in addition to the applications based on individual graphene and CNT, the graphene-CNT hybrid structure is also proposed owing to its highly beneficial applications in microelectronics as they can incorporate the advantages from individual properties of graphene and CNT in planner and axial directions respectively[21-23].

## 1.2. Dye sensitized solar cell

Now a day's it is a real challenge to develop permanent alternative energy devices which would constitute key elements for sustainable future energy sources. In order to reduce the impact of "Global Warming" on the earth continuous research and development is required to improve the performance of the energy harvesting devices and their transition into commercial use. Solar cells are one of the major components among them which are considered as potential future energy harvesting devices. In this regards, US Department of Energy (DOE) has already been established their objective to guide the solar energy research growth up to 75% within 2015 where as European Renewable Energy Council (EREC) set their goal to be 30-40% minimum growth rates expected till 2020. Till date there are no real cost effective solar cell devices with high photon to electron conversion efficiency and safe to reuse and disposal. Recently nano-materials attract keen attention of researchers to develop high energy efficient low cost hand on devices. DSSC is one of the low cost future generation energy harvesting devise currently exhibiting light to electricity conversion efficiency almost around 11.1%. Furthermore, it is considered as a potential alternative for conventional Si-solar cells due to their remarkable stability, easy fabrication process, low cost and no toxicity. DSSC consist of a dye coated $TiO_2$ semiconducting layer on FTO glass substrate (anode) and a coating of few nanometers thickness of platinum catalysts on FTO glass (Cathode). These two electrodes are sandwiched using a polymer spacer (15-20 micron thick) and liquid ionic electrolyte with $I^-/I^{3-}$ redox couples is used as charge carrier in between the electrodes[24, 25]. The anode part of DSSC is functioned as current collector and charge separator where as the cathode materials act as charge injector by impinging back the electrons into the

liquid electrolyte, hence reduced the $I^{3-}$ redox couple as per the mechanism given below in equation 1.1[26].

$$I^{3-} + 3e^{-} \leftrightarrow 3I^{-} \quad (1.1)$$

Counter electrode (CE) (Cathode) of DSSC is generally prepared by coating of few nanometers Pt thin film on FTO/ITO glass substrate or polymer substrate. However several articles have been reported to date regarding the catalytic activity of carbon morphologies in order to replace Pt from DSSC for increasing its stability[27-29]. Carbon nanomaterials are promising future CE materials showed potential alternative to replace Pt due to their remarkable electrochemical performance, large surface charge carriers, high conductivity and long term stability[27, 30, 31]. Large surface carrier concentration and catalytic activities of carbon nanomaterials (e.g. graphene CNT) occurs due to its large surface to volume ratio and no space charge layer formation at the electrode-electrolyte interface.

## 1.3. Motivation and goal

Commercialization of Dye Sensitize solar Cells has already been started and slowly acquiring the market of conventional high cost Si solar cells. Systematic studies with scientific calculations and explanations will enhance the performance of DSSC and promote it for large scale prototype device fabrication. Similarly, improvement in efficiency and long term stability of DSSC will significantly increase DSSC's applications as a potential source for low power electronics, household electricity and industrial high power devices at a significant low cost. On the other hand, disadvantages

like high cost, low abundance impedes the scalability and application of Pt based conventional DSSC in real life. Therefore, scalability as well as high efficiency and long term stability are the major concerns which appear as challenges to improve the overall performance of the device.

The motivation of this research is first optimize the synthesis of high quality large scale few layer graphene, carbon Nanotubes and graphene-CNT hybrid structure using thermal chemical vapor deposition technique. The transfer of carbon nanomaterials on different flexible and transparent substrates is also an another goal to replace toxic and fragile indium tin oxide (ITO) type conventional transparent conducting oxide which limits its future applications in flexible electronics devices as well as flexible solar cells. Moreover, due to remarkable mechanical properties, graphene is an ideal material which exhibits wide range of transparency from ultra violet (UV) to near infra-red (NIR) regions which can be used as potential window for its application in high efficiency solar cell for harvesting more light photons from the entire solar spectrum range. More specifically, graphene exhibits transparency in the entire infra-red (IR) region which is an added advantage of its use as infra-red solar cells[18, 32]. In this context, graphene could be most suitable for solar cell use as it can be transfer on any flexible substrates using several facile and scalable methods. In addition to this, graphene also possess high surface charge carrier concentrations, excellent thermal conductivity and chemical inertness which can be potentially used as transparent conducting electrodes as well as catalytic electrodes, hence can be readily opt out one interface in DSSC.

Several approaches have been made for replacing platinum counter electrode by graphite, carbon black, glassy carbon, carbon-nanotube, conducting polymers etc[27, 33].

Nevertheless, Carbon based materials are highly promising for DSSC-CE, as they are highly stable, low in cost and electro-catalytically active towards tri-iodide reduction[28, 29]. Till date, several reports on graphene for solar cell were focused on replacing indium tin oxide (ITO) by graphene as a transparent conducting electrode.

In this context, there has been substantial interest for applying graphene as counter electrode towards tri-iodide reduction would offer enticing possibilities in flexible conducting counter electrode for dye-sensitized solar cells[15, 34, 35]. In DSSCs, counter electrode (CE) is one of the indispensable components which inject electrons into the electrolyte in order to catalyze the iodine reduction ($I^{3-}$ to $I^-$) after the charge injection from photo-oxidized dye[24, 28]. The electro-catalytic reduction $I_3^-$ to $I^-$ at CE dictating the cathodic activity of DSSCs and influences on current generation at photo-anode counter-part through dye-regeneration. In this context, utilizing the high surface area of 2-D graphene sheet (2630 $m^2/g$) in addition to its intrinsic high transmittance and charge mobility, provide greater versatility as a counter electrode in DSSCs. The surface modification protocols, either via chemical modification or physical treatment of graphene, are paid great attraction to increase the chemical reactivity of graphene for counter electrode for DSSCs[35]. It has been well reported that graphite intercalation compounds (GICs) significantly improve the conductivity and in-plane charge transfer compare to the graphite[36]. However the inert nature of graphene basal plane often restricts the graphene/liquid interfacial charge transfer although it shows high in-plane charge mobility, so tri-iodide reduction occurs only through their edge planes. Thus, surface modification is required for improving their in-line charge transfer characteristic and being performed as efficient catalytic counter electrode for tri-iodide reduction in

DSSCs. Till date, all the major reports concern about the surface modification of graphene using water-soluble polymers (polyelectrolyte) whose ionic charge has modifying the surface adsorption properties of graphene toward $I^-/I_3^-$ reduction and the enhancement of the apparent electro-catalytic activity of graphene by functionalization using poly(ethylene-oxide)-poly (propylene-oxide)- poly(ethylene-oxide) tri-block copolymer[34, 35]. However, improved charge transfer characteristic of graphene itself toward $I^-/I_3^-$ reduction in DSSCs is still unexplored and remains challenge.

## 1.4. Scope of this dissertation

Chapter 2 provides the background and literature reviews of the dissertation and discusses the properties of carbon nanomaterials like graphene, CNT and graphene-CNT hybrid materials. Here, structural, electrical and optical properties of carbon nanostructures like graphene, CNT and graphene-CNT hybrid structure are described. The progress of the graphene nanostructure for transistors, solar cells and electrochemical applications are also discussed. A recent development in graphene based transparent and flexible electrodes has also been mentioned in this chapter.

Chapter 3 contain the major experimental part of this dissertation and describes the detail synthesis of different carbon nanomaterials like Graphene, Carbon nanotubes and graphene-CNT hybrid structure using chemical vapor deposition process. This chapter includes the brief description of CVD process parameters for different carbon nanomaterials growth. Furthermore, it also contains the detail process of graphene transfer and graphene-CNT hybrid structure transfer on different flexible or transparent flexible substrates using different facile and scalable methods. The electrochemical

measurements like cyclic voltammetry and electrochemical impedance spectroscopy experimental set up is also included in this chapter. This chapter also covers the in detail experimental procedure of dye sensitized solar cell fabrication and the current-voltage (J-V) characterization method.

Chapter 4 addresses the detail structural characterization of different carbon nanostructures on different substrates. The detail structural characterizations includes, scanning electron microscopy (SEM), high resolution transmission electron microscopy (HRTEM) of graphene, carbon nanotubes and graphene-CNT hybrid structures. Atomic force microscopy and RAMAN spectroscopy was characterized for the carbon nanostructures also included in this chapter.

Chapter 5 describes the surface functionalization protocols of graphene nano-structures and their structural and electrochemical characterizations. This chapter also addresses the in detail analysis of functionalized graphene for solar cell applications with detail mechanism study. In detail experimental techniques along with the charge transfer mechanism and the calculated electrochemical parameters are also described in this chapter. A brief application of graphene-CNT as cathode of flexible field emission devices was also described in this chapter. Finally, Chapter 6 and 7 describes the summary and the scope for the future work of this dissertation respectively.

**References**

1. Zach, M.; Hagglund, C.; Chakarov, D.; Kasemo, B., Nanoscience and nanotechnology for advanced energy systems. *Current Opinion in Solid State & Materials Science* 2006, 10, 132-143.

2. Park, J. U.; Nam, S.; Lee, M. S.; Lieber, C. M., Synthesis of monolithic graphene-graphite integrated electronics. *Nature Materials* 2012, 11, 120-125.

3. Zhang, Z. Y.; Wang, S.; Peng, L. M., High-performance doping-free carbon-nanotube-based CMOS devices and integrated circuits. *Chinese Science Bulletin* 2012, 57, 135-148.

4. Aziziyan, M. R.; Ahmadi, V.; Moghadam, N., A quantum model for light emission performance of carbon nanotube field effect transistor. *Applied Physics Letters* 2012, 100, 3.

5. Geim, A. K., Graphene: Status and Prospects. *Science* 2009, 324, 1530-1534.

6. Yang, E. H., Engineered low-dimensional nanomaterials for sensors, actuators, and electronics. *Journal of Micro-Nanolithography Mems and Moems* 2010, 9, 5.

7. Geim, A. K.; Novoselov, K. S., The rise of graphene. *Nat Mater* 2007, 6, 183-191.

8. Geim, A. K.; Kim, P., Carbon wonderland. *Scientific American* 2008, 298, 90-97.

9. Novoselov, K. S.; Jiang, Z.; Zhang, Y.; Morozov, S. V.; Stormer, H. L.; Zeitler, U.; Maan, J. C.; Boebinger, G. S.; Kim, P.; Geim, A. K., Room-Temperature Quantum Hall Effect in Graphene. *Science* 2007, 315, 1379-1379.

10. Castro Neto, A. H.; Guinea, F.; Peres, N. M. R.; Novoselov, K. S.; Geim, A. K., The electronic properties of graphene. *Reviews of Modern Physics* 2009, 81, 109-162.

11. Novoselov, K. S.; Morozov, S. V.; Mohinddin, T. M. G.; Ponomarenko, L. A.; Elias, D. C.; Yang, R.; Barbolina, II; Blake, P.; Booth, T. J.; Jiang, D.; Giesbers, J.; Hill, E. W.; Geim, A. K., Electronic properties of graphene. *Physica Status Solidi B-Basic Solid State Physics* 2007, 244, 4106-4111.

12. Novoselov, K. S.; Geim, A. K.; Morozov, S. V.; Jiang, D.; Zhang, Y.; Dubonos, S. V.; Grigorieva, I. V.; Firsov, A. A., Electric field effect in atomically thin carbon films. *Science* 2004, 306, 666-669.

13. Lee, C.; Wei, X. D.; Kysar, J. W.; Hone, J., Measurement of the elastic properties and intrinsic strength of monolayer graphene. *Science* 2008, 321, 385-388.

14. Balandin, A. A., Thermal properties of graphene and nanostructured carbon materials. *Nat Mater* 2011, 10, 569-581.

15. Das, S.; Sudhagar, P.; Verma, V.; Song, D.; Ito, E.; Lee, S. Y.; Kang, Y. S.; Choi, W., Amplifying Charge-Transfer Characteristics of Graphene for Triiodide Reduction in Dye-Sensitized Solar Cells. *Advanced Functional Materials* 2011, 21, 3729-3736.

16. Landi, B. J.; Ganter, M. J.; Cress, C. D.; DiLeo, R. A.; Raffaelle, R. P., Carbon nanotubes for lithium ion batteries. *Energy & Environmental Science* 2009, 2, 638-654.

17. Grobert, N., Carbon nanotubes - becoming clean. *Materials Today* 2007, 10, 28-35.

18. Wang, X.; Zhi, L. J.; Mullen, K., Transparent, conductive graphene electrodes for dye-sensitized solar cells. *Nano Letters* 2008, 8, 323-327.

19. Dai, L.; Chang, D. W.; Baek, J.-B.; Lu, W., Carbon Nanomaterials for Advanced Energy Conversion and Storage. *Small* 2012, n/a-n/a.

20. Simon, P.; Gogotsi, Y., Materials for electrochemical capacitors. *Nature Materials* 2008, 7, 845-854.

21. Das, S.; Seelaboyina, R.; Verma, V.; Lahiri, I.; Hwang, J. Y.; Banerjee, R.; Choi, W., Synthesis and characterization of self-organized multilayered graphene-carbon nanotube hybrid films. *Journal of Materials Chemistry* 2011, 21.

22. Lee, D. H.; Kim, J. E.; Han, T. H.; Hwang, J. W.; Jeon, S.; Choi, S.-Y.; Hong, S. H.; Lee, W. J.; Ruoff, R. S.; Kim, S. O., Versatile Carbon Hybrid Films Composed of Vertical Carbon Nanotubes Grown on Mechanically Compliant Graphene Films. *Advanced Materials* 2010, 22, 1247-1252.

23. Lee, D. H.; Lee, J. A.; Lee, W. J.; Choi, D. S.; Kim, S. O., Facile Fabrication and Field Emission of Metal-Particle-Decorated Vertical N-Doped Carbon Nanotube/Graphene Hybrid Films. *Journal of Physical Chemistry C* 2010, 114, 21184-21189.

24. O'Regan, B.; Gratzel, M., A low-cost, high-efficiency solar cell based on dye-sensitized colloidal TiO2 films. *Nature* 1991, 353, 737-740.

25. Grätzel, M., Conversion of sunlight to electric power by nanocrystalline dye-sensitized solar cells. *Journal of Photochemistry and Photobiology A: Chemistry* 2004, 164, 3-14.

26. Gratzel, M., Photoelectrochemical cells. *Nature* 2001, 414, 338-344.

27. Imoto, K.; Takahashi, K.; Yamaguchi, T.; Komura, T.; Nakamura, J.-i.; Murata, K., High-performance carbon counter electrode for dye-sensitized solar cells. *Solar Energy Materials and Solar Cells* 2003, 79, 459-469.

28. Trancik, J. E.; Barton, S. C.; Hone, J., Transparent and Catalytic Carbon Nanotube Films. *Nano Letters* 2008, 8, 982-987.

29. Suzuki, K.; Yamaguchi, M.; Kumagai, M.; Yanagida, S., Application of Carbon Nanotubes to Counter Electrodes of Dye-sensitized Solar Cells. *Chemistry Letters* 2003, 32, 28-29.

30. Nugent, J. M.; Santhanam, K. S. V.; Rubio, A.; Ajayan, P. M., Fast Electron Transfer Kinetics on Multiwalled Carbon Nanotube Microbundle Electrodes. *Nano Letters* 2001, 1, 87-91.

31. Britto, P. J.; Santhanam, K. S. V.; Rubio, A.; Alonso, J. A.; Ajayan, P. M., Improved Charge Transfer at Carbon Nanotube Electrodes. *Advanced Materials* 1999, 11, 154-157.

32. Bi, H.; Huang, F.; Liang, J.; Xie, X.; Jiang, M., Transparent Conductive Graphene Films Synthesized by Ambient Pressure Chemical Vapor Deposition Used as the Front Electrode of CdTe Solar Cells. *Advanced Materials* 2011, 23, 3202-3206.

33. Xia, J. B.; Masaki, N.; Jiang, K. J.; Yanagida, S., The influence of doping ions on poly(3,4-ethylenedioxythiophene) as a counter electrode of a dye-sensitized solar cell. *Journal of Materials Chemistry* 2007, 17, 2845-2850.

34. Hasin, P.; Alpuche-Aviles, M. A.; Wu, Y. Y., Electrocatalytic Activity of Graphene Multi layers toward I-/I-3(-): Effect of Preparation Conditions and Polyelectrolyte Modification. *Journal of Physical Chemistry C* 2010, 114, 15857-15861.

35. Roy-Mayhew, J. D.; Bozym, D. J.; Punckt, C.; Aksay, I. A., Functionalized Graphene as a Catalytic Counter Electrode in Dye-Sensitized Solar Cells. *ACS Nano* 2010, 4, 6203-6211.

36. Delhaes, P., *Graphite and precursors*. Gordon & Breach: Australia, 2001; p xiv, 297 p.

CHAPRER 2

# BACKGROUND AND LITERATURE REVIEW

## 2.1. Graphene

No doubt that graphene is rapidly proliferating in the horizon of materials science and condensed matter physics and bringing up a new paradigm of relativistic quantum phenomena due to is unusual electronics properties. Since its invention, graphene, two-dimensional (2D) graphitic allotropes of carbon creates an immense research interest due to its exotic electronics, optoelectronics, thermal and mechanical properties[1-5]. The most fascinating properties of graphene include room temperature quantum Hall effect[6, 7], ballistic charge transport[2, 8], high charge carrier density[1, 8], tunable band gap[9], high thermal conductivity[10] and ultra-high transmittance[11, 12]. Graphene can be defined as a $sp^2$ bonded two dimensional honeycomb graphitic carbon materials whose properties are strictly varied with its number of layers. The mother of all the graphitic allotropes are consisting of a single sheet of graphite called graphene as shown in Figure 2.1. Figure 2.1 illustrate the single graphite layer, when forms sphere is well known as 0 (zero) - dimensional fullerene, when rolled up with respect to its axis forms 1-dimensional cylindrical structure, known as carbon nanotube and when it exhibit the planner 2D structure from one to few layers stacked upon each other called graphene. More specifically, graphene has a high electron (or hole) mobility with low Johnson noise (electronic noise generated by the thermal agitation of the charge carriers inside an electrical conductor at equilibrium, which appears regardless of any applied voltage), allowing it to be utilized as the quantum channel in a field effect transistor (FET). The

high optical and electrical conductivity promote graphene as a candidate for transparent conducting electrodes, required for applications in touch-screens, liquid crystal displays, organic photovoltaic cells and organic light-emitting diodes (OLEDs). Moreover, remarkable mechanical properties as well as flexibility of graphene are an added advantage of producing flexible transparent conducting electrodes for future transparent electronics. Owing to its unusual electronic spectrum, graphenes' properties are strictly dependent upon the number of layers, surface defects, ripples, substrate orientations and the formation of edge plane structures as well. In so called materials science point of view one graphitic layer is well known as monolayer or single layer graphene and two and three graphitic layers are known as bi-layer and tri-layer graphene respectively. More than 5 stacked layers up to 10 layers graphene is generally called as few layer graphene, around ~20-30 layered stacked graphene is addressed as multilayer graphene and more than 100-200 layers graphene structure are called as thick graphene or nano-crystalline thin graphite. This chapter reviews in detail the crystal structure, electronics properties, mechanical properties, thermal properties and electrochemical properties of graphene with current research status and future prospects. In addition to this a brief overview of recent research progresses of graphene will be described along with the future goal projected to the next generation electronics devices correlating the entire goal of this dissertation.

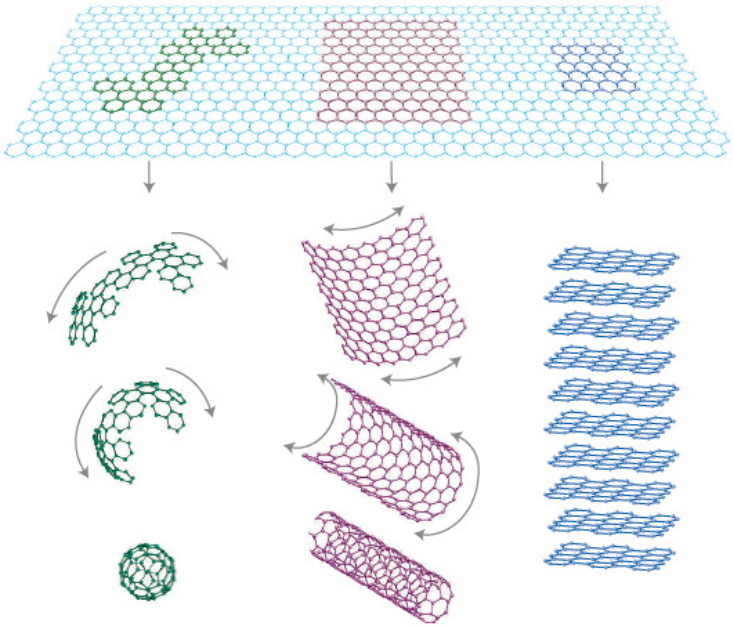

Figure 2.1: An atomic sheet of honeycomb carbon layer (top); when it forms a sphere, called 0-dimensional fullerene (left); cylindrical structure known as carbon nanotubes (center); and forms graphite when the layers stacked to each others in 3-dimension [Reprinted with permission from Reference [1]].

### 2.1.1. Graphene electronic structure and crystal lattice

Graphene lattice is consists of $sp^2$ hybridized three in-plane ($\sigma$) (known as graphene basal plane) bonds/atom which are extremely strong and form the rigid backbone of the hexagonal honeycomb structure (as shown in Figure 2.2a). Due to the strong in plane sigma bonds, graphene exhibit the excellent in-plane mechanical properties like elasticity, young modulus, flexural strength[13] etc. The unusual electronic properties of graphene is owing to its partially filled $p_z$ orbitals (known as $\pi$ orbitals) perpendicular to the basal plane (as shown in Figure 2.2b). When stacked, this

unsaturated π orbitals results in the layer dependent electronics properties like semi metallic behavior, band gap openings landau level quantization etc[14-18]. Similarly, the substrate dependent electronics properties and phonon dispersions of graphene are also due to the partially filled $p_z$ orbitals which forms various unsaturated dangling bond with different substrates surfaces as reported elsewhere[19].

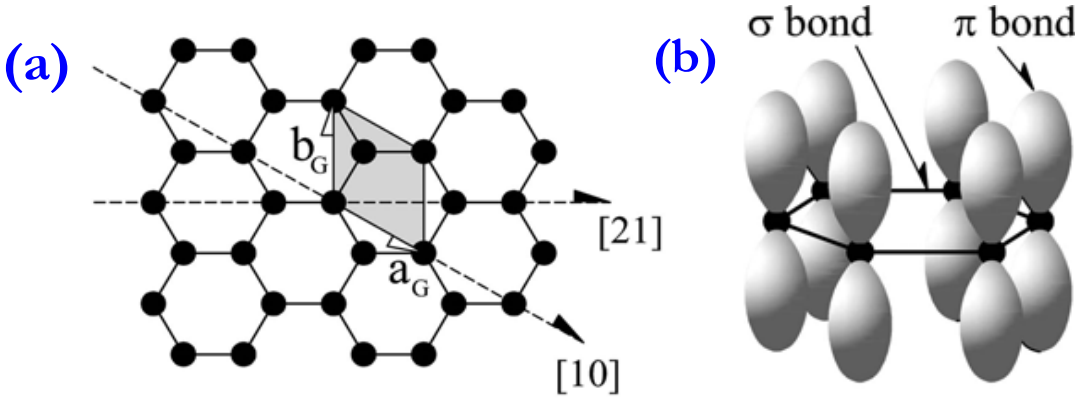


Figure 2.2: (a) Honeycomb single layer graphite lattice representing graphene crystal structure; (b) atomic structure of graphene illustrating in-plane sigma bond and out of plane pi bonds [Reprinted with permission from Reference [20]].

The stacking of graphene layers occurred in three different ways to create materials like bi-layer, tri-layer, few-layer, multi-layer graphene and even graphite. Those three are most commonly named as: hexagonal or AA . . . stacking, Bernal or AB. . . stacking and rhombohedral or ABC. . . stacking as described earlier[20]. In this context, Bernal stacking is the minimal energy stacking order and most abundant form (80%) in single crystal graphite, which are strictly tailor the graphene's band gap opening and electrical properties [21, 22].

### 2.1.2. Properties of Graphene

High crystalline pristine mono-atomic graphene exhibits unusual intrinsic electronic properties owing to its semi-metallic behavior as the k and k/ bands touches in a single point at the Fermi Level ($E_f$) at the each of the corners of the Brillouin zone as shown in Figure 2.3 [6]. Moreover, graphene became the center of attraction of condensed matter physicist owing to its' resemblance of the Dirac spectrum for mass-less fermions[6] and Landau level quantization under applied vertical magnetic field to the graphene basal plane [2]. On the other hand, bi-layer graphene is of great research importance because its bandgap can be opened up to 250 meV by applying an external vertical electric field. Furthermore, most fascinating electronics properties of graphene include its high conductivity, significant carrier mobility, and quantum hall effect.

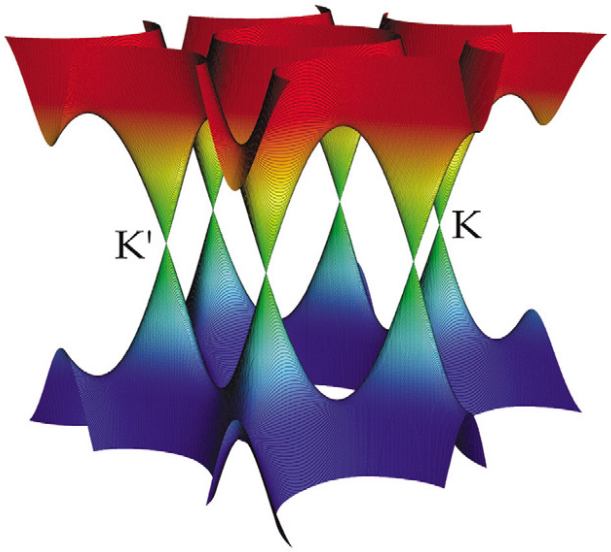


Figure 2.3: Electronics band structure of graphene. The schematic illustrates the touching of K and K/ point at the Brillouin Zone a representative of semi-metallic behavior of graphene [Reprinted with permission from Reference [23]].

Intrinsic graphene is characterized as a semi-metal or zero-gap semiconductor exhibiting remarkably high electron mobility at room temperature, with experimentally reported values in excess of 15,000 $cm^2\ V^{-1}s^{-1}$ [8]. The electron and hole mobility of graphene are the same and independent of the temperature in between 10K to 100K[6, 24]. Hence, the scattering by intrinsic defects plays predominant role in limiting graphenes' intrinsic carrier mobility which is also dependent upon its charge carrier concentrations[25, 26]. Similarly, at low dimensions, phonons are also play an important role in charge scattering at room temperature. However, it has already been demonstrated that the mobility in bi-layer graphene exhibiting ~ 200,000 $cm^2V^{-1}s^{-1}$ at a carrier density of $10^{12}$ $cm^{-2}$ due to the weak electron phonon scattering[24]. Table 2.1 shows the recently reported values of carrier mobility of graphene under different condition. At its outset, graphene possess lowest ever specific resistance which is even less than the Silver (Ag)[25].

Monolayer graphene exhibits ultra-high transparency through the entire light spectrum from ultra violet (UV) to near infra-red (NIR) region. On the other hand, the optical transparency is decreasing with increasing number of layers. For example, monolayer graphene exhibits ~97% optical transmittance[27] with ~2.2 KΩ/sq sheet resistance. Furthermore, transmittance and sheet resistance are inversely proportional to the number of graphene layers. More specifically, bi-layer, tri-layer and 4-layers graphene possess ~ 95%, ~ 92% and ~ 89% transmittance with corresponding sheet resistance of 1 KΩ/sq, ~700 Ω/sq and ~400 Ω/sq respectively as reported elsewhere [27]. The Table 2.2 represents an overview of recent research status of sheet resistance and transmittance of graphene electrodes.

Table 2.1: Demonstrates a brief summary of Graphene mobility reported till date.

| Graphene Synthesis Process | Number of graphene layers | Transfer Process | Mobility ( $cm^2V^{-1}s^{-1}$) | | References |
|---|---|---|---|---|---|
| | | | Field Effect | Hall | |
| *CVD grown graphene on Pt* | 1 | Bubbling Transfer | 7,100 | N/A | [28] |
| *CVD grown graphene on Cu* | 1-few | Chemical Transfer to $SiO_2$/Si | 3600 under $V_{GS}$ = -3.2 V and 2860 under $V_{GS}$ = 3 V | N/A | [29] |
| *CVD grown graphene on Cu* | 1 | Chemical Transfer to $SiO_2$/Si | 4000 | N/A | [30] |
| *CVD grown graphene on Cu* | 1 | Chemical Transfer to $SiO_2$/Si | 4050 | | [31] |
| *CVD grown graphene on Cu* | 1 | Chemical Transfer to $SiO_2$/Si | - | 7350 at 6K 5100 at 295K | [32] |
| *CVD grown graphene on Ni* | 1-few | Chemical Transfer to $SiO_2$/Si | - | 3700 | [33] |
| *Epitaxial Graphene on SiC* | 1-few | N/A | - | 2000 at 27K | [34] |
| *Epitaxial Graphene on SiC* | 1-few | N/A | - | 1500000 (000$\bar{1}$) 5800 on (0001) At 300 K | [35] |
| *Suspended Grpahene* | 1 layer | N/A | 200,000 | - | [36] |

| | | | | | |
|---|---|---|---|---|---|
| *Mechanically Exfoliated* | 1 layer | Scotch tape method | 10,000 | - | [8] |

Table 2.2: Demonstrates a summary of recent reports on transmittance and sheet resistance of graphene electrodes prepared using different synthesis techniques.

| **Graphene on Different Substrates** | **Synthesis Process** | **Substrate Used For growth** | **Transfer Method** | **Sheet Resistance (Ω/sq.)** | **% Transmittance** | **References** |
|---|---|---|---|---|---|---|
| **Chemical Vapor Deposition** | | | | | | |
| *Graphene on glass* | CVD | Ni | Chemical Transfer | 620 | 85 | [37] |
| *Graphene on quartz* | CVD | Ni | Chemical Transfer | 280 | 80 | [33] |
| *Graphene on PET*[a] | CVD | Cu | Hot Press Lamination method | 1.1k | 89 | [38] |
| *Graphene on quartz* | CVD | Cu | Chemical Transfer | ~2000 | 90 | [27] |
| *Graphene on Cu* | CVD | Cu | Roll to Roll transfer | ~125 | 97.4 | [32] |
| **Chemical methods/RGO** | | | | | | |
| *Graphene on quartz* | RGO[b]-Chemical Process | - | Spin coating | 800 | 82 | [39] |

| | | | | | | |
|---|---|---|---|---|---|---|
| *Reduced Graphene Oxide* | RGO chemical process | - | Dip coating | 1.8k | 80 | [12] |
| *Graphene* | RGO | - | Spin coating | $10^5$ | 65 | [40] |

[a] *Polyethylene tetrapthalate;* [b] *Reduced Graphene oxide*

Graphene exhibit remarkable mechanical properties and well known as one of the strongest materials ever measured. In the year 2009, Lee et. al. measured the breaking strength of graphene ~ 42 $Nm^{-1}$ which resemblance of the graphene's in-plane theoretical strength which represents almost defect free graphene sheet. Using atomic force microscopy (AFM) tips they further measured the Young's modulus, third-order elastic stiffness and intrinsic strength of suspended graphene is ~ 1 Tpa (150,000,000 psi), -2.0 TPa and 130 GPa respectively which are higher than steel [13].

## 2.2. Graphene synthesis

### 2.2.1. Overview

Till date, several methods have been developed for graphene synthesis. However, Mechanical Cleaving (Exfoliation)[8], Chemical Exfoliation[41, 42], Chemical Synthesis[43] and Thermal CVD Synthesis are most commonly used methods for graphene synthesis. Some other techniques are also reported so far like unzipping nanotube, microwave synthesis etc; however, those techniques are further required to explore more. The overview of the graphene synthesis techniques are shown in the schematic flow chart in Figure 2.4. In the year of 1975, few graphite layers was synthesized on single crystal platinum surface via chemical decomposition methods but not designated as graphene;

however, due to lack of characterization techniques or may be the scarcity of its possible applications the graphene research were completely ignored that time[44].

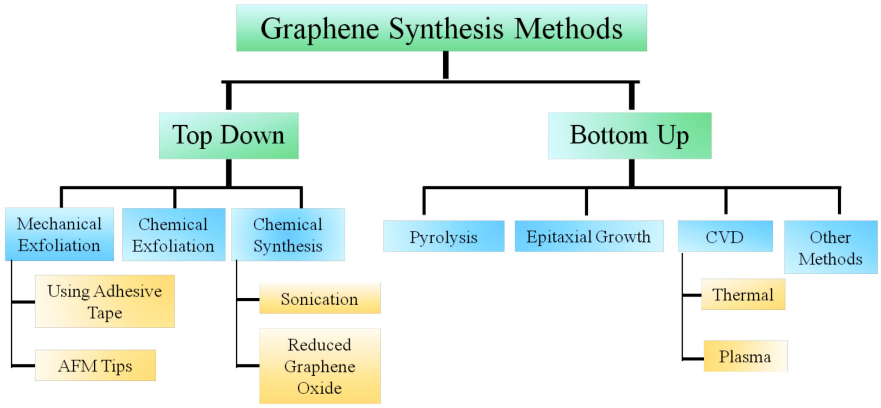


Figure 2.4: A schematic representation of the overview of different graphene synthesis methods [Reprinted with permission from Reference[46]].

In 1999, mechanical cleaving of HOPG by AFM tips was first developed in order to fabricate few layers to monolayer graphite [45]. Nevertheless, mono layer graphene was first produced and reported in the year 2004 where simple scotch tape was used for repeatedly sliced down the graphene layers on any substrate [8]. This technique was found as capable enough to produce different layers of graphene and relatively easy fabrication technique.

Mechanical exfoliation using AFM cantilever also found equally capable of fabricating few layer graphene but the process is limited to production of graphene thickness ~10 nm which is comparable to 30 monolayer graphene or nano-crystalline graphite. Similarly, chemical exfoliation is another method where solution dispersed graphite flakes are exfoliated by inserting large alkali ions between inter-planner layers. On the other hand, reduced graphene oxide method (RGO) consist of several fabrication

steps namely preparation of graphite oxide, disperse in a solution down to the monolayer followed by reduce it with hydrazine are generally called as reduced graphene oxide. Like, carbon nanotube synthesis, catalytic thermal chemical vapor deposition (CVD) is proved to be the best for large scale graphene fabrication where thermally dissociated carbon is deposited on to a catalytically active transition metal catalyst surface to form a honeycomb graphene lattice at elevated temperature under ambient or low pressure. When thermal CVD process is carried out under resistive heating furnace, it is known as thermal CVD, and when the process consists of plasma assisted growth called Plasma Enhanced CVD or PECVD. Particularly, all the techniques stand popular in their individual field of researchers. However, all synthesis methods have their own advantages as well as disadvantages depending upon the desired properties and applications of graphene. For example, mechanically exfoliation method is capable to fabricate different layers of graphene (from monolayer to few layer), whereas the reliability of obtaining similar structure throughout the substrate is quite difficult. Moreover large area, defect free graphene production using mechanical cleaving is a serious challenge at present scenario. Furthermore, chemical synthesis processes (that involve the synthesis of graphite oxide and reduced it back to graphene in a solution disperse condition) are low temperature processes which make easier to fabricate graphene on any types and dimensions of substrates at ambient temperature, particularly on polymeric substrates (those have low melting point). However homogeneity and uniformity of the large area graphene synthesized by this method is not up to the mark. Surface coated with a solution disperse graphene exhibit several layers stacked to each other results in the formation of inhomogeneous film that can gradually degrades the

optical and electrical properties of the film. Furthermore, graphene synthesized from reduced graphene oxides (RGO) are often causes incomplete reduction of graphite oxide (which is insulator) results in the successive degradation of electronics and optoelectronics properties depending on its degree of reduction. In contrast, CVD methods are comparatively advantageous for large area device fabrication and favorable for future CMOS technology by replacing Si[47]. Epitaxial Graphene or thermal graphitization of a SiC surface is one of the candidate, but the excessive high process temperature and inability to transfer on any substrates is a serious drawback of this method. In this context, thermal chemical vapor deposition methods can comparatively produce uniform layer of thermally chemically catalyzed carbon atoms deposited on to the catalyst metal surfaces and thereby can be transferred over a wide range of substrates. However, graphene layer controllability and low temperature graphene fabrication on any substrates, (specifically, substrates with low melting point, like polymer substrate) is another serious limit of this technique.

### 2.1.2. Different methods for graphene synthesis

#### 2.1.2.1. Mechanical exfoliation, chemical exfoliation and RGO method

Mechanical exfoliation was the first recognized method of Graphene synthesis and is one of the top down techniques in nanotechnology, by which a longitudinal or transverse stress is generated on the surface of the layered structure materials using simple scotch tape or AFM tip in order to slice down a single or few layers from the material on to the substrates. Graphite interlayer distance and interlayer Van-der-Walls bond energy is 3.34 Å and 2 eV/nm$^2$ respectively and due to the interlayer weak Van-der

wall force it is relatively easy to separate an atomic layer thin graphite from its bulk. For mechanical cleaving, 300 $nN/\mu m^2$ external forces is required in order to separate one mono-atomic layer from graphite, which is subsequently low [48]. In the year 1999, Ruoff et. al.[45] first proposed the mechanical exfoliation technique of plasma etched pillared HOPG using AFM tip to fabricate layer graphite down to the single layer which later on named as graphene. Later on an abrupt impact has been created on the field of carbon nano-electronics when K. S Novoslov and A. K. Geim from Manchester University first reported the isolation of single graphene on $SiO_2$/Si substrate and its unusual electronics properties. Their novel approach of synthesis and extraordinary properties of thin flake of simple graphite brought them Nobel Prize in Physics in the year of 2010 [49]. The graphene produced by this adhesive tape exfoliation technique was used for Field effect Transistor (FET) brought up a research boom in the field of carbon nanoelectronics. Now days the number of publications based on graphene research increased exponentially due to its scientific and technological significances for future applications. In this context, the process can further be extended for fabricating some of the layered structured materials like Boron Nitide (BN), Molybdenum Di-Silicide ($MoS_2$), $NbSe_2$ and $Bi_2Sr_2CaCu_2O$ [50].

Chemical exfoliation is another top down approach by which alkali metals are intercalated in the graphite structure in order to separate out the 2D graphene layer out of its 3D structure. Alkali metals are periodic table are highly reactive and can easily forms graphite intercalate structure by forming various stoichiometric compounds of graphite with wide range from lower to higher stage of intercalated compounds. R. B. Kanar and his research group from UCLA, first reported their work in Science[42] on chemically exfoliated few layer graphite (later on named as graphene) using potassium (K).

Potassium (K) forms $KC_8$ intercalated complex ($KC_8$) when reacting with graphite at 200$^oC$ under inert helium atmosphere (Less than 1 ppm $H_2O$ and $O_2$). The interacted compound $KC_8$ undergoes an exothermic reaction when reacting with the aqueous solution of Ethanol ($CH_3CH_2OH$) as per the equation 2.1.

$$KC_8 + CH_3CH_2OH \longrightarrow 8C + KOCH_2CH_3 + 1/2H_2 \quad (2.1)$$

Later on, the area was further explored using the exfoliation process with a variety of alkali metals like Cs and their alloys like $NaK_2$[51]. Unlike Li and Na, K ionization potential (4.34 eV) is less than graphite's electron affinity (4.6 eV), thus react directly with graphite in order to form intercalated compounds. Cs (3.894 eV) possesses lower ionization potential than K (4.34 eV), therefore, react with graphite more violently than potassium which brings into a significant improvement in intercalation of graphite at sufficiently low temperature and pressure. Similarly, Sodium-potassium alloy (Na-$K_2$) form eutectic melt at -12.62$^oC$, expected to occur rapid exfoliation reaction at room temperature which can separate out the graphene layers of thickness from 2 nm to 150 nm.

Chemical Synthesis is a top-down indirect synthesis method of graphene and more preciously, first ever method which demonstrated the graphene synthesis by chemical route. In the year 1962, Boehm et al. first demonstrated monolayer flakes of reduced graphene oxide which is recently acknowledged by the graphene inventor A. K. Geim[52-54]. The method involve the synthesis of a graphite derivative namely graphite oxide (GO), disperse the flakes by sonication followed by reduced it back to graphene. Three typically used for GO synthesis methods are knows as follows: i) Brodie[55], ii) Staudenmaier[56] , and iii) Hummers and Offeman[57] method. All three methods involve

graphite as a precursor material which turns into GO in presence of strong acids and oxidants. The degree of the oxidation can be varied by the reaction conditions (e.g. temperature, pressure etc.), stoichiometry and the type of precursor graphite used for the reaction. Despite of a wide range of research has been carried out already to describe the atomic structure of GO, still several models are under debate to explain the atomic structure of GO. GO was first prepared by Brodie et. al.[55], a chemist of Oxford University, in the nineteenth century by mixing graphite with potassium chlorate and nitric acid. However, the process contains several steps which are time consuming, unsafe and hazardous. In the year of 1958, W .S. Hummers [57] developed the oxidation method for graphite by the mixing graphite with sodium nitrite, sulphuric acid and potassium permanganate, very popular as Hummers method.

As graphite turns into graphite oxide, the interlayer spacing is increased two or three times higher than the graphite. For graphite, the interlayer distance is 3.34 Å which expanded up to 5.62 Å after 1 hour oxidative reaction and then further expands to 7.0 ±0.35 Å upon prolonged oxidation to 24 hours. Boehm et. al. reported that the interlayer distance can be further increased by inserting polar liquids e.g. sodium hydroxide. Therefore it helps to expand further interlayer distance which in fact separates a single layer from the bulk GO. Furthermore, GO reduces back to graphene by reacting with hydrazine hydrate. The whole process flow chart is illustrated as follows in the schematic in Figure 2.5.

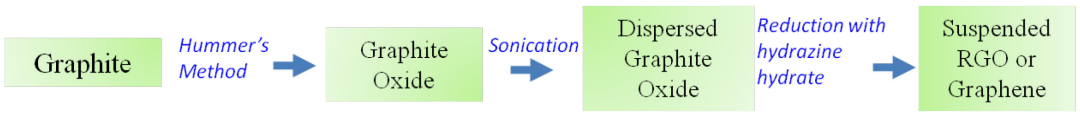


Figure 2.5: A schematic representation of the process steps of graphene synthesis by chemical method [Reprinted with permission from Reference[46]].

Chemical reduction process is carried out using dimethylhydrazine or hydrazine in the presence of either polymer or surfactant in order to produce homogeneous colloidal suspensions of electrically conducting graphene. The method was brought into focus again in the year of 2006 when Ruoff and his coworkers from Northwestern University, was the first to report the solution-based process for producing mono-atomic graphene layer[58, 59]. GO is a stacked layer of squeezed sheets with AB stacking which exhibit oxygen containing functional group like hydroxyl and epixoide to their basal plane when highly oxidized as reported in a separate report [60]. Stankovich et al. showed that chemical functionalized GO flakes by organic molecules can homogeneously suspended in organic solvents [59]. They reported that reaction of graphite oxide with isocyanate group results in isocyanate-modified graphene oxide sheets those are well dispersed in polar solvents like DMF, N-methylpyrrolidone (NMP), dimethyl sulfoxide (DMSO), hexamethylphosphoramide (HMPA) etc. Xu et. al.[61] further reported the colloidal suspensions of chemically modified graphene (CMG) decorated with small non-covalently functionalized organic molecules like 1-pyrenebutyrate ($PB^-$). In this regard, few reports have also been found related to the stabilizers or surfactants free synthesis methods. Li. et. al. demonstrated the surfactants and stabilizer free aqueous suspension (0.5 mg $ml^{-1}$) of RGO sheets under basic conditions (pH 10)[62]. Tung et. al. reported

oxygen functionalities free GO and restore the planar geometry of the single sheets of graphene at large scale. In this report, large-scale (~20 mm × 40 mm) solution processed production of single-layer chemically converted graphene (CCG) over the entire area of a $SiO_2$/Si wafer has been demonstrated[63]. However, the approach of Tung et al. is somewhat different as they reduced as well as dispersed the GO film directly in hydrazine which creates hydrazinium graphene (HG) through the formation of counter ions. Nevertheless, the process needs to be improved further for large scale, defect free, high purity graphene for its feasible applications in nano-electronics. In this regard, Liang et. al. proposed an interesting method for wafer scale graphene fabrication by cut-and-choose transfer printing method for integrated circuit, but still uniform large scale graphene fabrication with controlled layer is still under challenge[64].

Chemical Synthesis or RGO process is versatile as it is a low cost solution-phase method, scalable, and would be capable of depositing graphene in wide range of substrates which is comparatively difficult using other process as mentioned before. Furthermore, the method can be extended to produce graphene-based composites/films which are the key requirement for many other composite applications, such as thin-film transistors, transparent conductive electrodes in order to replace costly, fragile and toxic existing indium tin oxide.

Chemical synthesis possesses several advantages like, low temperature process therefore, readily processed on any polymeric substrates. The low temperature process always beneficial to control the wide range of large scale fabrication. In-situ functionalization of graphene sheet with different polymers, organic functional group,

hydrophobic and hydrophilic groups can easily carried out using this method for several chemical and bio applications. Despite all, the most exciting features of this process is low cost as graphite is abundant (supplied natural graphite worldwide has been estimated at 800M tones) in the nature. Free Standing graphene produced by this method also exhibit high tensile strength up to 42 GPa. However, the chemical synthesis process has several disadvantages like small yield, defective graphene, partially reduced GO which readily degrade graphene properties. On the other hand, the process involves lot many hectic and tedious steps which involve the handling of hazardous explosive chemicals etc. During chemical reduction of GO, incomplete reduction dictate the possible deterioration of the conductivity, charge carrier concentration, carrier mobility etc. As GO is an insulator, a sharp degradation in electrical properties are observed based on the degree of reduction. Similarly, introduction of defects in the final product results in the lowering in electronics properties of graphene. Although GO well disperse in a solvent due to the hydrophilic ions are attached with the basal planes, however, to prepare suspended pure graphene is another challenge of this synthesis technique as monolayer graphene exhibits high surface area, therefore readily segregated when reduced. During the chemical synthesis, complete removal of residue amount of chemicals like, acids, bases, hydrazine etc. are difficult; therefore, the purity of the final product is still not up to the mark.

Several other methods of graphene synthesis have already been established. Few of them are as follows: unzipping nanotubes, epitaxial growth on SiC, direct pyrolysis etc. The unzipping of nanotube yields the thin elongated strip of graphene with straight edges, named as graphene nano-ribbons (GNR). Graphene, when narrowing down along

the width, deliberately transforms its electronic state from semimetals to semiconductors[65]. Therefore the electronics properties of thin strip of graphene nano ribbons are also under vigorous investigation at this moment[66, 67]. Depending upon the starting nanotube, whether they are multi-walled or single walled, final product will be multi-layered graphene or single layer graphene respectively.

### 2.1.2.2. Graphene synthesis using chemical vapor deposition process

Thermal Chemical vapor deposition (CVD) is a high temperature chemical process by which a substrate is exposed to volatile precursors/gases which when react to each other formed the desired product deposited onto the substrate surface. The process is well known in the academic and industry as a thermal chemical vapor deposition process or chemical vapor deposition process. In the early research of graphite synthesis Eizenberg and his coworkers reported the graphite layer formation on Ni (111) at high temperatures[68]. They reported the carbon phase condensation on Ni (111) with detail thermodynamic analysis which shows the enthalpy and entropy of carbon segregation on Ni (111) is $\Delta H_{seg}$ = -0.55 +/- 0.01 eV; $\Delta S_{seg}$ = 0.17+0.13-0.07 k respectively. Finally, they concluded that, the carbon phase segregation on Ni (111) is solely depending upon the rate of quenching.

Table 2.3: Represents a brief summary of graphene synthesis status using CVD method.

| Substrate used | Substrate Preparation | Growth Temperature ($^oC$) | Growth Pressure | Precursor Materials | No. of Layer of graphene | Reference |
|---|---|---|---|---|---|---|
| *Cu* | Annealing at 990$^o$C, 20 mbar | 880-980 | 0.1-1 mbar | $CH_4$, Ar and $H_2$ | 1- Few layers | 29 |

| | | | | | | |
|---|---|---|---|---|---|---|
| *Cu* | Annealing at 1000°C | 1000 | 1 atm pr. | $CH_4$, $H_2$ and Ar | Few Layers | 69 |
| *Cu* | Annealing | 1000 | 500 mTorr | $CH_4$, $H_2$ and Ar | Monolayer | 31 |
| *Cu* | Chemical Treatment using 1M acetic acid | 850 | 1 torr | Liquid precursors like methanol, ethanol, and propanol | Monolayer | 70 |
| *Thin film Cu* | Epitaxial Thin film on Alumina | 1000 | 700 mTorr | $CH_4$, $H_2$ | Monolayer | 71 |
| *Cu* | Spin coating with PMMA | 800-1000 | 30 mTorr | Solid Carbon: poly(methyl methacrylate) (PMMA) | Monolayer | 72 |
| *Ni Thin Film* | - | 1000 | - | $CH_4$, $H_2$, Ar | 1- Few layers | 33 |
| *$SiO_2$/Si* | 100-400 nm e-beam evaporated Cu | 1000 | 100-500 mTorr | | | 73 |
| *$SiO_2$/Si* | Formation of diffusion couple made up of carbon-nickel/substrate | 25-160 | - | carbon-nickel/substrate | 1-few | 74 |
| *Ni-Mo Alloy* | - | 1000 | 1 atm pr. | $CH_4$, $H_2$ | Monolayer graphene | 75 |
| *Pt* | - | 750 | 1 atm pr. | $CH_4$, $H_2$ | Monolayer | 28 |

Several other reports were also found regarding different condition and morphologies of graphene formation over several noble and transition metals. Large area graphene synthesis traverse a unique direction when Ruoff group discovered catalytic graphene deposition on Cu occurs at elevated temperature, by decomposition of hydrocarbon gases[31]. They showed single layer uniform large area (1 $cm^2$) graphene growth on Cu foil by thermal CVD technique. This method involve heating the quartz tube furnace ~ 1000$^oC$ in hydrogen atmosphere with pressure of 40 mTorr under a 2 sccm flow, annealed the Cu film at 1000$^oC$ followed by introducing 35 sccm of methane gas ($CH_4$) at ~500 mTorr ambient pressure. The following Table 2 illustrates different graphene synthesis techniques in CVD using different catalyst, temperatures, pressures, gas flow rates etc by a wide number of research groups worldwide reported recently.

### 2.3. Graphene transfer to any substrates

Due to some technical constraints as grown graphene layers cannot be used for electronics applications and hence need to be transfer in different dielectric substrates. Presently, the major graphene transfer process is chemical floating process. Different other methods like hot press lamination methods for graphene/polymer flexible film and roll to roll production of graphene on Flexible PET has also been demonstrated. Several graphene transfer processes like stamping technique and bubbling transfer also proposed for large scale direct transfer methods[32, 38]. Bae et al.[32] reported the roll to roll production of graphene of area as large as 30 inch diagonal length as shown in the Figure and demonstrated as touch screen panel. The transfer process involve the following steps: i) Attachment of a thermal release tape on the top surface of Cu foil coated with graphene

ii) Etched away Cu using Cu-etchant iii) then the thermal release tape was inserted between the rollers together with a target substrate and finally, iv) exposed the whole system together in a mild heat (90–120 $^{o}$C). They demonstrated the transparent conducting film of transparency ~ 97.4% and sheet resistance ~ 125/sq.

## 2.4. Graphene: doping and functionalization: tailoring properties

Till date doping of graphene or functionalization of graphene create a lot research interest in order to tailor graphenes' properties for further device applications. Table 2.4: summarizes the different doping elements with their corresponding effects on development of graphene properties. Correspondingly, several other reports are also found based on graphene functionalization with poly (m-phenylenevinylene-co-2,5-dioctoxy-p-phenylenevinylene)(PmPV)[96], 1,2-distearoyl-sn-glycero-3-phosphoethanolamine-N[methoxy(polyethyleneglycol)-5000](DSPE-mPEG) [97], poly(tert-butyl acrylate) and so on. In view of technological applications, several recent reports are found based on the poly(N-vinyl pyrrolidone) graphene naocomposite for humidity sensing[98], GO-polymer for organic solar cells[99], Dye sensitized solar cell[100, 101] Organic memory devices[102], Li ion battery[103] and so on. Apart from the stable dispersion of graphene with different polymer and surfactants, some recent reports also available based on the modification of graphene with inorganic nano-particles like Au[104], $TiO_2$[105, 106], $Fe_3O_4$[107]and CuO[108] etc.

Table 2.4: Illustrates the list of doping elements with their corresponding effect on the improvement of graphene properties.

| Graphene doping or functionalization with | Properties | Applications | References |
|---|---|---|---|
| *Chlorine ($Cl^-$)* | The graphene resistance increases 4 folds of magnitude and a band gap appears upon photochlorination<br><br>Band Gap opening | Electronics and Photochemical<br><br>Field Effect Transistors | 76 |
| *Bromine ($Br^-$)* | Band gap opening<br><br>Work Function Shifts, band gap formation | Semiconductor technology, Sensors<br><br>- | 77<br><br>78 |
| *Iodine ($I^-$)* | Work Function shifts, band gap formation | - | 78 |
| *Sodium ($Na^+$)* | Work function Changes | - | 79 |
| *Potassium ($K^+$)* | charged impurity density can be controlled by potassium doping | - | 80 |
| *Fluorine ($F^-$)* | p-type doping, work function changes<br><br>Perfluorographane (CF) formation with the calculated band gap ~3.07 eV<br><br>Excessive hole doping | Electrochemical applications,<br><br>Electronics and optoelectronics applications<br><br>Transistors applications p-n-n device | 69<br><br>81<br><br>82 |

| | | | |
|---|---|---|---|
| *Nitric Acid ($HNO_3$)* | Conductivity Increases | Transparent Conducting Oxide | 83 |
| *Gold nanoparticles (Au)* | Conductivity Increases | Transparent Conducting Oxide | 84 |
| *Nitrogen (N)* | charge-carrier densities and enhance the electrical or thermal conductivities<br><br>n-type doping<br><br>Electro-catalytic activity | Electrochemical Sensing, energy storage<br><br>Li ion battery<br><br>Fuel Cells | 85<br><br>86 |
| *Boron (B)* | Electro-catalyst<br><br>Electronics Structure, Carrier concentrations<br><br>p-type doping | Fuel Cells<br><br>-<br><br>Li ion battery | 87<br><br>88, 89<br><br>85 |
| *Oxygen (O)* | Hole doping<br><br>electron–hole transport asymmetry, intrinsic energy gap | -<br><br>Electronics | 90<br><br>91 |
| *Hydrogen* | Enhances thermal conductivity | Electronics, heat dissipation | 92 |
| *Sulfur (S)* | Enhances Electro-catalytic activity | Oxygen reduction for fuel cells | 93 |
| *Selenium (Se)* | Enhances Electro-catalytic activity | Oxygen reduction for fuel cells | 93 |
| *Toluene ($C_6H_5CH_3$)* | toluene acts as a donor, but that the transfer of electrons can be controlled by an electric field, Fermi energy shift | Electrochemical Charge transfer | 94 |

| | | | |
|---|---|---|---|
| *Sulfonated polyaniline* | Electro-catalyst | Electro-catalysis and electrochemical sensing | 95 |

## 2.5. Graphene carbon nanotube hybrid structure synthesis: status & prospects

Graphene and carbon nanotubes(CNTs) have significant potential for applications in electronics, but the discontinuities in the metal to graphene (or CNTs) contacts is the primary source for the reduction in thermal and electrical conductivity. In recent years two-dimensional (2D) carbon nano structure, graphene, and one-dimensional (1D) carbon nanotubes(CNTs) have initiated enormous research activities due to their exceptional properties like high current carrying capacity, ballistic charge transport, high thermal conductivity, chemical inertness, high mechanical strength and excellent electron emission at nanometer scale [1, 4, 5, 8, 23, 109-119]. The outcome of those exceptional properties have led to demonstration of various prototype devices in every aspect including field emission cathode, sensors, alternative energy generations and storage and so on [5, 110-112, 116, 118-120]. Despite of the applications based on individual graphene and individual CNT, applications based on the hybrid composite structure of graphene and CNT have also been proposed in few reports to utilize both the planner and axial properties [117, 118, 121]. This hetero-junction structure of graphene and CNT combine their individual properties in nano-scale including both planar and axial directions respectively. As we know, the thermal conductivity of a multi wall nanotube (MWNT) is ~3000 W/mK which reduces by several orders even up to 20 W/mK or lower when the MWNTs forms as a mat or forest structure [116, 117]. The discontinuities in the metal contacts joining the bottom part of CNT mat structure forms the schottky junction which is the primary reason for the

reduction in thermal conductivity [116, 117]. Similarly, electrical conductivity is also affected due to the hybrid junction formed between the CNT and metals (i.e. ohmic or schottky) that also influences the electrical transport properties in nano-scale [109, 116, 117, 121-123]. Some of these limitations can be solved by the unique graphene-carbon nanotube hybrid film, consisting of CNTs connected perpendicularly to graphene layers. This hetero-junction formed in-situ during the growth process can result in a junction between all the concentric walls of the CNT with graphene thus forming an electrically and mechanically stable nano-contact. One most interesting approach was found to grow vertically aligned MWNTs on spin coated stacked graphene oxide platelets in a two step process in order to prepare a composite graphene-MWNT hybrid structure and transfer it to a flexible polymer substrate [124]. Several hybrid structures have also been demonstrated till date in focus to other electronics applications.

## 2.6. Dye sensitized solar cell

Carbon nanomaterials are potential low cost counter electrodes for tri-iodide reduction in dye sensitized solar cells due to its good catalytic activity and excellent stability. The electrocatalytic reduction $I_3^-$ to $I^-$ at CE dictating the cathodic activity of DSSCs and influences on current generation at photo-anode counter-part through dye-regeneration[105, 120, 125-127]. Different allotropes of carbon like Carbon black, amorphous carbon, glassy carbon etc. has been demonstrated as unique low cost high stability electrocatalytic electrodes for DSSC. The advantages of carbonaceous materials are i) chemically inert, ii) high surface area, iii) conductive and iv) electro-catalytically active. However, the further improvement of conductivity and catalytic activity of the

carbonaceous materials is required for improved performance of DSSCs. In this context, MWCNT and SWCNT have been widely proposed as potential materials for dye sensitized solar cell counter electrodes as utilizing the high surface area of carbon nanomaterials provide greater versatility as a counter electrode in DSSCs. The potential advantages of the carbon nanotubes are their high surface area and high conductivity. However, the transparency and the uniform bottom contacts are not up to the mark which limits the voltage drops at the CE-electrolyte interface. Moreover the carbon nanotubes based DSSC CE possesses low catalytic activities as the surface of the CNTs are not so electro-catalytically active.

Graphene is newly discovered 2D material exhibits high carrier mobility, good mechanical properties, high transparency and excellent thermal stability[1, 8, 128-130]. To date, considerable works have been demonstrated in applications of graphene including transistors, super-capacitors, solar cells etc [5, 8, 12, 131, 132]. In particular, application of graphene as an electro-catalytic electrode in electrochemical solar cells with the enhanced efficiency is of great interest[12, 99, 101, 133-135]. Since graphene has been exhibited remarkable transmittance in the entire light spectrum including near infra-red (IR) region, it is an added advantage of its application in high efficiency solar cell for absorbing more light photons from the solar spectrum[12, 38, 136, 137]. In addition to this, graphene exhibits remarkable mechanical properties with excellent flexibility which can transfer on any flexible substrates using several facile and scalable methods[32, 38]. This versatile transformation property remains a promising opportunity for developing light-weighted flexible electrodes for flexible electronics[32, 33, 38]. The transferred graphene layer shows excellent continuity in its electrical properties even under different stretching and

bending conditions. In this context, there has been substantial interest for applying graphene as counter electrode towards tri-iodide reduction would offer enticing possibilities in flexible conducting counter electrode for dye-sensitized solar cells (DSSCs). However, the inert graphene basal planes restrict faster charge transfer at the counter electrodes-electrolyte interfaces with limited catalytic activities. The surface modification protocols, either via chemical modification or physical treatment of graphene, are paid great attraction to increase the chemical reactivity of graphene for counter electrode for DSSCs[100, 134, 138, 139]. It has been well reported that graphite intercalation compounds (GICs) significantly improve the conductivity and in-plane charge transfer compare to the graphite[140]. Although high in-plane charge conductivity and mobility the inert nature of graphene basal plane often restricts the graphene/liquid interfacial charge transfer, hence tri-iodide reduction occurs only through their edge planes. Thus, surface modification is required for improving their in-line charge transfer characteristic and being performed as efficient catalytic counter electrode for tri-iodide reduction in DSSCs. Recently, Hasin et.al. report surface modification of graphene using water-soluble polymers (polyelectrolyte) whose ionic charge has modifying the surface adsorption properties of graphene toward $I^-/I_3^-$ reduction[100]. Similarly, Roy-Mayhew et. al. demonstrate the enhancement of apparent electro-catalytic activity of graphene by functionalize graphene using poly(ethylene-oxide)-poly (propylene-oxide)-poly(ethylene-oxide) tri-block copolymer[101]. Apart from the tri-iodide reduction, other Co-based redox couples can be easily reduced at the graphene based CE interface, therefore can be used in a wide range of redox electrolytes. However, improved charge

transfer characteristic of graphene towards $I^-/I_3^-$ reduction in DSSCs is still unexplored and remains challenge.

**References**


1. Geim, A. K.; Novoselov, K. S., The rise of graphene. *Nat Mater* 2007, 6, 183-191.

2. Castro Neto, A. H.; Guinea, F.; Peres, N. M. R.; Novoselov, K. S.; Geim, A. K., The electronic properties of graphene. *Reviews of Modern Physics* 2009, 81, 109-162.

3. Geim, A. K., Graphene: Status and Prospects. *Science* 2009, 324, 1530-1534.

4. Geim, A. K.; Kim, P., Carbon wonderland. *Scientific American* 2008, 298, 90-97.

5. Choi, W.; Lahiri, I.; Seelaboyina, R.; Kang, Y. S., Synthesis of Graphene and Its Applications: A Review. *Critical Reviews in Solid State and Materials Sciences* 2010, 35, 52-71.

6. Novoselov, K. S.; Geim, A. K.; Morozov, S. V.; Jiang, D.; Katsnelson, M. I.; Grigorieva, I. V.; Dubonos, S. V.; Firsov, A. A., Two-dimensional gas of massless Dirac fermions in graphene. *Nature* 2005, 438, 197-200.

7. Novoselov, K. S.; Jiang, Z.; Zhang, Y.; Morozov, S. V.; Stormer, H. L.; Zeitler, U.; Maan, J. C.; Boebinger, G. S.; Kim, P.; Geim, A. K., Room-Temperature Quantum Hall Effect in Graphene. *Science* 2007, 315, 1379-1379.

8. Novoselov, K. S.; Geim, A. K.; Morozov, S. V.; Jiang, D.; Zhang, Y.; Dubonos, S. V.; Grigorieva, I. V.; Firsov, A. A., Electric field effect in atomically thin carbon films. *Science* 2004, 306, 666-669.

9. Kozlov, S. M.; Viñes, F.; Görling, A., Bandgap Engineering of Graphene by Physisorbed Adsorbates. *Advanced Materials* 2011, 23, 2638-2643.

10. Balandin, A. A.; Ghosh, S.; Nika, D. L.; Pokatilov, E. P., Thermal Conduction in Suspended Graphene Layers. *Fullerenes Nanotubes and Carbon Nanostructures* 2010, 18, 474-486.

11. Bi, H.; Huang, F.; Liang, J.; Xie, X.; Jiang, M., Transparent Conductive Graphene Films Synthesized by Ambient Pressure Chemical Vapor Deposition Used as the Front Electrode of CdTe Solar Cells. *Advanced Materials* 2011, 23, 3202-3206.

12. Wang, X.; Zhi, L. J.; Mullen, K., Transparent, conductive graphene electrodes for dye-sensitized solar cells. *Nano Letters* 2008, 8, 323-327.

13. Lee, C.; Wei, X. D.; Kysar, J. W.; Hone, J., Measurement of the elastic properties and intrinsic strength of monolayer graphene. *Science* 2008, 321, 385-388.

14. Yuan, S. J.; De Raedt, H.; Katsnelson, M. I., Electronic transport in disordered bilayer and trilayer graphene. *Physical Review B* 2010, 82.

15. Shih, C.-J.; Vijayaraghavan, A.; Krishnan, R.; Sharma, R.; Han, J.-H.; Ham, M.-H.; Jin, Z.; Lin, S.; Paulus, G. L. C.; Reuel, N. F.; Wang, Q. H.; Blankschtein, D.; Strano, M. S., Bi- and trilayer graphene solutions. *Nat Nano* 2011, 6, 439-445.

16. Jhang, S. H.; Craciun, M. F.; Schmidmeier, S.; Tokumitsu, S.; Russo, S.; Yamamoto, M.; Skourski, Y.; Wosnitza, J.; Tarucha, S.; Eroms, J.; Strunk, C., Stacking-order dependent transport properties of trilayer graphene. *Physical Review B* 2011, 84, 161408.

17. Yan, J.-A.; Ruan, W. Y.; Chou, M. Y., Phonon dispersions and vibrational properties of monolayer, bilayer, and trilayer graphene: Density-functional perturbation theory. *Physical Review B* 2008, 77, 125401.

18. Ohta, T.; Bostwick, A.; Seyller, T.; Horn, K.; Rotenberg, E., Controlling the electronic structure of bilayer graphene. *Science* 2006, 313, 951-954.

19. Wang, Y. Y.; Ni, Z. H.; Yu, T.; Shen, Z. X.; Wang, H. M.; Wu, Y. H.; Chen, W.; Wee, A. T. S., Raman studies of monolayer graphene: The substrate effect. *Journal of Physical Chemistry C* 2008, 112, 10637-10640.

20. Hass, J.; de Heer, W. A.; Conrad, E. H., The growth and morphology of epitaxial multilayer graphene. *Journal of Physics-Condensed Matter* 2008, 20, 27.

21. Lui, C. H.; Li, Z. Q.; Chen, Z. Y.; Klimov, P. V.; Brus, L. E.; Heinz, T. F., Imaging Stacking Order in Few-Layer Graphene. *Nano Letters* 2011, 11, 164-169.

22. Bao, W.; Jing, L.; Velasco, J.; Lee, Y.; Liu, G.; Tran, D.; Standley, B.; Aykol, M.; Cronin, S. B.; Smirnov, D.; Koshino, M.; McCann, E.; Bockrath, M.; Lau, C. N., Stacking-dependent band gap and quantum transport in trilayer graphene. *Nat Phys* 2011, 7, 948-952.

23. Katsnelson, M. I., Graphene: carbon in two dimensions. *Materials Today* 10, 20-27.

24. Morozov, S. V.; Novoselov, K. S.; Katsnelson, M. I.; Schedin, F.; Elias, D. C.; Jaszczak, J. A.; Geim, A. K., Giant Intrinsic Carrier Mobilities in Graphene and Its Bilayer. *Physical Review Letters* 2008, 100, 016602.

25. Chen, J.-H.; Jang, C.; Xiao, S.; Ishigami, M.; Fuhrer, M. S., Intrinsic and extrinsic performance limits of graphene devices on SiO2. *Nat Nano* 2008, 3, 206-209.

26. Akturk, A.; Goldsman, N., Electron transport and full-band electron-phonon interactions in graphene. *Journal of Applied Physics* 2008, 103, 053702-8.

27. Li, X. S.; Zhu, Y. W.; Cai, W. W.; Borysiak, M.; Han, B. Y.; Chen, D.; Piner, R. D.; Colombo, L.; Ruoff, R. S., Transfer of Large-Area Graphene Films for High-Performance Transparent Conductive Electrodes. *Nano Letters* 2009, 9, 4359-4363.

28. Gao, L.; Ren, W.; Xu, H.; Jin, L.; Wang, Z.; Ma, T.; Ma, L.-P.; Zhang, Z.; Fu, Q.; Peng, L.-M.; Bao, X.; Cheng, H.-M., Repeated growth and bubbling transfer of graphene with millimetre-size single-crystal grains using platinum. *Nat Commun* 2012, 3, 699.

29. Liu, W.; Li, H.; Xu, C.; Khatami, Y.; Banerjee, K., Synthesis of high-quality monolayer and bilayer graphene on copper using chemical vapor deposition. *Carbon* 2011, 49, 4122-4130.

30. Li, X.; Magnuson, C. W.; Venugopal, A.; Tromp, R. M.; Hannon, J. B.; Vogel, E. M.; Colombo, L.; Ruoff, R. S., Large-Area Graphene Single Crystals Grown by Low-Pressure Chemical Vapor Deposition of Methane on Copper. *Journal of the American Chemical Society* 2011, 133, 2816-2819.

31. Li, X. S.; Cai, W. W.; An, J. H.; Kim, S.; Nah, J.; Yang, D. X.; Piner, R.; Velamakanni, A.; Jung, I.; Tutuc, E.; Banerjee, S. K.; Colombo, L.; Ruoff, R. S., Large-Area Synthesis of High-Quality and Uniform Graphene Films on Copper Foils. *Science* 2009, 324, 1312-1314.

32. Bae, S.; Kim, H.; Lee, Y.; Xu, X. F.; Park, J. S.; Zheng, Y.; Balakrishnan, J.; Lei, T.; Kim, H. R.; Song, Y. I.; Kim, Y. J.; Kim, K. S.; Ozyilmaz, B.; Ahn, J. H.; Hong, B. H.; Iijima, S., Roll-to-roll production of 30-inch graphene films for transparent electrodes. *Nature Nanotechnology* 2010, 5, 574-578.

33. Kim, K. S.; Zhao, Y.; Jang, H.; Lee, S. Y.; Kim, J. M.; Ahn, J. H.; Kim, P.; Choi, J. Y.; Hong, B. H., Large-scale pattern growth of graphene films for stretchable transparent electrodes. *Nature* 2009, 457, 706-710.

34. Emtsev, K. V.; Bostwick, A.; Horn, K.; Jobst, J.; Kellogg, G. L.; Ley, L.; McChesney, J. L.; Ohta, T.; Reshanov, S. A.; Rohrl, J.; Rotenberg, E.; Schmid, A. K.; Waldmann, D.; Weber, H. B.; Seyller, T., Towards wafer-size graphene layers by atmospheric pressure graphitization of silicon carbide. *Nature Materials* 2009, 8, 203-207.

35. Tedesco, J. L.; VanMil, B. L.; Myers-Ward, R. L.; McCrate, J. M.; Kitt, S. A.; Campbell, P. M.; Jernigan, G. G.; Culbertson, J. C.; Eddy, J. C. R.; Gaskill, D. K., Hall effect mobility of epitaxial graphene grown on silicon carbide. *Applied Physics Letters* 2009, 95, 122102-3.

36. Bolotin, K. I.; Sikes, K. J.; Jiang, Z.; Klima, M.; Fudenberg, G.; Hone, J.; Kim, P.; Stormer, H. L., Ultrahigh electron mobility in suspended graphene. *Solid State Communications* 2008, 146, 351-355.

37. Jo, G.; Choe, M.; Cho, C. Y.; Kim, J. H.; Park, W.; Lee, S.; Hong, W. K.; Kim, T. W.; Park, S. J.; Hong, B. H.; Kahng, Y. H.; Lee, T., Large-scale patterned multi-layer graphene films as transparent conducting electrodes for GaN light-emitting diodes. *Nanotechnology* 2010, 21.

38. Verma, V. P.; Das, S.; Lahiri, I.; Choi, W., Large-area graphene on polymer film for flexible and transparent anode in field emission device. *Applied Physics Letters* 2010, 96.

39. Wu, J.; Agrawal, M.; Becerril, H. c. A.; Bao, Z.; Liu, Z.; Chen, Y.; Peumans, P., Organic Light-Emitting Diodes on Solution-Processed Graphene Transparent Electrodes. *ACS Nano* 2009, 4, 43-48.

40. Eda, G.; Lin, Y.-Y.; Miller, S.; Chen, C.-W.; Su, W.-F.; Chhowalla, M., Transparent and conducting electrodes for organic electronics from reduced graphene oxide. *Applied Physics Letters* 2008, 92, 233305-3.

41. Allen, M. J.; Tung, V. C.; Kaner, R. B., Honeycomb Carbon: A Review of Graphene. *Chemical Reviews* 2010, 110, 132-145.

42. Viculis, L. M.; Mack, J. J.; Kaner, R. B., A Chemical Route to Carbon Nanoscrolls. *Science* 2003, 299, 1361-1361.

43. Park, S.; Ruoff, R. S., Chemical methods for the production of graphenes. *Nature Nanotechnology* 2009, 4, 217-224.

44. Lang, B., A LEED study of the deposition of carbon on platinum crystal surfaces. *Surface Science* 1975, 53, 317-329.

45. Lu, X. K.; Yu, M. F.; Huang, H.; Ruoff, R. S., Tailoring graphite with the goal of achieving single sheets. *Nanotechnology* 1999, 10, 269-272.

46. Choi, W.; Lee, J.-w., *Graphene : synthesis and applications*. CRC Press ; Taylor & Francis: Boca Raton London, 2012; p xv, 370 p.

47. Sutter, P., EPITAXIAL GRAPHENE How silicon leaves the scene. *Nature Materials* 2009, 8, 171-172.

48. Zhang, Y. B.; Small, J. P.; Pontius, W. V.; Kim, P., Fabrication and electric-field-dependent transport measurements of mesoscopic graphite devices. *Applied Physics Letters* 2005, 86.

49. The rise and rise of graphene. *Nature Nanotechnology* 2010, 5, 755-755.

50. Novoselov, K. S.; Jiang, D.; Schedin, F.; Booth, T. J.; Khotkevich, V. V.; Morozov, S. V.; Geim, A. K., Two-dimensional atomic crystals. *Proceedings of the National Academy of Sciences of the United States of America* 2005, 102, 10451-10453.

51. Viculis, L. M.; Mack, J. J.; Mayer, O. M.; Hahn, H. T.; Kaner, R. B., Intercalation and exfoliation routes to graphite nanoplatelets. *Journal of Materials Chemistry* 2005, 15, 974-978.

52. Hanns-Peter, B., Graphen - wie eine Laborkuriosität plötzlich äußerst interessant wurde. *Angewandte Chemie* 2010, n/a.

53. Hanns-Peter, B., Graphene-How a Laboratory Curiosity Suddenly Became Extremely Interesting. *Angewandte Chemie International Edition* 2010, n/a.

54. Boehm, H. P.; Clauss, A.; Fischer, G. O.; Hofmann, U. D., Adsorptionsverhalten sehr dunner Kohlenstoff-Folien. *Anorg. Allg. Chem.* 1962, 316, 119–127

55. Brodie, B. C., Sur le poids atomique du graphite. *Ann. Chim. Phys.* 1860, 59, 466

56. Staudenmaier, L., Verfahren zur Darstellung der Graphitsaure. *Ber. Deut. Chem. Ges.* 1898, 31, .

57. Hummers, W. S.; Offeman, R. E., Preparation of Graphitic Oxide. *Journal of the American Chemical Society* 1958, 80, 1339-1339.

58. Stankovich, S.; Dikin, D. A.; Dommett, G. H. B.; Kohlhaas, K. M.; Zimney, E. J.; Stach, E. A.; Piner, R. D.; Nguyen, S. T.; Ruoff, R. S., Graphene-based composite materials. *Nature* 2006, 442, 282-286.

59. Stankovich, S.; Piner, R. D.; Nguyen, S. T.; Ruoff, R. S., Synthesis and exfoliation of isocyanate-treated graphene oxide nanoplatelets. *Carbon* 2006, 44, 3342-3347.

60. Jeong, H. K.; Lee, Y. P.; Lahaye, R.; Park, M. H.; An, K. H.; Kim, I. J.; Yang, C. W.; Park, C. Y.; Ruoff, R. S.; Lee, Y. H., Evidence of graphitic AB stacking order of graphite oxides. *Journal of the American Chemical Society* 2008, 130, 1362-1366.

61. Xu, Y. X.; Bai, H.; Lu, G. W.; Li, C.; Shi, G. Q., Flexible graphene films via the filtration of water-soluble noncovalent functionalized graphene sheets. *Journal of the American Chemical Society* 2008, 130, 5856-+.

62. Li, D.; Muller, M. B.; Gilje, S.; Kaner, R. B.; Wallace, G. G., Processable aqueous dispersions of graphene nanosheets. *Nature Nanotechnology* 2008, 3, 101-105.

63. Tung, V. C.; Allen, M. J.; Yang, Y.; Kaner, R. B., High-throughput solution processing of large-scale graphene. *Nature Nanotechnology* 2009, 4, 25-29.

64. Liang, X.; Fu, Z.; Chou, S. Y., Graphene transistors fabricated via transfer-printing in device active-areas on large wafer. *Nano Letters* 2007, 7, 3840-3844.

65. Chen, Z. H.; Lin, Y. M.; Rooks, M. J.; Avouris, P., Graphene nano-ribbon electronics. *Physica E-Low-Dimensional Systems & Nanostructures* 2007, 40, 228-232.

66. Jiao, L. Y.; Wang, X. R.; Diankov, G.; Wang, H. L.; Dai, H. J., Facile synthesis of high-quality graphene nanoribbons. *Nature Nanotechnology* 2010, 5, 321-325.

67. Jiao, L. Y.; Zhang, L.; Wang, X. R.; Diankov, G.; Dai, H. J., Narrow graphene nanoribbons from carbon nanotubes. *Nature* 2009, 458, 877-880.

68. Eizenberg, M.; Blakely, J. M., CARBON MONOLAYER PHASE CONDENSATION ON NI(111). *Surface Science* 1979, 82, 228-236.

69. Das, S.; Sudhagar, P.; Verma, V.; Song, D.; Ito, E.; Lee, S. Y.; Kang, Y. S.; Choi, W., Amplifying Charge-Transfer Characteristics of Graphene for Triiodide Reduction in Dye-Sensitized Solar Cells. *Advanced Functional Materials* 2011, 21, 3729-3736.

70. Guermoune, A.; Chari, T.; Popescu, F.; Sabri, S. S.; Guillemette, J.; Skulason, H. S.; Szkopek, T.; Siaj, M., Chemical vapor deposition synthesis of graphene on copper with methanol, ethanol, and propanol precursors. *Carbon* 2011, 49, 4204-4210.

71. Reddy, K. M.; Gledhill, A. D.; Chen, C.-H.; Drexler, J. M.; Padture, N. P., High quality, transferrable graphene grown on single crystal Cu(111) thin films on basal-plane sapphire. *Applied Physics Letters* 2011, 98, 113117-3.

72. Sun, Z.; Yan, Z.; Yao, J.; Beitler, E.; Zhu, Y.; Tour, J. M., Growth of graphene from solid carbon sources. *Nature* 2010, 468, 549-552.

73. Ismach, A.; Druzgalski, C.; Penwell, S.; Schwartzberg, A.; Zheng, M.; Javey, A.; Bokor, J.; Zhang, Y. G., Direct Chemical Vapor Deposition of Graphene on Dielectric Surfaces. *Nano Letters* 2010, 10, 1542-1548.

74. Kwak, J.; Chu, J. H.; Choi, J.-K.; Park, S.-D.; Go, H.; Kim, S. Y.; Park, K.; Kim, S.-D.; Kim, Y.-W.; Yoon, E.; Kodambaka, S.; Kwon, S.-Y., Near room-temperature synthesis of transfer-free graphene films. *Nat Commun* 2012, 3, 645.

75. Dai, B.; Fu, L.; Zou, Z.; Wang, M.; Xu, H.; Wang, S.; Liu, Z., Rational design of a binary metal alloy for chemical vapour deposition growth of uniform single-layer graphene. *Nat Commun* 2011, 2, 522.

76. Li, B.; Zhou, L.; Wu, D.; Peng, H.; Yan, K.; Zhou, Y.; Liu, Z., Photochemical Chlorination of Graphene. *ACS Nano* 2011, 5, 5957-5961.

77. Fan, X.; Liu, L.; Kuo, J.-L.; Shen, Z., Functionalizing Single- and Multi-layer Graphene with Br and Br2. *The Journal of Physical Chemistry C* 2010, 114, 14939-14945.

78. Jung, N.; Kim, N.; Jockusch, S.; Turro, N. J.; Kim, P.; Brus, L., Charge Transfer Chemical Doping of Few Layer Graphenes: Charge Distribution and Band Gap Formation. *Nano Letters* 2009, 9, 4133-4137.

79. Choi, S.-M.; Jhi, S.-H., Electronic property of Na-doped epitaxial graphenes on SiC. *Applied Physics Letters* 2009, 94, 153108-3.

80. Chen, J. H.; Jang, C.; Adam, S.; Fuhrer, M. S.; Williams, E. D.; Ishigami, M., Charged-impurity scattering in graphene. *Nat Phys* 2008, 4, 377-381.

81. Robinson, J. T.; Burgess, J. S.; Junkermeier, C. E.; Badescu, S. C.; Reinecke, T. L.; Perkins, F. K.; Zalalutdniov, M. K.; Baldwin, J. W.; Culbertson, J. C.; Sheehan, P. E.; Snow, E. S., Properties of Fluorinated Graphene Films. *Nano Letters* 2010, 10, 3001-3005.

82. Walter, A. L.; Jeon, K.-J.; Bostwick, A.; Speck, F.; Ostler, M.; Seyller, T.; Moreschini, L.; Kim, Y. S.; Chang, Y. J.; Horn, K.; Rotenberg, E., Highly p-doped epitaxial graphene obtained by fluorine intercalation. *Applied Physics Letters* 2011, 98, 184102-3.

83. Kasry, A.; Kuroda, M. A.; Martyna, G. J.; Tulevski, G. S.; Bol, A. A., Chemical Doping of Large-Area Stacked Graphene Films for Use as Transparent, Conducting Electrodes. *ACS Nano* 2010, 4, 3839-3844.

84. Gunes, F.; Shin, H. J.; Biswas, C.; Han, G. H.; Kim, E. S.; Chae, S. J.; Choi, J. Y.; Lee, Y. H., Layer-by-Layer Doping of Few-Layer Graphene Film. *Acs Nano* 2010, 4, 4595-4600.

85. Wu, Z. S.; Ren, W. C.; Xu, L.; Li, F.; Cheng, H. M., Doped Graphene Sheets As Anode Materials with Superhigh Rate and Large Capacity for Lithium Ion Batteries. *Acs Nano* 2011, 5, 5463-5471.

86. Qu, L.; Liu, Y.; Baek, J.-B.; Dai, L., Nitrogen-Doped Graphene as Efficient Metal-Free Electrocatalyst for Oxygen Reduction in Fuel Cells. *ACS Nano* 2010, 4, 1321-1326.

87. Sheng, Z. H.; Gao, H. L.; Bao, W. J.; Wang, F. B.; Xia, X. H., Synthesis of boron doped graphene for oxygen reduction reaction in fuel cells. *Journal of Materials Chemistry* 2012, 22, 390-395.

88. Panchokarla, L. S.; Subrahmanyam, K. S.; Saha, S. K.; Govindaraj, A.; Krishnamurthy, H. R.; Waghmare, U. V.; Rao, C. N. R., Synthesis, Structure, and Properties of Boron- and Nitrogen-Doped Graphene. *Advanced Materials* 2009, 21, 4726.

89. Panchakarla, L. S.; Govindaraj, A.; Rao, C. N. R., Boron- and nitrogen-doped carbon nanotubes and graphene. *Inorganica Chimica Acta* 2010, 363, 4163-4174.

90. Ryu, S.; Liu, L.; Berciaud, S.; Yu, Y.-J.; Liu, H.; Kim, P.; Flynn, G. W.; Brus, L. E., Atmospheric Oxygen Binding and Hole Doping in Deformed Graphene on a SiO2 Substrate. *Nano Letters* 2010, 10, 4944-4951.

91. Cresti, A.; Lopez-Bezanilla, A.; Ordejón, P.; Roche, S., Oxygen Surface Functionalization of Graphene Nanoribbons for Transport Gap Engineering. *ACS Nano* 2011, 5, 9271-9277.

92. Chien, S.-K.; Yang, Y.-T.; Chen, C. o.-K., Influence of hydrogen functionalization on thermal conductivity of graphene: Nonequilibrium molecular dynamics simulations. *Applied Physics Letters* 2011, 98, 033107-3.

93. Yang, Z.; Yao, Z.; Li, G.; Fang, G.; Nie, H.; Liu, Z.; Zhou, X.; Chen, X. a.; Huang, S., Sulfur-Doped Graphene as an Efficient Metal-free Cathode Catalyst for Oxygen Reduction. *ACS Nano* 2011, 6, 205-211.

94. Kaverzin, A. A.; Strawbridge, S. M.; Price, A. S.; Withers, F.; Savchenko, A. K.; Horsell, D. W., Electrochemical doping of graphene with toluene. *Carbon* 2011, 49, 3829-3834.

95. Bai, H.; Xu, Y.; Zhao, L.; Li, C.; Shi, G., Non-covalent functionalization of graphene sheets by sulfonated polyaniline. *Chemical Communications* 2009, 1667-1669.

96. Li, X. L.; Wang, X. R.; Zhang, L.; Lee, S. W.; Dai, H. J., Chemically derived, ultrasmooth graphene nanoribbon semiconductors. *Science* 2008, 319, 1229-1232.

97. Li, X. L.; Zhang, G. Y.; Bai, X. D.; Sun, X. M.; Wang, X. R.; Wang, E.; Dai, H. J., Highly conducting graphene sheets and Langmuir-Blodgett films. *Nature Nanotechnology* 2008, 3, 538-542.

98. Zhang, J. L.; Shen, G. X.; Wang, W. J.; Zhou, X. J.; Guo, S. W., Individual nanocomposite sheets of chemically reduced graphene oxide and poly(N-vinyl pyrrolidone): preparation and humidity sensing characteristics. *Journal of Materials Chemistry* 2010, 20, 10824-10828.

99. Li, S. S.; Tu, K. H.; Lin, C. C.; Chen, C. W.; Chhowalla, M., Solution-Processable Graphene Oxide as an Efficient Hole Transport Layer in Polymer Solar Cells. *Acs Nano* 2010, 4, 3169-3174.

100. Hasin, P.; Alpuche-Aviles, M. A.; Wu, Y. Y., Electrocatalytic Activity of Graphene Multi layers toward I-/I-3(-): Effect of Preparation Conditions and Polyelectrolyte Modification. *Journal of Physical Chemistry C* 2010, 114, 15857-15861.

101. Roy-Mayhew, J. D.; Bozym, D. J.; Punckt, C.; Aksay, I. A., Functionalized Graphene as a Catalytic Counter Electrode in Dye-Sensitized Solar Cells. *ACS Nano* 2010, 4, 6203-6211.

102. Li, G. L.; Liu, G.; Li, M.; Wan, D.; Neoh, K. G.; Kang, E. T., Organo- and Water-Dispersible Graphene Oxide-Polymer Nanosheets for Organic Electronic Memory and Gold Nanocomposites. *Journal of Physical Chemistry C* 2010, 114, 12742-12748.

103. Chen, S. Q.; Wang, Y., Microwave-assisted synthesis of a Co3O4-graphene sheet-on-sheet nanocomposite as a superior anode material for Li-ion batteries. *Journal of Materials Chemistry* 2010, 20, 9735-9739.

104. Muszynski, R.; Seger, B.; Kamat, P. V., Decorating graphene sheets with gold nanoparticles. *Journal of Physical Chemistry C* 2008, 112, 5263-5266.

105. Qian, J.; Liu, P.; Xiao, Y.; Jiang, Y.; Cao, Y.; Ai, X.; Yang, H., TiO2-Coated Multilayered $SnO_2$ Hollow Microspheres for Dye-Sensitized Solar Cells. *Advanced Materials* 2009, 21, 3663-3667.

106. Yang, N. L.; Zhai, J.; Wang, D.; Chen, Y. S.; Jiang, L., Two-Dimensional Graphene Bridges Enhanced Photoinduced Charge Transport in Dye-Sensitized Solar Cells. *Acs Nano* 2010, 4, 887-894.

107. Zhou, K. F.; Zhu, Y. H.; Yang, X. L.; Li, C. Z., One-pot preparation of graphene/Fe3O4 composites by a solvothermal reaction. *New Journal of Chemistry* 2010, 34, 2950-2955.

108. Zhu, J. W.; Zeng, G. Y.; Nie, F. D.; Xu, X. M.; Chen, S.; Han, Q. F.; Wang, X., Decorating graphene oxide with CuO nanoparticles in a water-isopropanol system. *Nanoscale* 2010, 2, 988-994.

109. Avouris, P.; Chen, Z.; Perebeinos, V., Carbon-based electronics. *Nat Nano* 2007, 2, 605-615.

110. Roy, S.; Vedala, H.; Roy, A. D.; Kim, D.-h.; Doud, M.; Mathee, K.; Shin, H.-k.; Shimamoto, N.; Prasad, V.; Choi, W., Direct Electrical Measurements on Single-Molecule Genomic DNA Using Single-Walled Carbon Nanotubes. *Nano Letters* 2007, 8, 26-30.

111. Kim, D.-H.; Huang, J.; Shin, H.-K.; Roy, S.; Choi, W., Transport Phenomena and Conduction Mechanism of Single-Walled Carbon Nanotubes (SWNTs) at Y- and Crossed-Junctions. *Nano Letters* 2006, 6, 2821-2825.

112. Choi, W. B.; Chung, D. S.; Kang, J. H.; Kim, H. Y.; Jin, Y. W.; Han, I. T.; Lee, Y. H.; Jung, J. E.; Lee, N. S.; Park, G. S.; Kim, J. M., Fully sealed, high-brightness carbon-nanotube field-emission display. *Applied Physics Letters* 1999, 75, 3129-3131.

113. Kuzmenko, A. B.; van Heumen, E.; Carbone, F.; van der Marel, D., Universal Optical Conductance of Graphite. *Physical Review Letters* 2008, 100, 117401.

114. Recent Progress of Carbon Nanotube Field Emitters and Their Application. *Recent Patents on Nanotechnology* 2007, 1, 238-244.

115. Kondo, D.; Sato, S.; Awano, Y., Self-organization of Novel Carbon Composite Structure: Graphene Multi-Layers Combined Perpendicularly with Aligned Carbon Nanotubes.

116. Cao, A.; Dickrell, P. L.; Sawyer, W. G.; Ghasemi-Nejhad, M. N.; Ajayan, P. M., Super-Compressible Foamlike Carbon Nanotube Films. *Science* 2005, 310, 1307-1310.

117. Xie, S. H.; Liu, Y. Y.; Li, J. Y., Comparison of the effective conductivity between composites reinforced by graphene nanosheets and carbon nanotubes. *Applied Physics Letters* 2008, 92, 243121-3.

118. Kondo, D.; Sato, S.; Awano, Y., Self-organization of novel carbon composite structure: Graphene multi-layers combined perpendicularly with aligned carbon nanotubes. *Applied Physics Express* 2008, 1.

119. Seelaboyina, R.; Choi, W., Recent Progress of Carbon Nanotube Field Emitters and Their Application. *Recent Patents on Nanotechnology* 2007, 1, 238-244.

120. Suzuki, K.; Yamaguchi, M.; Kumagai, M.; Yanagida, S., Application of Carbon Nanotubes to Counter Electrodes of Dye-sensitized Solar Cells. *Chemistry Letters* 2003, 32, 28-29.

121. Li, Y. F.; Li, B. R.; Zhang, H. L., The computational design of junctions between carbon nanotubes and graphene nanoribbons. *Nanotechnology* 2009, 20.

122. Lee, D. H.; Kim, J. E.; Han, T. H.; Hwang, J. W.; Jeon, S.; Choi, S.-Y.; Hong, S. H.; Lee, W. J.; Ruoff, R. S.; Kim, S. O., Versatile Carbon Hybrid Films Composed of Vertical Carbon Nanotubes Grown on Mechanically Compliant Graphene Films. *Advanced Materials* 2010, 22, 1247-1252.

123. Rodriguez-Manzo, J. A.; Banhart, F.; Terrones, M.; Terrones, H.; Grobert, N.; Ajayan, P. M.; Sumpter, B. G.; Meunier, V.; Wang, M.; Bando, Y.; Golberg, D., Heterojunctions between metals and carbon nanotubes as ultimate nanocontacts. *Proceedings of the National Academy of Sciences of the United States of America* 2009, 106, 4591-4595.

124. Lee, D. H.; Kim, J. E.; Han, T. H.; Hwang, J. W.; Jeon, S.; Choi, S. Y.; Hong, S. H.; Lee, W. J.; Ruoff, R. S.; Kim, S. O., Versatile Carbon Hybrid Films Composed of Vertical Carbon Nanotubes Grown on Mechanically Compliant Graphene Films. *Advanced Materials* 2010, 22, 1247.

125. Trancik, J. E.; Barton, S. C.; Hone, J., Transparent and Catalytic Carbon Nanotube Films. *Nano Letters* 2008, 8, 982-987.

126. Li, G.-r.; Wang, F.; Jiang, Q.-w.; Gao, X.-p.; Shen, P.-w., Carbon Nanotubes with Titanium Nitride as a Low-Cost Counter-Electrode Material for Dye-Sensitized Solar Cells. *Angewandte Chemie International Edition* 2010, 49, 3653-3656.

127. Wang, M. K.; Anghel, A. M.; Marsan, B.; Ha, N. L. C.; Pootrakulchote, N.; Zakeeruddin, S. M.; Gratzel, M., CoS Supersedes Pt as Efficient Electrocatalyst for Triiodide Reduction in Dye-Sensitized Solar Cells. *Journal of the American Chemical Society* 2009, 131, 15976.

128. Stankovich, S.; Dikin, D. A.; Piner, R. D.; Kohlhaas, K. A.; Kleinhammes, A.; Jia, Y.; Wu, Y.; Nguyen, S. T.; Ruoff, R. S., Synthesis of graphene-based nanosheets via chemical reduction of exfoliated graphite oxide. *Carbon* 2007, 45, 1558-1565.

129. Schedin, F.; Lidorikis, E.; Lombardo, A.; Kravets, V. G.; Geim, A. K.; Grigorenko, A. N.; Novoselov, K. S.; Ferrari, A. C., Surface-Enhanced Raman Spectroscopy of Graphene. *ACS Nano* 2010, 4, 5617-5626.

130. Schwierz, F., Graphene transistors. *Nat Nano* 2010, 5, 487-496.

131. De Arco, L. G.; Zhang, Y.; Schlenker, C. W.; Ryu, K.; Thompson, M. E.; Zhou, C. W., Continuous, Highly Flexible, and Transparent Graphene Films by Chemical Vapor Deposition for Organic Photovoltaics. *Acs Nano* 2010, 4, 2865-2873.

132. Wang, Y.; Shi, Z.; Huang, Y.; Ma, Y.; Wang, C.; Chen, M.; Chen, Y., Supercapacitor Devices Based on Graphene Materials. *The Journal of Physical Chemistry C* 2009, 113, 13103-13107.

133. Kavan, L.; Yum, J. H.; Grätzel, M., Optically Transparent Cathode for Dye-Sensitized Solar Cells Based on Graphene Nanoplatelets. *ACS Nano* 2010, null-null.

134. Zhan, D.; Sun, L.; Ni, Z. H.; Liu, L.; Fan, X. F.; Wang, Y.; Yu, T.; Lam, Y. M.; Huang, W.; Shen, Z. X., FeCl3-Based Few-Layer Graphene Intercalation Compounds: Single Linear Dispersion Electronic Band Structure and Strong Charge Transfer Doping. *Advanced Functional Materials* 2010, 20, 3504-3509.

135. Hasin, P.; Alpuche-Aviles, M. A.; Wu, Y., Electrocatalytic Activity of Graphene Multilayers toward−/I3−: Effect of Preparation Conditions and Polyelectrolyte Modification. *The Journal of Physical Chemistry C* 2010, 114, 15857-15861.

136. Reina, A.; Jia, X.; Ho, J.; Nezich, D.; Son, H.; Bulovic, V.; Dresselhaus, M. S.; Kong, J., Large Area, Few-Layer Graphene Films on Arbitrary Substrates by Chemical Vapor Deposition. *Nano Letters* 2008, 9, 30-35.

137. Acik, M.; Lee, G.; Mattevi, C.; Chhowalla, M.; Cho, K.; Chabal, Y. J., Unusual infrared-absorption mechanism in thermally reduced graphene oxide. *Nat Mater* 2010, 9, 840-845.

138. Joseph D. Roy-Mayhew, D. J. B., Christian Punckt, and Ilhan A. Aksay, Functionalized Graphene as a Catalytic Counter Electrode in Dye-Sensitized Solar Cells. ACS NANO, 2010; Vol. 4, pp 6203-6211.

139. Shi, Y.; Kim, K. K.; Reina, A.; Hofmann, M.; Li, L.-J.; Kong, J., Work Function Engineering of Graphene Electrode via Chemical Doping. *ACS Nano* 2010, 4, 2689-2694.

140. Delhaes, P., *Graphite and precursors*. Gordon & Breach: Australia, 2001; p xiv, 297 p.223.

CHAPTER 3

# EXPERIMENTAL

## 3.1. Synthesis of Graphene

### 3.1.1. Graphene synthesis using chemical vapor deposition

In Thermal Chemical vapor deposition (CVD) process, a substrate is exposed to one or mixtures of volatile precursors which dissociate at high temperatures and the final byproducts of the reaction is deposited on the substrate surface.

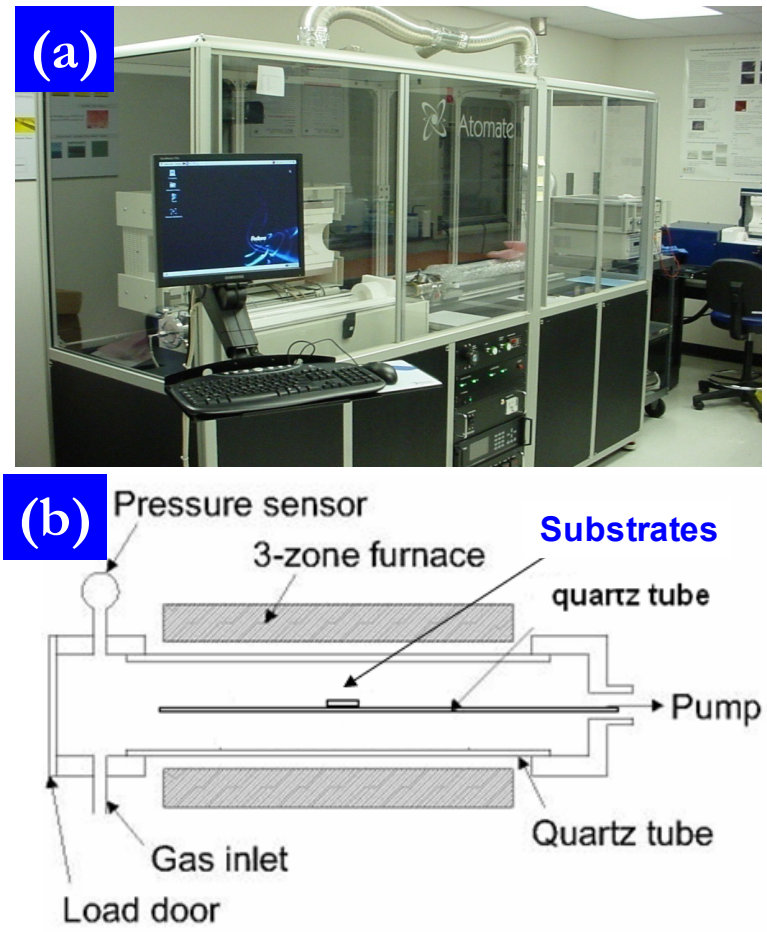


Figure 3.1: (a) Thermal low pressure chemical vapor deposition (LPCVD) system (ATOMATE, USA) for graphene growth; (b) schematic representation of the LPCVD system.

The CVD process is very well known in nanotechnology research and widely applied in semiconductor industries for the fabrication of complex semiconductor devices. In our lab we have one low pressure thermal CVD system which is dedicated for the graphene synthesis at different ambient conditions as shown in Figure 3.1a. Figure 3.1b is the schematic representation of the thermal CVD system as shown in Figure 3.1a. The system consist of $2^{//}$ 99.99% pure quartz tube which is connected with both ends using a vacuum sealing clamp. One end is connected with a gas inlet and a pressure sensor where as the other part is associated with a roughing pump, one gas outlet (exhaust) and a loader. The samples loader is also consist of two horizontally placed quartz tubes (in a cantilever configuration) connected with the end part. The whole system is covered up with porous alumina ($Al_2O_3$) insulation with kanthal heating elements which can withstand temperature up to $1000^oC$.

Nanometer thick graphite fabrication on the metal substrates were an well established methods using CVD on different metals like, Pt[1], Pd[2], Ru[3], Ir[4], Rh[2],Co[5] and Ni[6-8]. These noble/transition metals surfaces are highly susceptible to absorb carbon and formed graphene at high temperature because of the highly catalytic metal surfaces. Furthermore, these transition/noble metals have strong electron affinity towards carbon and they have strong lattice matched with graphene basal plane, hence used as substrate for graphene growth. However, monolayer to few layer graphene growth using CVD became very popular recently due to the high quality graphene film can be obtained with layer controllability and the process is easy to industrially scalable.

Commercial grade Cu foils (99.9% Purity) of different thicknesses 25 -500 μm was purchased from NIMROD Hall, USA and sonicate it in 2- propanol, methanol and

acetone followed by dry nitrogen spray in each steps. The cleaned substrates were placed in a tube furnace and increased the temperature up to 1000°C at a heating rate of 25°C/min.

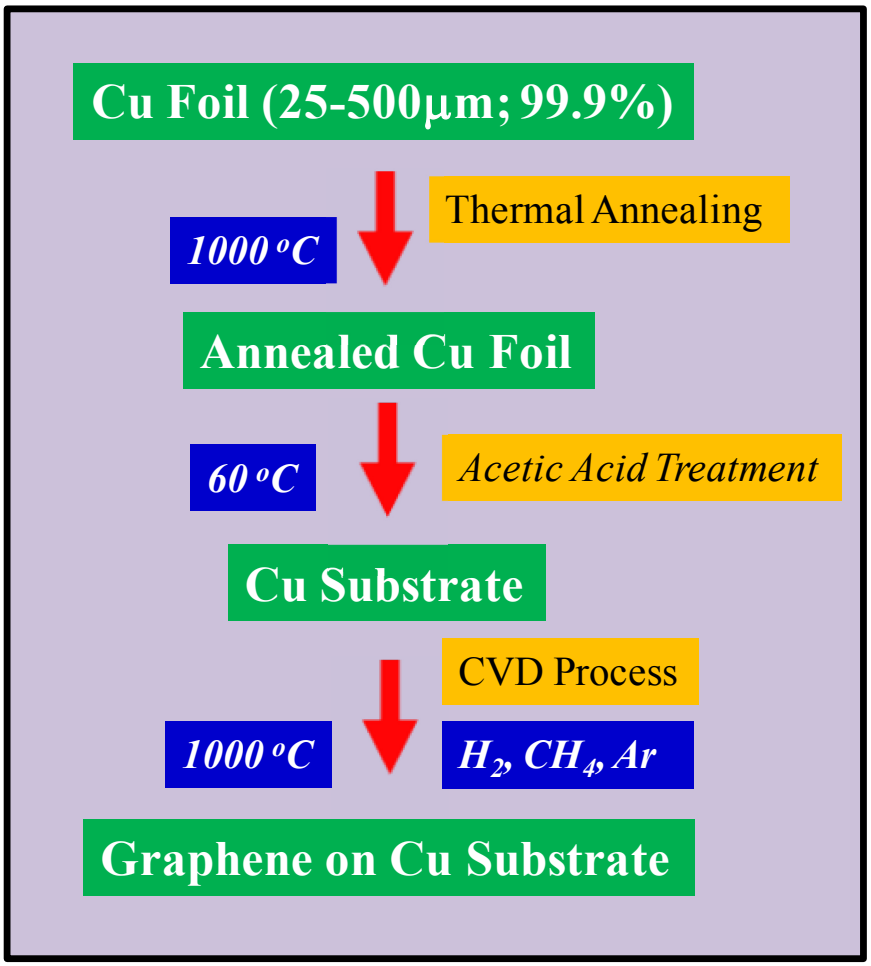


Figure 3.2: Schematic showing the process flow of graphene growth process.

The substrates were soaked at 1000°C for 1 hr in Ar gas atmosphere and slowly cooled down to room temperature at a heating rate of 25°C/min. The objective of this annealing step is to reduce the inbuilt stress in the Cu foil during cold-rolling process. Now the Cu foil is acid treated with hot acetic acid for 20 min in order to remove the

surface oxide layers followed by the further sonication with 2-propanol, methanol and acetone. The cleaned substrates were dried with blowing dry nitrogen carefully to avoid the bending and crumpling of the thin foils.

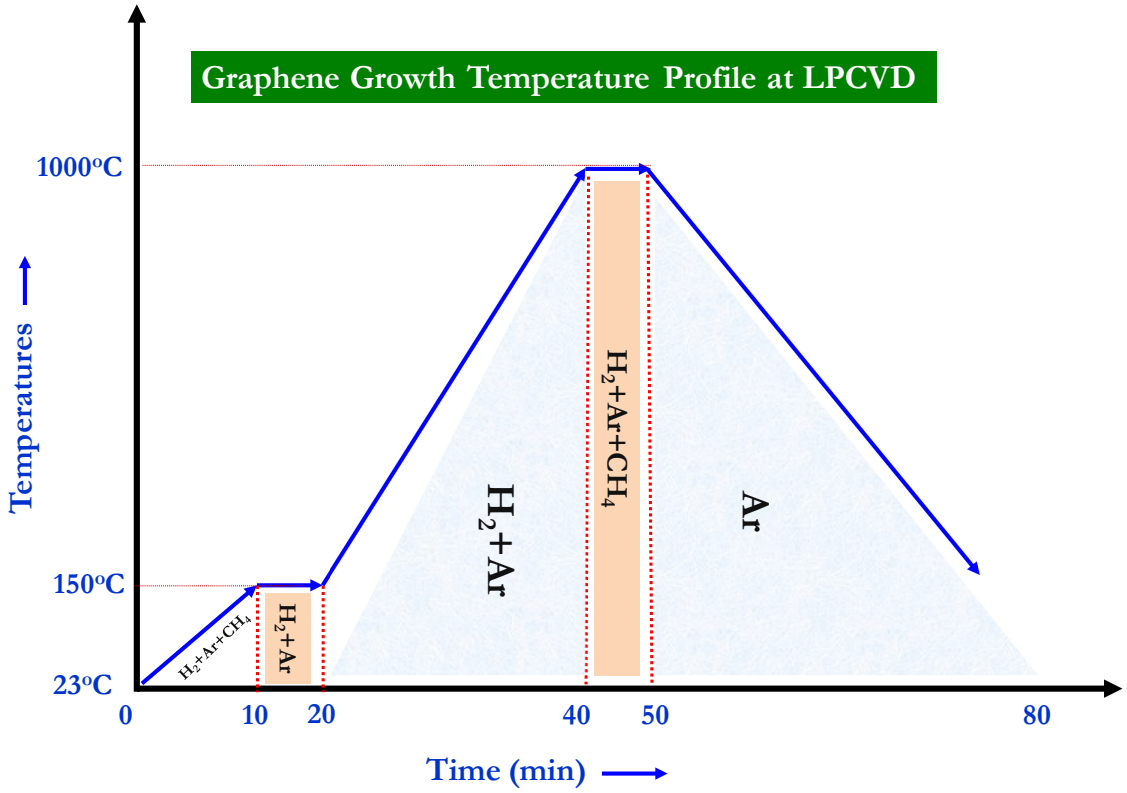


Figure 3.3: LPCVD furnace time-temperature profile with the flow of corresponding gases required for graphene growth..

Now the metal foils were ready to be used for graphene growth. In case of Ni metal, we used Ni thin film (thickness ~ 300 nm) on $SiO_x$/Si (500 nm) for graphene growth. The thin film Ni was fabricated using CHA e-beam evaporators at room temperature deposition with 5 Å/sec deposition rate.

Furthermore, the metal foils or thin films were placed inside a 2// quartz tube of a low pressure thermal CVD system and increased the temperature up to 1000$^{o}$C as shown in the furnace temperature profile in Figure 3.3. The ambience of LPCVD furnace was kept under the constant flow of inert gas (Ar) and $CH_4$ (methane):$H_2$ (0.25:1) was used as a precursor gas mixture for graphene growth at 1000$^{o}$C for 10 minutes. After the furnace was cooled down to room temperatures, the substrates were taken out for further structural characterizations and transfer process.

### 3.1.2. Graphene-CNT hybrid structure synthesis using chemical vapor deposition method

In past, several other research groups reported the graphene-CNT hybrid structure synthesis using two step methods[9-11]. Kondo et. al. first reported the self organized graphene-CNT structure using thermal CVD[12]. In-situ synthesis of Graphene-CNT hybrid structure was consist of following steps of (i) Substrate preparations, (ii) Thin film catalyst deposition followed by (iii) growth of graphene-CNT hybrid structure at high temperature using thermal CVD system (Firstnano, USA) as shown in Figure 3.4 a and b. The substrate preparation steps consist of the cleaved the boron (B)-doped $p^+$ type $SiO_2$ (500 nm)/Si (111) substrate (from University wafers, USA) for required size and shape using diamond cutter and washed those wafers in a high power sonicator with 2-propanol, methanol and acetone followed by dry $N_2$ blowing. The substrates were again cleaned using reactive oxygen ($O_2$) plasma etching at 150 W power and 300 mT pressure for 60 sec. The cleaned substrates were further placed in a CHA ebeam evaporator system and pull down the vacuum up to 2.3 x $10^{-6}$ Torr. 20 nm Fe Thin films were deposited at a

deposition rate of 1-2 Å/sec . On the other hand, patterning was done on a $SiO_2$/Si substrate using standard photolithography (μPG 101 from Hieldelbergh Instruments) and Fe catalyst was deposited on the substrate by varying thickness of ~10 to 30 nm. The photolithography process was consist of spin coating the substrates with AZ 1518 photoresist (Microchem Inc., USA) with spin sped 6000 rpm for 30 sec in order to achieve the desire film thickness. The spin coated photoresist were baked at 110$^{o}$C for 8 min followed by oven backing at 90$^{o}$C for 5 min. The photoresist coated substrates were placed inside a micro-laser writer for photolithography (μPG 101 from Hieldelbergh Instruments) and exposed under laser with 3 mW power in order to fabricate a patterned area of size 100 μm x 100 μm. After that, the developing process consists of preparing a solution of AZ400K and water (1:4) and mixed it thoroughly followed be dipping the exposed substrates for 50 sec. The whole process was optimized by changing the spin speed of photo resist, baking temperatures, baking time, laser dose power and developing time. It was found that the parameters are well optimized for obtaining very good undercut patterning with smooth side walls. The each row of patterning were further covered with mask properly followed by Fe Thin film deposition of corresponding thickness of 10 nm, 20 nm and 30 nm. The objective of different patterning over the same substrate is to observe the effect of thin film thickness effects on the graphene-CNT hybrid structure growth. All the thin film deposition was done under the identical e-beam evaporation conditions. The further investigation on this work was found to be very justified Fe thin film thickness effect which plays a major role in order to construct the hybrid structure was will be discussed in chapter 4 section 4.2.5.

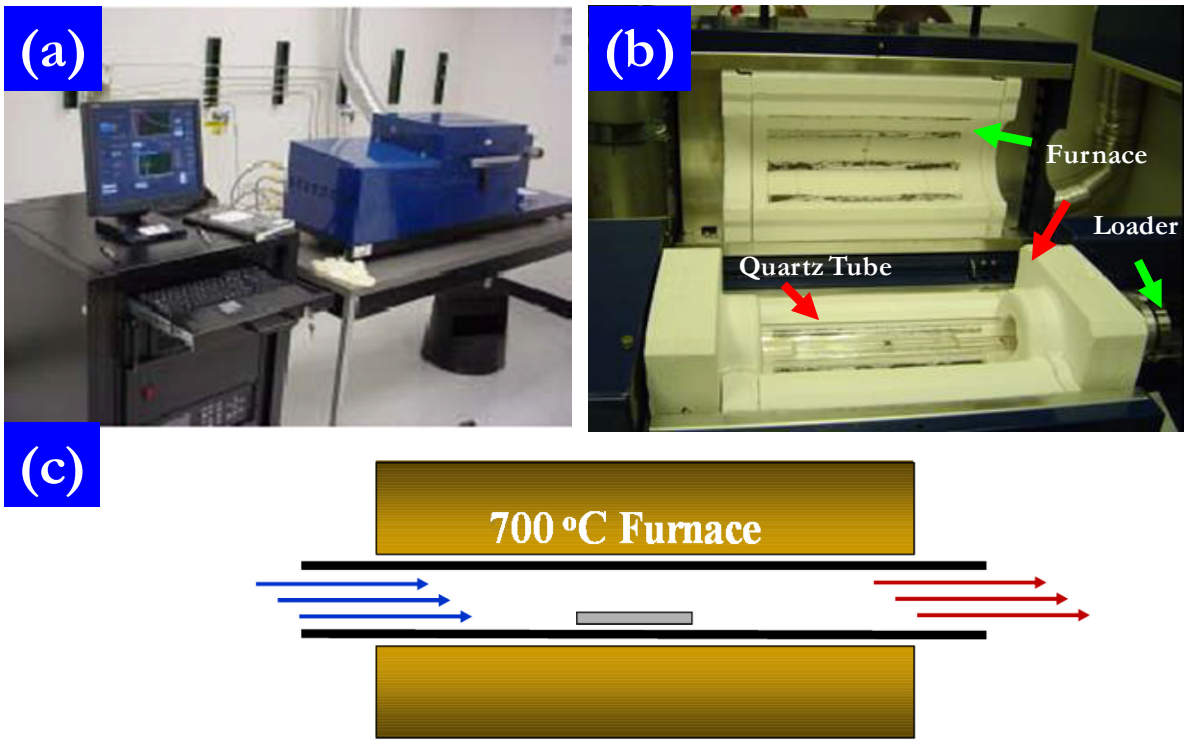


Figure 3.4: (a) & (b) Picture showing the atmospheric pressure chemical vapor deposition system (FIRSTNANO, USA) for graphene-CNT hybrid structure growth; (c) schematic representation of the growth process and gas flow mechanisms at the CVD.

After the thin film deposition process, Graphene-CNT hybrid structure was synthesized on $Si/SiO_2$ substrate, by thermal chemical vapor deposition method. The substrates with different catalyst thin film was placed in a $2^{//}$ quartz tube of an atmospheric thermal CVD system (as shown in Figure 3.4c) and purge the ambient furnace atmosphere with hydrogen ($H_2$), Ar and ethylene ($C_2H_4$) for 15 min. As shown in figure 3.5c, the quartz tube is completely covered with the $Al_2O_3$ insulation embedded with kanthal heating system.

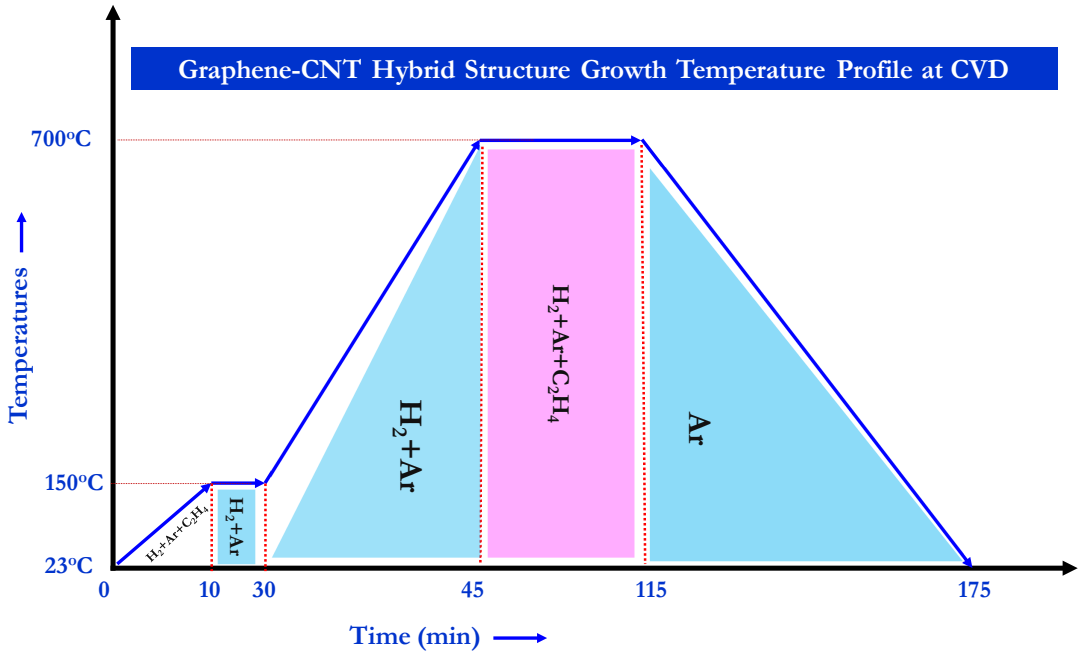


Figure 3.5: Temperature-Time profile for graphene-CNT hybrid structure growth with corresponding gas flow rates during the growth process.

The furnace was ramped up to 700°C at a heating rate of 60°C/min and soaked at 700°C for 1 hr. During the ramping, Ar and $H_2$ gas mixtures were flow constantly in order to achieve a oxygen free atmosphere at 760 Torr pressure. Now, Ethylene ($C_2H_4$) and Argon (Ar) (1:7) of total 800 sccm precursor gas mixtures were flowed inside the furnace for ~60 minutes at 700°C under constant pressure of 760 Torr. After completion of the growth process, the substrate was cooled under a constant flow of (1000 sccm) Ar to room temperature with average cooling rate 7°C/sec. The detailed temperature-time profile for graphene-CNT hybrid structure growth is shown in Figure 3.5 with corresponding area represents the total flow of gas mixtures.

## 3.2. Graphene transfer

### 3.2.1. Graphene transfer on polyethylene tetrapthalate.

#### 3.2.1.1. Hot press lamination method

We used a unique roll to roll transfer process which we recognized as hot press lamination technique for graphene transfer. The process is versatile and industrially scalable and the process can be easily optimized towards the transfer process suggests that the method could be applied to transfer of graphene onto wide range of flexible polymer electrodes. The process consist of a combination of hot press lamination of graphene/Cu to PET/graphene/Cu where top surface of graphene get attached with the flexible Polyethylene Tetrapthalate (PET) film (200 μm) followed by chemical etching process. The schematic of Figure 3.6 is briefly demonstrating the process flow chart consisting of each and every transfer step. First, Cu foils with graphene were hot press rolled with a transparent flexible PET film having thickness ~25-50 μm. A PET film was placed on the top surface of the graphene/Cu foil and hot press rolled by a hot press roller followed by etched away the Cu using concentrated $FeCl_3$ solution. As we observed, the higher the thickness of the Cu foil, the quality of transfer getting less.

The optimized pressure for the transfer process is ~1 MPa and temperature of the process is optimized at ~130$^{o}$C. Further, the higher the thickness of the Cu foils, the larger the time it takes to dissolve the Cu in $FeCl_3$ solution hence the process gets slower. The temperature was optimized at ~130$^{o}$C as the glass transition temperature of the PET film is known to be in the range of ~75$^{o}$C which facilitate transfer the polymer into a viscous melt which adhere the graphene/PET interface. However, a slight deformation is observed at the Cu foil due the hot rolling process which doesn't make very difference in

etching process. After the completion of etching process the film was washed thoroughly with deionized water, 2-propanol, methanol, acetone followed by dry nitrogen blowing at room temperature.

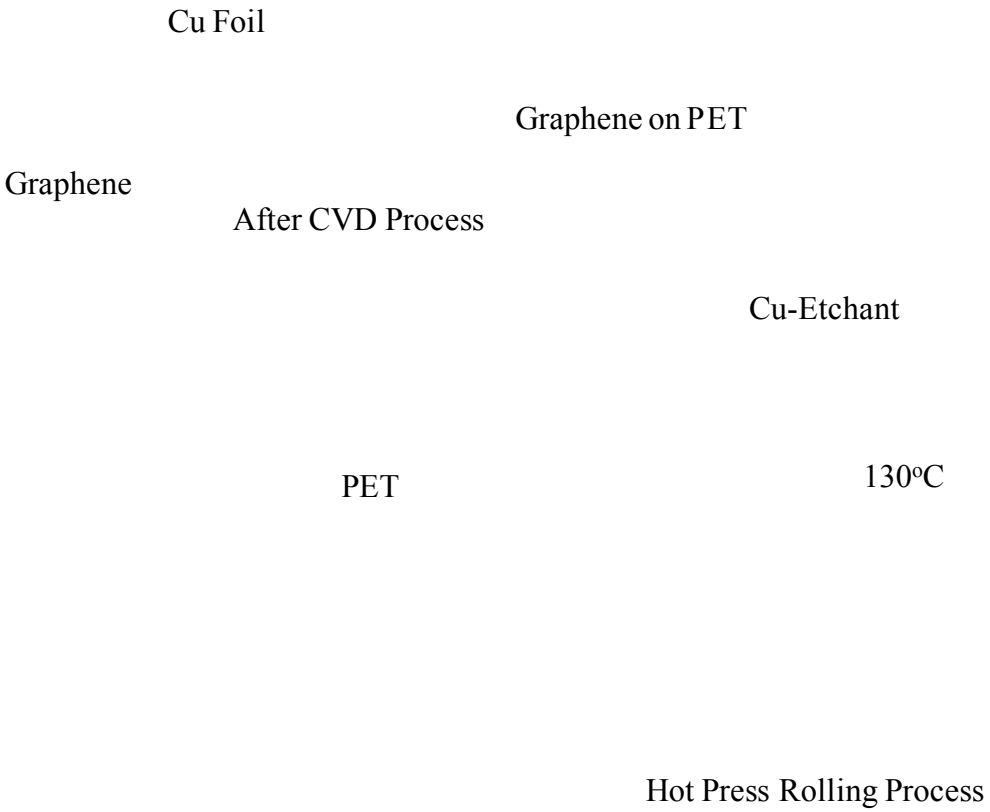


Figure 3.6: Schematic flow chart represents the graphene transfer using hot press lamination method followed by the chemical etching process.

### 3.2.2. Graphene transfer on glass and $SiO_2$/Si and free standing graphene

#### 3.2.2.1. Chemical transfer

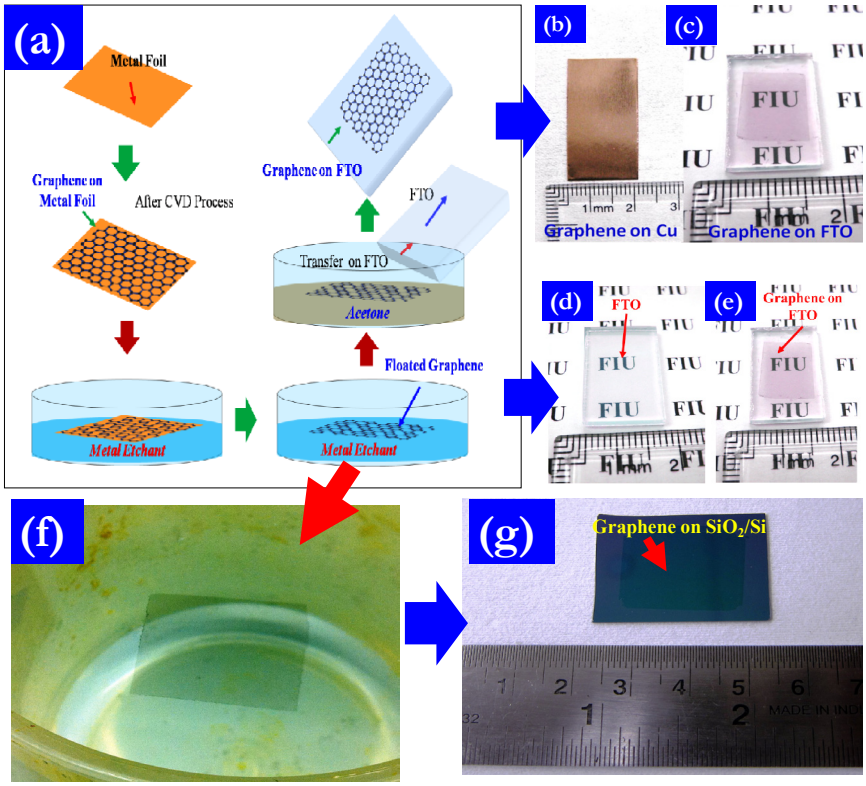


Figure 3.7: Chemical transfer of graphene on different substrates: (a) schematic represents the process flow charts of the chemical transfer of graphene from metal substrates to any other substrates. (b) Graphene grown on Cu foil; (c) graphene transfer on glass substrates using chemical transfer process; (d) & (e) illustrates the glass substrates before and after graphene transfer respectively; (f) floated graphene on water; (g) transferred graphene layers on $SiO_2$(300 nm)/Si substrates as large as 40 mm x 30 mm.

Thermal CVD grown graphene on Cu foil was placed floated on a Cu etchant ($FeCl_3$) in order to etch away the Cu foil. The total time required for etching of Cu foil is

40 min and 20 min for 54 μm and 25 μm Cu foil respectively. The floated graphene on the top of the $FeCl_3$ solution was transferred carefully on a FTO substrate subsequently washing with water, acetone, and IPA as shown in schematic Figure 3.7a. Figure 3.7d and e demonstrates the picture of FTO glass before and after graphene transfer respectively. Similarly, the same floated graphene samples can be transferred on to any other dielectric substrates like $Al_2O_3$, $SiO_2$/Si, quartz and sapphire.

The mechanism of Cu dissolution in $FeCl_3$ occurs according to redox reactions as follows:

$Fe^{3+}$ is a strong oxidizer and $Cl^-$ is a strong complexing agent for $Cu^{2+}$ions.

The etching process in solution often occur as

$$2Fe^{3+} + Cu \rightarrow 2Fe^{2+} + Cu^{2+}$$

Now, the chloride ions plays an essential role as follows

$$2Fe^{3+} + Cu + 4Cl^- \rightarrow 2Fe^{2+} + CuCl_4^{2-}$$

$$2FeCl_4^- + Cu \rightarrow 2Fe^{2+} + CuCl_4^{2-} + 4Cl^-$$

When all $Fe^{3+}$ is converted to $Fe^{2+}$, then the $CuCl_4^{2-}$ ion in turn also oxidizes copper metal very easily, where $Cu^+$ species are formed:

$$CuCl_4^{2-} + Cu \rightarrow 2CuCl_2^-$$

The overall reaction processes are occurring as follows:

$$FeCl_3 + Cu \rightarrow FeCl_2 + CuCl$$

$$FeCl_3 + CuCl \rightarrow FeCl_2 + CuCl_2$$

Similarly, in case of graphene/Ni thin film/$SiO_2$/Si, the transfer process includes two additional step as shown in the process flow chart of Figure 3.8. First the substrate was spin coated with 2% Poly-(methyl methacrylate) (PMMA) solution in PMMA

thinner (Microchem Inc.) and bake it at 180°C for 3 min. In case of Ni thin film, the PMMA/graphene/Ni on $SiO_2$/Si was immersed into a 50% hydrofluoric acid (HF) solution in order to dissolve amorphous $SiO_2$ as shown in Figure 3.8 (c) and (d). When $SiO_2$ get completely dissolve in the HF solution, the

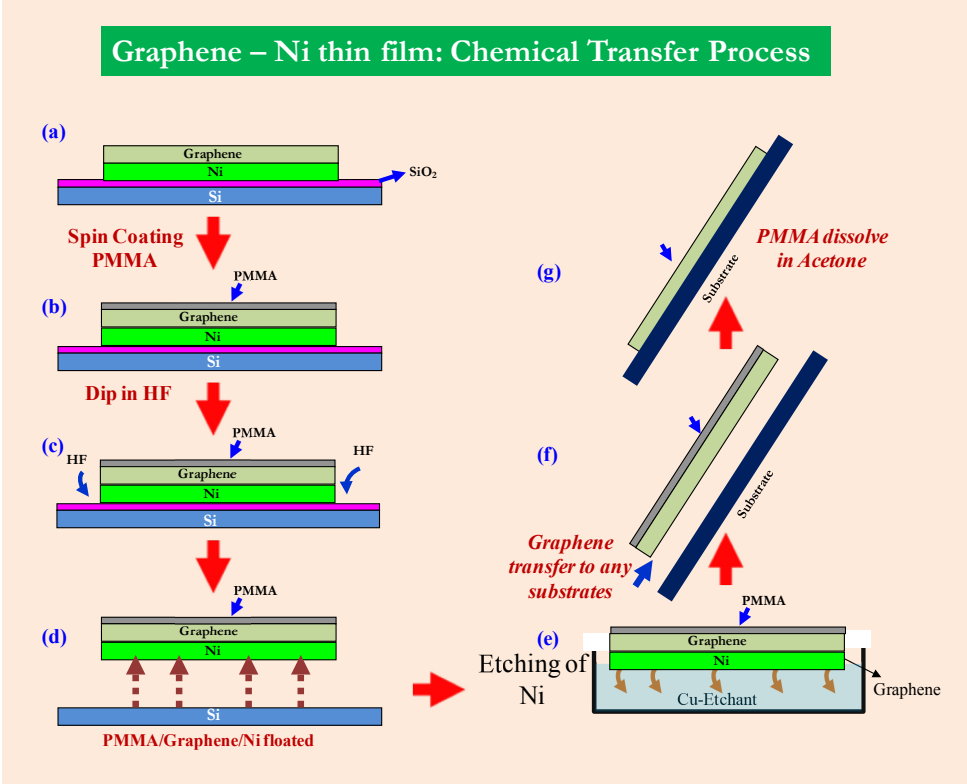


Figure 3.8: Schematic representation of the process flow charts of the graphene transfer process from Ni thin film to any substrates.

PMMA/graphene/Ni was floated out of the solution and was transferred carefully on the top of the Ni etchant (Transee Company, USA) solution as shown in Figure 3.8(e). When Ni gets dissolved in the Ni etchant the PMMA/graphene was transferred on to any

substrate by scooping method after subsequesnt washing with 2-propanol, methanol, and acetone. Finally, PMMA on the top surface of graphene was dissolve with acetone.

The subsequent graphene substrate bonding is not that much good in order to handle the substrate for further fabrication process. For this reason, we applied different thermal annealing process in order to achieve the good graphene-substrate adherence strength. We found that different substrate graphene adherence is increases with different annealing process. We applied the rapid thermal annealing (RTA) at 600 $^{o}$C for 30 sec and found that the graphene substrate adherence energy increases compared to the un-annealed samples.

### 3.2.3. Graphene transfer on Parylene (Biocompatible Polymers)

Graphene on parylene was transfer in a STS parylene coater (speciality coating systems PDS 2010, SCS, USA). The graphene on Cu foil was placed on a $SiO_2$/Si substrate and the conjugated system was placed in the STS parylene coater vacuum chamber. The typical 50-60 gm parylene C dimer (SCS coatings, USA) was used in order to achieve 20-30 μm target thickness of the parylene coating. There were four parts of the system for e.g. i) Chamber ii) furnace, iii) vaporizer and iv) vacuum pump. The corresponding temperature of furnace and vaporizers were maintained at 690$^{o}$C and 175$^{o}$C respectively. The deposition chamber vacuum pr should be maintained at 10-17 mTorr in order to achieve very clean and homogeneous deposition. The total deposition time was kept at 22 hr long in order to achieve the ~30 micron parylene film thickness. The as deposited parylene over the Cu foil was taken out from the furnace and then float

over the Cu etchant in order to etch away the metal substrate. The complete process flow chart is shown in Figure 3.9a.

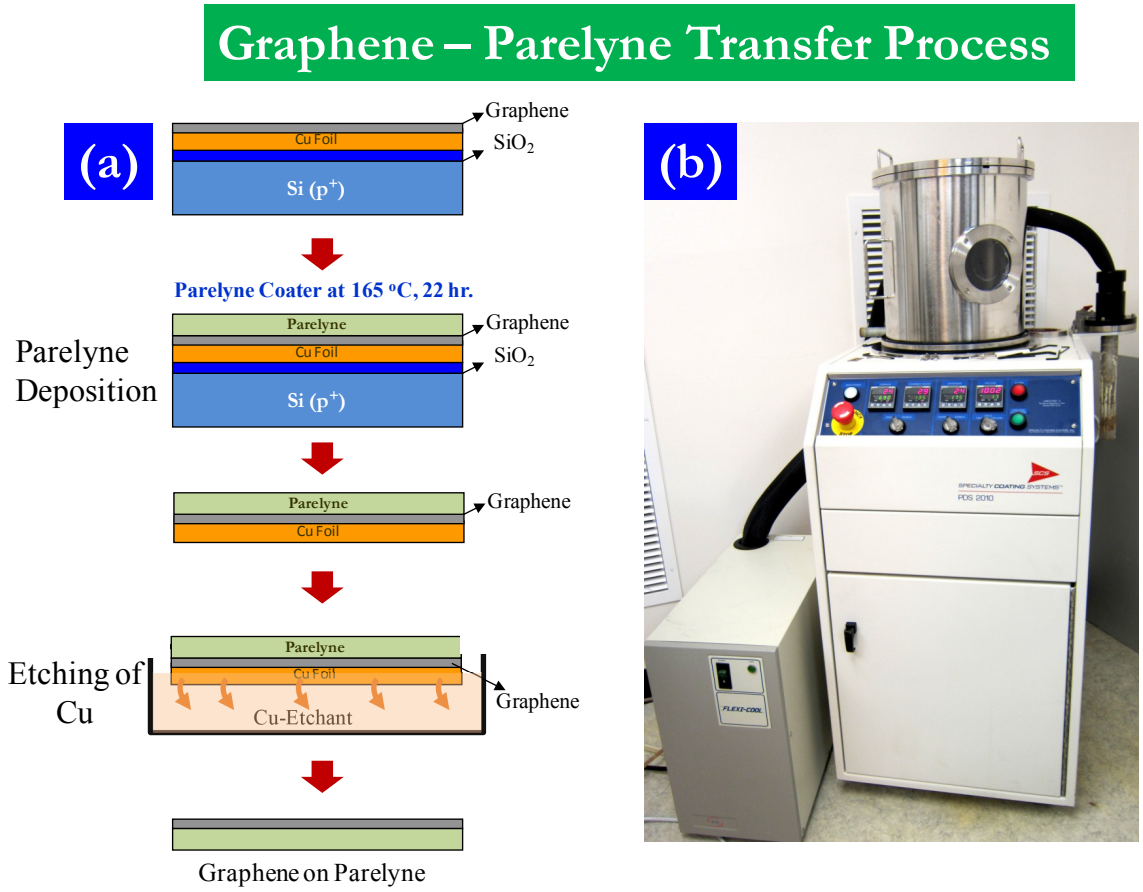


Figure 3.9: (a) Shows the process flow chart of Graphene transfer from metals to parylene and (b) the parylene coater system.

Figure 3.10a shows the graphene on parylene deposited using parylene coater. The graphene on parylene substrate is flexible transparent and conducting. The corner to corner resistance of the graphene parylene sample was found to be ~1.2-1.5 kΩ/sq. The advantage of this process is the adherence of the graphene on parylene is very good with robust mechanical properties and flexibility. Furthermore the transfer process is unique as

it can be extended to a wide range of parylene thickness as per the requirements; the process is also scalable and controllable for wide range of applications. However, the major disadvantages of the process are very slow and time consuming. Sometimes, the parylene doesn't comes out from the substrate surface as it stick to the substrates surface very strongly which create a lot problems of peeling off of the samples.

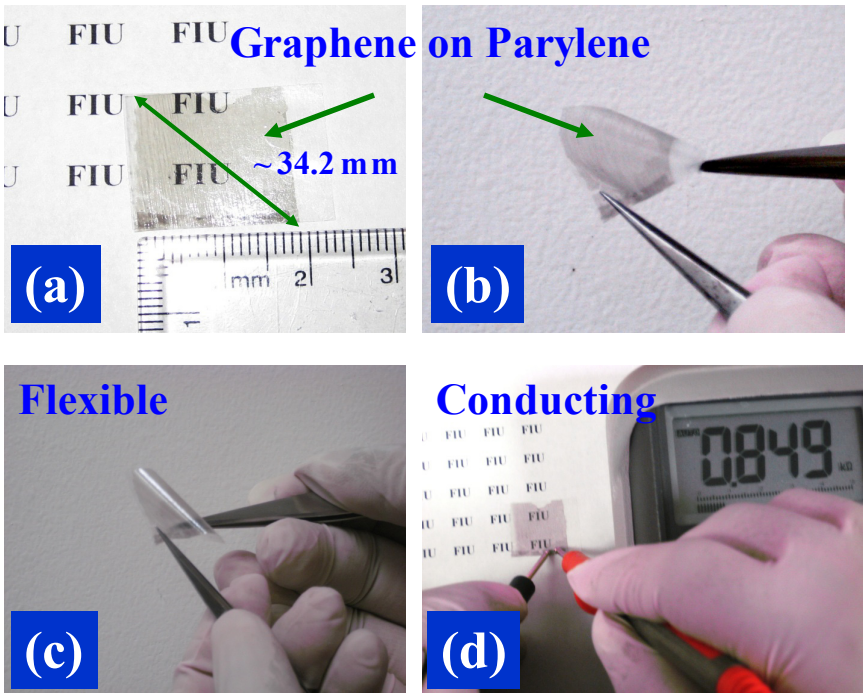


Figure 3.10: (a) Pictures of graphene on parylene showing (b) &(c) Flexible, and (d) conducting.

Graphene on parylene via was fabricated in two step fabrication methods, as follows: i) parylene via fabrication followed by ii) graphene transfer onto it using chemical transfer process. The first process parelyne via fabrication is shown in a process flow schematic in the Figure 3.11. The process consist of spin coating of AZ 1518 photo-resist over the $SiO_2$(500nm)/Si substrate followed by two step baking at 110$^{o}$C and 95$^{o}$C

over the hot plate and inside a pre-heated oven respectively. After that parylene film was deposited on the photo-resist coated wafer in the parylene coater chamber followed by 300 nm aluminium (Al) deposition using CHA e-beam evaporation. Furthermore, the substrate again spin coated with AZ 1518 photo-resist followed by one step baking at 110$^{o}$C over the hot plate. Patterning was done on the substrate using standard photolithography (µPG 101 from Hieldelbergh Instruments) process with different diameter of holes from 5 µm to 100 µm.

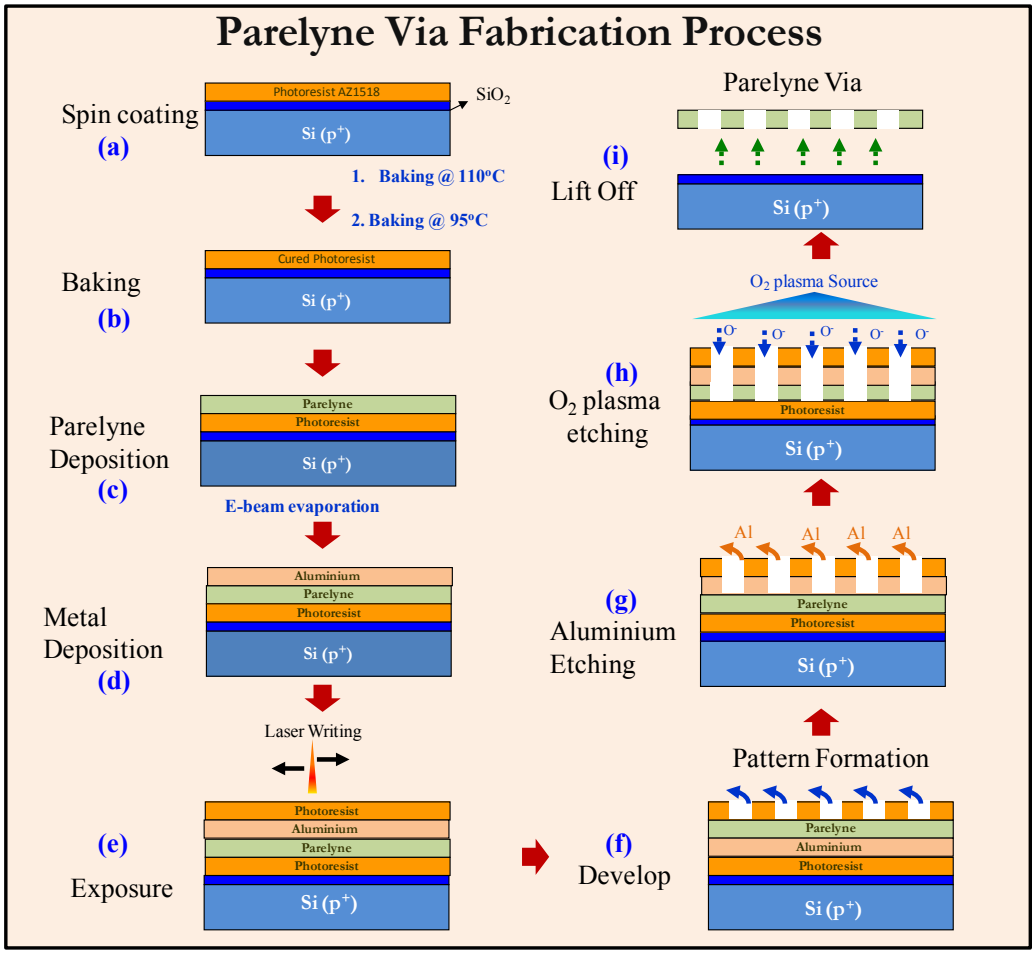


Figure 3.11: Process flow chart of parylene via fabrication.

The photolithography process was consist of spin coating the substrates with AZ 1518 photo-resist (Microchem Inc., USA) with spin sped 6000 rpm for 30 sec in order to achieve the desire film thickness. The spin coated photoresist were baked at 110$^{o}$C for 8 min on a hot plate. The photo-resist coated substrates were then placed inside a micro-laser writer for photolithography (μPG 101 from Hieldelbergh Instruments) and exposed under laser with 3 mW dose power in order to fabricate a patterned area of required size. After that, the developing process consists of preparing a solution of AZ400K and water (1:4) and mixed it thoroughly followed by dipping the exposed substrates for 50 sec. The whole process was optimized by changing the spin speed of photo resist, baking temperatures, baking time, laser dose power and developing time as shown in Figure 3.11 e and f. Aluminium etching was done using Al etchant (Transee company, USA) for required time followed by cleaning the substrates with 2-propanol, methanol, acetone and dry nitrogen blowing. Reactive ion etching (RIE) was applied in order to etch the open position of the parelyne as shown in Figure 3.11h. Care has been taken to slowly etch the parylene film using oxygen plasma of power 150 W under 150 mTorr pressure and 5 sccm $O_2$ flow rate. Finally, the substrate was immersed correspondingly in acetone, Al etchant and acetone in order to obtain the parylene via on the parylene film as shown in the Figure 3.12. Figure 3.12 illustrating the optical micrograph of the parylene via with homogeneous spacing between each hole over a large area.

Now, graphene has been transferred on to parylene via using the process flow chart showing at the flow chart 3.13. The final graphene over the parylene via has been demonstrated in Figure 3.14. Figure 3.14 a&b and Figure 3.14 c&d shows the scanning electron micrograph (SEM) of the parelyne via of 8 μm diameter before graphene transfer

and after the graphene transfer. A homogeneous graphene film has been transfer successfully over the parylene surface followed by the RTA under the nitrogen ($N_2$) atmosphere.

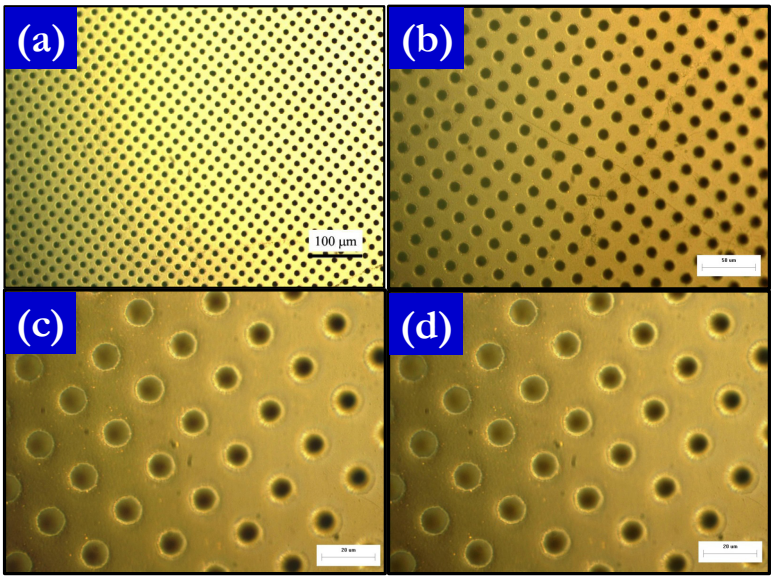


Figure 3.12: Optical micrograph of parylene Via under different magnifications.

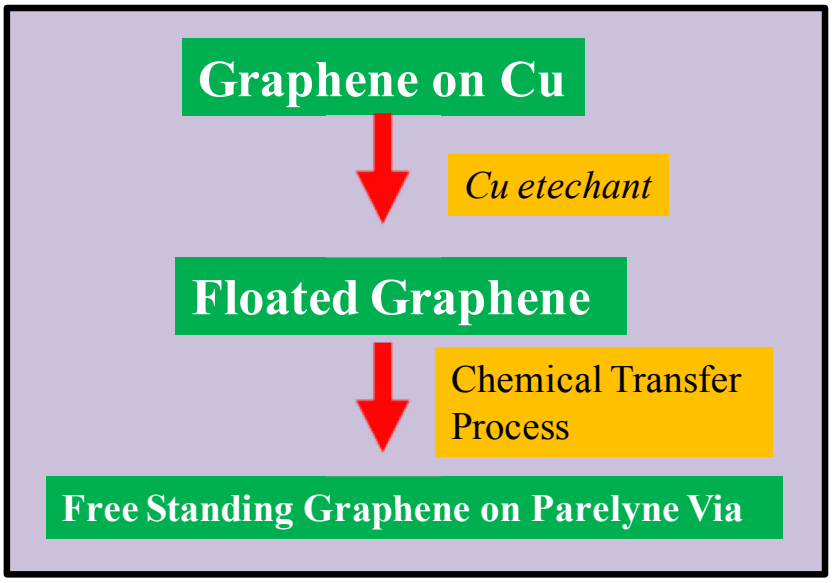


Figure 3.13: Process flow chart showing the free standing graphene transfer process on parylene via.

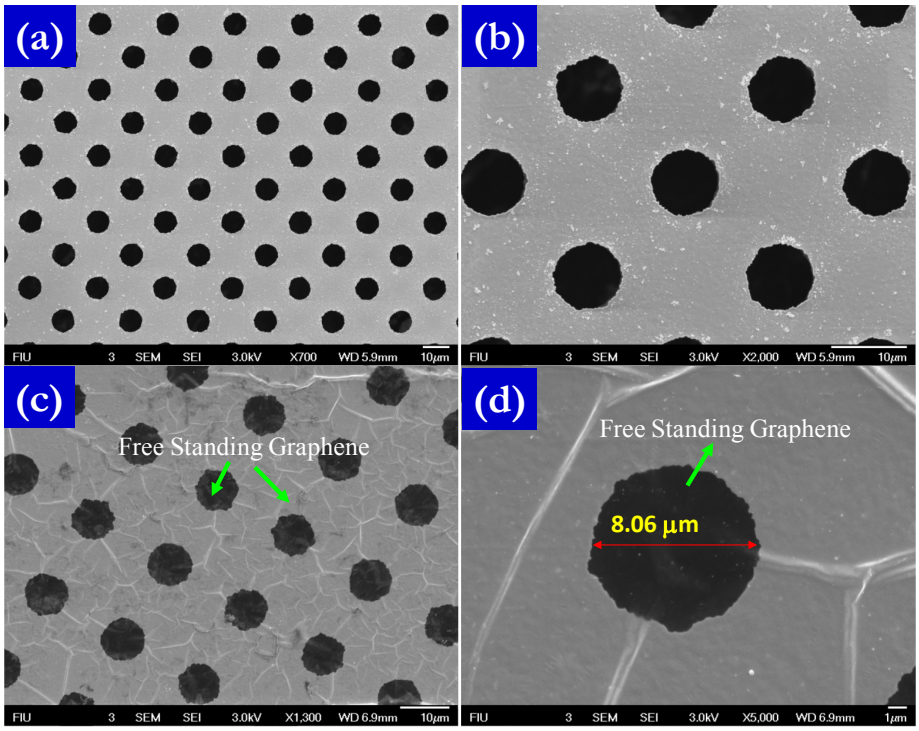


Figure 3.14: (a) & (b) Scanning electron micrograph of parylene via before graphene transfer; (c) & (d) free standing graphene on parylene via.

A graphene structure with full of ripple can be observed over the parylene surface as shown in Figure 3.14 c & d. We believe that the formation of ripple in graphene is due to the substrate surface roughness and also due to the different thermal conductivities of metals and graphene which generates a mismatch during thermal cooling. Furthermore, the free standing graphene can also covered/partially covered of the parylene holes as shown in Figure 3.15. Figure 3.15a, b, c and d showing the graphene covered over the parylene holes of almost ~1/4$^{th}$ , half , 3/4$^{th}$ and full respectively which could have a wide potential applications as nano-mechanical resonators/cantilever in MEMS or NEMS system.

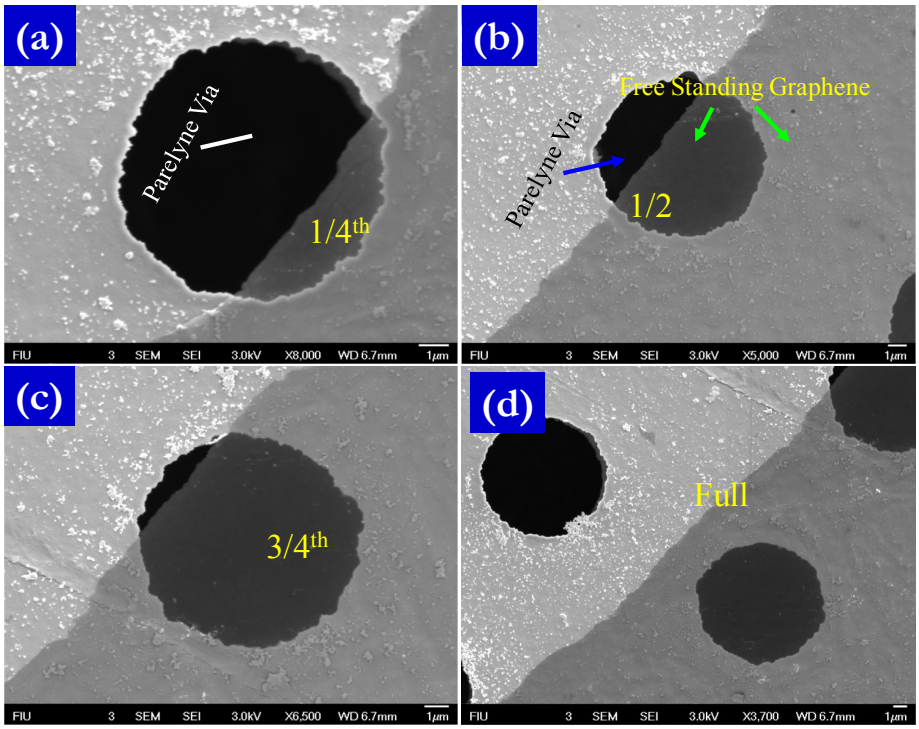


Figure 3.15: Scanning electron micrograph of free standing graphene on parylene via showing different coverage of graphene on 8 μm holes.

## 3.3. Graphene-CNT hybrid structure transfer

### 3.3.1. Graphene-CNT hybrid structure transfer on to PDMS

In this section we will discuss the fabrication of different transfer process of graphene-CNT hybrid structure over the different polymer substrates for its ultimate use in flexible electronics. We fabricated polymer electrodes by impregnating the Graphene-CNT hetero-junction composite into a transparent PDMS matrix. Our approach of fabricating the PDMS structures is shown schematically in a flow chart in Figure 3.16. The process involve first, PDMS polymer (DOW Corning, USA) solution preparation i.e.

mixing of base and curing agent with a weight ratio of 10:1and poured over the substrates containing the graphene-CNT hetero-junction structure in a Petri-dish. Second, the excessive PDMS solution was removed carefully in order to obtain the optimum thickness PDMS composite film.

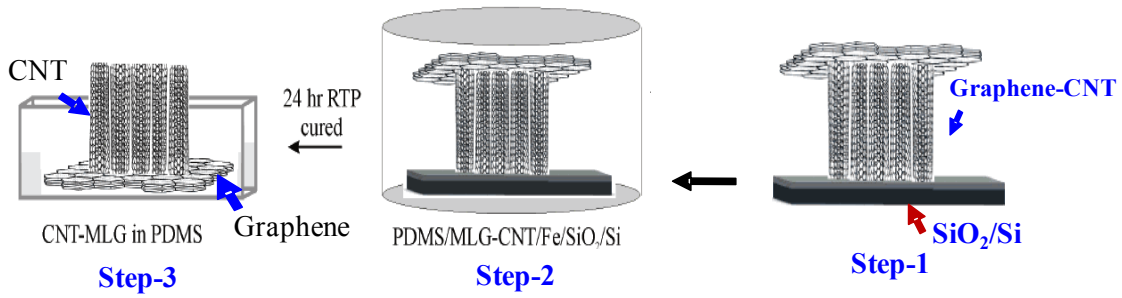


Figure 3.16: Schematic Illustrating the graphene-CNT hybrid structure transfer on to flexible PDMS substrates

Third, the PDMS was cured for 24 hours in normal atmospheric conditions or 6 hr. at 70$^{o}$C inside an oven and finally the PDMS composite films (800-1000 μm thick) were peeled off carefully from the native $SiO_2$/Si substrates as shown in Figure 3.16. Further structural characteristics and surface of the transferred graphene-CNT hybrid structure over the PDMS will be discussed in next chapter sec.

### 3.3.2. Graphene-CNT hybrid structure transfer on to Nitto-Denko and conducting adhesive Cu.

This transfer method of graphene-CNT hybrid structure over the Cu adhesive tapes or over the Nittodenko adhesive tape is relatively direct method and easily accessible without any hazards. This transfer process consist of cutting the adhesive Cu

tapes or Nitto-Denko thermal release tape in required size and shapes and applied with adhesive side facing towards the Graphene-CNT was placed on as grown substrates. By applying uniform pressure and careful peeling off, the hybrid film was transferred on to the Cu and Nitto Denko polymer substrates with uniform graphene layer underneath with vertically aligned CNTs are on top of it as shown in Figure 3.17.

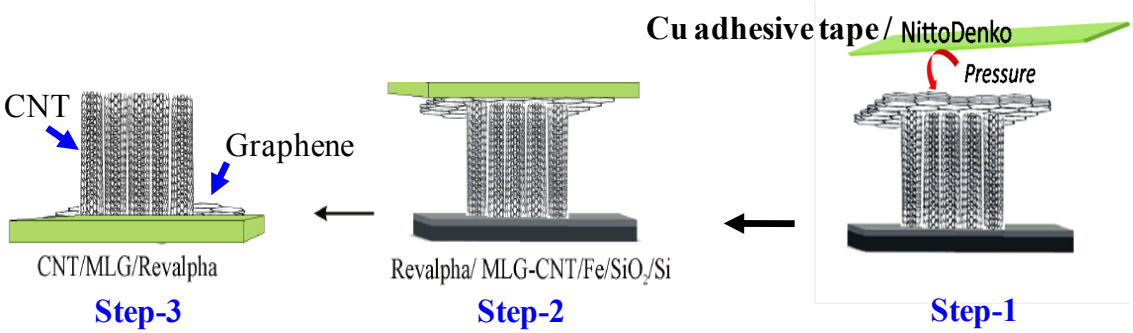


Figure 3.17: Illustrate the transfer of graphene-CNT hybrid structure on adhesive tape (Nittodenko) and conducting adhesive Cu tape.

### 3.4. Electrochemical Characterization

All electrochemical characterization was carried out under symmetric cell configuration using pristine and functionalized graphene multilayers counter electrodes and Pt coated FTO glass referred as a standard cell. Symmetric half cell was prepared by sandwiching 2 identical electrodes separated with Surlyn (Solaronix) spacer (thickness ~ 25 micron) and a liquid electrolyte (Same electrolyte used for DSSC full cell test) is filled in between. Cyclic voltametry was done for all the symmetric cells using GAMRY Reference 6000 potentiostat/ galvanostat (GAMRY, USA) from -1.0 V to 1.0 V with 50mV/s scan rate. EIS spectra of symmetrical half cell was performed using GAMRY Reference 6000 potentiostat/ galvanostat (GAMRY, USA) from the frequency range 1

MHz to 100 mHz under open circuit voltage condition at different temperature (From 0°C to 60°C). The charge transfer resistance ($R_{ct}$) was determined by fitting the EIS data by Randles circuit (inset of Figure 3b) in Echem Analyst software (GAMRY, USA).

## 3.5. Dye sensitized solar cell fabrication

### 3.5.1. Photo-anode fabrication and dye solution preparation

The $TiO_2$ working photoanodes about ~12 µm were prepared on FTO substrate using $TiO_2$ paste(Ti-nanooxide T20/SP) by doctor blade technique and subsequently sintered at 450 ºC for 30 minutes in ambient atmosphere.

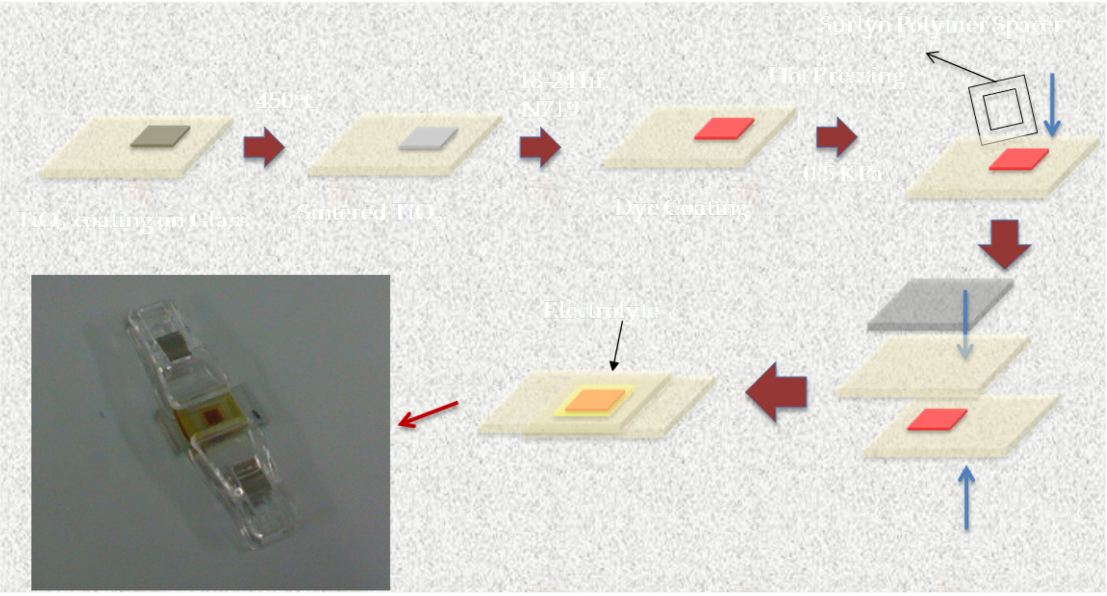


Figure 3.18: Process flow chart showing dye sensitized solar cells fabrication methods.

$TiO_2$ electrodes were immersed overnight in the 0.3mM dye solution containing a mixture of acetonitrile (ACN) and t-butyl alcohol (1:1 v/v) and dried at room temperature.

To avoid the back travel electron flow from FTO substrate to electrolyte, thin TiO2 blocking layer was prepared in between $TiO_2$ photoanode and FTO layer by spin coating of 0.2 M di-isopropoxy titanium bis (acetylacetonate) solution in anhydrous ethanol and subsequent calcination at 450 °C. The Ru(dcbpy)2(NCS)2 (dcbpy = 2,2-bipyridyl-4,4-dicarboxylato)dye (535-bisTBAN719, Solaronix) was used to sensitize the TiO2 photo electrodes.

### 3.5.2. Electrolyte preparation

The electrolyte was prepared as follows: 0.6M MPII (1-methyl-3-propylimidazolium iodide), 0.03M $I_2$, 0.1M of GuSCN and 0.5M of tBP was mixture with acetronitrile/valeronitrile (85:15) solvent and it was loaded into the cell through capillary force. A sandwich-type configuration was employed to measure the performance of the dye-sensitized solar cells as is depicted in Figure 3.20.

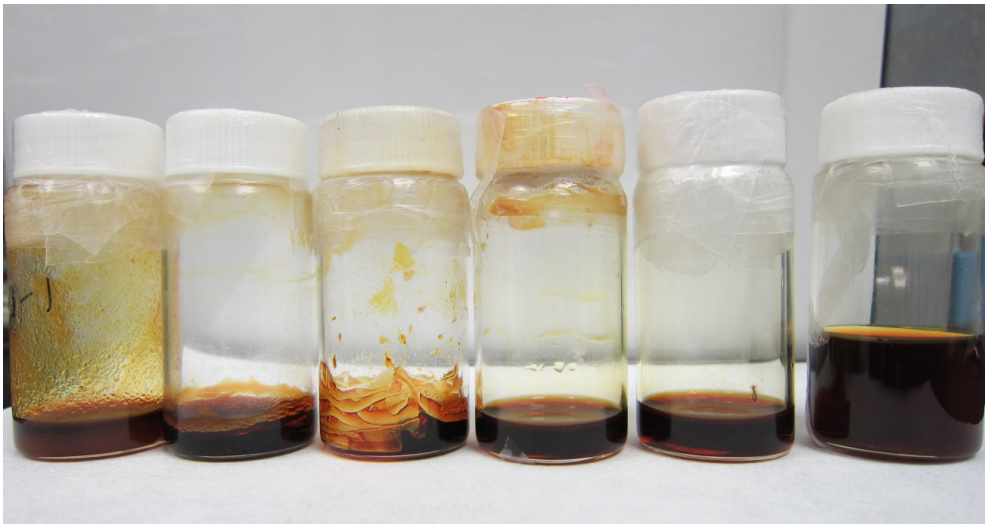

Figure 3.19: Photograph showing the liquid electrolytes and solid state electrolytes used for dye sensitized solar cell fabrication.

### 3.5.3. Solar cell assembly and Testing

A sandwich-type configuration was employed to measure the performance of the dye-sensitized solar cells (as shown in process flow chart in Figure 3.18), using GMLs on F-doped $SnO_2$ glass and 0.5M MPII (1-methyl-3-propylimidazolium iodide) with 0.05M $I_2$ in ACN as the electrolyte solution. Pt-coated F-doped $SnO_2$ film also used as a counter electrode for the reference cell. Current–voltage characteristics of DSSCs were obtained under 1 sun illumination (AM 1.5G, 100 mW $cm^{-2}$) with a Newport (USA) solar simulator (300W Xe source) (Figure 3.21) and a Keithley 2400 source meter (Figure 3.21).

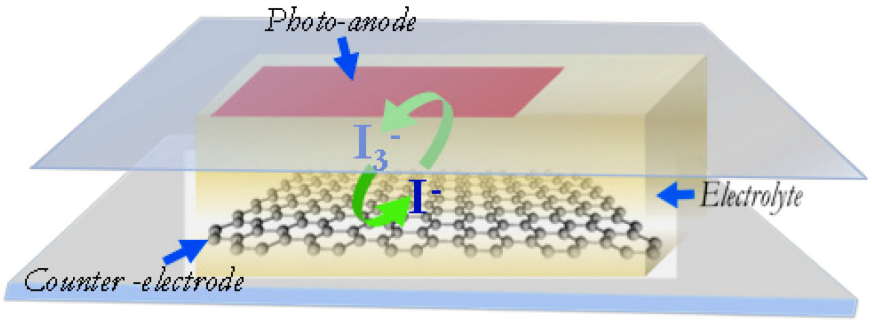


Figure 3.20: Schematic showing the assembly of dye sensitized solar cell using graphene counter electrodes.

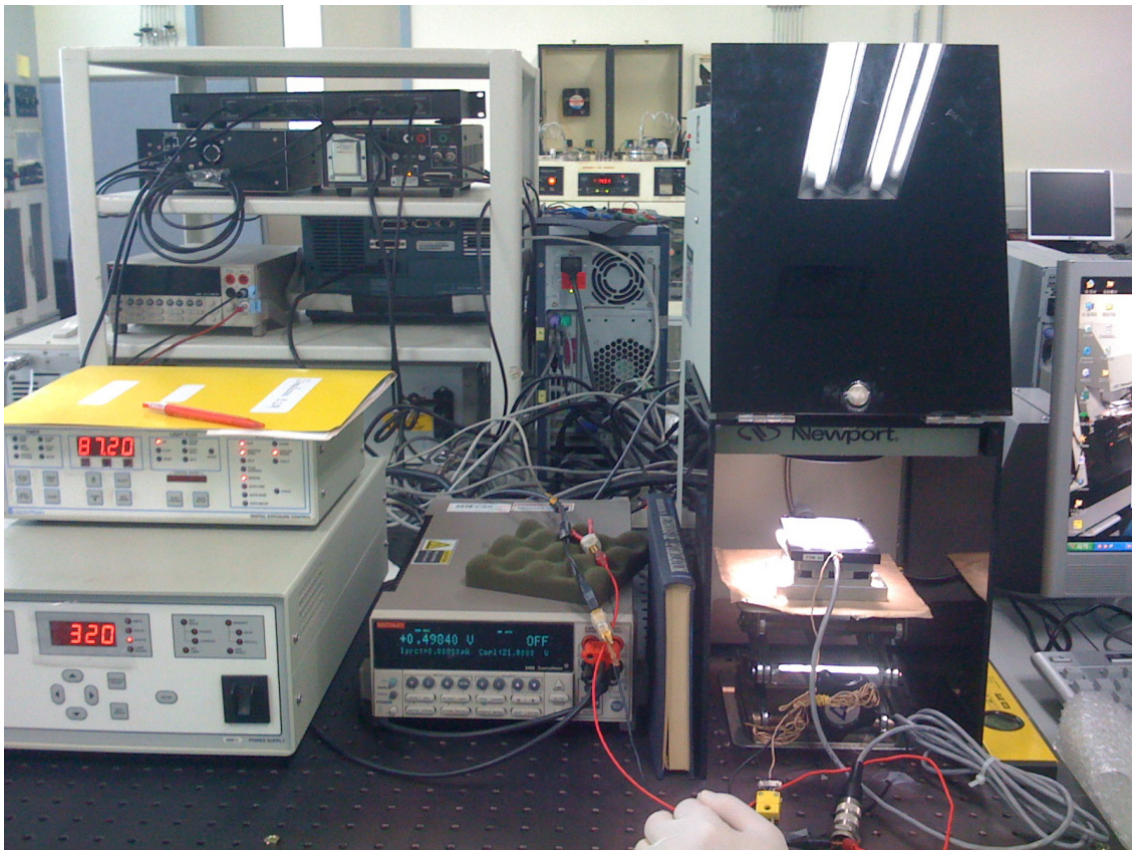


Figure 3.21: Solar simulator attached with Kiethley multimeter used for dye sensitized solar cells J-V characterization [Source: Prof. Kang's Lab in Hanyang University].

**References**

1. Gao, L.; Ren, W.; Xu, H.; Jin, L.; Wang, Z.; Ma, T.; Ma, L.-P.; Zhang, Z.; Fu, Q.; Peng, L.-M.; Bao, X.; Cheng, H.-M., Repeated growth and bubbling transfer of graphene with millimetre-size single-crystal grains using platinum. *Nat Commun* 2012, 3, 699.

2. Wintterlin, J.; Bocquet, M. L., Graphene on metal surfaces. *Surface Science* 2009, 603, 1841-1852.

3. Sutter, P.; Hybertsen, M. S.; Sadowski, J. T.; Sutter, E., Electronic Structure of Few-Layer Epitaxial Graphene on Ru(0001). *Nano Letters* 2009, 9, 2654-2660.

4. Coraux, J.; N'Diaye, A. T.; Engler, M.; Busse, C.; Wall, D.; Buckanie, N.; Heringdorf, F.; van Gastei, R.; Poelsema, B.; Michely, T., Growth of graphene on Ir(111). *New Journal of Physics* 2009, 11, 22.

5. Wang, S. M.; Pei, Y. H.; Wang, X.; Wang, H.; Meng, Q. N.; Tian, H. W.; Zheng, X. L.; Zheng, W. T.; Liu, Y. C., Synthesis of graphene on a polycrystalline Co film by radio-frequency plasma-enhanced chemical vapour deposition. *Journal of Physics D-Applied Physics* 2010, 43, 6.

6. He, P. L.; Mao, Y. L.; Sun, L. Z.; Zhong, J. X., First-Principles Study of the Initial Growth Stages of Carbon Chain on Ni(111) Surface. *Journal of Computational and Theoretical Nanoscience* 2010, 7, 2063-2067.

7. Sanchez-Barriga, J.; Varykhalov, A.; Scholz, M. R.; Rader, O.; Marchenko, D.; Rybkin, A.; Shikin, A. M.; Vescovo, E., Chemical vapour deposition of graphene on Ni(111) and Co(0001) and intercalation with Au to study Dirac-cone formation and Rashba splitting. *Diamond and Related Materials* 2010, 19, 734-741.

8. Kim, K. S.; Zhao, Y.; Jang, H.; Lee, S. Y.; Kim, J. M.; Ahn, J. H.; Kim, P.; Choi, J. Y.; Hong, B. H., Large-scale pattern growth of graphene films for stretchable transparent electrodes. *Nature* 2009, 457, 706-710.

9. Duck Hyun, L.; et al., Versatile Carbon Hybrid Films Composed of Vertical Carbon Nanotubes Grown on Mechanically Compliant Graphene Films. *Advanced Materials* 2010, NA.

10. Lee, D. H.; Lee, J. A.; Lee, W. J.; Choi, D. S.; Kim, S. O., Facile Fabrication and Field Emission of Metal-Particle-Decorated Vertical N-Doped Carbon Nanotube/Graphene Hybrid Films. *Journal of Physical Chemistry C* 2010, 114, 21184-21189.

11. Lee, D. H.; Lee, J. A.; Lee, W. J.; Kim, S. O., Flexible Field Emission of Nitrogen-Doped Carbon Nanotubes/Reduced Graphene Hybrid Films. *Small* 2010, n/a-n/a.

12. Kondo, D.; Sato, S.; Awano, Y., Self-organization of novel carbon composite structure: Graphene multi-layers combined perpendicularly with aligned carbon nanotubes. *Applied Physics Express* 2008, 1.

CHAPTER 4

# STRUCTURAL CHARACTERIZATIONS OF CARBON NANOSTRUCTURES ON DIFFERENT SUBSTRATES

## 4.1. Graphene

Structural Characterizations of chemically vapor deposited graphene on different substrates were done using scanning electron microscopy (SEM), High resolution Transmission microscopy (HRTEM), Atomic force microscopy (AFM) and Raman Spectroscopy. HRTEM was used to visualize the number of layers formation during the CVD process. Raman spectroscopy is one of the historically used probe for nondestructive structural characterizations and electronic characteristics of graphite allotropes[1, 2]. The technique was ignored earlier till the invention of the laser of specified wavelength as carbon materials are the ideal absorber of the visible and IR light. Raman spectroscopy provides the useful information regarding the graphitic structures namely, defects structure, substrate mismatch, crystal vibration, phonon transitions etc. More specifically, defects and substrate mismatch in the graphene lattices can be recognized using the appearance of D band, in-plane vibration can be identified G band which is the key signature of $sp^2$ bonded carbon atoms in the graphitic lattice and the order of stacking can be distinguished using 2D band. We investigated the structural morphologies of graphene on different substrates such as Cu, Ni, $SiO_2$/Si, glass, quartz, Mica, fluorinated tin oxide (FTO) coated glass, polyethylene tetrapthalate (PET) and parylene. We also investigated the structural behavior of free standing graphene (as described the fabrication procedure in chapter 3 section 3.2.2) and a comparison of graphene different structure over different substrates.

### 4.1.1. Scanning electron microscopy

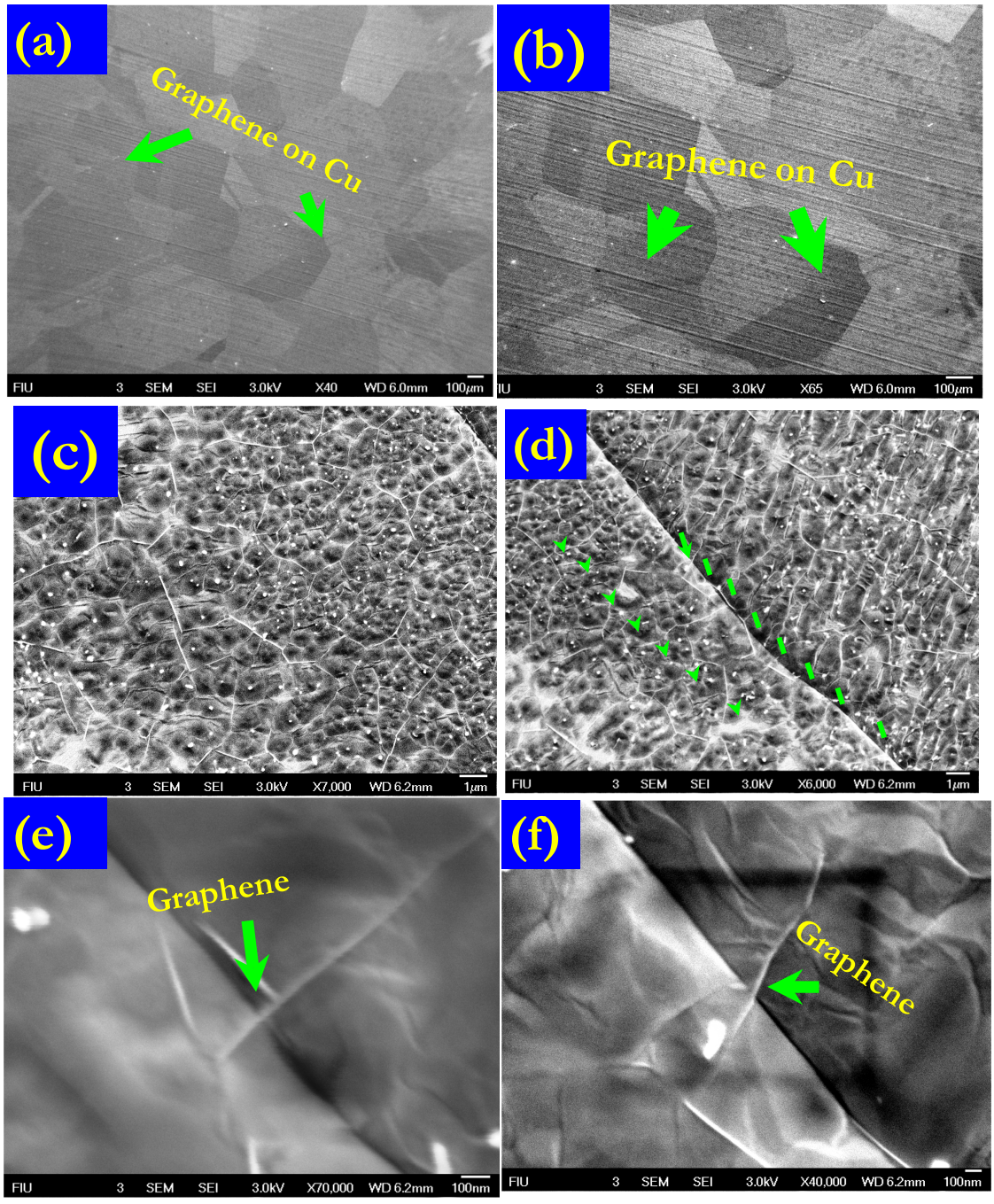


Figure 4.1: (a) & (b) graphene on Cu; (c-f) illustrating the different magnification of graphene film on Cu grain and grain-boundaries.

Generally, Scanning electron microscopy was used for characterizing the surface morphology, crystallographic information, grain and grain boundaries in graphene on Cu and Ni. Surface topography and interface of graphene-CNT hybrid film was observed using a field emission scanning electron microscopy (FE-SEM) from JEOL of model no JSM7000F using bias Voltage: 1-5 KVolt in a distance from 5 to 6 mm. Figure 4.1 a-f, shows the as grown graphene on Cu substrates under different magnifications. As could be observed from the Figure 4.1a & b, the large scale graphene growth occurs on the Cu substrates with overlapping patches of the different layers on each others. Figure 4.1c and f clearly reveals the deposition of graphene over the Cu grain boundaries. Transition metal like Cu, Ni, Co are acts as catalyst for graphene growth as reported earlier where catalytic decomposition of hydrocarbon gases occurs at high temperature and graphene growth occurs on Ni and Cu via different growth mechanisms like segregation-precipitation and decomposition-absorption respectively[3-5]. Figure 4.2 a & b shows the graphene deposition on Ni using chemical vapor deposition method. In comparison between graphene growth on Cu and Ni, we need to first compare the basic structure of Cu and Ni. Both Cu and Ni exhibit same FCC crystal structure along with equal coordination number and almost equivalent electro negativity which is 1.9 and 1.91 for Cu and Ni respectively. However the basic difference is the electronics structure of Cu and Ni. Cu possesses the completely filled 3d band where Ni exhibits the partially filled 3d band. One recent report nicely correlates those properties with the calculated adsorption energy of both the Cu and Ni surface.

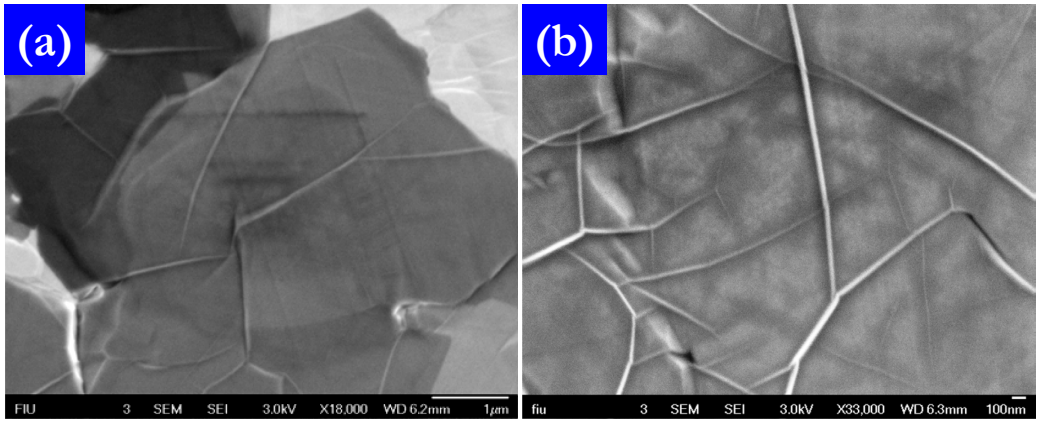


Figure 4.2: (a) and (b) Graphene on Ni thin film under different magnifications.

Hu et al. [6] reported the first principles calculations of the low-index Cu and Ni surfaces, namely (100), (110) and (111) by using Density Functional Theory (DFT). It was found that the absorption energies of C atom on those stable low-index Cu and Ni sites as tabulated in their report[6]. The report says that i) (100) sites for Ni and Cu are most stable absorption sites which can accommodate C atoms easily; ii) (111) planes exhibit lowest diffusion barrier which facilitate the easy movement of adsorbed "C" atoms; iii) Adsorption energy of carbon on Ni is ~ 2 eV higher than the Cu. In this context, d-bands at Fermi level plays the significant role in the C adsorption on Cu and Ni surfaces where partially filled Ni d orbital hybridized with the carbon atoms more strongly than the completely filled in Cu d orbital. Therefore the binding energy of carbon with Ni is stronger than the binding energy of C with Cu.

### 4.1.2. High resolution transmission electron microscopy

Figure 4.3 a, b, c and d showing the high resolution transmission electron microscopy of graphene on Cu. A thin silver (Ag) layer was deposited on the graphene

before the sample preparation in order to avoid any structural damage during the sample preparation. Furthermore, the sample for HRTEM was prepared by conventional cross section method using dimple grinder.

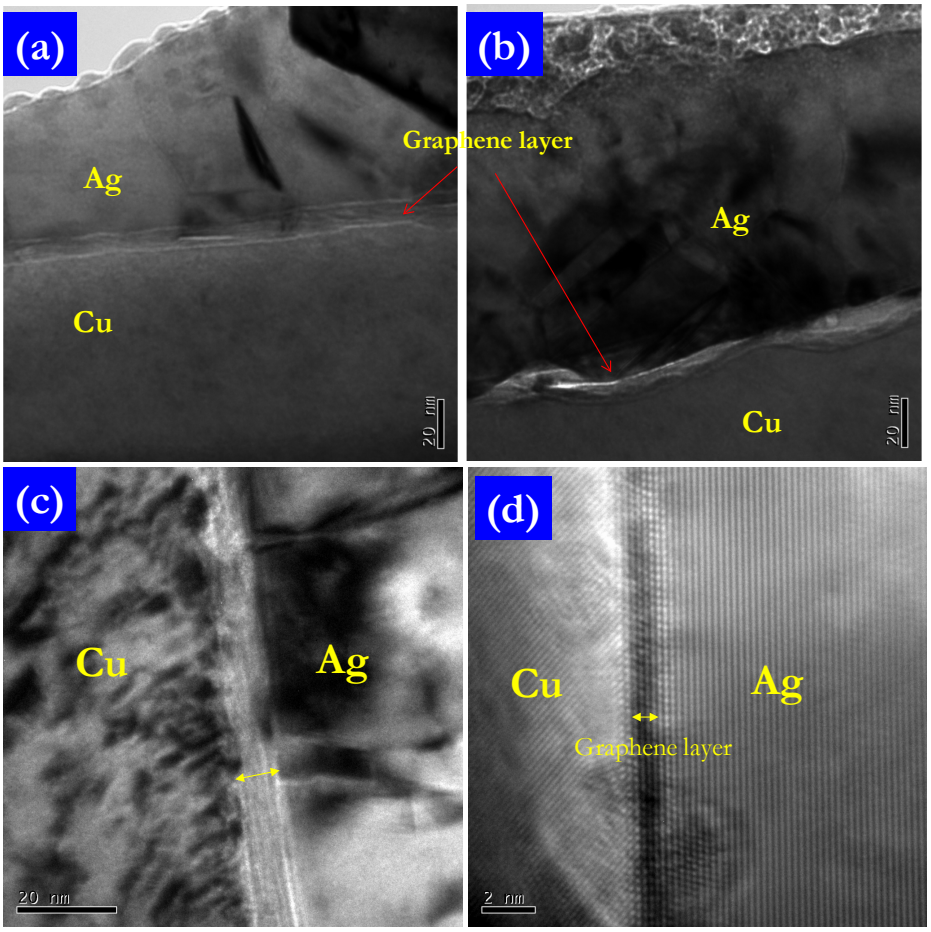


Figure 4.3: (a) & (b) Shows transmission electron microscopy of graphene on cu foil; (c) & (d) showing few layer graphene depositions on Cu surface by chemical vapor deposition of methane at 1000oC.

Then High Resolution Transmission Electron Microscopy (HRTEM) was carried out using FEI Technai F20 field emission gun microscopy.

### 4.1.3. Micro-Raman spectroscopy

Raman spectroscopy is a form of vibrational spectroscopy, and can be thought of in its simplest form as a process where a photon of light interacts with a sample to produce scattered radiation of different wavelengths. The spectrograph shows the recorded vibrations of covalent bonds in the molecules and provides highly detailed molecular information. Raman scattered light is frequency-shifted with respect to the excitation frequency, but the magnitude of the shift is independent of the excitation frequency. This "Raman shift" is therefore an intrinsic property of the sample[7].

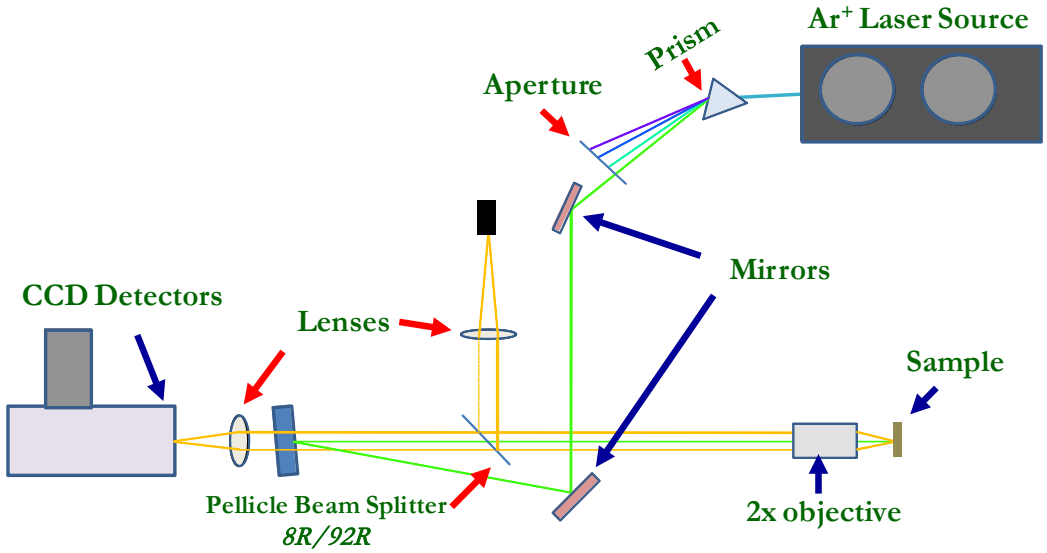


Figure 4.4: Schematic representing Raman spectroscopy set up.

The RAMAN SPECTROSCOPY setup is consist of a 514.5 nm $Ar^+$ ion laser source, Beam splitter 50/50; 514/NOTHC mirror; COHERENT 53-2218 mirror and a CCD detector as shown in Figure 4.5. CW argon ion ($Ar^+$) laser form Spectra Physic (model177G02) of 514.5 nm in wavelength was used as a source of monochromatic

radiation for the experiment. Backscattered Raman spectra were collected using a high-throughput holographic imaging spectrograph from Kaiser Optical System (model HoloSpec f/1.8i) inbuilt with volume transmission gratings associated with a holographic notch filter, and a thermoelectrically cooled CCD detector from Andor Technology. The Raman system has spectral resolution of 4 $cm^{-1}$.

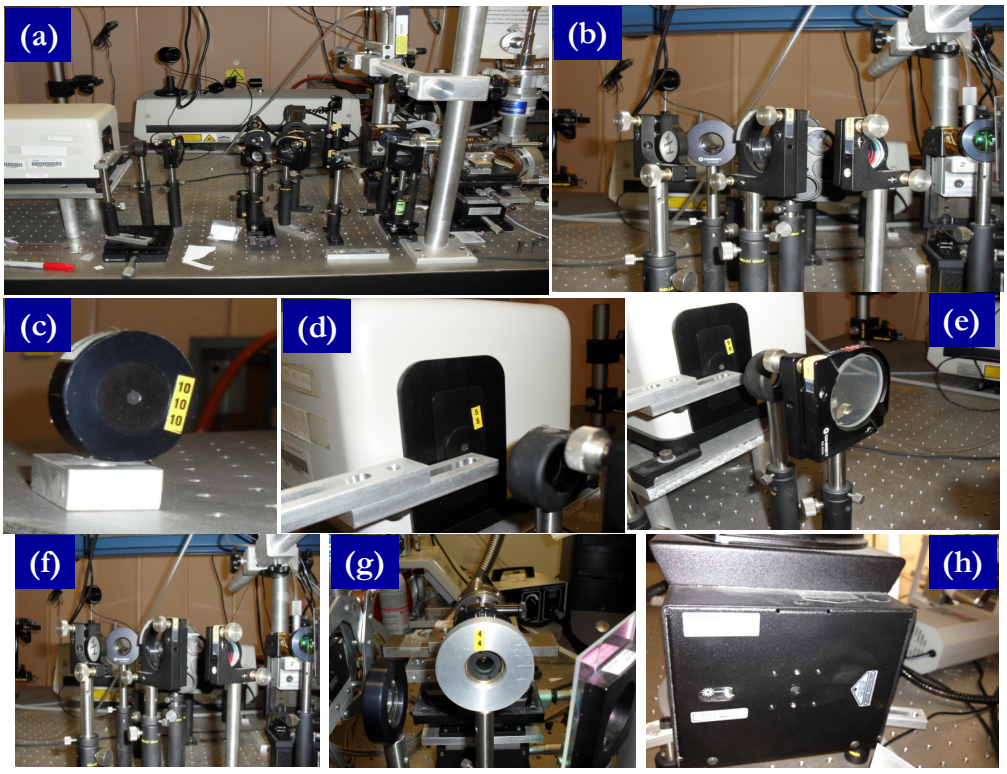


Figure 4.5: Pictures showing different components of Raman spectroscopy as shown in the schematic Figure 4.4 (a) Raman setup; (b) Beam splitter 50/50; (c) Pinhole; (d) spectrometer pinhole; (e) 514/NOTHC mirror; (f) COHERENT 53-2218 mirror (g) The last lens which laser goes through before hitting the sample [Source: CESMEC. FIU].

Raman spectroscopy has widely been used to characterize the structural and electronic characteristics of carbonaceous materials specially graphite materials[2]. The

technique provides us the useful information regarding defects and substrate mismatch in graphene lattices which can be recognized using the appearance of D band. Moreover, in-plane $sp^2$ bond vibration is represented by the intensity and position G band which is the key signature of $sp^2$ bonded carbon atoms in the graphitic lattice and the order of stacking can be distinguished by 2D band position. The typical band positions of D band, G band and 2D band are appears at the frequencies of ~1350 $cm^{-1}$, 1580 $cm^{-1}$ and 2690 $cm^{-1}$ respectively for single layer graphene[8]. Monolayer graphene exhibits unique characteristics of intensity ratios of G band and 2D band (i.e. $I_G/I_{2D}$) which is ~ 0.4-0.5[9]. Similarly the defect structure can also be scrutinized using the D and G band ratio i.e. $I_D/I_G$[1]. The increasing value of $I_D/I_G$ ratios represents the degree of incorporation of defects in the graphene structures[8]. The ratio of $I_G/I_{2D}$ for graphene also increases with increasing number of layers and this is another fingerprint to characterize the number of layers in graphene structure. However, peak positions of the 2D peaks are also important which get blue-shifted with increasing no of layers[10]. Similarly, different intensity ratios of the different bands like $I_D/I_G$ and $I_G/I_{2D}$ also one of the key identification marks of the graphene defect intensities and the number of layers.

Figure 4.6 illustrates the comparison Raman spectra obtained from the graphene on Cu and Ni both. The characteristics spectra consist of a signature of G band and D band at 1579.5 $cm^{-1}$ and 2709 $cm^{-1}$ for Ni and 1580 $cm^{-1}$ and 2709 $cm^{-1}$ respectively. A tiny D band appears for graphene/Cu foil which is absent in case of Ni thin film. The $I_G/I_{2D}$ intensity ratios for graphene/Cu foil and graphene/Ni thin film is calculated as 0.43 and 0.88 respectively depicting the signature of few layers graphene on the both the

substrates[11]. However, from the intensity ratios it could be specified that the number of graphene layers on Ni is higher than the no of layers on Cu.

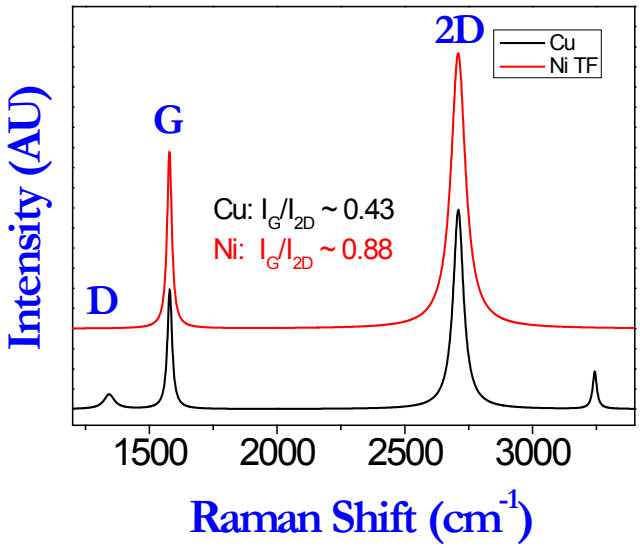


Figure 4.6: A comparison Raman Spectra of graphene on Cu foil and graphene on Ni thin film.

(a) (b)

(c) (d)

Figure 4.7: (a) Characteristics Raman spectra of graphene on different substrates (b) 2D band, (c) showing the magnified view of 2D band and (d) G band.

Furthermore, Raman spectra collected from samples of graphene on a wide range of substrates under identical conditions and plotted in a single plot and found that all the spectral band intensity is strictly influenced via substrates[12]. As seen in Figure 4.7 a-d all the G and 2D band intensity is higher for metal substrates compared to the dielectric substrates. We believe that the free electrons in conducting substrates intensify the in-plane phonon transitions of the $sp^2$ bonded carbon atoms as well as the vibrational transition of phonons due to the stacking order of graphene[1, 8].

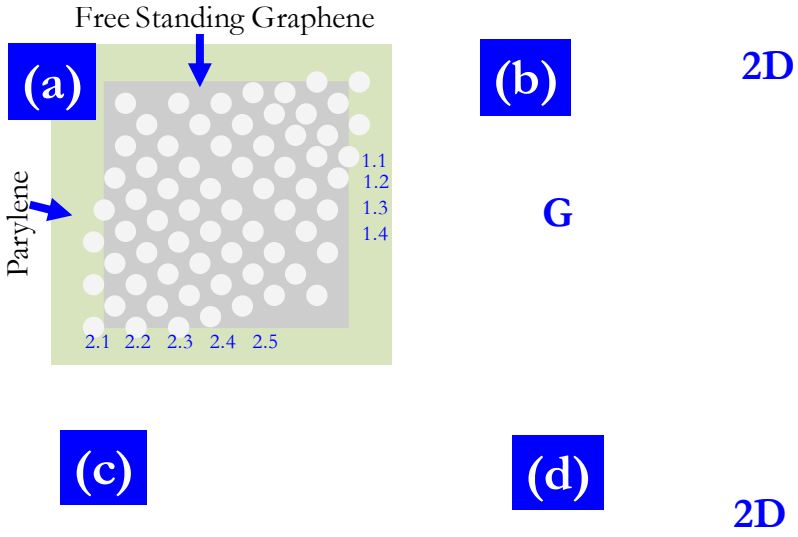


Figure 4.8: (a) Schematic showing free standing graphene and the procedure for the marking of different holes for Raman spectroscopy. (b) Comparison plot of Raman spectra of free standing graphene on parylene transferred from Cu and Ni respectively, (c) G band and (d) 2D band.

In this context, we also justifies the graphene phonon responses without substrates using Raman spectroscopy and for this reason, we fabricate free standing graphene on parylene by transferring the graphene from different Ni and Cu substrates on parylene. Further we observed that graphene from Cu has higher 2D band intensity compare to the graphene from Ni which is due to the higher number of graphene layers formation on Ni than Cu (as shown in Figure 4.7b & d) whereas the G band intensity is almost same for both the cases (Figure 4.7 c).

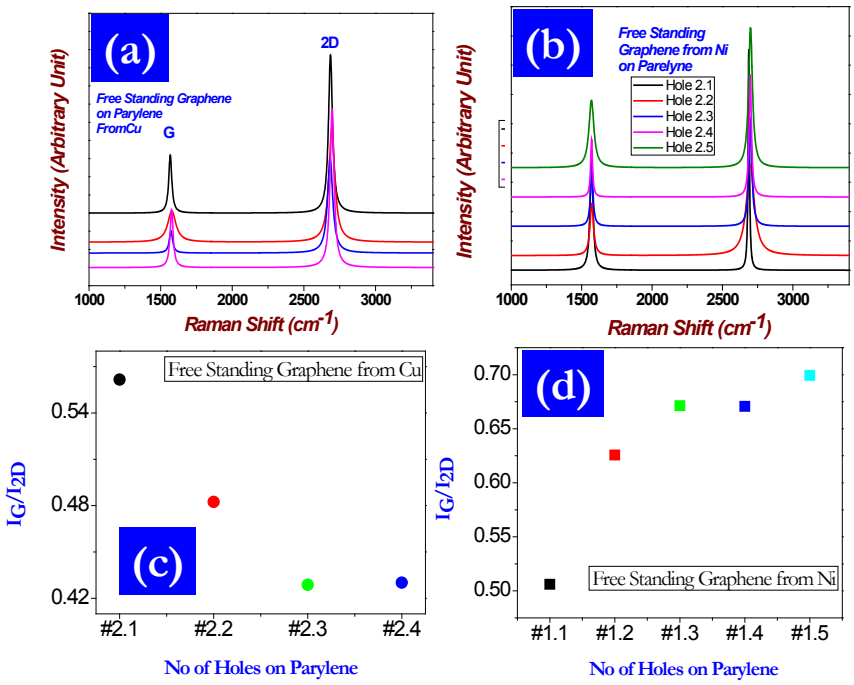


Figure 4.9: Raman spectroscopy of free standing graphene on different marked holes on parylene (a) transferred from Cu and (b) transferred from Ni, (c) and (d) showing the variations in $I_G/I_{2D}$ ratio on different holes for Cu-graphene and Ni-graphene respectively.

Figure 4.7 b shows the $I_G/I_{2D}$ ratio for Ni & Cu exhibit ~0.7 and 0.33 which corroborate that Ni has higher no. of layers than Cu. Moreover, we can see the blue-shift

in 2D peak positions for Ni/graphene than Cu/graphene which is 17 $cm^{-1}$ shift as shown in Figure 4.8 d which also may be due to the higher number of layers on Ni than Cu[10]. Figure 4.8 a & b, shows the Raman mapping from the free standing graphene from Cu and Ni respectively on different marked holes on parylene as shown in Figure 4.7a. As could be seen from the Figure 4.8 a & b there is no as such distinguishable difference on different holes. However, the Figure 4.8 c and d shows the $I_G/I_{2D}$ ratios of graphene from Cu and Ni respectively. In case of Cu/graphene the majority of the ratios varies ~0.4 ranges whereas for graphene from Ni majority of the points ~0.7. The significant difference in the peak intensity ratios manifests that the Ni substrates has much more graphene layers than in Cu[11].

### 4.1.4. Atomic force microscopy

AFM reveals the surface topography of the graphene at atomic scale and is used here to measure the step height of graphene over the atomically cleaved mica substrates. The surface topography of graphene on mica (Ted Pella Inc.) was investigated using AFM (NanoScope IIIa, Veeco Instruments Inc., USA) under tapping mode. The Non-contact/TappingMode AFM probes were purchased from NanoWorld AG (NANOSENSORS™, Switzerland) which had relatively stiff cantilevers with a high spring constant (30.0 - 59.0 N/m). Figure 4.10 shows the homogeneous surface topology of graphene with vertical step height of ~2.7 nm.

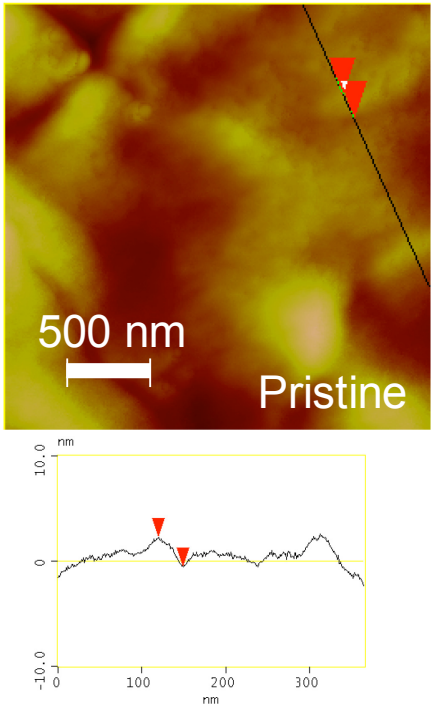


Figure 4.10: Atomic force micrograph showing the surface topology of graphene on mica with vertical step height of 2.7 nm.

## 4.2. Graphene-CNT hybrid structure

Graphene exhibit its in-pane high thermal and electrical conductivity in 2D whereas CNT exhibit its conductivity in its axial direction (1D). Therefore nano-hybrid structure consisting vertically aligned CNT with 2D graphene is always beneficial to combine the effect of both 2D and 1D structure in a single structure[13]. Several recent reports[14-16] shows an interesting approach to grow vertically aligned MWCNTs on reduced graphene oxide platelets using CVD method or using dispersed graphene and dispersed CNT separately and coat those consecutively on flexible substrates in order to fabricate the high performance transparent graphene-CNT hybrid structure[17]. In this

context, several other applications have been proposed of this hybrid structure in flexible and bendable electronics devices. However, the reduced graphene oxide involve lot of issues like, low conductivity, less uniformity and high temperature robustness that deteriorate its heat dissipation even at high temperature. Similarly, incorporation of volatile ingredients from the RGO makes the hybrid structure not useful for applications in vacuum electronics. At the same time, the proposed multi-step method involves several rigorous processing steps like, graphene fabrication from reduced graphene oxide, spin coating, catalyst deposition, CNT growth followed by the transfer process onto a flexible substrate. Therefore, in-situ growth of graphene-CNT hybrid structure using CVD is the purest method as well as bypasses those processing steps. On the other hand, spin coated graphene flakes produced short range graphene structure, which readily deteriorate the film electrical conductivity as well as heat dissipative properties[14]. Hence, the utmost concern at this moment is to fabricate large scale in-situ graphene-CNT hybrid structure and transfer it to a flexible polymer substrate. Some of these shortcomings of this process can be overcome by growing in-situ graphene-CNT hybrid structure consisting of CNTs connected perpendicularly to graphene layers. In this regards, even few layer thick graphene bottom layer could be more advantageous as it could provide the vigorous mechanical properties along with good electrical and thermal conductivities.

Therefore, controlled growth of self-organized graphene-CNT hybrid structure and a single step transfer process on to a flexible substrate is more practical approach for devising flexible electronics and vacuum-electronics like field emission, vacuum gauge etc. Furthermore, a controlled fabrication technique of the graphene-CNT hybrid structure would open new possibilities for nanoscale devices including interconnect,

flexible nano-electronics, flexible field emission displays, and strain gauges and so on[18-23].

In our lab we grow the in-situ graphene-CNT hybrid structure consists of multilayered graphene connected with vertically aligned carbon nanotube and its electrical and electro-mechanical properties. After that we performed a comprehensive analysis of the structure, morphology, and bonding chemistry of the hybrid graphene-VACNTs structure using a combination of high resolution transmission electron microscopy (HRTEM), field-emission scanning electron microscopy (FESEM), X-ray photoelectron spectroscopy (XPS), Auger electron spectroscopy (AES) and micro-Raman spectroscopy. A thorough correlation with different oxide and carbide formation with CNT growth at high temperature is also explained in order to elucidate probable growth mechanism of the hybrid. We further investigate the effect of catalyst thickness on hybrid structure growth and we elaborate the growth mechanism. In-addition, we present a facile and scalable method for transferring the film on to different flexible substrates i.e. a soft poly di-methylsiloxane (PDMS) matrix and a Cu foil. The resulting flexible graphene-CNT films are demonstrated as strain gauges and field emission devices as a function of bending radius.

### 4.2.1. Electron microscopy

#### 4.2.1.1. Scanning electron microscopy

Electron Microscopy is scientific techniques that examine objects on a micro to nano scale using beam of highly energetic electrons under high applied bias. This

technique can yield the following information regarding the sample to be investigated: (a) Surface Topography, (b) Morphology and (c) Crystallographic information.

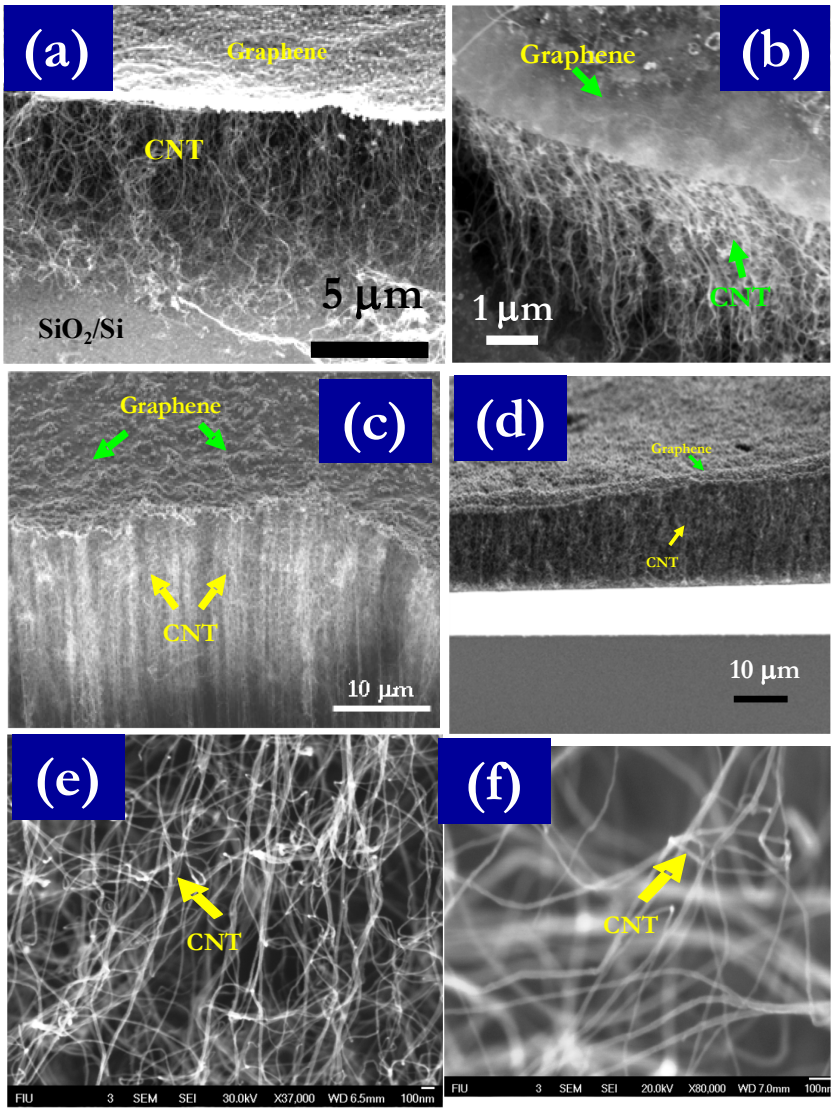


Figure 4.11: (a) (b) and (c) Scanning Electron Micrograph (SEM) of graphene-CNT hybrid structure on $SiO_2$/Si substrates with different morphologies; (d) Crosssectional view of the hybrid structure showing vertically aligned CNT covered with a top graphene layers; (e) and (f) showing the vertically entangled CNT in graphene-CNT hybrid film.

Surface Morphology and interface of graphene-CNT hybrid film was observed using a field emission scanning electron microscopy (FE-SEM) (JEOL, JSM7000F) using bias Voltage: 3-5 KVolt in a distance from 5 to 6 mm. The representative FE-SEM images showing morphology of the hybrid structure is presented in Figure 4.11 a b c & d. The structure is composed of vertically aligned multiwall carbon nanotubes on $SiO_2$/Si substrate and a multilayered graphene film on top of it. Average length of MWCNTs was measured as ~30-40 μm. Morphology of the MWCNTs are known to be related to the size of catalytic nano-particles, which in turn, is dictated by the catalyst film thickness. The MWCNT growth by thermal CVD process is strongly dependant on the nature of the catalysts through; transformation of metal catalyst particles into metal carbide particles; nucleation and growth of catalyst particles and diffusion of carbon atoms inside the catalyst matrix[24, 25].

#### 4.2.1.2. High resolution transmission electron microscopy

High Resolution Transmission Electron Microscopy (HRTEM) (FEI Technai F20 field emission gun microscopy). The sample for HRTEM was prepared by conventional cross section method using dimple grinder, and subsequently thinned using 691 Gatan-PIPS™ ion mills from the graphene-carbon nanotube hybrid film on as grown substrates. As seen in the HRTEM image, Figure 4.12a shows the top portion of the hybrid structure consist of multilayered graphene and the bottom portion is CNT. The graphene thickness is ~15-20 nm which consists of ~40 graphene monolayer and the measured distance between each monolayer is 3.4 Å [26].

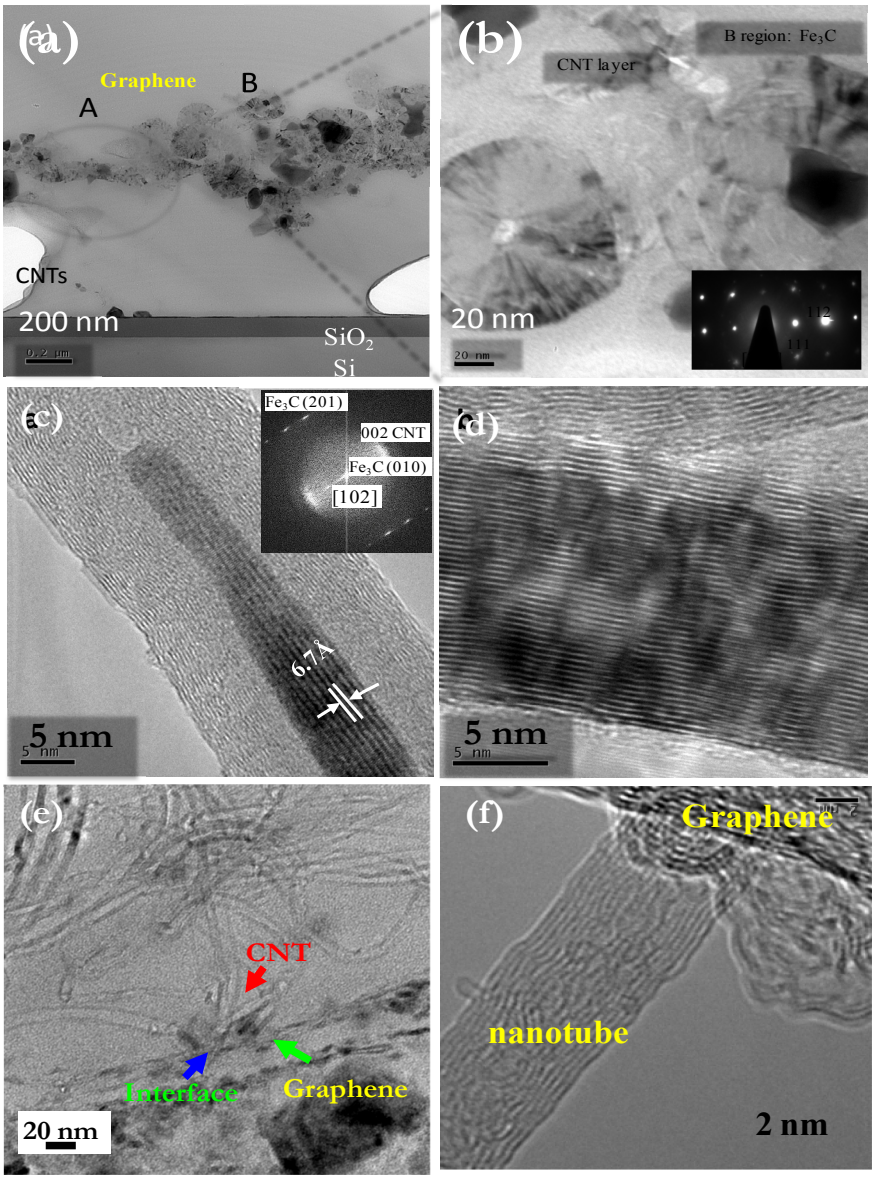


Figure 4.12: (a) Transmission electron micrograph showing the microstructure of as-deposited graphene-CNT hybrid film (b) Bright field transmission electron microscopy of the "B" region as shown in Figure 4.12 a. (c) High resolution TEM image of CNT showing the presence of iron carbide particles inside the CNT tube (d) high resolution of TEM image of Graphene film (about 40 graphene mono layer) on the top of the nano-hybrid film. (e) & (f) HRTEM showing the clear interface between graphene and CNT.

Figure 4.12 b and c manifests the iron carbide ($Fe_3C$) nanoparticles were (as shown in the SAD pattern in the inset of Figure 4.12b) found at the interface between the graphene and CNT layer and also inside the CNT tube (Figure 4.12c). Therefore, it can be concluded that $Fe_3C$ plays the major role in CNT growth. From the HRTEM we found that the average diameter of CNT was ~10-15 nm as shown in Figure 4.12c & f) and the presence of iron carbide particles at the interface between graphene and MWCNT. The presence of nano-scopic iron carbide particles evidenced the tip growth of CNTs from the iron carbide catalyst particles as explained in the previous section. A clear interface between a CNT and graphene film is illustrated in the Figure 4.12 e & f which demonstrates the catalyst assisted interface formation between graphene and CNT.

Although the mechanisms of co-formation of CNTs and graphene are still not very cleat but Chernozatonskii et al.[27], proposes the van der Waals force between tubes and graphene layers may be the main forces that keep this attachment stable. As mentioned earlier, the axial/planar arrangement of elemental carbon would be beneficial to obtain higher thermal conductivity in three dimensions. On the other hand, as mentioned by Ho et al.[28], Lennard-Jones potential model shows both metallic or semiconducting behavior of this structure which is highly dependent on alignment of nanotubes and graphene layers. However, the interface formation mechanism between graphene and CNT needs further systematic investigations and optimizations of the growth parameters.

### 4.2.2. Micro-Raman spectroscopy

The basic difference between highly ordered pyrolytic graphite (HOPG) and graphene is the shape of 2D Raman band, for graphene, it is symmetric and for HOPG, it is un-symmetric with a shoulder or small peak to the left [29-31]. The symmetric 2D Raman band of graphene-CNT indicates that it is not HOPG. The representative D, G and 2D band positions and full width half maxima (FWHM) of graphene-CNT and MWCNT are shown in Table 4.1. For mono and bi layer graphene, the FWHM of 2D band is ~30 and for graphene-CNT it is ~69.14[30]. We believe that the 2D peak broadening can be attributed to the number of layer increases in graphene structure[1]. The blue shift in band positions of graphene -CNT also indicates relatively stronger bonding between graphene and CNT.

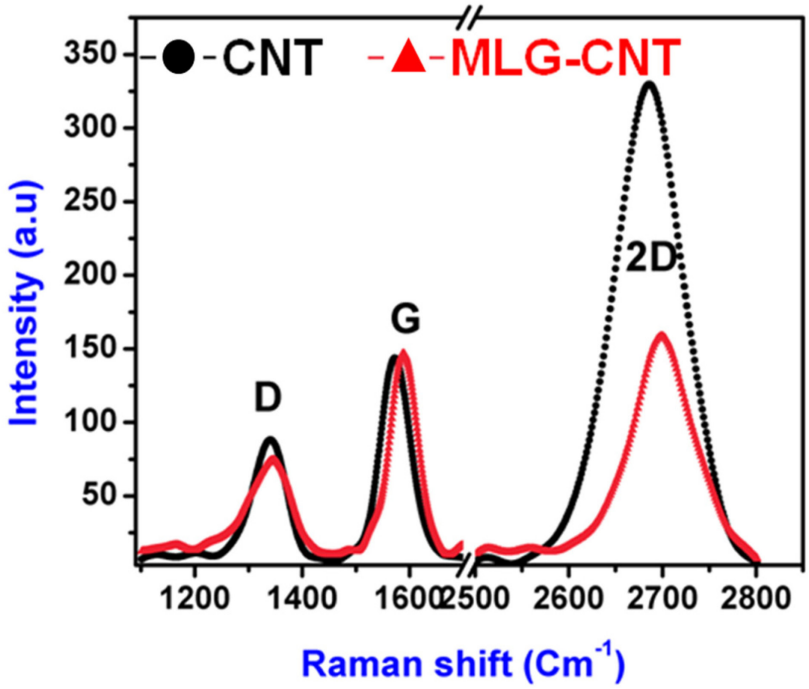


Figure 4.13: Comparative Raman spectra showing the CNT and graphene-CNT hybrid structure.

The Raman spectroscopy results statistically agreed with eight separate studies conducted on three samples. G and 2D band position of graphene is also related to its supporting substrate and shape is the function of number of layers and synthesis method[1, 30]. The Raman spectrum in Figure 4 is from graphene present on top of ~40 μm tall CNT on $SiO_2$/Si substrate. The length of CNT is much higher than the penetration depth (60 nm) of the 514.5 nm wavelength (λ) $Ar^+$ laser, so we expect minimal influence of the substrate on graphene-CNT Raman spectrum. However, further analysis is required in order to understand the differences in the shape and position of the observed Raman bands.

Table 4.1: Comparison RAMAN peak-positions and full width half maxima for carbon nanotubes and graphene-CNT hybrid film.

| **Structure** | **D band** | | **G band** | | **2D band** | |
|---|---|---|---|---|---|---|
| | Position [$cm^{-1}$] | FWHM | Position [$cm^{-1}$] | FWHM | Position [$cm^{-1}$] | FWHM |
| MLG-CNT | 1345.7 | 77.3 | 1587.9 | 47.62 | 2700.2 | 69.14 |
| CNT | 1339.3 | 75.81 | 1573.4 | 64.26 | 2685.2 | 87.5 |

Furthermore, the Raman spectra and images of as grown CNT and iron compounds ($Fe_2O_3$, $Fe_3C$) nanoparticles were observed from the sample shown in Figure 4.11 a. Figure 4.14 shows the Raman spectra of CNT representing characteristic D, G and 2D band. Figure 4.14 b and c showing the Raman spectrum of $Fe_3C$ and $Fe_2O_3$ nanoparticles respectively. Optical image of micro Raman mapping for CNT and iron

oxide is shown in Figure 4.14 d and Figure 4.14 e & f depicts the Raman mapping from both CNT and $Fe_2O_3$. A higher magnification of SEM image on the boundary between CNT rich area and iron oxide region which shows the faceted $Fe_2O_3$ nanoparticles homogeneously distributed on the substrates (as shown in the inset of the Figure 4.12 d). Presence of $Fe_3C$ nanoparticles (as shown in the HRTEM Figure 4.12b) was also detected during Raman analysis.

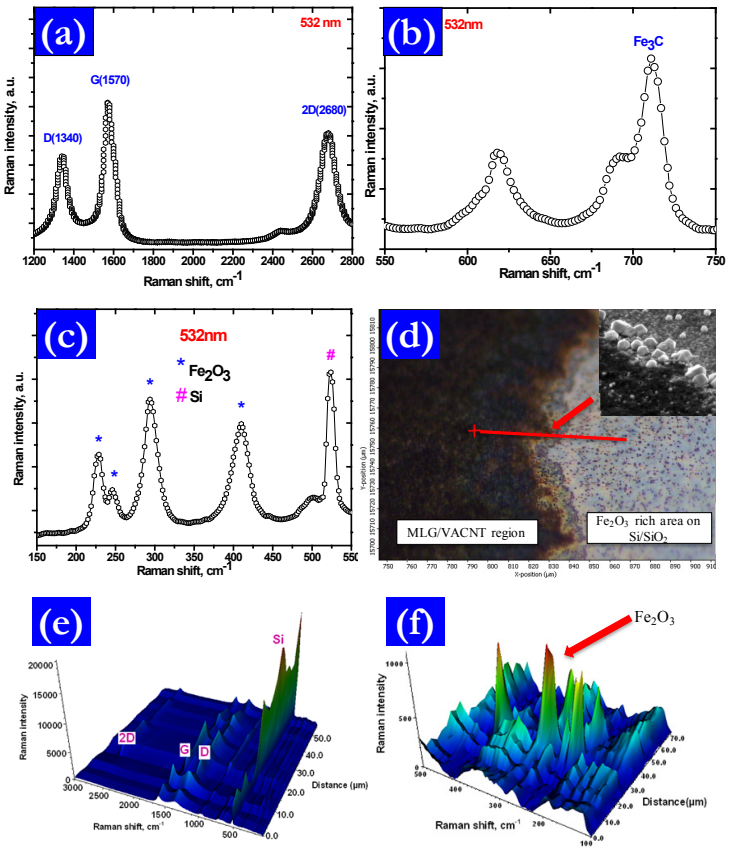


Figure 4.14: (a) Raman spectra of as grown CNT; (b) & (c) Raman spectroscopy of catalyst particles on the substrate showing the iron compounds (Fe2O3 , Fe3C nanoparticles) formed during CNT growth; (d) Optical microscopy image of micro Raman mapping for CNTs and iron oxide particles, which is illustrated in Figure 4.14 e and f.

In Figure 4.14 b, the characteristics peaks of iron carbide nanoparticles obtained in lower frequncies regions. In particular, the signaure of $Fe_3C$ peaks at 710 $cm^{-1}$ appeared at the graphene-CNT interface region which also justifies the growth mechanism of CNT via catalytic activity of Fe to $Fe_3C$. Therefore, it should be mentioned that since iron nanoparticles is a well known catalyst for CNt growth, it is probable that iron carbide nanoparticles formed during nucleation and growth of CNT[24, 32]. On the other hand, main signature of iron oxide nanoparticles ($Fe_2O_3$) was also observed by Raman spectroscopy, and is represented in Figure 4.14 c. However, $Fe_2O_3$ rich area was not found in between CNT and graphene interface regions. The spectrum closely matchs with the spectrum of $Fe_2O_3$ phase. Additionally, a relatively sharp peak is seen at around 521 $cm^{-1}$, which is attributed to Si substrate. In order to characterized the distribution of CNT and iron oxide nanoparticles, linear Raman mapping was carried out in the region as shown in the Figure 4.14 d. The Raman mapping was collected in the range of 100 to 3000 $cm^{-1}$, by keeping in mind that point to point resolution of Raman map was adjusted to 2 μm. Althoguh characterstic Raman peaks of CNT (especially multi-walled), Si and $Fe_2O_3$ are seen, but intensities of CNT and iron oxide peaks are highly influenced by Si substrate where $Fe_2O_3$ is not. Figure 4.14 e & f, illustrates the Raman maps from CNT and $Fe_2O_3$ respectively.

### 4.2.3. X-Ray photoelectron spectroscopy

The high resolution XPS spectra for core level of C and Fe compounds obtained for excitation energy of 1486.4 eV is shown in Figure 4.15. The core line of C1s photoelectron peak is located at 284.5 eV which associates with CNT in the binding

energy range of 278 to 298 eV which exhibit the electron attenuation length for photoelectron incident angle of 90° is about 2.11 nm. Furthermore, by considering the fact that CNT length is > 10 μm long, thus detection of C1s associated with graphene is unlikely and only adatoms or atoms nearer to surface are discernible. However, applying XPS for detection of iron species indicates the existence of iron compound as shown in Figure 4.16. Position of Fe2p3 peak is attributed to chemical state of $Fe_2O_3$ (Figure 4.16), which is in agreement with the Raman spectroscopy results as shown in Figure 4. 14 f.

Figure 4.15: High resolution XPS spectra of CNTs showing carbon with C1s peak.

### 4.2.4. Auger Electron spectroscopy

Elemental distribution of the carbon and iron was mapped by Auger electron spectroscopy from 670xi Scanning Auger Nanoprobe. In order to identify the role of the iron catalyst for the CNT or graphene growth, AES analysis was carried out on the iron oxide rich layer. After the background subtraction AES spectrum is represented for

carbon (KLL), iron (LMM) and oxygen (KLL) are shown in Figure 4.17 a. The C (KLL) located at 275 eV represents auger peak for CNT. Keeping in mind the XPS and micro Raman results, position of Fe (LMM) and O (LMM) peaks suggests the co-existence of iron oxide (III). Figure 4.17 b shows elemental Auger maps of C, Fe and O which implies a relatively fine distribution of iron oxide nanoparticles.

Figure 4.16: High Resolution X-Ray photoelectron spectroscopy of Fe 2p3 core level photoelectron peak.

In addition, there is very less amount of carbon signature from the iron oxide, which indicates that the oxide particle would not participate in catalytic activity, instead iron or iron carbide nanoparticles were involved as key catalytic sites. We believe that the $SiO_2$ layer is likely to be a source of oxygen during the growth which plays an important

role in $Fe_2O_3$ formation. Thus, the control of the silicon oxide layer might be critical for the growth of the graphene-CNT composite structure.

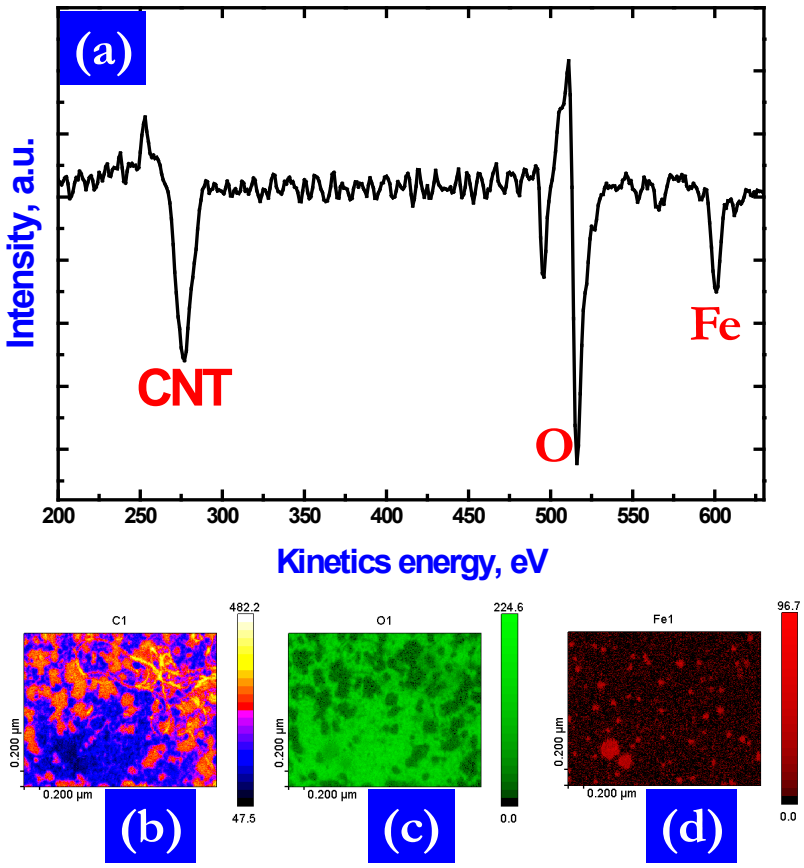


Figure 4.17: (a) $\frac{d(E.N)}{dE}$ Auger electron spectra obtained for C (KLL), Fe (LMM) and O (KLL) by using 10 KeV and 10 nAmp. (b) The elemental mapping obtained from Auger electron spectroscopy for C, Fe and O.

### 4.2.5. Graphene-CNT hybrid structure growth mechanism

So far using different experimentations we believe that, catalyst thin film thickness plays an important role in case of in-situ formation of different morphologies of carbon nanostructures during thermal CVD process. The mechanism of the formation of

graphene-CNT hybrid film on SiO2/Si substrates is yet to be understood clearly. However, as explained by Kondo et al, we believe that initially, multilayered graphene film precipitated on the top of the Fe thin film followed by the CNT growth (as shown in the schematic in Figure 4.18).

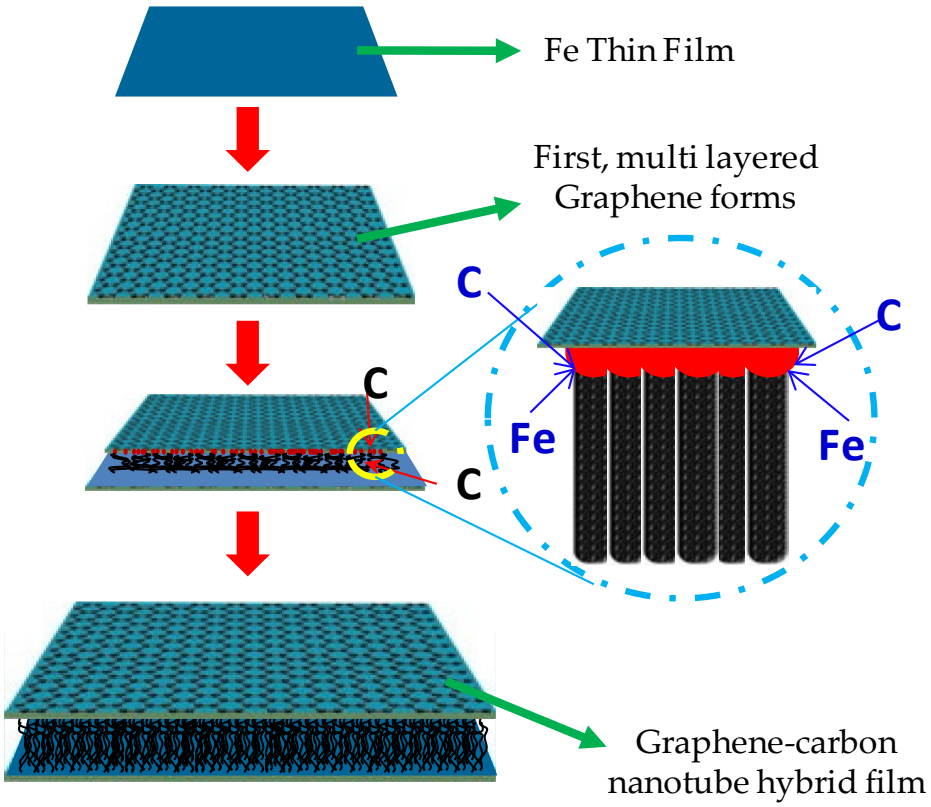


Figure 4.18: Schematic representating the growth mechanism of graphene-CNT hybrid nanostructure using CVD method.

Morphology of the MWCNTs are known to be related to the size of catalytic nano-particles, which in turn, is dictated by the catalyst film thickness[13]. However the precipitation of graphene is dependent upon the surface morphologies of the catalyst and type of the catalyst. In this context, the MWCNT growth by thermal CVD process is

consist of the following i) type of the catalysts ; ii) transformation of metal catalyst particles into metal carbide particles; iii) nucleation and growth of catalyst particles and iv) diffusion of carbon atoms inside the catalyst matrix[24, 25].

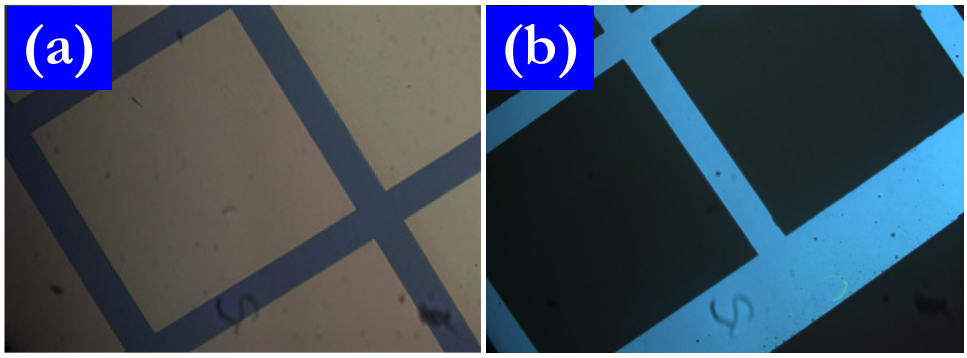


Figure 4.19: (a) Optical micrograph of patterened Fe catalyst on $SiO_2$/Si substrates (b) the hybrid structure growth after the growth process.

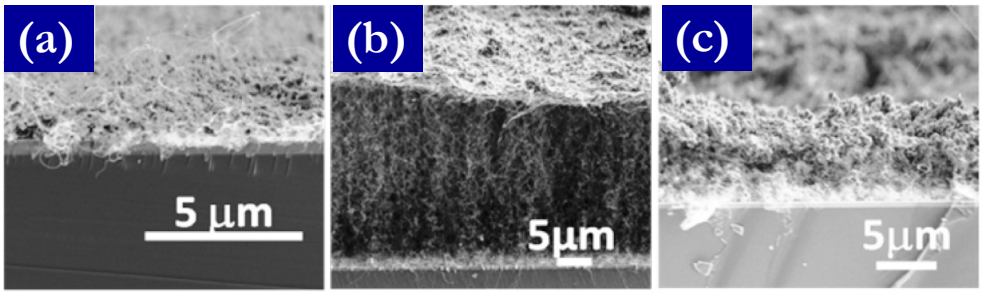


Figure 4.20: (a), (b) and (c) Scanning electron micrograph representing the growth of graphene-CNT hybrid structure from catalyst thickness 10 nm, 20 nm and 30 nm respectively.

Similarly, a clear distinction was observed among the morphologies of the hybrid films when different catalyst thicknesses were used. To showcase the effect of catalyst thickness, we used photolithography (as described in the chapter 3 scetion 3.1.2) to

prepare areas of different catalyst film thicknesses on a single substrate and carried out the graphene-CNT growth process under the same condition as shown in Figure 4.19 a &b which illustrates the before and after the hybrid growth structure respectively.

Figure 4.20 a, b & c are the characteristics FESEM pictures illustrating the effect of iron thin film thickness on in-situ formation of graphene-CNT hybrid film on a $SiO_2$/Si substrate. Figure 4.20a shows the formation of only thin CNT from the 10 nm thickness of Fe thin film catalyst. On the other hand, Figure 4.20 b shows the in-situ formation of graphene-CNT hybrid structure from the 20 nm Fe thin film, however Figure 4.20 c demonstrating no hybrid structure growth from 30 nm Fe thin film which just exhibited thick agglomerated catalyst particles after the CVD growth process.

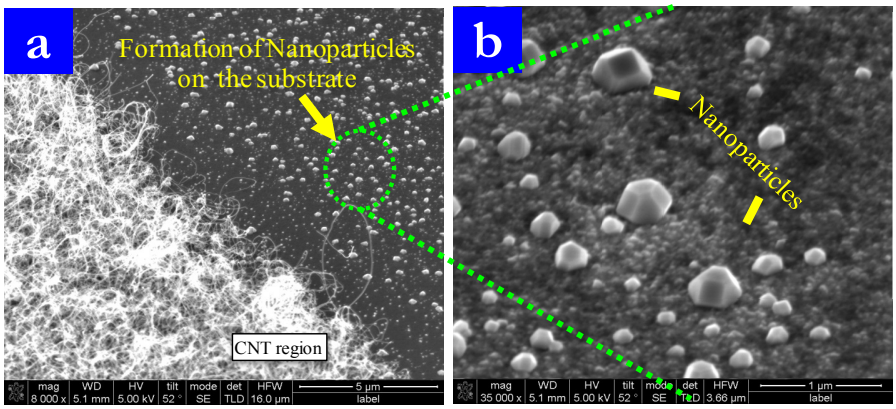


Figure 4.21: (a) & (b) Formation of nanoparticles on the substrate for CNT growth and the particles at higher magnifications respectively.

### 4.2.6. Electrical and electro-mechanical characterizations

Electrical conductance was measured to evaluate the conductivity and the continuity of the top layer along the lateral direction of the graphene-CNT hybrid film. In graphene transport properties are dependent on various factors including distribution of

carriers among the graphene layers and impurity density[33-37]. Since the low-energy bands of graphene are mostly localized on atoms which are not coupled to neighboring layers, the hybridization between graphene layers does not favor interlayer hopping[33, 35] . Therefore, the charge transport property in multi-layer graphene is significantly lower than mono or bi-layer graphene[33-36]. Nevertheless, a linear relationship of I-V characteristics was observed for all the measurements with low resistance values varying from 100-400 Ω with increasing electrode distance as shown in Figure 4.22. Moreover, uniform conductance over the large area of the hybrid film attributed to the ohmic contacts between graphene and CNT, thus indicating good structural integrity of the nanostructure.

In addition to the good electrical properties, the graphene-CNT hybrid film has excellent electro-mechanical properties and good structural integrity when used to make flexible film or stretchable electrodes. The fabrication process of graphene-CNT-PDMS film and its flexibility is demonstrated in Figure 4.23a & b and the morphology of the top surface of the polymer-hybrid film is shown in a FESEM picture in the inset of Figure 4.23b. Similarly the structure was also transferred onto a flexible adhesive Cu tape as illustrated in Figure 4.23a. After the transfer process, the hybrid structure on the Cu foil was observed in a SEM shows the graphene under layer on Cu foil an vertically aligned CNT are on the top of it as depicted in the Figure 4.24.

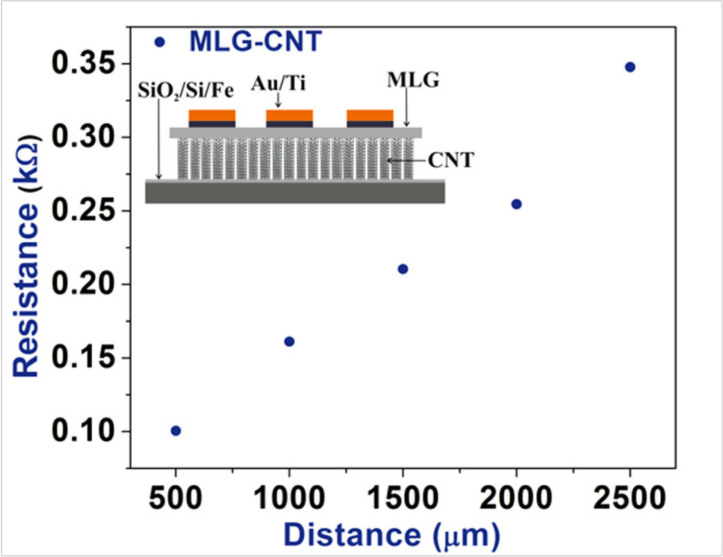


Figure 4.22: Representative plot of electrical resistance (R) as a function of distance curves measured form the graphene-CNT hybrid film on as grown $SiO_2$/Si substrate by two terminal measurement methods. Resistance measured as a function of distance to demonstrate the structural integrity and electrical performance of large area graphene-CNT hetero-junction composite electrode.

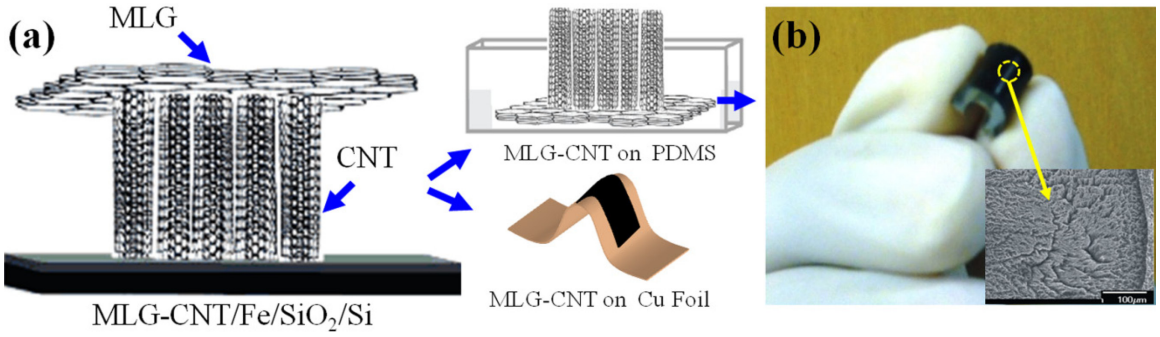


Figure 4.23: Schematic illustration of graphene-carbon nanotube hybrid film transfer process on flexible Poly di-methylsiloxane (PDMS) and Cu foil (b) Image demonstrating flexibility of the graphene-CNT hybrid film-PDMS composite and inset showing the FESEM pictures of the top surface of the composite.

We evaluated the flexibility (tension as well as compression) of as obtain graphene-CNT-PDMS polymer film by measuring the resistance with respect to the folding radii. In Figure 4.25a & b the resistance shows a distinguishable variation of 0.85-2.3 kΩ and 0.9-5.5 kΩ from the bending radius of flat to 3.3 mm in tension and flat to 1.4 mm in compression respectively. The resistance of the graphene-CNT-PDMS film is 850 Ω which is similar to the obtained CVD grown monolayer graphene film[38]. In addition to this, further resistance of the hybrid film can be improved when the quality of graphene film is enhanced. From Figure 4.25 a we can observe that the resistance of the film is linearly increasing from 0.85 kΩ to 2.1 kΩ with decreasing bending radius from flat to 13.5 mm (Figure 4.25a).

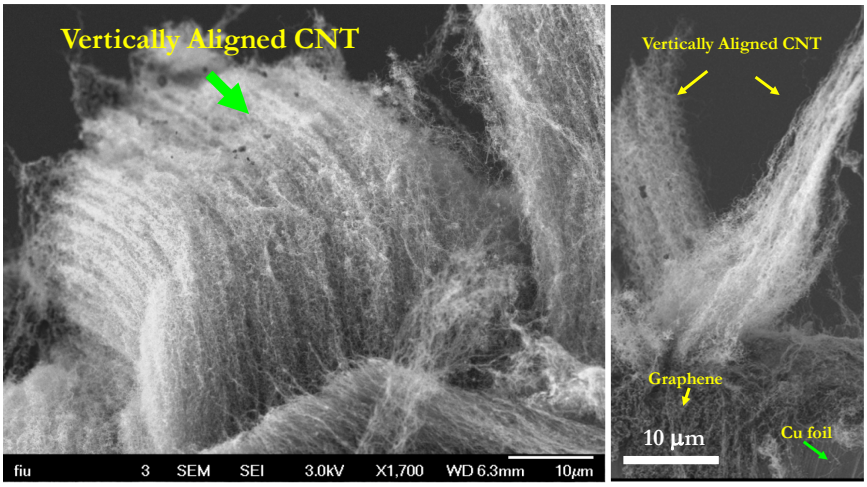


Figure 4.24: graphene-CNT structure after transfer over the adhesive Cu substrates illustrating the graphene at the bottom and CNT on the top.

The change in resistance is due to the stretching of the interface between CNT and graphene film as well as relative movement of the catalyst particles. Furthermore, decreasing bending radius from 1.5 mm to 3.3 mm leads to the decrease in slope of the

resistance curve on that region. Whereas, the resistance under compression (Figure 4.25b) illustrates a continue increase of resistance with decrease of bending radius. Finally, the resistance is completely recovered upon release of stress in both the cases of tension and compression. Several reports show that the electrodes prepared from aligned CNT pillars and PDMS, tensile loading destroyed the integrity of the nanotube pillars resulting in increased electrical resistance[21-23, 39-41]. In graphene-CNT hybrid film electrodes, the continuous graphene film connecting the MWCNT preserved the structural integrity of the PDMS electrode, underlining the possibility of utilizing these structures directly as mechanical (strain/ pressure/touch) sensors.

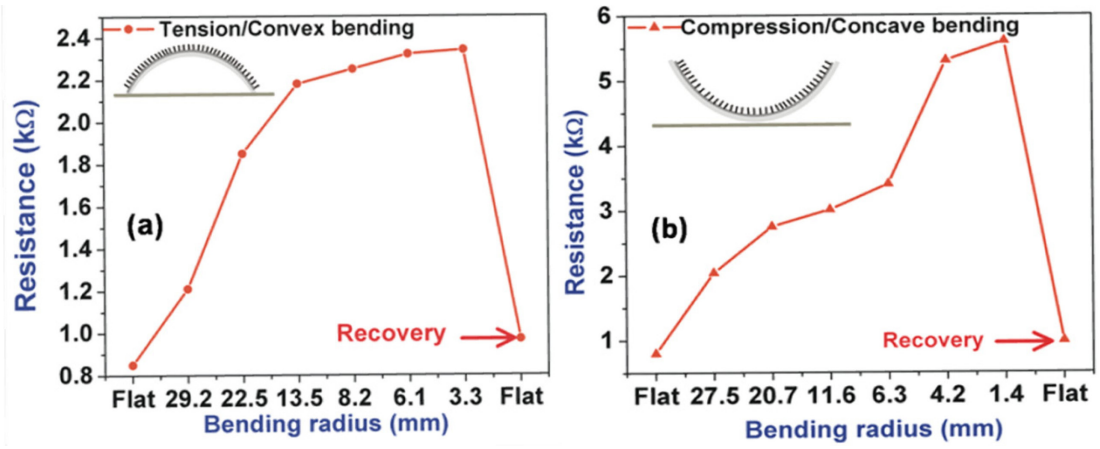


Figure 4.25: Illustrates the variations of electrical resistance as a function of bending radius (a) tension (b) compression, inset displays the test structure of graphene-CNT-PDMS composite electrode.

**References**


1. Malard, L. M.; Pimenta, M. A.; Dresselhaus, G.; Dresselhaus, M. S., Raman spectroscopy in graphene. *Physics Reports* 2009, 473, 51-87.

2. Dresselhaus, M. S.; Jorio, A.; Saito, R., Characterizing Graphene, Graphite, and Carbon Nanotubes by Raman Spectroscopy. *Annual Review of Condensed Matter Physics* 2010, 1, 89-108.

3. Li, X. S.; Cai, W. W.; Colombo, L.; Ruoff, R. S., Evolution of Graphene Growth on Ni and Cu by Carbon Isotope Labeling. *Nano Letters* 2009, 9, 4268-4272.

4. Lahiri, J.; Miller, T.; Adamska, L.; Oleynik, II; Batzill, M., Graphene Growth on Ni(111) by Transformation of a Surface Carbide. *Nano Letters* 2011, 11, 518-522.

5. Choi, W.; Lee, J.-w., *Graphene : synthesis and applications*. CRC Press ; Taylor & Francis: Boca Raton London, 2012; p xv, 370 p.

6. Hu, T.; Zhang, Q. M.; Wells, J. C.; Gong, X. G.; Zhang, Z. Y., A comparative first-principles study of the adsorption of a carbon atom on copper and nickel surfaces. *Physics Letters A* 2010, 374, 4563-4567.

7. Lyon, L. A.; Keating, C. D.; Fox, A. P.; Baker, B. E.; He, L.; Nicewarner, S. R.; Mulvaney, S. P.; Natan, M. J., Raman spectroscopy. *Analytical Chemistry* 1998, 70, 341R-361R.

8. Ni, Z. H.; Wang, Y. Y.; Yu, T.; Shen, Z. X., Raman Spectroscopy and Imaging of Graphene. *Nano Research* 2008, 1, 273-291.

9. Li, X. S.; Cai, W. W.; An, J. H.; Kim, S.; Nah, J.; Yang, D. X.; Piner, R.; Velamakanni, A.; Jung, I.; Tutuc, E.; Banerjee, S. K.; Colombo, L.; Ruoff, R. S., Large-Area Synthesis of High-Quality and Uniform Graphene Films on Copper Foils. *Science* 2009, 324, 1312-1314.

10. Rafiee, J.; Mi, X.; Gullapalli, H.; Thomas, A. V.; Yavari, F.; Shi, Y.; Ajayan, P. M.; Koratkar, N. A., Wetting transparency of graphene. *Nat Mater* 2012, 11, 217-222.

11. Das, A.; Chakraborty, B.; Sood, A. K., Raman spectroscopy of graphene on different substrates and influence of defects. *Bulletin of Materials Science* 2008, 31, 579-584.

12. Wang, Y. Y.; Ni, Z. H.; Yu, T.; Shen, Z. X.; Wang, H. M.; Wu, Y. H.; Chen, W.; Wee, A. T. S., Raman studies of monolayer graphene: The substrate effect. *Journal of Physical Chemistry C* 2008, 112, 10637-10640.

13. Kondo, D.; Sato, S.; Awano, Y., Self-organization of Novel Carbon Composite Structure: Graphene Multi-Layers Combined Perpendicularly with Aligned Carbon Nanotubes.

14. Lee, D. H.; Kim, J. E.; Han, T. H.; Hwang, J. W.; Jeon, S.; Choi, S. Y.; Hong, S. H.; Lee, W. J.; Ruoff, R. S.; Kim, S. O., Versatile Carbon Hybrid Films Composed of Vertical Carbon Nanotubes Grown on Mechanically Compliant Graphene Films. *Advanced Materials* 2010, 22, 1247-+.

15. Chen, S.; Chen, P.; Wang, Y., Carbon nanotubes grown in situ on graphene nanosheets as superior anodes for Li-ion batteries. *Nanoscale* 2011, 3, 4323-4329.

16. Lee, D. H.; Lee, J. A.; Lee, W. J.; Kim, S. O., Flexible Field Emission of Nitrogen-Doped Carbon Nanotubes/Reduced Graphene Hybrid Films. *Small* 2011, 7, 95-100.

17. Tung, V. C.; Chen, L.-M.; Allen, M. J.; Wassei, J. K.; Nelson, K.; Kaner, R. B.; Yang, Y., Low-Temperature Solution Processing of Graphene–Carbon Nanotube Hybrid Materials for High-Performance Transparent Conductors. *Nano Letters* 2009, 9, 1949-1955.

18. Kondo, D.; Sato, S.; Awano, Y., Self-organization of novel carbon composite structure: Graphene multi-layers combined perpendicularly with aligned carbon nanotubes. *Applied Physics Express* 2008, 1.

19. Li, Y. F.; Li, B. R.; Zhang, H. L., The computational design of junctions between carbon nanotubes and graphene nanoribbons. *Nanotechnology* 2009, 20.

20. Luo, C.; Zuo, X.; Wang, L.; Wang, E.; Song, S.; Wang, J.; Wang, J.; Fan, C.; Cao, Y., Flexible Carbon Nanotube–Polymer Composite Films with High Conductivity and Superhydrophobicity Made by Solution Process. *Nano Letters* 2008, 8, 4454-4458.

21. Jung, Y. J.; Kar, S.; Talapatra, S.; Soldano, C.; Viswanathan, G.; Li, X.; Yao, Z.; Ou, F. S.; Avadhanula, A.; Vajtai, R.; Curran, S.; Nalamasu, O.; Ajayan, P. M., Aligned Carbon Nanotube–Polymer Hybrid Architectures for Diverse Flexible Electronic Applications. *Nano Letters* 2006, 6, 413-418.

22. Connolly, T.; Smith, R. C.; Hernandez, Y.; Gun'ko, Y.; Coleman, J. N.; Carey, J. D., Carbon-Nanotube-Polymer Nanocomposites for Field-Emission Cathodes. *Small* 2009, 5, 826-831.

23. Tsai, T. Y.; Lee, C. Y.; Tai, N. H.; Tuan, W. H., Transfer of patterned vertically aligned carbon nanotubes onto plastic substrates for flexible electronics and field emission devices. *Applied Physics Letters* 2009, 95.

24. Yoshida, H.; Takeda, S.; Uchiyama, T.; Kohno, H.; Homma, Y., Atomic-scale in-situ observation of carbon nanotube growth from solid state iron carbide nanoparticles. *Nano Letters* 2008, 8, 2082-2086.

25. Deck, C. P.; McKee, G. S. B.; Vecchio, K. S., Synthesis optimization and characterization of multiwalled carbon nanotubes. *Journal of Electronic Materials* 2006, 35, 211-223.

26. Kim, K. S.; Zhao, Y.; Jang, H.; Lee, S. Y.; Kim, J. M.; Ahn, J. H.; Kim, P.; Choi, J. Y.; Hong, B. H., Large-scale pattern growth of graphene films for stretchable transparent electrodes. *Nature* 2009, 457, 706-710.

27. Chernozatonskii, L. A.; Sheka, E. F.; Artyukh, A. A., Graphene-nanotube structures: Constitution and formation energy. *Jetp Letters* 2009, 89, 352-356.

28. Lee, C. H.; Chen, S. C.; Yang, C. K.; Su, W. S.; Lin, M. F., Low-energy electronic structures of nanotube–nanoribbon hybrid systems. *Computer Physics Communications* 2011, 182, 68-70.

29. Calizo, I.; Bao, W. Z.; Miao, F.; Lau, C. N.; Balandin, A. A., The effect of substrates on the Raman spectrum of graphene: Graphene-on-sapphire and graphene-on-glass. *Applied Physics Letters* 2007, 91.

30. Gupta, A.; Chen, G.; Joshi, P.; Tadigadapa, S.; Eklund, P. C., Raman scattering from high-frequency phonons in supported n-graphene layer films. *Nano Letters* 2006, 6, 2667-2673.

31. Yu, Q. K.; Lian, J.; Siriponglert, S.; Li, H.; Chen, Y. P.; Pei, S. S., Graphene segregated on Ni surfaces and transferred to insulators. *Applied Physics Letters* 2008, 93.

32. Schaper, A. K.; Hou, H.; Greiner, A.; Phillipp, F., The role of iron carbide in multiwalled carbon nanotube growth. *Journal of Catalysis* 2004, 222, 250-254.

33. Nilsson, J.; Neto, A. H. C.; Guinea, F.; Peres, N. M. R., Electronic properties of bilayer and multilayer graphene. *Physical Review B* 2008, 78.

34. Guinea, F., Charge distribution and screening in layered graphene systems. *Physical Review B* 2007, 75.

35. Nagashio, K.; Nishimura, T.; Kita, K.; Toriumi, A., Mobility Variations in Mono- and Multi-Layer Graphene Films. *Applied Physics Express* 2009, 2.

36. Wang, H. M.; Wu, Y. H.; Ni, Z. H.; Shen, Z. X., Electronic transport and layer engineering in multilayer graphene structures. *Applied Physics Letters* 2008, 92.

37. Stadermann, M.; Papadakis, S. J.; Falvo, M. R.; Novak, J.; Snow, E.; Fu, Q.; Liu, J.; Fridman, Y.; Boland, J. J.; Superfine, R.; Washburn, S., Nanoscale study of conduction through carbon nanotube networks. *Physical Review B* 2004, 69.

38. Verma, V. P.; Das, S.; Lahiri, I.; Choi, W., Large-area graphene on polymer film for flexible and transparent anode in field emission device. *Applied Physics Letters* 2010, 96.

39. Hong, N. T.; Koh, K. H.; Lee, S.; Ngo, T. T. T.; Phan, N. M., Flexible carbon nanotube-array cathodes: Fabrication and bending effect on field-electron emission. *Journal of Vacuum Science & Technology B* 2010, 28, C2C5-C2C8.

40. Choi, J. H.; Park, J. H.; Moon, J. S.; Nam, J. W.; Yoo, J. B.; Park, C. Y.; Lee, C. G.; Choe, D. H., Fabrication of carbon nanotube emitter on the flexible substrate. *Diamond and Related Materials* 2006, 15, 44-48.

41. Chang, C. S.; Chattopadhyay, S.; Chen, L. C.; Chen, K. H.; Chen, C. W.; Chen, Y. F.; Collazo, R.; Sitar, Z., Band-gap dependence of field emission from one-dimensional nanostructures grown on n-type and p-type silicon substrates. *Physical Review B* 2003, 68.

CHAPTER 5

# SURFACE FUNCTIONALIZATION OF GRAPHENE FOR APPLICATION IN ELECTROCATALYTIC ELECTRODES FOR DYE SENSITIZED SOLAR CELLS

## 5.1. Graphene functionalization

Since its invention, graphene, two-dimensional (2D) graphitic allotropes of carbon creates an immense research interest due to its exotic electronics, optoelectronics, thermal and mechanical properties[1-4]. The most fascinating properties of graphene include room temperature quantum Hall effect[5, 6], ballistic charge transport[2, 7], high charge carrier density[1, 7], tuneable band gap[8], high thermal conductivity[9] and ultra-high transmittance [10, 11]. Numerous graphene based devices have already been demonstrated for the potential applications in transistors[7, 12], Li-ion battery[13, 14], supercapacitor[15-18] and solar cells[10, 11, 19-23]. Particularly, application of graphene in solar cells with high efficiency, large open circuit voltage and high current density is of primary interest[21-23].

It has already been reported that graphene exhibited remarkable transmittance through the entire solar spectrum from ultra-violate (UV) to infra-red (IR) region[10, 11]. Therefore, graphene based electrodes are quite advantageous for those types of solar cells/tandem solar cells which need to absorb entire range of photon energies (from UV-visible to IR) in order to generate excitons efficiently. On the other hand, large scale graphene can be grown and transferred on any flexible polymer substrates using various facile and scalable methods which are quite feasible towards industrialization[24, 25]. Therefore, the versatility of graphene and its fabrication process has been projected to offer immense opportunity for next generation efficient, lightweight, flexible device

applications. In particular, dye sensitized solar cells (DSSCs) are one of the major candidates among all[23, 26, 27]. In DSSCs, dye coated $TiO_2$ photo-anode and Pt coated FTO cathode is sandwiched between a liquid electrolyte in order to form a photo-electrochemical solar cell. The DSSC counter electrode (CE) is one of the indispensible components which directing the regeneration of oxidized dye back to their ground state. Concurrently, CE injects electrons into the electrolyte in order to catalyze the iodine reduction ($I_3^- + 2e^- \leftrightarrow 3I^-$) after the charge injection from the photo-oxidized dye[28, 29]. The catalytic effect of CE is expected to play a decisive role for the operation of DSSCs through controlling the current generation of the photo-anode. In this context, utilizing the high surface area of 2D graphene sheet (2630 $m^2/g$) in addition to its intrinsic high charge concentration and carrier mobility, provide greater versatility as a counter electrode in DSSCs. Recent reports demonstrate a very low resistance of graphene film with high transparency which can be further utilized for the replacement of both transparent conducting oxides (TCOs) and CEs. In particular, improvement of catalytic activity of graphene while maintaining its unique properties is of great interest in application of graphene as replacement of expensive and inadequate Pt counter electrode[30].

Doping or chemical functionalization is one of the prevailing methods among the various approaches which offer enticing possibilities to tune the charge carrier density[31-34], band gap[8], work function[35, 36] and catalytic activity[26, 37] of graphene. For example, Fermi energy ($E_F$) of graphitic allotropes can be tuned using chemical (like, halogens[38-40], acid[35, 41-43] and alkali metals[44]) or electrochemical doping[45]. However, the phlegmatic nature of graphene basal planes often restricts the charge transfer at the

electrode/electrolyte interface, thus limits its functionality in a wide range of electrochemical devices. Therefore, enriching electro-catalytically active sites of graphene is currently in demand in achieving efficient catalytic CEs for stipulating the charge transfer at the electrode/electrolyte interface[46-49]. Recently a few reports demonstrated the improvement of graphene catalytic activity by surface modification protocols using water-soluble polymers (polyelectrolyte) and poly(ethylene-oxide)-poly (propylene-oxide)- poly (ethylene-oxide) tri-block copolymer[26, 27]. However, the electro-catalytic activities of large scale chemically vapour deposited (CVD) graphene has not been well scrutinized and possesses a serious challenge.

Apart from these functionalities, enhanced chemical reactivity of graphene is indispensable as a CE for DSSCs, which can be proceeded by surface modification protocols, either via chemical modification or physical treatment of graphene [26, 42, 50]. It has been well reported that graphite intercalation compounds (GICs) significantly improve the conductivity and in-plane charge transfer, as compared to graphite[51]. However inert nature of graphene basal plane often restricts graphene-liquid interface charge transfer although it shows high in-plane charge mobility, so tri-iodide reduction occurs only through their edge planes. Thus, surface modification is required for improving their in-plane charge transfer characteristic and application as efficient catalytic counter electrode for tri-iodide reduction in DSSCs. Furthermore, functional nano-particle decorated graphene film instantly increase the electrode-electrolyte contact area which is known as triple junction catalytic effect; hence improves the electron transfer kinetics at the interface[52]. Additionally, decoration with catalytically active functional nanoparticles (NPs) are highly beneficial for enhancing electro-catalytic

reactions for practical applications such as hydrogen generation [53], Li-ion batteries [54], pseudo-supercapacitors [55] etc.

This chapter describes the different functionalization protocols applied to graphene in order to improve its electrocatalytic behaviour. First, Fluorine functionalized graphene fabrication process is descried and explains its electrocatalytic activity towards tri-iodide reduction. A mechanism is also proposed to explain the possible reason for enhancing electrocatalytic activity of tri-iodide reduction. Second, the chapter also included how acid doping enhances the electrocatalytic activity of graphene. As, Niric acid ($HNO_3$) doped in graphene lattice as p-type, therefore enhances its conductivity and catalytic activity by Fermi level pinning. Hence, this section included all the structural and electrochemical characterizations of $HNO_3$ doped graphene and its final device application as counter electrode for DSSC. Furthermore, graphene-CoS hybrid structure was synthesized using successive ionic layer absorption and reactions (SILAR) method and applied for DSSC counter electrode. In this case, the graphene-CoS triple junction catalytic effects enhance the further charge transfer kinetics, hence improve the catalytic activities of graphene. Finally, the last section included the graphene-CNT hybrid structure applied as flexible field emission (FE) devices and FE properties were measured with different bending radius.

### 5.1.1. Fluorine functionalization using low pressure plasma treatment

The plasma ion treatment is a promising tool offering several advantages such as precise control in surface treatment and thus higher reactivity with a functionalized surface with the carbon atoms. In particular, applying highly electronegative fluorine ion

stems from $CF_4$ reactive ion plasma seems to functionalize the carbon atoms of graphene with fluorine ion. This may improve graphene's characteristic properties i.e. density of states in Fermi energy level, ionization potential, etc. like halogen ion functionalized graphitic materials[56]. Apart from that, our focus is to create more catalytically active edges in graphene through plasma treatment and functionalize them with fluoride functional group for enhancing interfacial electron transfer sites at the graphene-electrolyte interface [38, 47, 57, 58]. The plasma treated edges are expected to tailor their surface properties as well as improve tri-iodide reduction capability, which paves a path way for improving the performance of DSSCs.

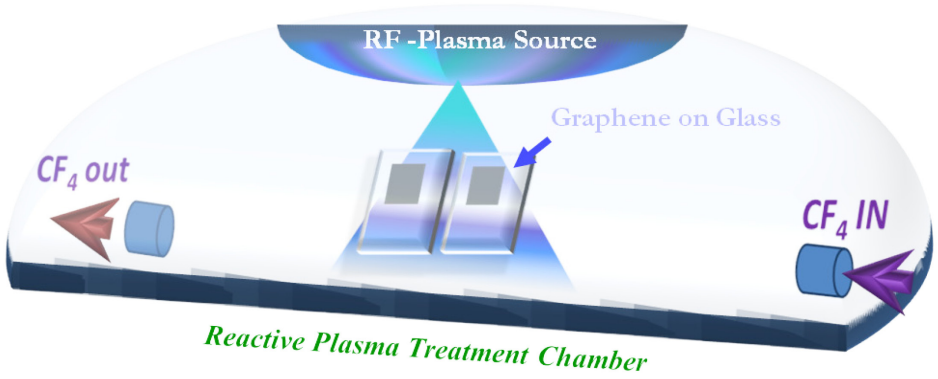


Figure 5.1: Schematic showing the graphene functionalization procedure in a plasma treatment chamber.

After the CVD growth process, the graphene was transferred on a FTO substrates as described in chapter 3 section 3.2.2. Then graphene /FTO was treated with $CF_4$ reactive ion plasma (RIP) for 15 seconds & 45 seconds which we addressed as 15 second surface treated graphene (ST15-G) and 45 second surface treated graphene (ST45-G)

respectively. The graphene/FTO substrates were placed inside a reactive ion etching chamber and pull down the vacuum up to 50 mT. Then $CF_4$ gas was passed through the chamber while maintaining the vacuum pressure 100 mT. The flow of the $CF_4$ gas was kept constant at 5 sccm as shown in the schematic Figure 5.1. Graphene film on FTO substrates were also characterized by Raman spectroscopy before and after the plasma treatments as described in upcoming section.

### 5.1.2. Micro-Raman spectroscopy

Raman spectra was measured in a system with a spectral resolution of 4 $cm^{-1}$ inbuilt argon ion ($Ar^+$) laser (Spectra Physics, model 177G02 wavelength of 514.5 nm). As could be observed from Figure 5.2, pristine graphene (P-G) on FTO exhibit symmetrical strong 2D band, G band and D band peaks of corresponding positions of D, G and 2D bands which are ~1345 $cm^{-1}$, ~1582 $cm^{-1}$ and ~2701 $cm^{-1}$ respectively. Like pristine graphene, strong symmetric 2D band and G band peaks appears for ST15-G and ST45-G, which confirm the presence of graphene multilayer even after plasma treatment with $CF_4$ reactive ions.

As could be seen from Figure 5.3a, the intensity of D band peaks was found to increase with increasing plasma treatment time for P-G, ST15-G and ST45-G respectively. The increase in D band peak intensity indicates the introduction of $F^-$ ions (surface defects) inside the graphene and transformation of $sp^2$ to $sp^3$ bonds between the carbon atoms [59, 60]. Further, the peak intensity ratio of D and G bands, i.e. $I_D/I_G$, increases with an increase in plasma treatment time as shown in Figure 5.3d. On the other hand, there is a distinct peak shift of the 2D band with increasing $CF_4$ plasma treatment time as

shown in the Figure 5.3c. The 2D peak position of P-G, ST15-G and ST45-G is found to be ~2701 $cm^{-1}$, ~2709 $cm^{-1}$ and ~2711 $cm^{-1}$, respectively corroborating the formation of intercalated compounds of graphene. In this context, there are no peak shift was found for the G band peaks which represents the existence of graphene structure remain same even after the plasma treatment.

Figure 5.2: Comparative Raman spectra of different fluorine functionalized graphene.

Furthermore, the blue shift in the 2D band with increasing plasma treatment time justifies the incorporation of $F^-$ ions with an increase in number of edge plane like active carbon sites in graphene as reported earlier [59]. Furthermore, the peak intensity ratio of G and 2D bands, i.e. $I_G/I_{2D}$ is found to be ~0.5 pristine graphene. Figure 5.3d designates the significant increase in $I_G/I_{2D}$ ratio with an increase in plasma treatment time initially, but

no further increase is found after that. However, the substantial evidence of fluorine doping in graphene layer is discussed in the upcoming XPS section 6.1.4.

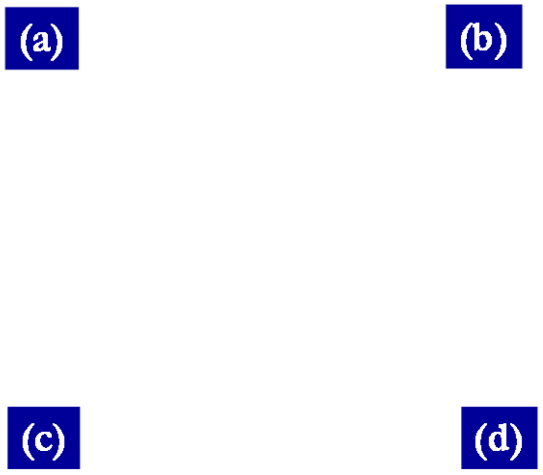


Figure 5.3: Comparative Raman spectra of (a) D band, (b) G band and (c) 2D band of different fluorine functionalized graphene. (d) Illustrate the changes in Raman peak intensity ratios (□, $I_D/I_G$ and Δ, $I_G/I_{2D}$) with increasing plasma treatment time.

### 5.1.3. Atomic force microscopy

The graphene samples (ST15-G and ST45-G) for Atomic Force microscopy (AFM) were prepared under the same condition using $CF_4$ reactive plasma ion on a cleaved mica surface (Ted Pella Inc.). The surface topography of all the samples was investigated using atomic force microscopy (AFM) (NanoScope IIIa, Veeco Instruments

Inc., USA) under tapping mode condition. Figure 5.4 a, b and c illustrates the AFM images of the surface topography of P-G, ST15-G and ST45-G respectively. The subsequent increase in surface roughness is clearly seen with increasing chemical functionalization of graphene with plasma treatment time. The RMS values ($R_q$) of surface roughness are found to be 2.6 nm, 2.94 nm and 3.6 nm for P-G, ST15-G and ST45-G sheet respectively. It infers that the surface of P-G, ST15-G and ST45-G films are modified with fluorine functionalization which causes the variation in vertical deviations The change in vertical deviations is increased significantly for ST15-G and ST45-G compare to the P-G as illustrated in Figure 5.4 d, e and f [46, 48].

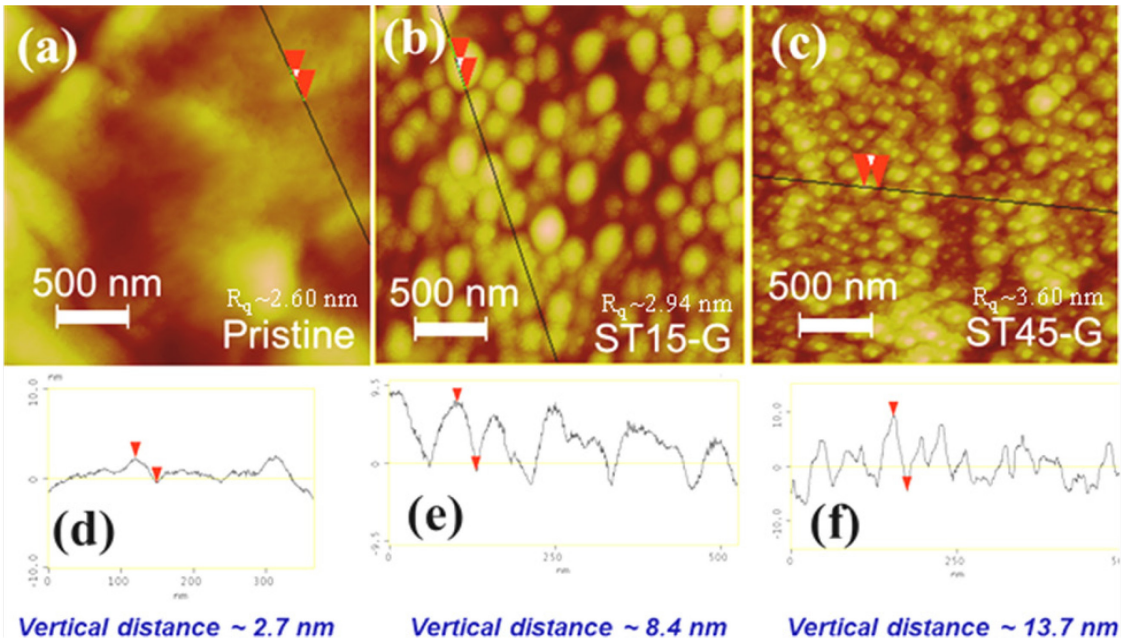


Figure 5.4: Show of Atomic Force Micrographs of (a) Pristine Graphene (P-G); (b) Low surface treated graphene(ST15-G); (c) High surface treated graphene ST45-G; (d), (e), and (f) represents the corresponding surface roughness profiles of the Figure 5.4 (a), (b) and (c) respectively.

The increase in surface roughness attributes to the fluorine functionalization with basal plane carbon atoms of graphene film thus increases in edge planes leads to the enhancement of the catalytic activity of graphene. Therefore, edge planes of graphene contribute to the enhancement of in-plane charge transfers at the electrode-electrolyte interface leads to the increase in catalytic activity of graphene towards charge transfer at the electrode-electrolyte interface.

### 5.1.4. X-ray photoelectron spectroscopy

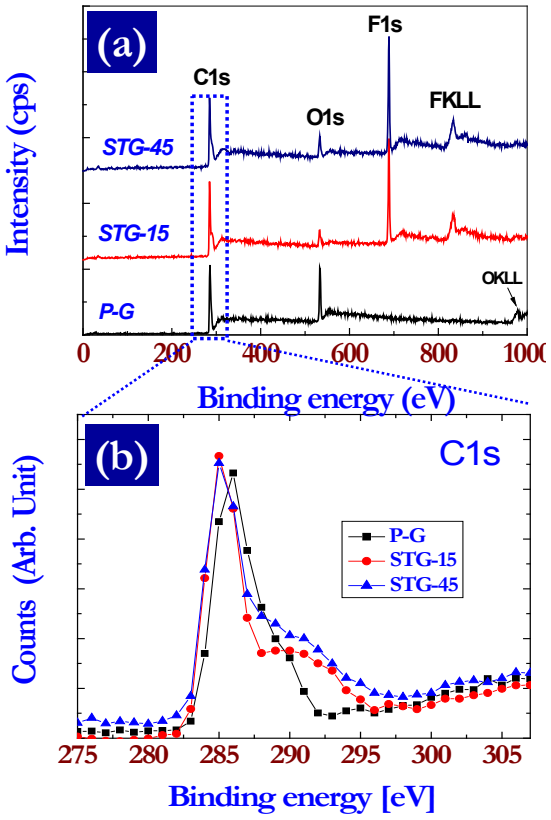


Figure 5.5: (a) X-ray Photoelectron Spectra of three different counter electrodes of PG, ST15-G and ST45-G (b) showing the carbon (C1s) peaks from graphene.

It is well reported that edge planes of graphene show more catalytic effects than the basal planes [18, 46, 48, 61]. It is assumed that $F^-$ ions may react in graphene electronic structure during $CF_4$ reactive ion treatment resulting in a semi ionic or covalent bond, thus bringing structural modification in basal planes. This assumption was further verified with XPS spectra, in which (as illustrated in Figure 5.6) a peak at ~688.4eV attributed to the characteristic of a C-F covalent bond in ST15-G and ST45-G electrodes. $F^-$ ions are more electronegative than that of carbon atom leading to the formation of C-F covalent bonds. Therefore the basal plane turns electrochemically active and offers in-plane charge transfer than pristine graphene (P-G) layer [26, 39].

Figure 5.6: Illustrates the XPS spectra of F1s orbital peak shows that intensity increases with increasing $CF_4$ plasma treatment time compare to the pristine graphene.

These structural changes in graphene under $CF_4$ plasma treatment were previously discussed in Raman section 5.1.2 and confirmed with the $I_G/I_{2D}$ band ratio from Raman

spectroscopy (as shown in Figure 5.2 & 5.3). As is evident, reactive ion plasma fluorination in graphene sheets (ST45-G) improve their electrochemical reactivity with redox species ($I_3^-/I^-$), and raise the possibility in tri-iodide reduction. This thus enhances the dye regeneration, which leads to the high short-circuit current density in this system [50, 62].

### 5.1.5. Ultra-violet photoemission spectroscopy

For further understanding this behavior, the work function of $CF_4$ reactive ion plasma treated graphene multi-layers was characterized by the Kelvin probe method and the values are listed in Table 5.1. As shown in Figure 5.7 a & b of ultraviolet photoemission spectra of graphene electrodes, the intensity of the peak increases for ST15-G and then decreases for ST45-G. The work function of the pristine graphene initially increases about 0.57 eV because of the plasma treatment for 15 s and was found to decrease about 0.02 eV when further increasing plasma treatment time to 45 s. It clearly reveals that due to long duration of plasma treatment (45s), an excess amount of negative charge formation takes place in graphene leading to lower work function. This is attributed to the widening of the graphene band gap due to the subsequent chemical functionalization of $F^-$ ions with carbon atoms. We believe that the lowering in the valence band is due to the interaction of the p orbital of $F^-$ ion with the $\pi$ orbital of carbon atom resulting in the formation of $sp^3$ bonds [42, 63].

Work function changes by fluorine doping were determined in air by a Kelvin probe method (model KP-6500, McAllister). We obtained contact potential difference

(CPD, $\Delta V$) relative to a stainless steel reference electrode from this method, which is related to a work function difference $\Delta\Phi$, ($\Delta V$= -e$\Delta\Phi$).

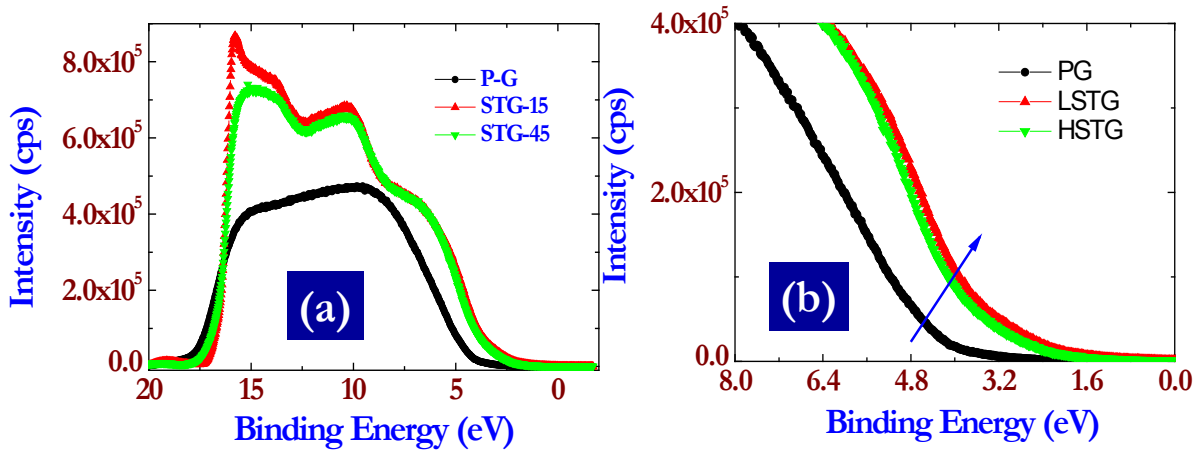


Figure 5.7: Ultraviolet photoemission spectra of different plasma treated and pristine graphene and (b) the magnified view of the UP spectra showing a clear shift of graphene work function.

Table 5.1: The contact potential difference and change in work function of different graphene electrodes measured using Kelvin Probe Microscopy.

| Electrodes | Contact potential difference (V) | Change in work function (eV) |
|---|---|---|
| P-G | -0.16 | 0 |
| ST15-G | -0.73 | 0.57 |
| ST45-G | -0.71 | 0.55 |

### 5.1.6. Electrochemical characterizations

Electrochemical characterization was carried out under symmetric cell configuration using pristine and functionalized graphene counter electrodes and Pt coated FTO glass referred as a standard cell as delineated in chapter 3 section 3.4.

As is observed from Figure 5.8, the limiting current ($I_{lim}$) of symmetric dummy cells and $I_{lim}$ for P-G is apparently lower when compared to the ST15-G and ST45-G, which is in agreement with the J-V characteristics of the DSSCs illustrated in Figure 5.11. The current density which is measured under a slow scan rate (50 mV/s) is a representative of the diffusion of the ionic carriers in the electrolytes between two electrodes of the symmetric cell. In fact, the diffusion coefficient is proportional to the $I_{lim}$ as per the equation 5.1 [30].

$$D_{I3^-} = \{[l]/2nFC_{I3^-}\}\, I_{lim} \qquad (5.1)$$

Here, $l$ is the inter-electrode distance; n = 2, the number of electrons contributing to the charge transfer; F is Faraday's Constant; $C_{I3^-}$ is tri-iodide ion concentration per unit volume ($5x10^{-6}$ mol/cm$^3$).

The estimated diffusion coefficient values of I3- redox species at different counter electrodes were estimated and listed in Table 5.2. It is inferred that diffusivity of P-G electrodes are apparently improved by F- ion treatment and is comparable to Pt electrode. Therefore, the diffusion coefficient of the ionic carriers at counter electrode-electrolyte interface is increased with increasing catalytic activities of graphene. Tafel plot is applied to investigate the insight of interfacial charge-transfer property at the interface of graphene-electrolytes under symmetric cell configuration (electrode/electrolyte/electrode) using different counter electrodes.

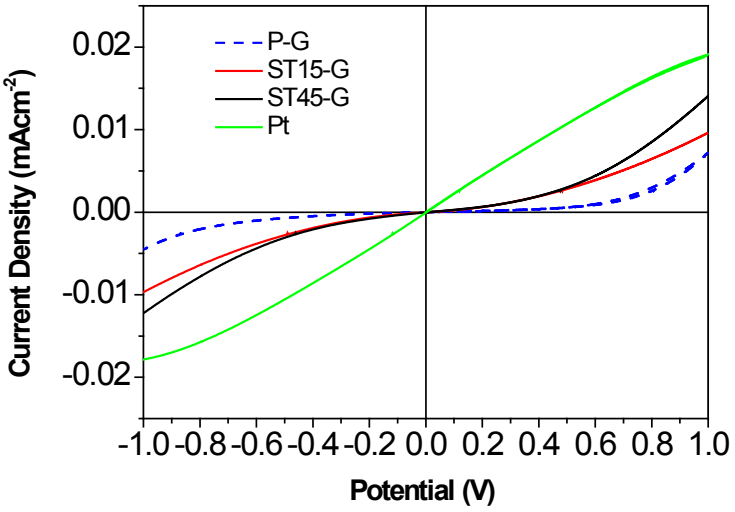


Figure 5.8: Steady state cyclic voltammogram of symmetric cell based on plasma treated graphene counter electrodes at 20$^{o}$C.

Table 5.2: Illustrates the electrochemical parameters calculated from Tafel plots with different counter electrodes.

| Electrode | $D_n$ ($cm^{-2}s^{-1}$) | α | β | Cathodic Tafel | Anodic Tafel | Exchange Current Density (A) | Over potential (mV) |
|---|---|---|---|---|---|---|---|
| **PG** | $3.59 \times 10^{-6}$ | 0.71 | 0.28 | 12.3 | 4.8 | $0.31 \times 10^{-6}$ | 528 |
| **STG-15** | $7.92 \times 10^{-6}$ | 0.76 | 0.23 | 13.1 | 3.9 | $0.94 \times 10^{-6}$ | 557 |
| **STG-45** | $1.04 \times 10^{-5}$ | 0.73 | 0.26 | 12.6 | 4.5 | $0.13 \times 10^{-3}$ | 460 |
| **Pt** | $2.0 \times 10^{-5}$ | 0.68 | 0.31 | 11.6 | 5.4 | $1.11 \times 10^{-3}$ | 332 |

The experimental polarization curves were fitted with the Butler-Volmer equation (equation 5.2), describing the dependence of electrical current on electrode potential by assuming that both cathodic and anodic reactions occur on the same electrode.

$$I = nFAK_s \{C_o^{surf} \exp((\alpha nF)\,\eta/RT) - C_R^{surf} \exp((\beta nF)\,\eta/RT)\} \quad (5.2)$$

For estimating the tri-iodide reduction rate at the counter electrode, over potential is calculated by,

$$\eta = (RT/\alpha F)\ ln\ (I_0) - (RT/\alpha F)\ ln\ (I_{lim}) \qquad (5.3)$$

Here $I_{lim}$ is the limiting current, $I_0$ exchange current, $A$ is the electrode active surface area, $K_s$ is the standard rate constant, η is the over potential (estimated from equation 5.3), $C_o^{surf}$ is the reactant concentration near the electrode, $C_R^{surf}$ is the product concentration near the electrode, α is the anodic transfer coefficient, and β is the cathodic transfer coefficient [64].


Figure 5.9: (a) J-V plot of different graphene electrodes (b) Nyquist plot of symmetric half cell with different counter electrodes (■, Pristine Graphene) (●, ST15-G) (▲, ST45-G) and (▼, Pt ).

Figure 5.9a shows the polarization curves of the symmetric electrodes cells configured with different counter electrodes. The exchange current density was calculated from the intersection of the linear anodic and cathodic curves for different

electrode (PG, STG-15, STG-45 and Pt) and listed in Table 5.2. By substituting equation 5.3 in equation 5.2 with necessary parameters (as shown in Table 5.2), rate constant (Ks) of redox species conversion at different counter electrode can be derived.

From Table 5.2, the exchange current density for P-G is apparently lower when compared to the ST15-G and ST45-G. This implies that pristine graphene has poor interfacial charge transfer activity with $I_3^-$ redox species, since there are fewer numbers of active edge planes in the crystal lattice. Furthermore, $F^-$ ion treatment drastically improves the construction of edge plane sites at the pristine graphene electrode, which promote their interfacial transfer activity with $I_3^-$ redox species [46]. This reflects on exchange current density, for instance, a 45s plasma treated graphene electrode (ST45-G) sample shows a higher exchange current density value which indicates that $I_3^-$ reduction kinetics are faster at this electrode/electrolyte interface than other graphene electrode/electrolyte interfaces.

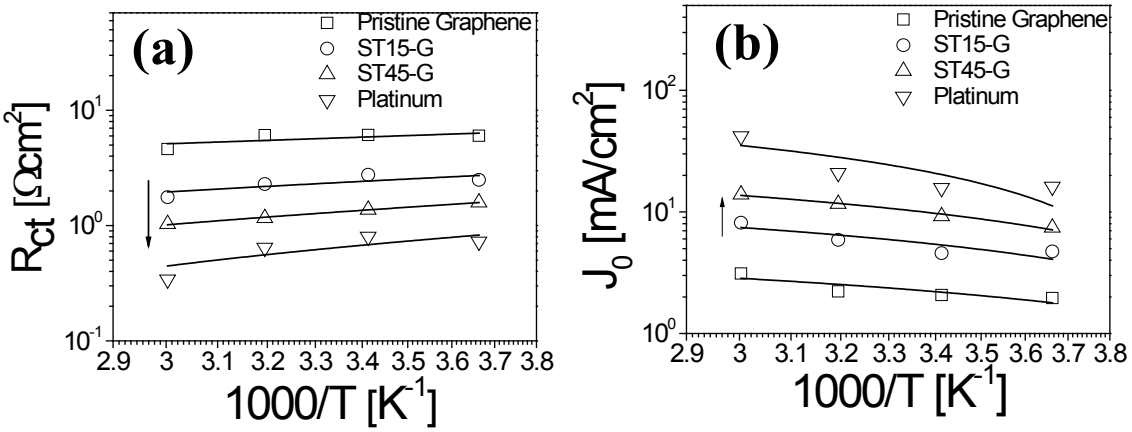


Figure 5.10: (a) Charge transfer resistance vs. temperature plot and (b) exchange current density vs. temperature plot of different counter electrodes.

In view of understanding the electron transport phenomena at graphene/electrolyte interfaces, electrochemical impedance spectroscopy (EIS) was utilized for testing a thin symmetry cell (graphene/electrolyte/graphene) and resultant Nyquist spectra of different samples is presented in Figure 5.9b. As shown in the inset of Figure 5.9b, the equivalent circuit of the symmetric cell is denoted by Randles circuit which consists of $R_{ct}$ (charge transfer resistance) in series of $Z_w$ (Warburg Impedance) where both elements are in parallel with $C_{dl}$ (double layer capacitance). A series resistance $R_s$ is included in the circuit as it arises from the total contribution from the load and the FTO resistance. The charge transfer resistance ($R_{ct}$) and Nernst diffusion impedance ($Z_w$) at the counter electrodes was estimated from the diameters of the leftmost semicircles using Echem Analyst software with the Randles circuit. Figure 5.10a illustrates the decrease in charge transfer resistance with increases in plasma treatment time of graphene and temperature. The charge transfer resistance $R_{ct}$ of pristine graphene was apparently reduced under $CF_4$ plasma treatment and shows comparable resistance with conventional Pt electrode (Table 5.3).

Table 5.3: Illustrates Photovoltaic parameters of different counter electrodes and the simulated EIS parameters. [a]

| Counter Electrodes | $V_{OC}$ (V) | JSC ($mAcm^{-2}$) | FF (%) | η (%) | $R_{ct}$ (Ω) | $Z_w$ (Ω) |
|---|---|---|---|---|---|---|
| **PG** | 0.69 | 7.8 | 26.0 | 1.43 | 38.0 | 76.1 |
| **STG-15** | 0.74 | 8.3 | 38.8 | 2.41 | 17.2 | 34.4 |
| **STG-45** | 0.66 | 10.9 | 35.9 | 2.56 | 8.5 | 17.1 |
| **Pt** | 0.68 | 15.7 | 61.1 | 6.65 | 4.6 | 10.0 |

*[a] $V_{OC}$: Open circuit voltage, $J_{SC}$: Short circuit current density, FF: Fill factor and: efficiency, $R_{ct}$: charge transfer resistance and $Z_W$: diffusion impedance.*

As a result, $CF_4$ plasma treatment enhances the reaction kinetics of redox species at ST15-G and ST45-G electrodes yielding high exchange current density (As shown in Figure 5.10b). This observation is satisfactory with earlier discussions for the predominant catalytic behavior of the ST45-G electrode. $Z_w$ values of pristine and plasma treated graphene electrodes are significantly different. The low $Z_w$ value (17.1Ω) obtained at the ST45-G electrode/electrolyte interface implying that there is less resistance for the $I_3^-/I^-$ electrolyte species due to faster in-line charge transfer. As is evident, the enhanced electrocatalytic behaviors of graphene by $F^-$ functionalization through enhancing electron charge transfer sites is responsible for efficient tri-iodide reduction in this system. Furthermore, the temperature dependence of charge transfer resistance of pristine and surface treated graphene electrodes is shown in Figure 5.10 a & b. The result illustrates that the $R_{ct}$ decreases as exchange current density increases with increasing temperature from 273K to 333K. Likewise, decreases in charge transfer resistance are also associated with the increase in exchange current density $J_0$ (calculated using the equation 5.4) at the electrode-electrolyte interface as shown in Figure 5.10b).

$$J_0 = RT/nFR_{ct} \qquad (5.4)$$

Here, $R_{ct}$ is the charge transfer resistance calculated from the EIS spectra, R is the universal gas constant, T is the temperature in K, n is number of electrons contributing to the charge transfer at the interface and F is the Faraday's constant. Exchange current density is a kinetic component that arises due to the charge transfer from the counter electrode to the tri-iodide ions at the electrode-electrolyte interface. The temperature dependent exchange current density curves for different graphene counter electrodes (Figure 5.10b) follow the Arrhenius equation as per the equation 5.5.

$$J_0 = I_0 \exp(-E_a/RT) \quad (5.5)$$

Here, $E_a$ is the activation energy, and the other terms follow their usual meanings. As shown in Figure 5.10b, the successive increase in exchange current density with the plasma treatment time and temperature for PG, ST15-G ST45-G substantiates the enhancement of higher catalytic activity of the fluorinated graphene electrodes. As explained earlier, the creation of graphene active sites in graphene contribute enhancing the catalytic activity of the graphene for tri-iodide reduction. We believe that the increase in exchange current density is attributed to the enhancement of electrocatalytic activity of the large scale CVD graphene. Therefore, $F^-$ functionalized graphene with active edge-plane sites can be further applied in a wide range of electrocatalytic systems for iodine reduction apart from the DSSC.

### 5.1.7. DSSC full cell characterizations using fluorine doped graphene counter electrodes

The $TiO_2$ working photoanodes of ~12 μm thickness were prepared on FTO substrate using $TiO_2$ paste by doctor blade technique and, subsequently, sintered at 450 ºC for 30 minutes in ambient atmosphere. The $Ru(dcbpy)_2(NCS)_2$ (dcbpy = 2,2-bipyridyl-4,4-dicarboxylato)dye (535-bisTBAN719, Solaronix) was used to sensitize the $TiO_2$ photo electrodes. A sandwich-type configuration was employed to measure the performance of the dye-sensitized solar cells, using graphenes on F-doped $SnO_2$ (FTO) glass and 0.5M MPII (1-methyl-3-propylimidazolium iodide) with 0.05M $I_2$ in ACN as the electrolyte solution. Current–voltage characteristics of DSSCs were carried out under

1 sun illumination (AM 1.5G, 100 mW $cm^{-2}$) with a Newport (USA) solar simulator (300W Xe source) and a Keithley 2400 source meter.

Figure 5.11 compares the performance of DSSCs employing the three different counter electrodes (CE) of P-G, ST15-G and ST45-G. The Pt coated CE was also tested under similar condition for elucidating the feasibility of graphene as a CE of DSSC. The short-circuit current density ($J_{sc}$) of DSSCs based on graphene is found to be increasing with an increase in plasma treatment time as listed in Table 5.3. The improvement of $J_{sc}$ in surface treated graphene electrodes can be explained based on the progress of catalytic behavior in reduction of tri-iodide to iodine ($I_3^- + 2e^- \rightarrow 3I^-$), which determines the actual driving force for dye regeneration at the photoanode part. On the other hand, a shift in open circuit voltage (Table 5.3) for ST15-G electrode evidenced a shift in graphene surface redox potential towards the more negative side due to $F^-$ ion functionalization as illustrate in Figure 5.12. To decipher these phenomena further, we applied steady state cyclic voltammetry for exploring the mass transfer of tri-iodide in different graphene electrodes (Figure 5.8) which are discussed elaborately in the section 6.1.6. It is clearly seen in the Tafel plot (Figure 5.9a) that slopes of the cathodic and anodic part of the J-V plot increases for ST15-G and ST45-G in comparison to the P-G.

Evidently, the increase in slope of Tafel plot corresponds to the enhancement in exchange current density (J0) at the electrode-electrolyte interface which is quite harmonious with the solar cell measurements where a sharp increase in current density was found in the fluorine functionalized graphene compared to the pristine one. This

implies that $CF_4$ plasma treated graphene (ST15-G and ST45-G) substantially increase the mass transport pathway and render efficient tri-iodide reduction.

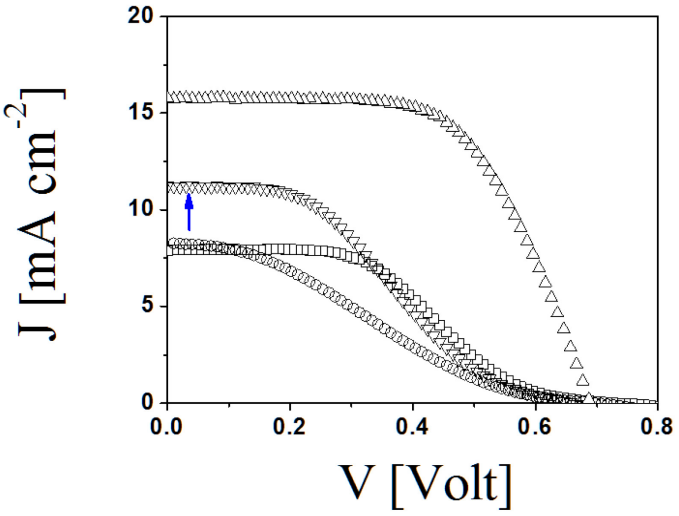


Figure 5.11: J-V measurements of DSSCs using different plasma etched graphene counter electrodes (○, Pristine Graphene) (□, ST15-G) (∇, ST45-G) and (Δ, Pt ), performed under light illumination.

Figure 5.12: J-V measurements of DSSCs using different plasma etched graphene counter electrodes (○, Pristine Graphene) (□, ST15-G) (∇, ST45-G) and (Δ, Pt ), performed under dark condition.

## 5.2. Graphene functionalization using nitric acid

### 5.2.1. Functionalization of graphene with $HNO_3$

So far, it has been well reported that nitric acid ($HNO_3$) introduces p-type donors in graphitic materials[43, 65, 66] which significantly improves the conductivity and charge transfer efficiency of the carbon structures [46-49 51, 67]. Furthermore, graphene doped with $HNO_3$ does not cause any detrimental oxidants and results in thermally stable structure which is beneficial for robust solar cell applications [68, 69]. Hence it is of fundamental interest to study how $HNO_3$ doped graphene affects tri-iodide reduction in DSSCs. Here we report a systematic investigation of enhancement in electro-catalytic properties of nitric acid doped graphene for tri-iodide reduction. We find that this strategy is easy to apply for a large scale CE of DSSCs with enhanced efficiency of the tri-iodide reduction. The large area graphene on Cu was transferred to FTO using chemical method as follows. First, graphene/Cu was placed floated on a Cu etchant ($FeCl_3$) in order to etch away the Cu foil. After etching away the Cu foil using Cu etchant and then transfer over the FTO using subsequent washing with water, isopropanol (IPA) and acetone. Furthermore the graphene/glass samples were annealed at 500$^{o}$C by using rapid thermal annealing method (RTA). The transferred graphene on glass was functionalized using different concentration of $HNO_3$ (ALFA-AESAR) solution by dip casting method for the same time followed by cleaning the surface by blowing dry nitrogen. The graphene layer was transferred onto FTO glass substrates by a chemical method as explained in the experimental section 3.2.2. Furthermore, pristine graphene on FTO (PG) was doped with different concentrations of $HNO_3$ solutions of 20%, 50%, 70% and 100% which we addressed as 20HDG, 50HDG, 70HDG and 100HDG graphene samples respectively.

### 5.2.2. Raman spectroscopy

The pristine and nitric acid treated graphene electrodes were further characterized with Raman spectroscopy (as shown in Figure 5.13) in order to elucidate graphene structures, in-plane $sp^2$ vibration of carbon atoms (which appear as G band) as well as any alteration in the $sp^2$-$sp^3$ hybridization due to doping. As could be seen in the comparison Raman spectra in Figure 5.13 that the pristine graphene (PG) shows a minuscule D band at 1342 $cm^{-1}$ with peak intensity ratio of $I_D/I_G$~0.2 which is corresponding to the presence of armchair like edges-planes at the graphene.[70]

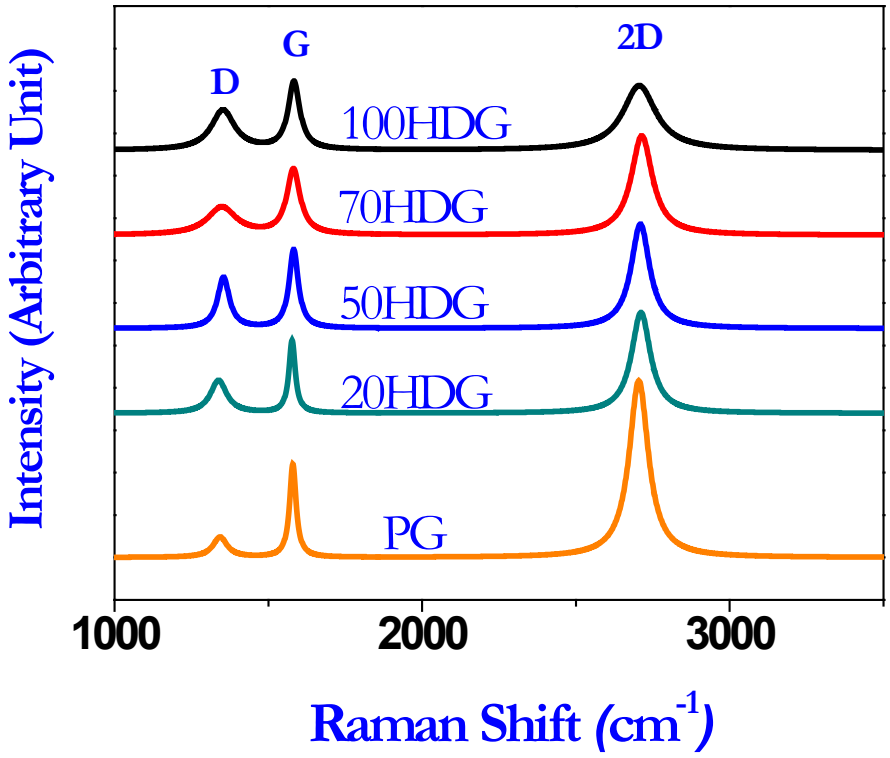


Figure 5.13: Comparison Raman spectra of large scale CVD-graphene doped with different concentration of nitric acid. The comparative spectra depicted the characteristics D, G and 2D Raman bands of pristine and nitric acid treated graphene.

Furthermore, the intensity of D-band increases (Figure 5.14a) with increasing nitric acid concentration which inferred that the electronic structure of graphene is altered. We believe that alteration of graphene electronic structure occurred by two ways. Firstly, changes take place in sp2 hybridization of carbon atoms due to the bond formation between the graphene carbon atoms with different functional moieties like C=O-, C(O)OH- and $NO_3^-$; and secondly, the formation of unsatisfied valance bonds may also play a key role in creation of edge-planes like catalytic sites in graphene60, 71. However, further evidences related to the alterations in hybridization and different bond formations are presented in the upcoming sections (XPS section).

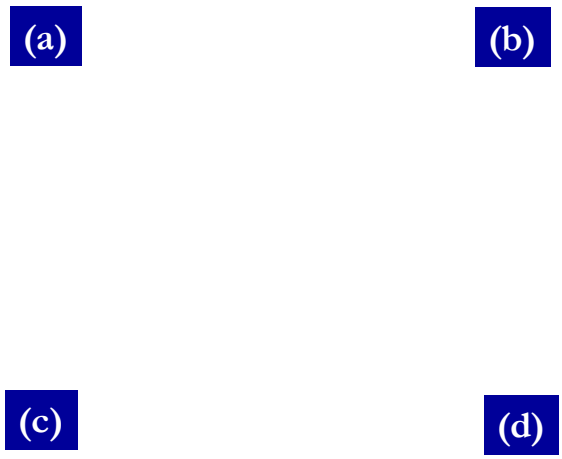


Figure 5.14: Raman spectra of different $HNO_3$ functionalized graphene showing comparative (a) D band, (b) G band, (c) 2D band and (d) a comparative plot of $I_G/I_{2D}$ ratio with different doping concentrations.

Furthermore, the G and 2D band position occurred at 1579 $cm^{-1}$ and 2704 $cm^{-1}$, respectively and their corresponding intensity ratio of G and 2D band ($I_G/I_{2D}$~ 0.5) confirms the few layer graphene structure on the FTO substrate[72]. As shown in Figure 5.14b, no significant variations are found in the intensity and position of G band peaks ~1579 $cm^{-1}$ even after employing acid doping which reveals that no massive structural deformation occurs in the graphene lattice/sub-lattice. There is small changes in full width half maxima (FWHM) of G peaks with increasing doping concentrations and a slight blue shift (~5 $cm^{-1}$) in G band peak for 100HDG ascribed to conventional fluctuation due to the hole doping in graphene[59]. We believe that, the G peak broadening is due to the splitting of band structure of the graphene.

We also observed the successive blue shift in 2D band peak at 70HDG (2714 $cm^{-1}$) samples (as shown in Figure 5.14c) compared to PG (2704 $cm^{-1}$), manifesting the functionalization of different functional groups with carbon atoms through $sp^3$ hybridization. In this context, the shift in the position of the 2D band with increasing acid doping concentration affirms that the $HNO_3$ carriers randomly doped in the graphene lattice, which clearly understands that numbers of edge-plane like active carbon sites in graphene are promoted. On the other hand, 2D peak broadenings (i.e. increase in FWHM) are found with successive increase in $HNO_3$ doping concentrations which proclaim the splitting of the electronic band structure of graphene[73]. As could be seen from the Figure 5.14d, the $I_G/I_{2D}$ ratio increases with increasing the doping concentration in graphene, represents the formation of graphene intercalated structures due to the attachments of different functional moieties. We believe that the splitting of the electronic band structure of graphene is due to the increase in proton concentration in graphene lattice which also

causes the Fermi level shift in graphene. However, we will further discuss (by using XPS and UPS) in upcoming sections how the electronic band structure splitting and Fermi level pinning of graphene occurs under acid doping and their subsequent effects on enhancing catalytic activity of graphene for tri-iodide reduction.

### 5.2.3. X-ray photoelectron spectroscopy

Figure 5.15: Illustrate comparison X-ray photoelectron spectra of pristine graphene and acid doped graphene electrodes.

X-ray Photoelectron Spectroscopy (XPS) is a potential tool to investigate the chemical environment of modified graphene lattice by foreign doping74. We performed XPS in order to ensure the $HNO_3$ doping in graphene lattice and study their chemical and

electronic state. X-ray photoemission spectra (XPS) were obtained using an angular resolved electron analyzer with a monochromatic Al Kα source (model Theta Probe, Thermo Fisher Scientific). The emitted electrons were detected at the angles between 23º and 83º. The conduction band maximum was studied using ultraviolet photo-emission spectroscopy. The resultant full comparative spectrum is presented in Figure 5.15. The full-width half maximum (FWHM) of C1s peak increases (as shown in Figure 5.16a) monotonically as the $HNO_3$ concentration increases which is ascribed to $sp^2$, $sp^3$ hybridizations. Such hybridizations affirm the occupancy of doping carriers in the graphene matrix which is analogous to the p-type doped carbon nanotube. The intensity of C-C bonds found to be gradually increases with increasing doping concentrations. This is also attributed to the formation of weak chemical bonding due to the $\pi - \pi$ interaction in the graphene interlayer, and leads to the de-screening of nucleus charges which results in the increase in core electron binding energies[25].

Further, the core level high resolution spectra represents the N1s (~399) and O1s (530 eV) peaks (as shown in Figure 5.16b and 5.16c respectively) confirm the presence of $NO_3$ entities in the graphene lattice. These atomic concentrations of C, N and O entities were estimated from Figure 5.16 and the results are summarized in Table 5.4. Table 5.4 inferred that the oxygen content of pristine graphene is drastically enhanced from 1.4% to ~21% upon $HNO_3$ doping, which is attributed to the electron restoration by oxygen (protonation). Figure 5.17 a, b. c and d shows the de-convoluted spectra of oxygen peaks represent the different stretching modes of C-O covalent bonds for different concentration of $HNO_3$ doping of 20HDG, 50HDG, 70HDG and 100HDG respectively.

However, it is noteworthy to comment that the XPS data were recorded where the graphene films are coated on FTO substrates. Therefore, it is inevitable to avoid the accountability of the oxygen molecules' contributions which may be arising from the FTO substrates. On the other hand, the N1s peak shifts to a higher energy at ~ 400.79 eV that infers the presence of nitrogen in oxygen rich environment. Therefore, atomic concentrations of nitrogen constituents are found to be reduced when increasing the $HNO_3$ concentration, since oxygen is more electronegative than nitrogen.

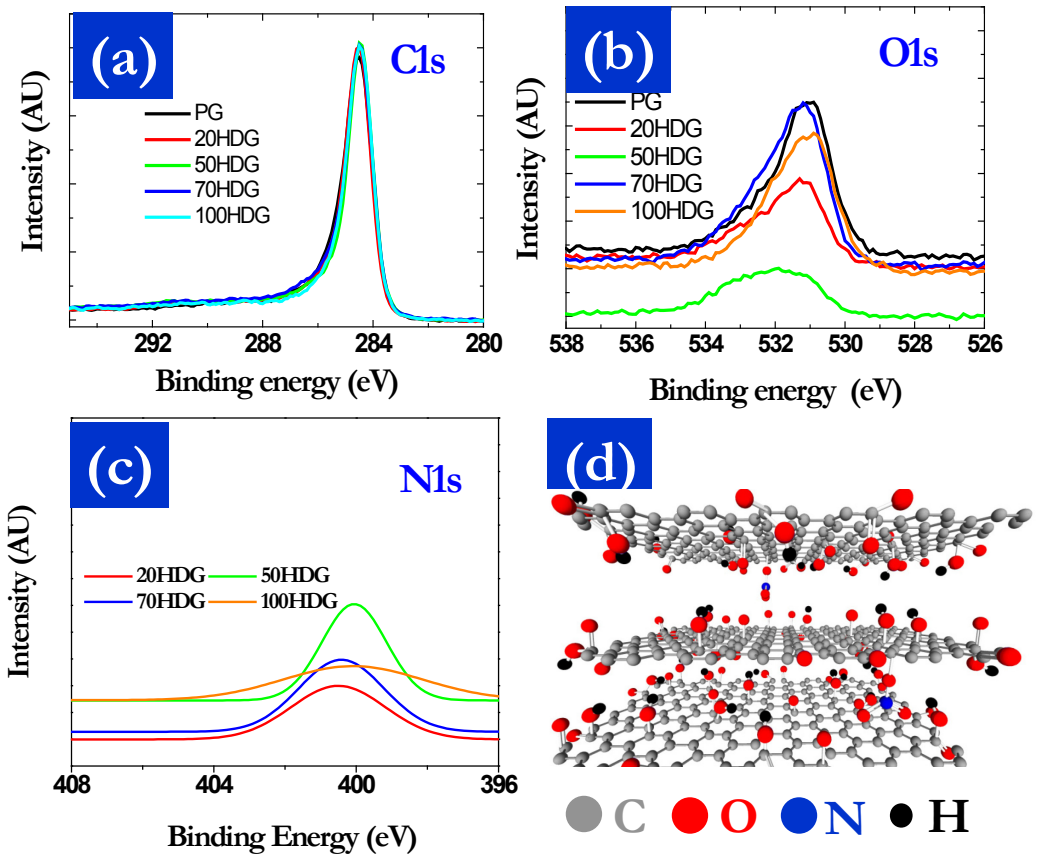


Figure 5.16: XPS core level spectra of (a) C1s (b) O1s (c) N1s and (d) schematic structure of $HNO_3$ doped few layer graphene (doping atoms are indicating different colors, grey: carbon, red: oxygen, black: hydrogen and blue: nitrogen)

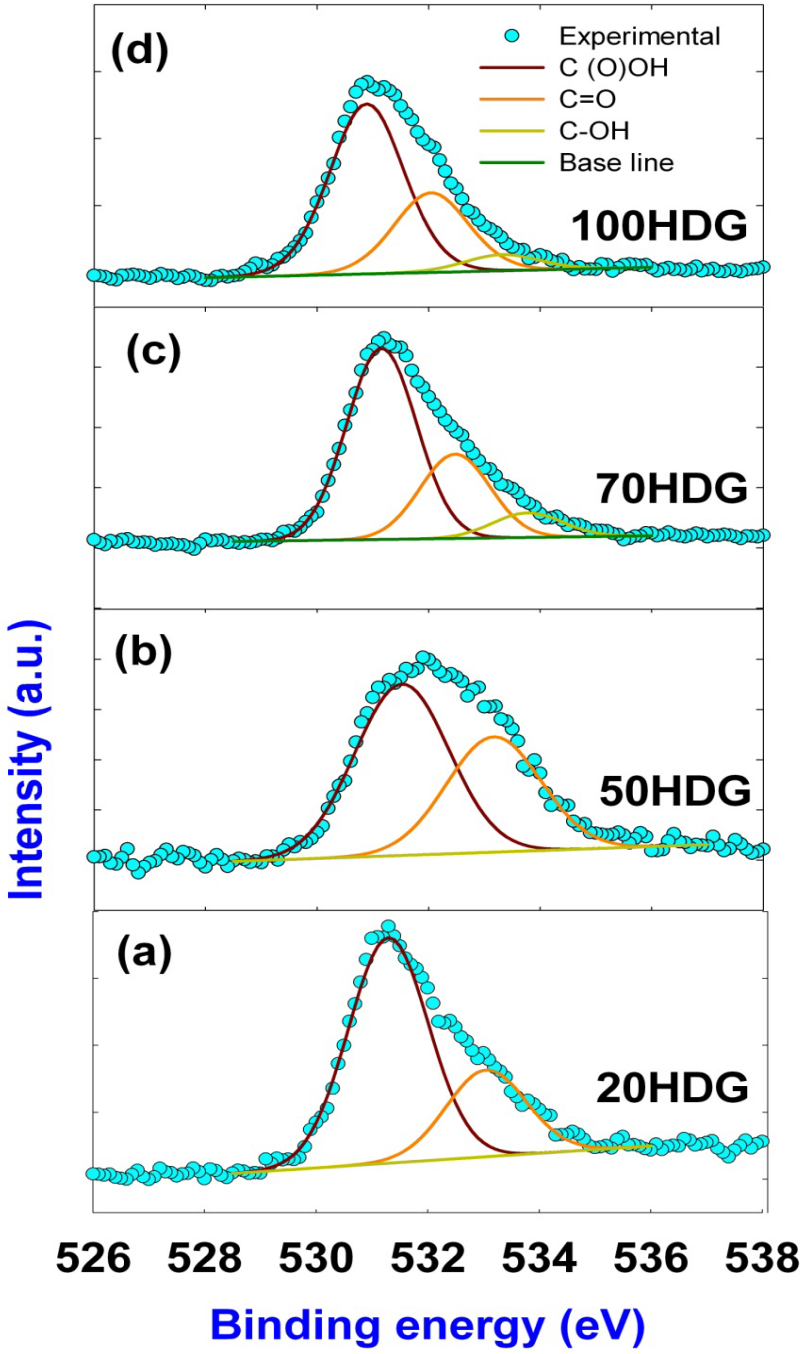


Figure 5.17: De-convoluted X-ray photoelectron spectra of oxygen peaks represent different stretching modes of C-O covalent bonds for (a) 20% $HNO_3$ treated (b) 50% $HNO_3$ treated (c) 70% $HNO_3$ treated and (d) 100% $HNO_3$ treated graphene.

Table 5.4: Atomic concentration of C, N and O of pristine (PG) and $HNO_3$ doped graphene (HDG).

| Samples | C1s (%) | N1s (%) | C(O)OH | O1s (%) | | |
|---|---|---|---|---|---|---|
| | | | | C=O | C-OH | |
| PG | 98.6 | - | - | 1.4 | - | |
| 20HDG | 90.6 | 0.43 | 0.43 | - | 4.02 | (9.0) |
| 50HDG | 84.6 | 0.91 | 5.42 | - | 3.65 | (14.4) |
| 70HDG | 77.2 | 0.40 | 13.87 | 6.12 | 1.79 | (21.7) |
| 100HDG | 78.8 | 0.33 | 13.31 | 6.23 | 1.27 | (20.8) |

It is noteworthy to mention that the protonation that occurred in the graphene lattice varying with doping concentration can be explained by the following relation75

$$6HNO_3+25C \rightarrow C_{25}+NO_3^-4HNO_3 + NO_2+H_2O \quad (5.6)$$

According to the chemical doping mechansim in equation 5.6, it is expected that $NO_3^-$ molecules are to be interclated with graphene layers. Primarily, when $HNO_3$ concentration increses from 20% to 50%, the bond formations of C(O)OH (~531.8 eV) and C-OH (534.5 eV) takes place. Furthermore, C= O groups (532.5 eV) are introduced into the graphene lattice upon high concentration (70 and 100%) of $HNO_3$ treatment.

### 5.2.4. Ultraviolet photoelectron spectroscopy (UPS)

The doping and electronic configurations is further scrutinized by ultraviolet photoemission spectroscopy (UPS) of pristine and $HNO_3$ doped graphenes as shown in Figure 5.18a&b.


Figure 5.18: (a) Ultraviolet photoelectron spectroscopy of pristine and $HNO_3$ doped graphene electrodes under various concentration (20 to 100%) and (b) Enlarge view of UPS Spectra in Figure 5.18a which depicts the shift in binding energy of the doped graphene.

The work function of these electrodes were estimated from the following relation[76] as shown in equation 5.7,

$$\varphi = h\omega - |E_{sec} - E_{FE}| \qquad (5.7)$$

Where, $h\omega$ = 21.2 eV (He I Source), $E_{sec}$ is the onset of the secondary emission, and $E_{FE}$ is the Fermi edge (sample bias at -20V in the beam line at RIKEN Nanoscience Laboratory).

The estimated work functions of graphene and $HNO_3$ modified graphenes are presented in the schematic Figure 5.19. From Figure 5.19, it is clearly illustrated that the work function of graphene is modulated from 4.52 eV ($\varphi_{PG}$) to 5.31eV ($\varphi_{100HDG}$) due to the effect of chemical doping of different functional moieties during $HNO_3$ treatment. It

seems that the doping of substantial amount of oxygen molecules in graphene lattice (protanation) successively increase the hole concentration, which further lowers the Fermi level of graphene from the Dirac point (p-doping). This observation supports our earlier discussion on XPS data in the previous section. It is also noted that the work function of pristine graphene prepared from our CVD method is consistent with other previous reports on CVD graphene (4.3 eV) [25, 77].

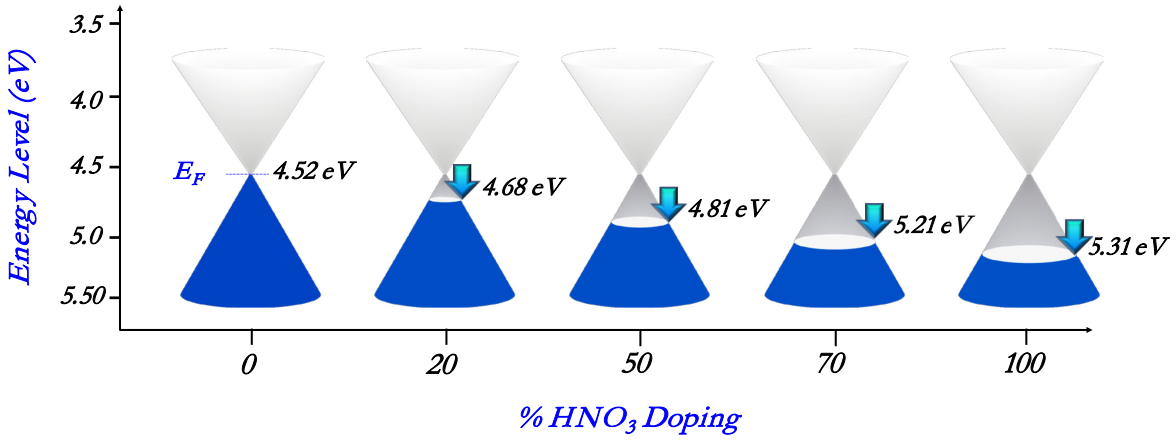


Figure 5.19: Schematic demonstrating the Fermi level pinning in graphene under different concentrations of $HNO_3$ doping.

These heavily doped p-type carriers in graphene catalytic counter electrodes of DSCs causes' band bending at the electrode/electrolyte interface which further results in the efficient charge injection from graphene to FTO substrate and effectively reached in the external circuit without having any charge recombination loss. Furthermore, electronic interface of $HNO_3$ doped graphene encounter a great potential for applications in the field of organic field effect transistors (OFETs) and organic photovoltaic devices with improved open-circuit potential and short circuit current.

### 5.2.5. Fourier transform infra-red spectroscopy

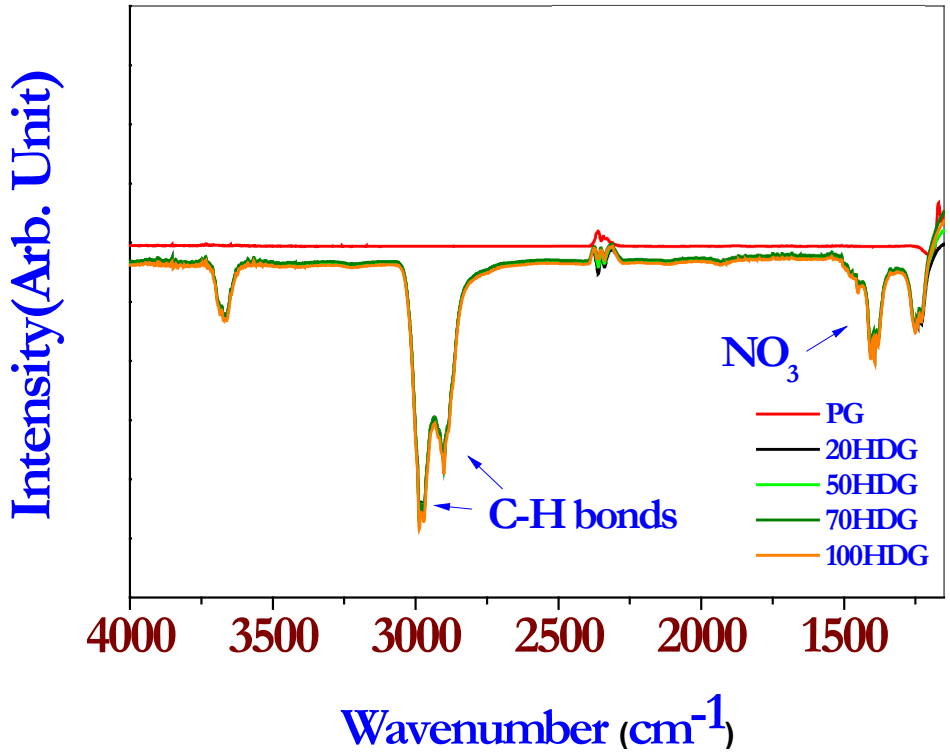


Figure 5.20: Comparison fourier transform infra-red spectra (FTIR) of Pristine and different concentrations of $HNO_3$ doped graphene show the formation of additional C-$NO_3$ and C-H stretching bonds.

The above discussion is further testified with FTIR analysis as shown in Figure 5.20, which illustrates the comparative spectra of pristine and different $HNO_3$ doped graphene. The predominant peak appeared at ~1398 $cm^{-1}$ in the doped sample over pristine sample, which corresponds to the vibrational stretching of $NO_3^-$ assigned to doubly degenerate IR-active vibrations of $\upsilon_3(E^l)$ along with $\alpha$, a non-degenerate IR-active mode of $NO_3^-$ peak at ~831 $cm^{-1}$ [78]. Figure 5.20 inset picture showing the systematic change in the $NO_3^-$ peaks with different doping concentration. In addition to

this, a strong C-H bond is identified at ~2970 $cm^{-1}$, this observation is quite consistence with XPS results in section 6.2.3. In general, there are several factors such as electronic configuration, energy level and structural properties which have a forthright influence over the electro catalytic reactions on the catalyst surface.

### 5.2.6. Electrochemical characterizations

In order to study the charge transfer characteristic of graphene counter electrodes, we performed impedance analysis using symmetric half cell configuration (see experimental section 3.4 for the detail experimental procedure) using the same electrolyte used for the full dye sensitized solar cell characterization. The resultant Nyquist spectra are presented in Figure 5.21a where the first semicircle is assigned to the charge transfer resistance ($R_{ct}$) of counter electrode/electrolyte interface and the second semicircle at low frequency region represents the Warburg diffusion impedance ($Z_w$) of the redox couple in the electrolyte. The $R_{ct}$ and $Z_w$ values of pristine and $HNO_3$ doped graphene counter electrodes are estimated by fitting the equivalent circuit (inset: Figure 5.21) model and their parameters are summarized in Table 5.5. The pristine graphene shows a very high charge transfer resistance [$R_{ct}$] value (45.2Ω -$cm^2$) compared to the doped graphene electrodes indicating the poor catalytic activity of their inherent basal planes. Surprisingly, the $HNO_3$ doped graphene electrodes showed a noticeably lower $R_{ct}$ value of 7.52 Ω-$cm^2$ (Table 5.5), which is ~ 6 times lower than pristine sample.

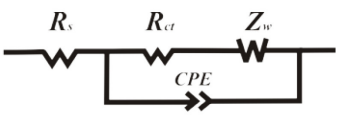


(b)

(a)

Figure 5.21: (a) Nyquist plot of different counter electrodes in symmetric cell configuration and (b) showing the effect of different doping concentration on the charge transfer resistance and exchange current density of the cells.

These results inferred that the $HNO_3$ doped graphene surface offered enhanced electro-catalytic activity by introducing active catalytic sites of C-H, C(O)OH and $NO_3^-$ in graphene lattice as mentioned in previous sections 6.2.3. Unambiguously, this enriched catalytic effect is responsible for enhanced catalytic activity of doped graphene electrodes which attributed to the amplified photocurrent in the cell. The decrease in charge transfer resistance is attributed to the increase in exchange current density $J_0$ at the electrode-electrolyte interface as shown in the Figure 5.22 a & b. The exchange current density was calculated using the following equation 5.8:

$$J_0 = \frac{RT}{nFR_{ct}} \qquad (5.8)$$

Where, $R_{ct}$ is the charge transfer resistance calculated from the EIS spectra, R is the universal gas constant, T is the temperature in K, n = number of electrons contributing to the charge transfer at the interface and F is the Faraday's constant.

Exchange current density is the kinetic component which arises due to the charge transfer from the counter electrode to the $I^{3-}$ ions at the counter electrode-electrolyte interface. The temperature dependent charge transfer resistance exchange current density curves for different graphene counter electrodes are illustrated in Figure 5.22 b which follows the Arrhenius equation as per the equation 5.9.

$$J_0 = I_0 e^{(-\frac{Ea}{RT})} \qquad (5.9)$$

Where, $E_a$ is the Activation Energy; R is the Universal gas constant; $I_0$ is the exchange current density at T = infinity; and T is the Temperature in K.

Figure 5.22 b, illustrates the exchange current density of the symmetric cell with the temperature for different un-doped and doped graphene electrodes. We found that, the exchange current density increases with increasing doping concentrations (enhancement of C-O bonds which attributed to the protonation in the graphene as described in the XPS section of the main manuscript) which is support the enhancement of improved electro catalytic activity of the graphene counter electrodes owing to its Fermi level shift. On the other hand, the temperature dependence of $R_{ct}$ and $J_0$ for the PG and $HNO_3$ doped graphene electrodes are demonstrated in Figure 5.22 a & b (supporting information) which clearly shows the $J_0$ and $R_{ct}$ are stable throughout the entire temperature range from 273K to 333K.

Figure 5.22: (a) Charge transfer resistance vs. temperature and (b) exchange current density vs. temperature plot for graphene and different concentration of acid doped graphenes represent the stability of different counter electrodes at temperature from 273K to 333K.

Table 5.5: Illustrates EIS parameters of pristine and $HNO_3$ doped graphene catalytic counter electrodes.

| Electrodes | $R_{ct}$ ($\Omega cm^{-2}$) | $Z_W$ ($\Omega cm^{-2}$) | $D_n$ ($cm^{-2}s^{-1}$) |
|---|---|---|---|
| PG | 45.2 | 161.4 | $1.38 \times 10^{-6}$ |
| 20HDG | 16.4 | 75.7 | $2.01 \times 10^{-6}$ |
| 50HDG | 13.3 | 46.5 | $2.31 \times \times 10^{-6}$ |
| 70HDG | 7.91 | 34.5 | $3.24 \times \times 10^{-6}$ |
| 100HDG | 19.3 | 63.9 | $1.68 \times \times 10^{-6}$ |

Figure 5.23: Linear sweep cyclic voltammogram of a graphene on FTO electrodes.

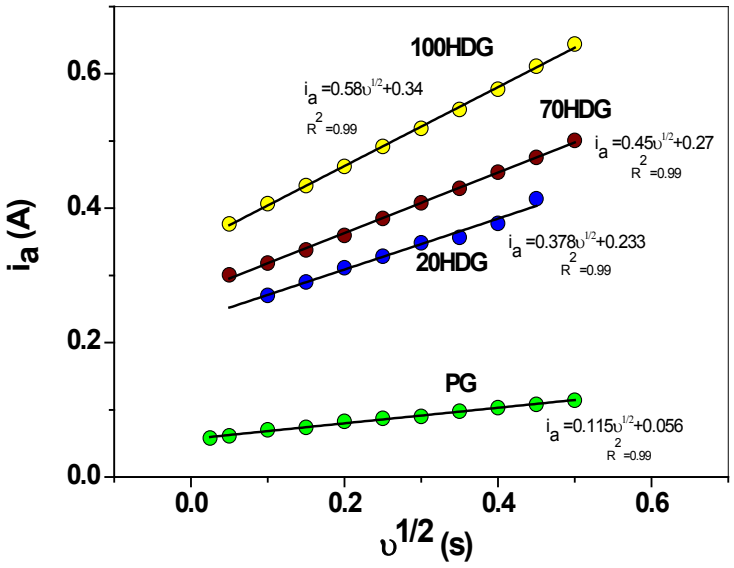


Figure 5.24: Illustrates frequency dependent scan rate of different $HNO_3$ doped graphene.

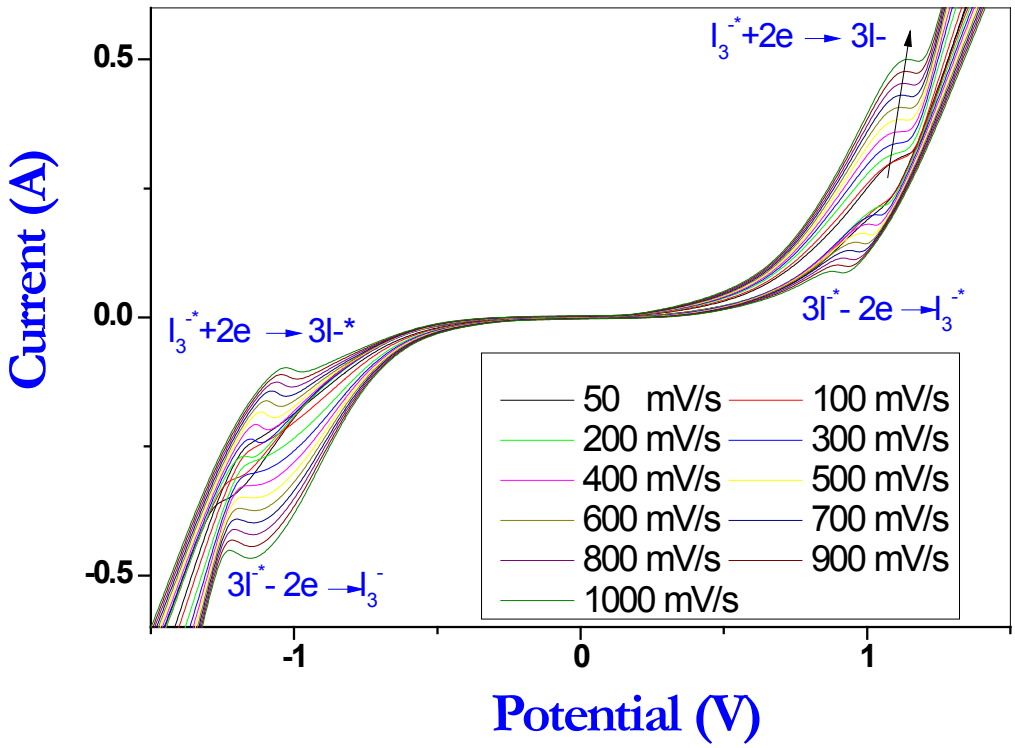


Figure 5.25: Cyclic voltammogram of 70HDG graphene on FTO electrodes with different scan rates.

Furthermore, it is also observed that the excessive doping of $HNO_3$ limits the active catalytic surface area of graphene and therefore results in higher charge transfer resistance of 19.3Ωcm $^{-2}$. On the other hand, the decrease in Warburg diffusion resistance [$Z_W$] of $HNO_3$ doped samples reveals that the high diffusivity [$D_n$] of the tri-iodide species at graphene catalytic surface is due to the presence of higher catalytically active doping carriers (C-H, C(O)OH and $NO_3^-$). We employed the polarization measurements using symmetry cell configuration as described in impedance measurements section chapter 3 sections 3.4. The apparent diffusion coefficient of $I_3^-$ can be obtained from the relation as described in equation (5.10) [79],

$$D_{I^{3-}} = \frac{i_{lim} l}{2NFC^{0}_{I_3^-}} \qquad (5.10)$$

Where, $i_{lim}$ is the limiting current derived from polarization measurements, $l$ is distance between two electrodes of symmetric cells, $n$ =2 number of electrons participating in the reduction, $F$=faraday constant, $C^{0}_{i3}{}^{-}$ is concentration of iodide. Figure 5.23 shows the typical cyclic voltammetry curve of symmetry cell. The hysteresis plot from Figure 5.23 exemplifies the steady state condition, and saturated portion denotes the limiting anodic current ($i_{lim}$). By applying those limiting current values in equation 5.10 we calculate the diffusion coefficient ($D_{app}$) of $I_3^-$ at pristine and modified graphene electrodes. All the electrochemical parameters obtained using equation 5.10 is listed in Table 5.5. From the Table 5.5, it is clearly depicted that the diffusivity of tri-iodide at pristine graphene CE ($1.38 \times 10^{-6}$) is inferior than the optimized $HNO_3$ doped (70HDG) graphene CE ($3.24 \times 10^{-6}$). On the other hand Figure 5.24 delineated the current vs. linear sweep cyclic voltammetry (as shown in Figure 5.23) scan rates plots of the different $HNO_3$ doped graphene samples. The increase in current with the scan rates shows the scan rates dependent catalytic behavior for tri-iodide reduction where at the counter electrodes/electrolyte interface the charge diffusion kinetics is increasing with increasing CV scan rates. Similarly, Figure 5.25 shows the cyclic voltammetry curve of 70HDG (the highest efficiency of solar cell as shown in Table 5.6) electrodes with different scan rates illustrate the sharp increase in the oxidation and reduction peaks in the counter electrode part with different scan rates. However, the increase in oxidation and reduction peaks with different scan rates is due to the oxidation and reduction kinetics at the electrodes as follows the equation $I_3^- + 2e^- \rightarrow 3I^*$ and $3I^{-*} - 2e^- \rightarrow I_3^-$ respectively. Furthermore, the

increase in oxidation and reduction peaks with different scan rates is also due to the enhancement of charge diffusion kinetics as explained earlier in this section.

This evidenced that $HNO_3$ doped graphene electrodes possesses additional in-plane charge transfer sites which can further accommodate and reduce tri-iodide species exceedingly on its surface. Thus, results in high catalytic reduction of tri-iodide compared to the PG, which is in good agreement with the photovoltaic performance of DSSCs constitutes with these counter electrodes.

### 5.2.7. DSSC full cell characterizations using $HNO_3$functionalized graphene counter electrodes

Figure 5.26 represents the current density-voltage curves which demonstrate the average values of at least three different cells. The device characteristics for DSSCs with pristine and $HNO_3$ doped graphene counter electrodes are summarized in Table 5.6. The device constitutes with $HNO_3$ doped graphene electrodes showed higher performance than that of pristine counter electrodes. To emphasize the phenomena, we believe that the low catalytic behaviour of pristine graphene attributed to its inert basal planes often limit the reduction feasibility under $I_3^-/I^-$ redox shuttle which severely impacted the dye regeneration[37]. Therefore regeneration of oxidized dye molecule is less progressive by pristine graphene ($J_{sc}$ = 8.3mAcm$^{-2}$) in comparison with $HNO_3$ doping electrodes ($J_{sc}$ = 11.8 mAcm$^{-2}$).

It is believed that amplifying catalytic sites through tailoring $HNO_3$ moieties in graphene lattice facilitate more iodine species reduction, which further affords the regeneration of oxidized dye molecules. The higher photo-conversion efficiency about

c.a 3.21% is achieved at 70% of $HNO_3$ doping where weak basal planes are triggered by C-H, C(O)OH and $NO_3^-$ foreign functional group formation in graphene lattice as discussed in XPS section, Figure 5.16. However, the device performance found to be reduced c.a 2.2% with a further increase in the doping concentration, which is ascribed to the detrimental effect in charge transfer at heavy dosage of $HNO_3$ on the counter electrode surface. It is noted that the enhancement in open-circuit voltage ($V_{oc}$) of doped electrodes may be related with the high dye regeneration at $TiO_2$/dye interfaces. Seemingly, high dye regeneration by $HNO_3$ doping in graphene electrodes substantially promotes the charge injection from the dye HOMO level to the $TiO_2$ conduction band.

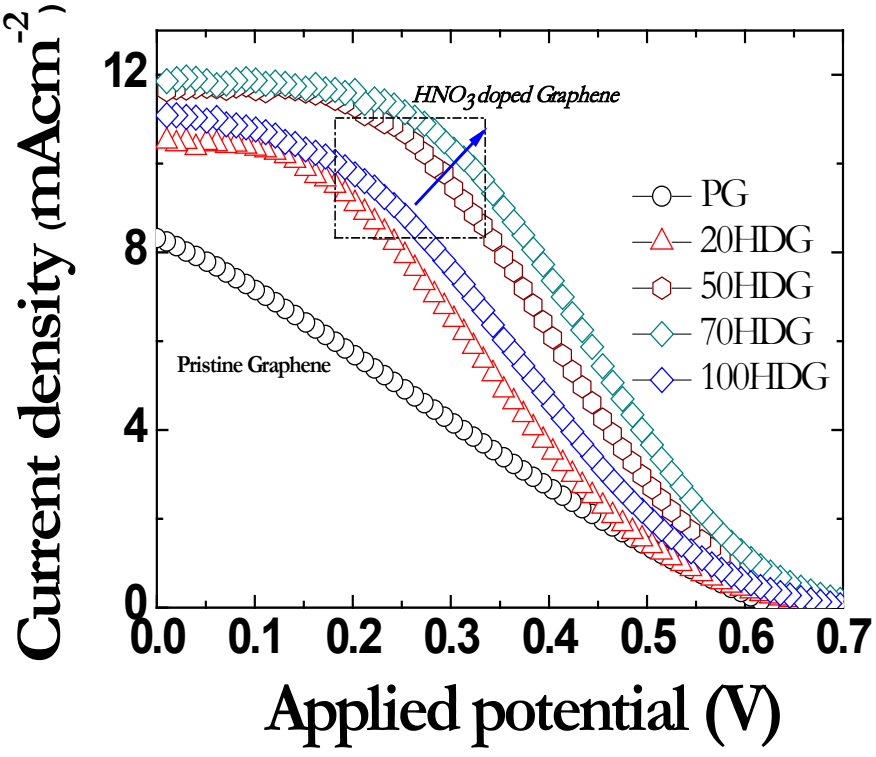


Figure 5.26: J-V curve of full DSSC cell consist of different $HNO_3$ doped graphene counter electrodes.

Table 5.6: Photovoltaic parameters of pristine and $HNO_3$ doped graphene catalytic counter electrodes

| Electrodes | $V_{OC}$ (V) | $J_{SC}$ ($mAcm^{-2}$) | FF (%) | η (%) |
|---|---|---|---|---|
| PG | 0.63 | 8.3 | 23.9 | 1.26 |
| 20HDG | 0.69 | 10.5 | 27.5 | 2.01 |
| 50HDG | 0.70 | 11.5 | 34.7 | 2.83 |
| 70HDG | 0.73 | 11.8 | 37.0 | 3.21 |
| 100HDG | 0.70 | 11.5 | 29.1 | 2.29 |

Now the Fermi level of $TiO_2$ is rising in the upward direction, which enhances the potential difference between redox species ($V_{oc} = E_f (TiO_2) - E_{redox}$) in the device. Therefore, we can argue that device performance improvement is attributed to the $HNO_3$ doping in graphene which offer efficient dye-regeneration through improving the catalytic properties of graphene counter electrodes. Apart from $V_{oc}$ and $J_{sc}$, the fill factor values of doped graphene based devices are also raised due to the $HNO_3$ doping (p-type). We consider that the interfacial contact between FTO/graphene is highly modified by doping carriers and offers high charge injection possibilities at the interfaces.

### 5.3. Graphene CoS hybrid structure

During past two decades people are in search for low cost efficient electrochemical energy harvesting devices like photo-electrochemical cells. In this context, graphene has been suggested as a new electrode in DSSC and organic cells due to its high transparency, prominent conductivity, high specific surface area and feasible

electro-catalytic activity [11, 23, 26]. In particular, to fabricate high performance graphene counter electrode of DSSC, surface functionalization plays a great role in rendering high catalytic activity in iodine reduction as reported elsewhere [63]. Graphene basal plane is not catalytically active in nature, thus inhibiting the charge transfer kinetics at the electrode/electrolyte interface [46]. In order to make efficient electro-catalytic graphene for electrochemical reactions, it is required to create catalytically active reaction sites in graphene while maintaining its high charge carrying capacity. In this context, surface functionalization of graphene has been employed to improve the catalytic function of graphene. Furthermore, functional nanoparticles decorated graphene film instantly increase the electrode-electrolyte contact area which is known as triple junction catalytic effect; hence improves the electron transfer kinetics at the interface [52]. Additionally, decoration with catalytically active functional nanoparticles (NPs) are also beneficial for enhancing electro-catalytic reactions for some other practical applications like hydrogen generation [53], Li-ion batteries [54], pseudo-supercapacitors [55] etc.

Cobalt sulphide (CoS) is newly introduced as a catalytic material for high efficiency energy generation and conversion [30]. Recently CoS has been suggested as a high efficiency catalysts for tri-iodide reduction and consequently is expected to replace expensive Pt electrode in DSSC [30, 80]. Quantum chemical calculations showed that the catalytic activity of $Co_xS_y$ is analogous to Pt due to the corresponding surface structure which creates electron transfer pathways for oxygen reduction kinetics [81]. Like Pt, a counter electrode in DSSC should exhibit low resistivity as well as high electro-catalytic activity towards iodine reduction. Although, CoS NPs are an active electro-catalytic species, their charge conductivity and mobility are not up to the mark. Hence, creating

synergistic catalytic CoS NPs cohered with ultra-conductive large scale graphene is more advantageous for low cost counter electrode application in DSSC.

This section describe the synthesis of CoS NPs on a large scale CVD grown graphene film by followed by successive ionic layer adsorption and reaction (SILAR) process [82] followed by their structural and electrochemical characterizations. We investigate the electro-catalytic activities of the CoS NPs decorated graphene electrode, by using impedance spectroscopy, cyclic voltammogram (CV), Raman and XPS, and explore in DSSC as a counter electrode relies to replace Pt electrode. The characterization condition of DSSC is described elsewhere (Supporting Information). We find that CoS NPs decoration boosts the graphene electrode efficiency by enhancing catalytic activity and reducing internal resistance.

### 5.3.1 Synthesis of CoS using SILAR method

In order to fabricate graphene-CoS hybrid structure, CoS nano-particles (NPs) were decorated on to the graphene surface by a step-by-step successive ionic layer absorption and reaction (SILAR) method. Two different chemical bath solutions of metal and sulfide precursors were prepared separately. 0.05M of Cobalt Nitrate is dissolved in ethanol and kept in first bath and second bath contains methanol solution of 0.05M of sodium sulfide ($Na_2S$). One coating cycle of CoS means 15 minute dip coating of graphene electrodes in to the first chemical bath ($Co^{2+}$) and subsequently in to the sulfide solutions. In order to remove the excess amount of un-reacted residuals on the graphene electrode, it is thoroughly rinsed with corresponding ion-exchange solvent about 15min after each dipping of respective chemical bath as shown in the schematic in Figure 5.27.

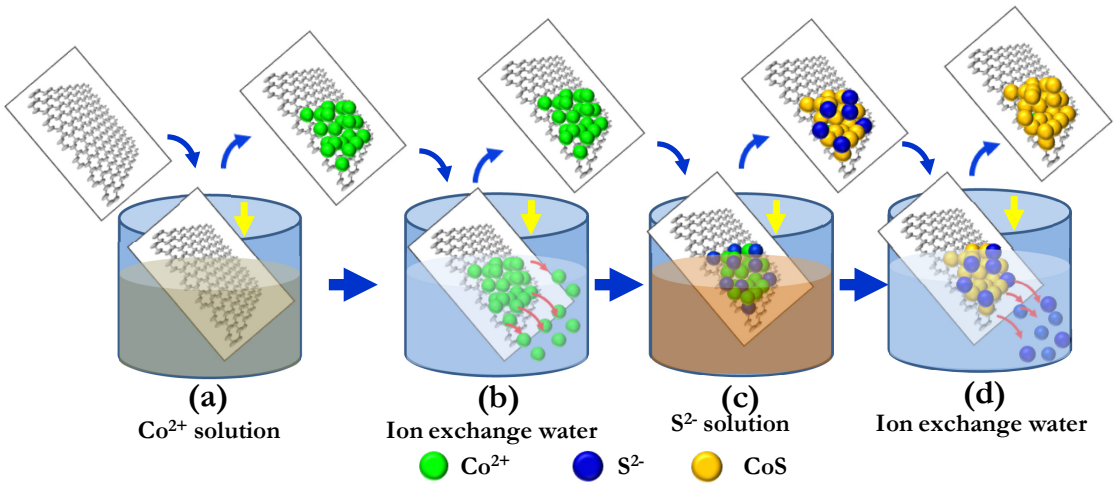


Figure 5.27: Schematic demonstrating the step-by-step SILAR process.

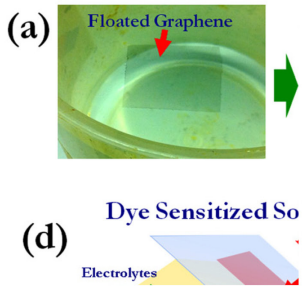


Figure 5.28: (a) Illustrates chemically etched floated graphene; (b) the floated graphene transferred to a FTO glass, (c) formation schematic of G-CoS through the step-by-step in-situ growth of CoS NPs in graphene film by successive ionic layer absorption and reaction method, (d) schematic represents the tested dye sensitized solar cell using CoS-graphene electrode.

Finally the CoS nanoparticles coated graphene electrode is dried in nitrogen for few minutes. We prepared 5 consecutive coating cycles of CoS on graphene matrix, which optically opaque compare to pristine graphene. In order to accommodate sufficient amount of CoS nanoparticles in graphene matrix, we fabricate few layer (4-5 layer) graphene on FTO electrode as described in the chapter 3 section 3.2.2.

### 5.3.2 High resolution transmission electron microscopy

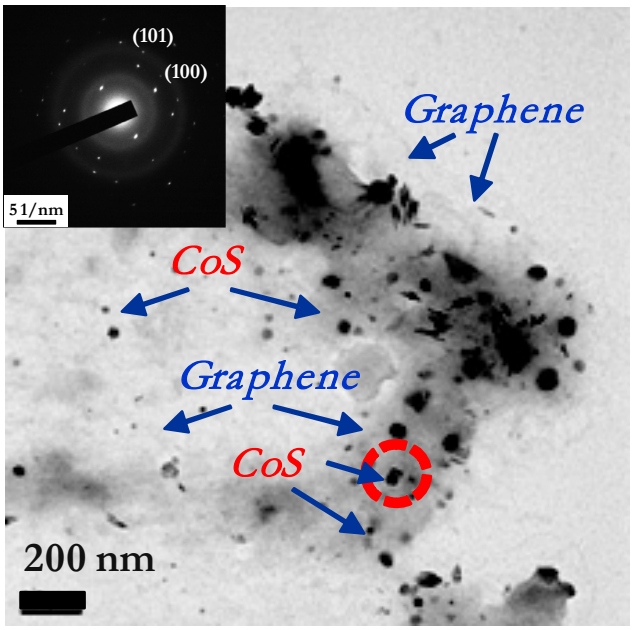


Figure 5.29: Transmission Electron Micrograph of Graphene-CoS shows the randomly dispersed CoS nano-particles on graphene membrane (Scale 400 nm), inset showing selected area diffraction patterns of Cobalt Sulphide formation over graphene film.

As evidenced in HRTEM (as shown in Figure 5.29) graphene film accommodates CoS NPs randomly on its surface with particle size of ~30-60 nm. The particle size and

their distribution on the graphene matrix will further described in the AFM section 6.3.4. Selected area diffraction (SAD) pattern of CoS nanoparticles confirm the existance of non-stoitiometric compound CoS on the graphene membrane with characteristics planes of (101) and (100) as shown in the inset of Figure 5.29.

### 5.3.3 Micro-Raman spectroscopy

Pristine graphene (PG) and G-CoS structure are characterized using Raman spectroscopy a nondestructive characterizations technique for graphene structural and electronic behavior. The characteristic D-band, G-band and 2D band peaks of graphene are observed at ~1352, 1579 and 2704 $cm^{-1}$ respectively as shown in Figure 5.30.

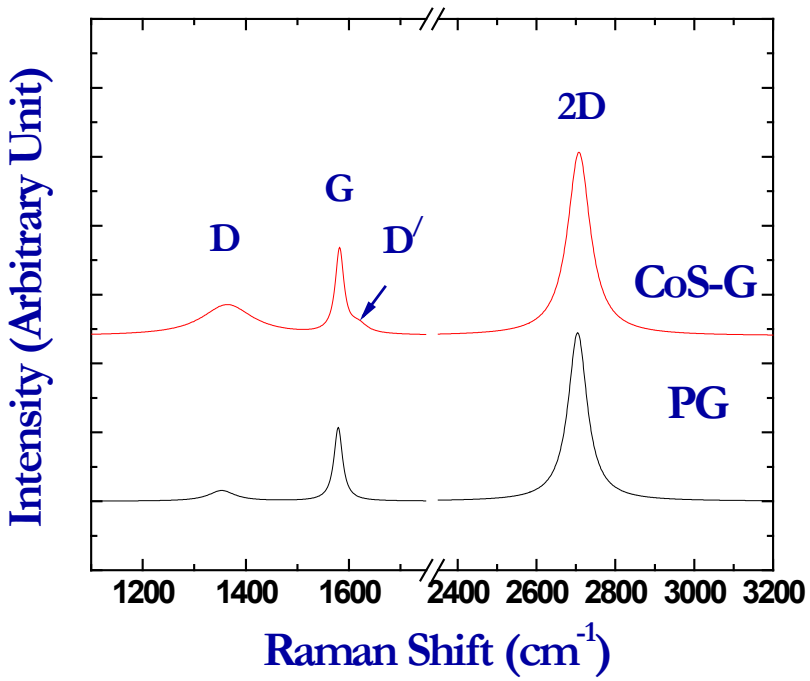


Figure 5.30: Depicts Raman spectra of PG and G-CoS demonstrating almost no change in graphene structure after CoS anchored.

The symmetric G band and 2D band positions and their corresponding band intensity ratio of $I_G/I_{2D}$~ 0.436 firmly depict the few layer graphene sheets on the glass substrates. A small D-band appears at 1352 $cm^{-1}$ for pristine graphene owing to the presence of armchair like graphene edges and incoherence between the graphene and substrates [70].


Figure 5.31: (a) and (b) Shows Raman spectra of D-band and G-band of graphene and graphene-CoS hybrid structure respectively.

Figure 5.30 shows no significant differences in both the peak position of G and 2D bands and their peak intensity ratios (IG/I2D of 0.436 and 0.44 respectively) for PG and G-CoS hybrid samples as shown in the Figure 5.31. This implies that the nearly unchanged graphene structure even after the decoration of CoS NPs on graphene film. As shown in the Figure 5.32b, CoS-Graphene Raman spectra shows the splitting of G band which results in the appearance of a D/ band at its base. In this context, the increase in the

D band intensity as well as the appearance of D/ band at ~ 1620 cm-1 also manifests the prevailing heterogeneous superstructure at the interface of graphene and CoS as depicted in the Figure 5.32.

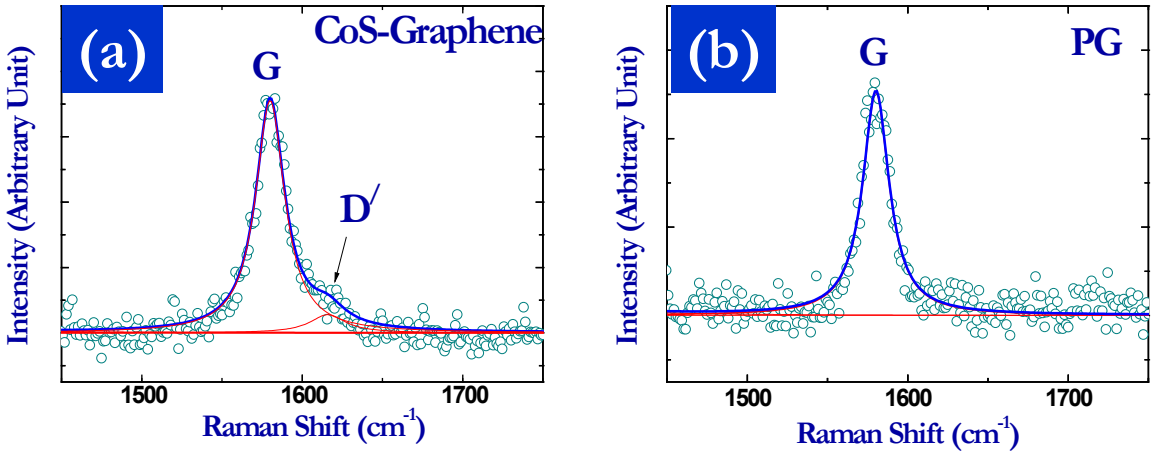


Figure 5.32: Demonstrates the G band of (a) CoS-Graphene hybrid structure and (b) pristine graphene.

However, $I_D/I_G$ ratio increases 2.21 times in G-CoS than PG which is attributed to the formation of incoherent interface between CoS NPs and graphene[83]. In this context, the D/ band at 1612 $cm^{-1}$ of G-CoS (As shown in Figure 5.32b) suggests the formation of dangling bonds between CoS NPs and carbon atoms at the interface [60].

### 5.3.4 Atomic force microscopy

Furthermore, surface morphology of the CoS-graphene was characterized using atomic force microscopy (AFM) and the graphene surface and graphene-CoS surface morphologies are clearly illustrated in the Figure 5.33 a & b respectively. As illustrated in Figure 5.34 a, b, c & d, the step height of the different CoS particle size are in the range

between 30-60 nm. Furthermore, the analysis of CoS particle size distribution shows in the Figure 5.35d. Form the Figure 5.35d it can be seen that a wide range of CoS particles were grafted on the graphene membrane from 20 nm to 90 nm. However the major portion of the particles size was covered in between the range of 30-60 nm.

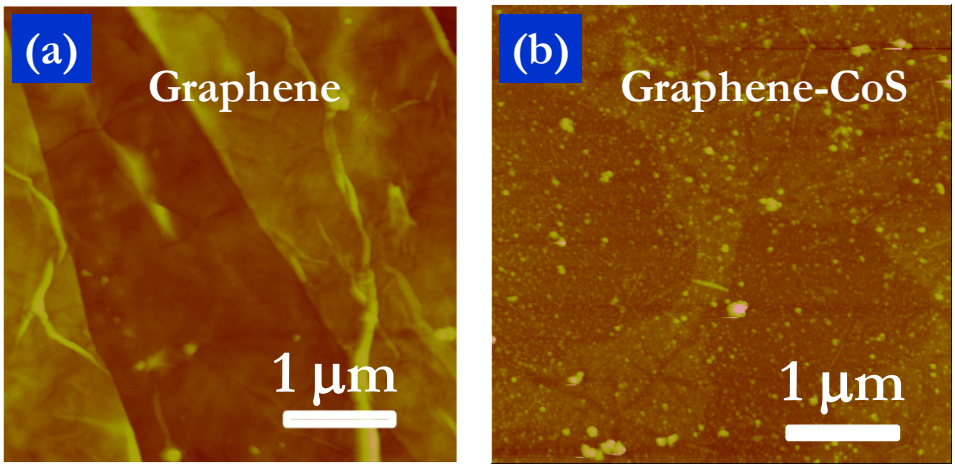


Figure 5.33: AFM images depicts the topological behavior of (a) pristine graphene (PG) and (b) CoS decorated graphene film (G-CoS).

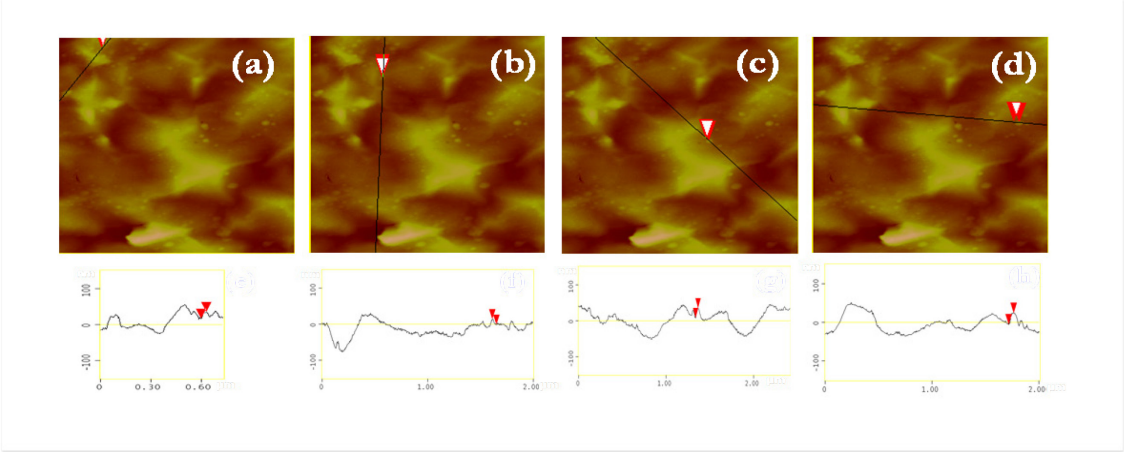


Figure 5.34: (a), (b), (c) and (d) Atomic force micrographs (AFM) illustrate the surface morphology of CoS decorated graphene film and (c), (d), (e) & (f) show the corresponding AFM height profiles.

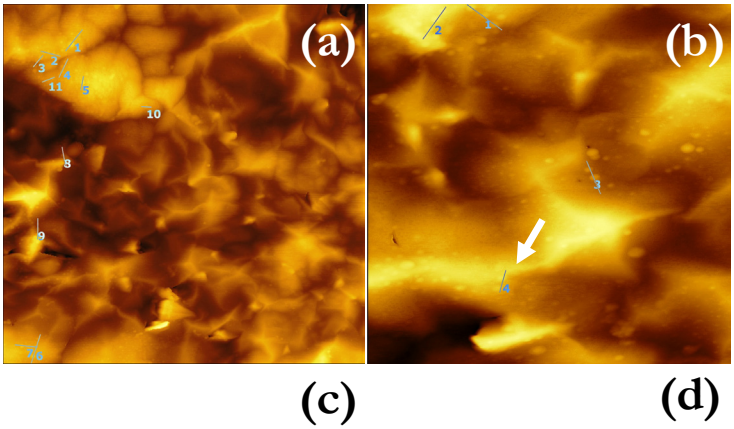


Figure 5.35: (a) & (b) Particles size measured using AFM on the surface of G-CoS composite electrodes; (c) Illustrates the step height of CoS particles along the line as indicated in Figure 5.35b; (d) CoS particle size distribution over graphene membrane depicts the formation of 30-60 nm size particles via SILAR method.

### 5.3.5 Optical transmittance measurement

UV-visible absorption/transmittance spectra were recorded using Jasco V-670 double beam spectrophotometer and the spectra recorded at 350nm to 2400nm wavelength with 1 nm interval. Thedeuterium and halogen lamps were used for light source. Initially the base line correction was achieved by reference to air, and then graphene electrode sample were placing in the sample holder and kept the pristine FTO substrate in reference holder during measurements. The CoS nanoparticles implantation

on graphene by SILAR process was further confirmed using the optical transmittance spectroscopy.

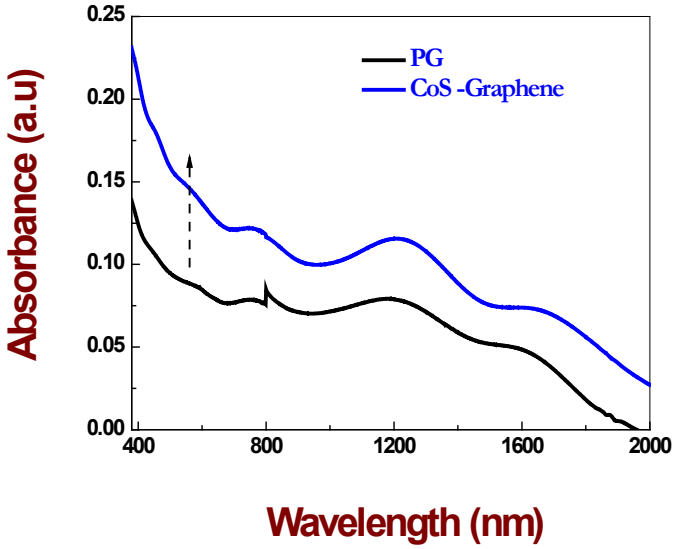


Figure 5.36: Optical Transmittance Spectroscopy of pristine and graphene-CoS hybrid electrodes from the visible to near infra-red regions.

Figure 5.36 shows the optical absorbance of the graphene-CoS hybrid film which is higher than the pristine graphene. The possible reason for the same is due to the CoS nanoparticles which exhibit the higher absorbance than the graphene. However, the absorbance in the near infra red regions is comparatively smaller than the visible spectrum regions which will further added advantage of this type of electrocatalytic electrodes for application in the IR based solar cells.

### 5.3.6 X-ray photoelectron spectroscopy

The electronic structure of the G-CoS interface was further characterized using X-ray photoelectron spectroscopy (XPS) exhibiting a broad peak in the binding energy range of

~779.5 - 782.5 eV attributable to cobalt (Co) $2p_{3/2}$ and confirming the presence of Co (II) and Co (III) species on the graphene film ( as shown in Figure 5.37a).


Figure 5.37: Illustrates X-Ray photoelectron spectra of CoS implanted graphene composite electrodes, (a) Cobalt Co2p peaks and (b) Sulfur S1s peaks.

Figure 5.38: X-ray Photoelectron Spectra of Carbon C1s peaks for pristine graphene and graphene-CoS hybrid film.

Similarly, Figure 5.37b represents the sulfur (S) $2p_{3/2}$ peaks at ~163.5. Since, CoS is a non-stoichiometric compound, we believe that inconsequential amount of $Co_xS_y$

(x=1, 2…4; y=1, 2, 3…9) compounds are formed which is based on a small peak shifts along with the appearance of additional peaks around ~166 - 172 eV. However, no change was found in the carbon peak (C1s) intensity and position in both the cases of PG and G-CoS as demonstrated in Figure 5.38.

### 5.3.7 Electrochemical characterizations

In order to elucidate the electro-catalytic behaviors of the G-CoS hybrid the electrochemical analysis was conducted by using symmetric cell configuration as described in section 3.4. Importantly, CoS NPs significantly improve the electro-catalytic properties of graphene electrode as could be evidenced from the Nyquist plot (Figure 5.39), polarization curve (Figure 5.40) and cyclic voltammogram (Figure 5.41).

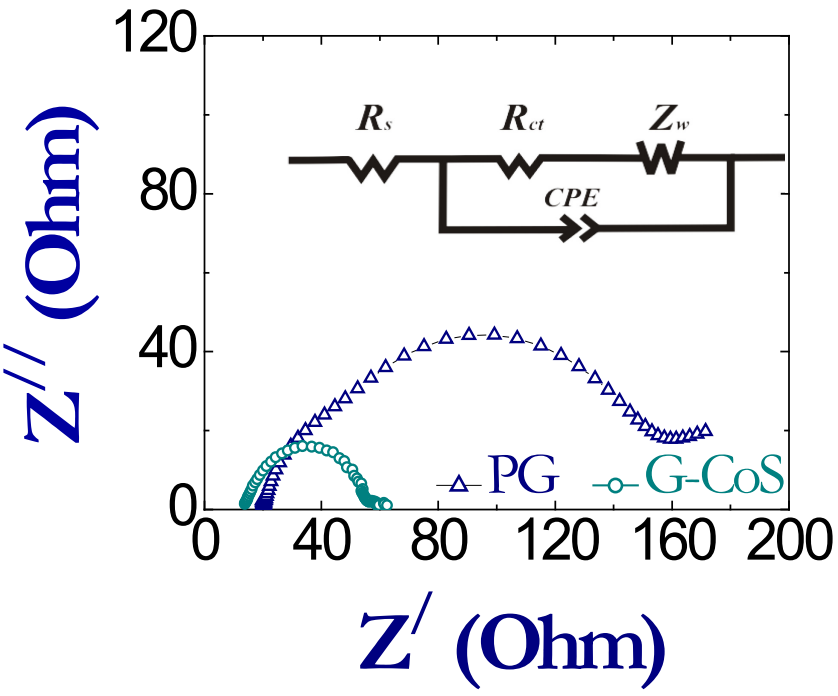


Figure 5.39: Nyquist spectra of PG and G-CoS counter electrode delinate substantial decrease of charge transfer resistance owing to CoS implantation in graphene film.

The Nyquist plot (as shown in Figure 5.39) manifests semi circle shift in PG towards the higher frequency owing to the catalytic effect of CoS NPs which drastically reduce the charge transfer resistance ($R_{ct}$) at graphene/electrolyte interfaces. Furthermore, CoS NPs in graphene film increases the electrode/electrolyte interfacial area which known as triple junction catalytic effect seems to be boosting the electron transfer from graphene electrode to electrolyte. On the other hand, CoS NPs may help facilitate the mass transport of redox carriers at graphene counter electrodes/electrolyte interfaces. This reflects on the reduction in Warburg resistance (W) of G-CoS hybrid electrode compare to the PG electrode (as shown in Table 5.7).

Here the reduction in Warburg impedance (W) implies that weak basal planes of PG are significantly modified upon inclusion of CoS NPs. In order to further testify this phenomenon, substantial evidences of G-CoS electro-catalytic activity are demonstrated in polarization curve (Figure 5.40). As shown in Figure 5.39, a sharp increase occurs in the slope of the G-CoS electrode owing to its increase in exchange current density ($J_0$) at the interface. Furthermore, Cyclic voltammogram of PG and G-CoS electrodes was carried out at 20$^{o}$C using electrolyte containing methoxypropionitrile solvent with 10 mM LiI, 1 mM $I_2$ and 0.1 M $LiClO_4$ under the scan rate of 50 $mVs^{-1}$ in an inert ($N_2$) atmosphere. As shown in Figure 5.41, a characteristic redox peak for G-CoS hybrid structure appears at -0.54 V which is attributed to the tri-iodide reduction reaction of $I_3^-$ $+2e \leftrightarrow 3I^-$. These results clearly indicate that the tri-iodide reduction kinetics is enhanced at the interface of G-CoS film.

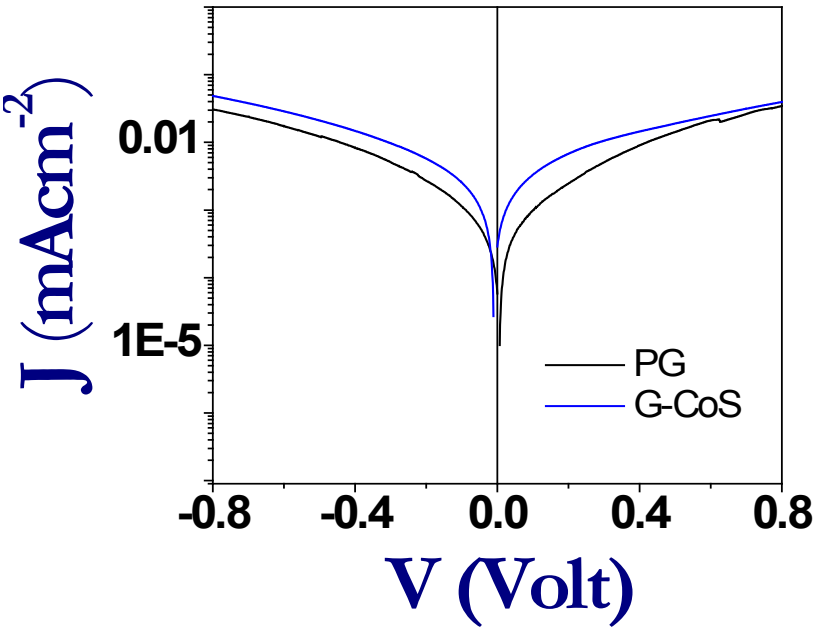


Figure 5.40: Polarization curves of PG and G-CoS under symmetric half cell configuration

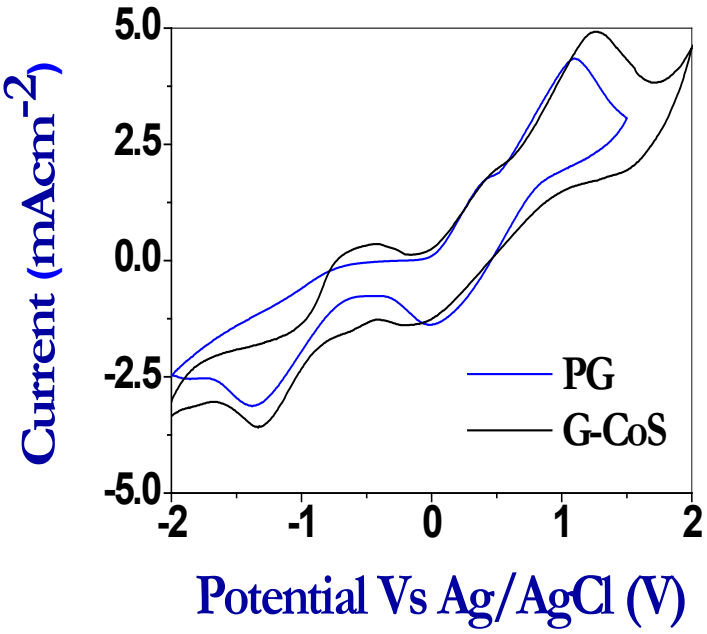


Figure 5.41: Cyclic voltammogram (CVs) of PG and G-CoS delineates the higher tri-iodide reduction capability of G-CoS owing to its faster electron transfer kinetics at the electrode/electrolyte interface compared to the PG.

### 5.3.8 DSSC full cell characterizations using graphene-CoS hybrid counter electrodes

The performance of G-CoS electrode is characterized in a test cell of DSSC (as shown in the schematic in the Figure 5.42) by employing two different electrodes of PG and G-CoS (Figure 5.43). The detail cell fabrication process and measurement conditions are delineated in "experimental chapter 3" section 3.5. We found short circuit current ($J_{SC}$) of graphene counter electrodes is improved by ~17% after anchoring CoS NPs on its surface as shown in Table 5.7. The improvement of $J_{sc}$ in G-CoS CE can be explained on basis of two successive phenomena occurred concurrently. Primarily, an increase in contact area of G-CoS CE/electrolyte than that of PG which creates triple junction catalytic area for electron transfer at electrode/electrolyte interface. Secondly, enhancing catalytic activity of graphene by CoS NPs for reducing tri-iodide to mono-iodide ($I_3^- + 2e^- \leftrightarrow 3I^-$), which is prevailing driving force for dye regeneration at the photo-anode counterpart**.**

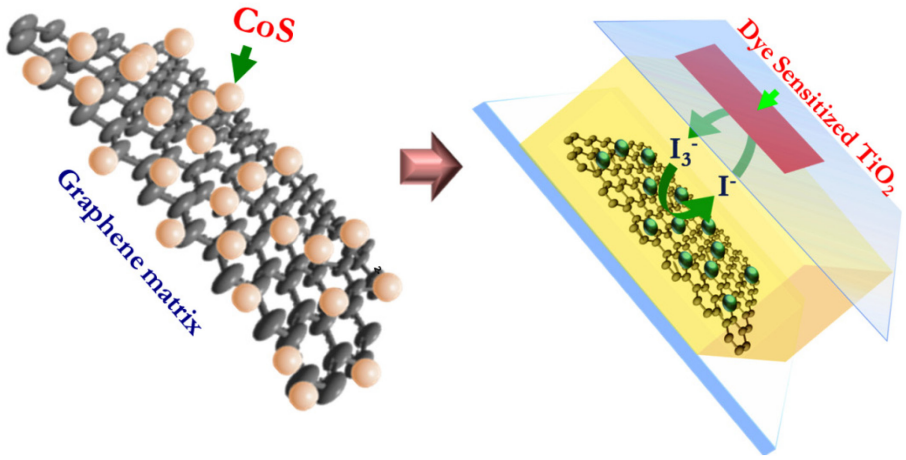


Figure 5.42: Schematic representing the assembly of graphene-CoS film counter electrode for DSSC.

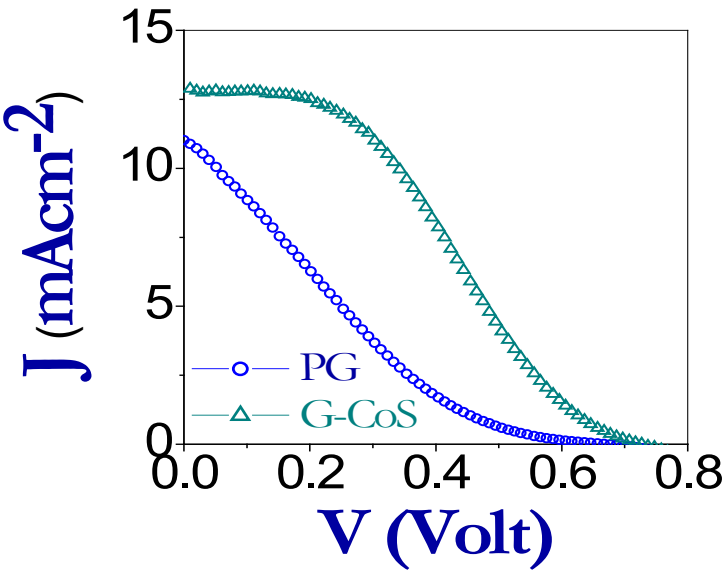


Figure 5.43: Current-density vs. voltage characteristics of DSSC consist of pristine graphene and graphene-CoS hybrid film.

Table 5.7: Photovoltaic and electrochemical parameters of dye sensitized solar cells and symmetric half cells with various counter electrodes.

| Counter Electrodes | $V_{OC}$ (V) | $J_{SC}$ (mAcm$^{-2}$) | FF (%) | η (%) | $R_{ct}$ (Ωcm$^{-2}$) | $J_0$ (mAcm$^{-2}$) | W (Ω) |
|---|---|---|---|---|---|---|---|
| PG | 0.67 | 11.0 | 17.1 | 1.27 | 16.3 | 0.77 | 171.6 |
| G-CoS | 0.72 | 12.8 | 36.4 | 3.42 | 5.05 | 2.50 | 53.67 |

In particular, a large improvement in fill factor (FF) is observed in G-CoS which are almost two times higher than the PG-DSSC, thus, doubling the efficiency of the G-COS-DSSC (as shown in Table 5.7). We believe that the increase in FF for G-CoS CE is attributed to both the improved catalytic activity by incorporation of CoS NPs and the electronic coupling between CoS NPs and underlying graphene film which forms an additional conducting pathway and accelerates electron transfer from CE to electrolyte. In other words, the lower $R_s$ value yields higher efficiency.

## 5.4. Graphene-CNT hybrid structure as field emission cathode

As described in the chapter 3 section 3.3.2 for transferring of the graphene-CNT hybrid film on to a adhesive Cu foil, the adhesive side of Cu foil (thickness ~100 μm) was placed on the top of the graphene-CNT substrate of area 5 mm x 13 mm by applying nominal pressures. Later, the tape was peeled off carefully in order to complete transfer of graphene-CNT hybrid structure on to the flexible Cu tape of area 5 mm x 13 mm. The resulting film was a top layer of vertically aligned CNT with a homogeneous bottom contact of a multilayered graphene film on a flexible copper foil as shown in the Figure 4.24. The transferred graphene-CNT film was used to study its flexible field emission behavior in AC bias, at different curvatures using another Cu foil as anode (as shown in schematic Figure 5.44a).

In order to measure the electron emission properties, field emission experiments were carried out in a parallel-plate diode configuration inside a field emission (FE) vacuum chamber of ~5 x $10^{-7}$ Torr vacuum level, with an inter-electrode distance (d) of ~1000 μm and using electrodes of surface area 5 mm x 13 mm. FE studies were performed after transferring the graphene-CNT structure on Cu foil and another Cu-foil was used as an anode. Electron emission was investigated under AC bias condition as a function of different curvatures of the devices and sufficient care was taken to keep the inter-electrode distance constant using a spacer while investigating FE as a function of curvatures. During the FE tests, an Agilent function generator (model 33220A), coupled with a Trek high voltage amplifier (model 20/20C) was used to generate the electric field, and the emission current was measured using a PEARSON current monitor (model 4100,

having 1.0 V/A), attached with an Agilent oscilloscope (model MSO6034A). Frequency of the sine-wave signal was kept at 400 Hz for all the tests.

Figure 5.44a-d illustrates the schematic of our flexible FE setup, effect of bending radius in electron emission, FN plots of each bending and FE stability data respectively. As could be observed from Figure 5.44b, with increasing curvature, turn-on field ($E_{TO}$, defined as field to produce 0.2 mA RMS emission current) shifts to higher values (from 0.8 V/μm for flat sample to 3.1 V/μm for the sample with sharpest bend) and the highest achievable emission current reduces from 4.2 mA for flat sample to 0.4 mA for the sample with sharpest bend respectively. This behavior suggests appearance of extra barriers to electron tunneling with higher bending. Presence of such barriers could also be related to the appearance of Fowler-Nordheim (F-N) plots, as shown in the Figure 5.44c. The emission current-voltage characteristics were interpreted using Fowler–Nordheim (F-N) equation as follows:

$$I = \left(\frac{aA\beta^2E^2}{\varphi}\right)\exp\left(-\frac{b\varphi^{\frac{3}{2}}}{\beta E}\right) \qquad (5.11)$$

*Where, $a=1.54x10^{-6}$ A eV $V^{-2}$ , $b=6.83x10^{7}$ eV $^{-3/2}$ V $cm^{-1}$, A is the emission area, $\beta$ is the field enhancement factor, E is the applied electric field in volt per centimeter and $\phi$ is the work function in electron volt.*

F-N plots show more deviation from linearity (expressed by lower degree of fit with a linear curve) with increasing bending of the flexible sample. The β value, calculated from the slope of the F-N plot, was found to be ~ 92347, 84508 and 23105 for different bending radius of FED of 0, 13.75 mm and 3.5 mm respectively. Higher resistivity of the graphene-CNT structure, with sharper bending could be related to this

kind of behavioral shift during field emission. Increasing resistivity imposes higher tunneling barrier to electrons, resulting to higher turn-on field and lower emission current.

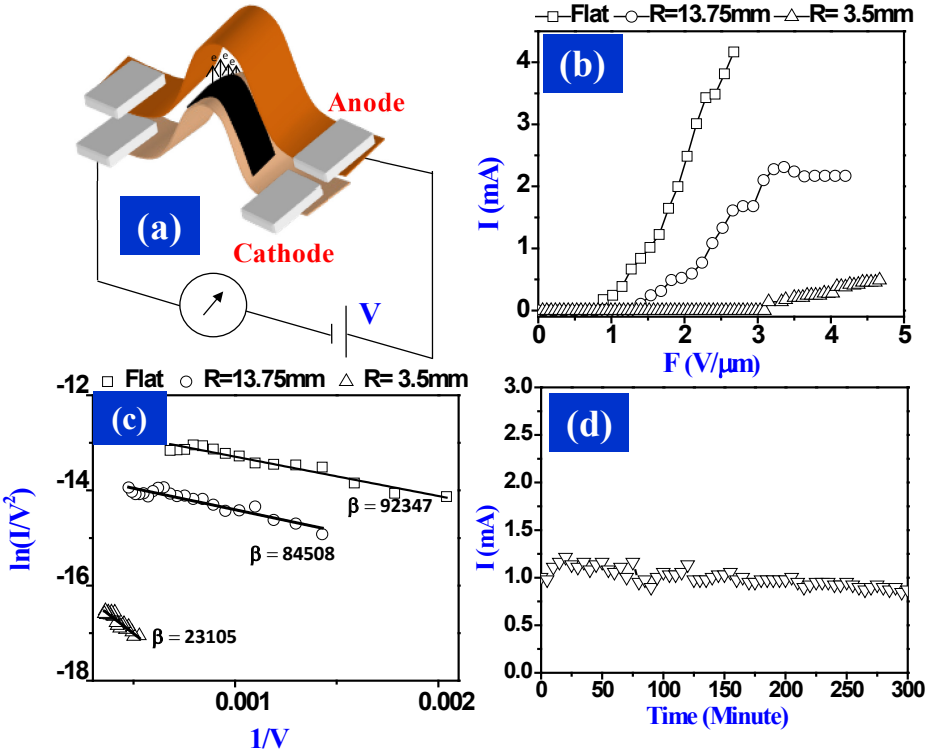


Figure 5.44: (a) Schematic representing the Flexible Field emission setup of graphene-CNT on Cu substrate (The black area representing the area of graphene-CNT hybrid structure transferred on Cu foil). Cu foil was also used as anode for the test. (b) Effect of bending on field emission response of graphene-CNT hybrid film on flexible Cu foil (c) FN plots of three consecutive bending (d) FE Stability test from the flat substrate.

Moreover, presence of extra tunneling barrier forces the nature of emission to be shifted from typical F-N behavior, as evident from deviation from linearity of F-N plots, with increasing curvature.[84] Stability of the field emission current from self-organized

graphene-CNT hybrid structure on a flat copper substrate is presented in Figure 5.44d and was found to be relatively stable for period of 5 hours, operated at an average emission current (RMS) of 1.4 mA. Difference between the initial and final emission current was observed to be negligible. It shows that the emission sources are quite stable, even when operated at higher operating fields and for longer duration. Such good stability of the structure at extreme operating conditions is beneficial for application of this hybrid film in practical devices.

**References**


1. Geim, A. K.; Novoselov, K. S., The rise of graphene. *Nat Mater* 2007, 6, 183-191.

2. Castro Neto, A. H.; Guinea, F.; Peres, N. M. R.; Novoselov, K. S.; Geim, A. K., The electronic properties of graphene. *Reviews of Modern Physics* 2009, 81, 109-162.

3. Geim, A. K., Graphene: Status and Prospects. *Science* 2009, 324, 1530-1534.

4. Geim, A. K.; Kim, P., Carbon wonderland. *Scientific American* 2008, 298, 90-97.

5. Novoselov, K. S.; Geim, A. K.; Morozov, S. V.; Jiang, D.; Katsnelson, M. I.; Grigorieva, I. V.; Dubonos, S. V.; Firsov, A. A., Two-dimensional gas of massless Dirac fermions in graphene. *Nature* 2005, 438, 197-200.

6. Novoselov, K. S.; Jiang, Z.; Zhang, Y.; Morozov, S. V.; Stormer, H. L.; Zeitler, U.; Maan, J. C.; Boebinger, G. S.; Kim, P.; Geim, A. K., Room-Temperature Quantum Hall Effect in Graphene. *Science* 2007, 315, 1379-1379.

7. Novoselov, K. S.; Geim, A. K.; Morozov, S. V.; Jiang, D.; Zhang, Y.; Dubonos, S. V.; Grigorieva, I. V.; Firsov, A. A., Electric field effect in atomically thin carbon films. *Science* 2004, 306, 666-669.

8. Kozlov, S. M.; Viñes, F.; Görling, A., Bandgap Engineering of Graphene by Physisorbed Adsorbates. *Advanced Materials* 2011, 23, 2638-2643.

9. Balandin, A. A.; Ghosh, S.; Nika, D. L.; Pokatilov, E. P., Thermal Conduction in Suspended Graphene Layers. *Fullerenes Nanotubes and Carbon Nanostructures* 2010, 18, 474-486.

10. Bi, H.; Huang, F.; Liang, J.; Xie, X.; Jiang, M., Transparent Conductive Graphene Films Synthesized by Ambient Pressure Chemical Vapor Deposition Used as the Front Electrode of CdTe Solar Cells. *Advanced Materials* 2011, 23, 3202-3206.

11. Wang, X.; Zhi, L. J.; Mullen, K., Transparent, conductive graphene electrodes for dye-sensitized solar cells. *Nano Letters* 2008, 8, 323-327.

12. Schwierz, F., Graphene transistors. *Nat Nano* 2010, 5, 487-496.

13. Chen, S. Q.; Wang, Y., Microwave-assisted synthesis of a Co3O4-graphene sheet-on-sheet nanocomposite as a superior anode material for Li-ion batteries. *Journal of Materials Chemistry* 2010, 20, 9735-9739.

14. Pollak, E.; Geng, B. S.; Jeon, K. J.; Lucas, I. T.; Richardson, T. J.; Wang, F.; Kostecki, R., The Interaction of Li+ with Single-Layer and Few-Layer Graphene. *Nano Letters* 2010, 10, 3386-3388.

15. Zhu, Y.; Murali, S.; Stoller, M. D.; Ganesh, K. J.; Cai, W.; Ferreira, P. J.; Pirkle, A.; Wallace, R. M.; Cychosz, K. A.; Thommes, M.; Su, D.; Stach, E. A.; Ruoff, R. S., Carbon-Based Supercapacitors Produced by Activation of Graphene. *Science* 2011, 332, 1537-1541.

16. Yan, J.; Wei, T.; Qiao, W. M.; Shao, B.; Zhao, Q. K.; Zhang, L. J.; Fan, Z. J., Rapid microwave-assisted synthesis of graphene nanosheet/Co3O4 composite for supercapacitors. *Electrochimica Acta* 2010, 55, 6973-6978.

17. Li, F.; Song, J.; Yang, H.; Gan, S.; Zhang, Q.; Han, D.; Ivaska, A.; Niu, L., One-step synthesis of graphene/$SnO_2$ nanocomposites and its application in electrochemical supercapacitors. *Nanotechnology* 2009, 20, doi:10.1088/0957-4484/20/45/455602.

18. Wang, Y.; Shi, Z.; Huang, Y.; Ma, Y.; Wang, C.; Chen, M.; Chen, Y., Supercapacitor Devices Based on Graphene Materials. *The Journal of Physical Chemistry C* 2009, 113, 13103-13107.

19. Li, X.; Zhu, H.; Wang, K.; Cao, A.; Wei, J.; Li, C.; Jia, Y.; Li, Z.; Li, X.; Wu, D., Graphene-On-Silicon Schottky Junction Solar Cells. *Advanced Materials* 2010, 22, 2743-2748.

20. Lin, T.; Huang, F.; Liang, J.; Wang, Y., A facile preparation route for boron-doped graphene, and its CdTe solar cell application. *Energy & Environmental Science* 2011, 4, 862-865.

21. De Arco, L. G.; Zhang, Y.; Schlenker, C. W.; Ryu, K.; Thompson, M. E.; Zhou, C. W., Continuous, Highly Flexible, and Transparent Graphene Films by Chemical Vapor Deposition for Organic Photovoltaics. *Acs Nano* 2010, 4, 2865-2873.

22. Li, S. S.; Tu, K. H.; Lin, C. C.; Chen, C. W.; Chhowalla, M., Solution-Processable Graphene Oxide as an Efficient Hole Transport Layer in Polymer Solar Cells. *Acs Nano* 2010, 4, 3169-3174.

23. Kavan, L.; Yum, J. H.; Grätzel, M., Optically Transparent Cathode for Dye-Sensitized Solar Cells Based on Graphene Nanoplatelets. *ACS Nano* 2010, 5, 165-172.

24. Verma, V. P.; Das, S.; Lahiri, I.; Choi, W., Large-area graphene on polymer film for flexible and transparent anode in field emission device. *Applied Physics Letters* 2010, 96, 203108-1-3.

25. Bae, S.; Kim, H.; Lee, Y.; Xu, X. F.; Park, J. S.; Zheng, Y.; Balakrishnan, J.; Lei, T.; Kim, H. R.; Song, Y. I.; Kim, Y. J.; Kim, K. S.; Ozyilmaz, B.; Ahn, J. H.; Hong, B. H.; Iijima, S., Roll-to-roll production of 30-inch graphene films for transparent electrodes. *Nature Nanotechnology* 2010, 5, 574-578.

26. Roy-Mayhew, J. D.; Bozym, D. J.; Punckt, C.; Aksay, I. A., Functionalized Graphene as a Catalytic Counter Electrode in Dye-Sensitized Solar Cells. *ACS Nano* 2010, 4, 6203-6211.

27. Hasin, P.; Alpuche-Aviles, M. A.; Wu, Y., Electrocatalytic Activity of Graphene Multilayers toward−/I3−: Effect of Preparation Conditions and Polyelectrolyte Modification. *The Journal of Physical Chemistry C* 2010, 114, 15857-15861.

28. O'Regan, B.; Gratzel, M., A low-cost, high-efficiency solar cell based on dye-sensitized colloidal TiO2 films. *Nature* 1991, 353, 737-740.

29. Grätzel, M., Dye-sensitized solar cells. *Journal of Photochemistry and Photobiology C: Photochemistry Reviews* 2003, 4, 145-153.

30. Wang, M. K.; Anghel, A. M.; Marsan, B.; Ha, N. L. C.; Pootrakulchote, N.; Zakeeruddin, S. M.; Gratzel, M., CoS Supersedes Pt as Efficient Electrocatalyst for Triiodide Reduction in Dye-Sensitized Solar Cells. *Journal of the American Chemical Society* 2009, 131, 15976-15977.

31. Liu, H.; Liu, Y.; Zhu, D., Chemical doping of graphene. *Journal of Materials Chemistry* 2011, 21, 3335-3345.

32. Chen, W.; Chen, S.; Qi, D. C.; Gao, X. Y.; Wee, A. T. S., Surface transfer p-type doping of epitaxial graphene. *Journal of the American Chemical Society* 2007, 129, 10418-10422.

33. Cheng, Y. C.; Schwingenschlogl, U., A route to strong p-doping of epitaxial graphene on SiC. *Applied Physics Letters* 2010, 97, 3, doi.org/10.1063/1.3515848.

34. Medina, H.; Lin, Y.-C.; Obergfell, D.; Chiu, P.-W., Tuning of Charge Densities in Graphene by Molecule Doping. *Advanced Functional Materials* 2011, 21, 2687-2692.

35. Shi, Y.; Kim, K. K.; Reina, A.; Hofmann, M.; Li, L.-J.; Kong, J., Work Function Engineering of Graphene Electrode via Chemical Doping. *ACS Nano* 2010, 4, 2689-2694.

36. Gunes, F.; Shin, H. J.; Biswas, C.; Han, G. H.; Kim, E. S.; Chae, S. J.; Choi, J. Y.; Lee, Y. H., Layer-by-Layer Doping of Few-Layer Graphene Film. *Acs Nano* 2010, 4, 4595-4600.

37. Das, S.; Sudhagar, P.; Verma, V.; Song, D.; Ito, E.; Lee, S. Y.; Kang, Y. S.; Choi, W., Amplifying Charge-Transfer Characteristics of Graphene for TriiodideReduction in Dye-Sensitized Solar Cells. *Advanced Functional Materials* 2011, 21, 3729–3736.

38. Paulo, V. C. M.; et al., A DFT study of halogen atoms adsorbed on graphene layers. *Nanotechnology* 2010, 21, 485701, doi:10.1088/0957-4484/21/48/485701.

39. Jung, N.; Kim, N.; Jockusch, S.; Turro, N. J.; Kim, P.; Brus, L., Charge Transfer Chemical Doping of Few Layer Graphenes: Charge Distribution and Band Gap Formation. *Nano Letters* 2009, 9, 4133-4137.

40. Jhi, S.-H.; Louie, S. G.; Cohen, M. L., Electronic properties of bromine-doped carbon nanotubes. *Solid State Communications* 2002, 123, 495-499.

41. Jia, Y.; Cao, A. Y.; Bai, X.; Li, Z.; Zhang, L. H.; Guo, N.; Wei, J. Q.; Wang, K. L.; Zhu, H. W.; Wu, D. H.; Ajayan, P. M., Achieving High Efficiency Silicon-Carbon Nanotube Heterojunction Solar Cells by Acid Doping. *Nano Letters* 2011, 11, 1901-1905.

42. Zhan, D.; Sun, L.; Ni, Z. H.; Liu, L.; Fan, X. F.; Wang, Y.; Yu, T.; Lam, Y. M.; Huang, W.; Shen, Z. X., FeCl3-Based Few-Layer Graphene Intercalation Compounds: Single Linear Dispersion Electronic Band Structure and Strong Charge Transfer Doping. *Advanced Functional Materials* 2010, 20, 3504-3509.

43. Zhou, W.; Vavro, J.; Nemes, N. M.; Fischer, J. E.; Borondics, F.; Kamar; aacute; s, K.; Tanner, D. B., Charge transfer and Fermi level shift in p -doped single-walled carbon nanotubes. *Physical Review B* 2005, 71, 205423.

44. Fischer, J. E., Chemical Doping of Single-Wall Carbon Nanotubes. *Accounts of Chemical Research* 2002, 35, 1079-1086.

45. Kavan, L.; Rapta, P.; Dunsch, L.; Bronikowski, M. J.; Willis, P.; Smalley, R. E., Electrochemical Tuning of Electronic Structure of Single-Walled Carbon Nanotubes: In-

situ Raman and Vis-NIR Study. *The Journal of Physical Chemistry B* 2001, 105, 10764-10771.

46. Hallam, P. M.; Banks, C. E., Quantifying the electron transfer sites of graphene. *Electrochemistry Communications* 2011, 13, 8-11.

47. Banks, C. E.; Davies, T. J.; Wildgoose, G. G.; Compton, R. G., Electrocatalysis at graphite and carbon nanotube modified electrodes: edge-plane sites and tube ends are the reactive sites. *Chemical Communications* 2005, 829-841.

48. Davies, T. J.; Hyde, M. E.; Compton, R. G., Nanotrench Arrays Reveal Insight into Graphite Electrochemistry. *Angewandte Chemie International Edition* 2005, 44, 5121-5126.

49. Davies, T.; Banks, C.; Compton, R., Voltammetry at spatially heterogeneous electrodes. *Journal of Solid State Electrochemistry* 2005, 9, 797-808-808.

50. Hasin, P.; Alpuche-Aviles, M. A.; Wu, Y. Y., Electrocatalytic Activity of Graphene Multi layers toward I-/I-3(-): Effect of Preparation Conditions and Polyelectrolyte Modification. *Journal of Physical Chemistry C* 2010, 114, 15857-15861.

51. Delhaes, P., *Graphite and precursors*. Gordon & Breach: Australia, 2001; p xiv, 297 p.

52. Kou, R.; Shao, Y.; Mei, D.; Nie, Z.; Wang, D.; Wang, C.; Viswanathan, V. V.; Park, S.; Aksay, I. A.; Lin, Y.; Wang, Y.; Liu, J., Stabilization of Electrocatalytic Metal Nanoparticles at Metal−Metal Oxide−Graphene Triple Junction Points. *Journal of the American Chemical Society* 2011, 133, 2541-2547.

53. Li, Y.; Wang, H.; Xie, L.; Liang, Y.; Hong, G.; Dai, H., MoS2 Nanoparticles Grown on Graphene: An Advanced Catalyst for the Hydrogen Evolution Reaction. *Journal of the American Chemical Society* 2011, 133, 7296-7299.

54. Wang, H.; Cui, L.-F.; Yang, Y.; Sanchez Casalongue, H.; Robinson, J. T.; Liang, Y.; Cui, Y.; Dai, H., Mn3O4−Graphene Hybrid as a High-Capacity Anode Material for Lithium Ion Batteries. *Journal of the American Chemical Society* 2010, 132, 13978-13980.

55. Wang, H.; Casalongue, H. S.; Liang, Y.; Dai, H., Ni(OH)2 Nanoplates Grown on Graphene as Advanced Electrochemical Pseudocapacitor Materials. *Journal of the American Chemical Society* 2010, 132, 7472-7477.

56. Grigorian, L.; Williams, K. A.; Fang, S.; Sumanasekera, G. U.; Loper, A. L.; Dickey, E. C.; Pennycook, S. J.; Eklund, P. C., Reversible Intercalation of Charged Iodine Chains into Carbon Nanotube Ropes. *Physical Review Letters* 1998, 80, 5560.

57. Hallam, P. M.; Banks, C. E., Quantifying the electron transfer sites of graphene. *Electrochemistry Communications* In Press, Corrected Proof.

58. Yang, R.; Zhang, L.; Wang, Y.; Shi, Z.; Shi, D.; Gao, H.; Wang, E.; Zhang, G., An Anisotropic Etching Effect in the Graphene Basal Plane. *Advanced Materials* 2010, 22, 4014-4019.

59. Casiraghi, C.; Pisana, S.; Novoselov, K. S.; Geim, A. K.; Ferrari, A. C., Raman fingerprint of charged impurities in graphene. *Applied Physics Letters* 2007, 91, 233108 1-3.

60. Ni, Z. H.; Wang, Y. Y.; Yu, T.; Shen, Z. X., Raman Spectroscopy and Imaging of Graphene. *Nano Research* 2008, 1, 273-291.

61. Stankovich, S.; Dikin, D. A.; Piner, R. D.; Kohlhaas, K. A.; Kleinhammes, A.; Jia, Y.; Wu, Y.; Nguyen, S. T.; Ruoff, R. S., Synthesis of graphene-based nanosheets via chemical reduction of exfoliated graphite oxide. *Carbon* 2007, 45, 1558-1565.

62. Kavan, L.; Yum, J. H.; Grätzel, M., Optically Transparent Cathode for Dye-Sensitized Solar Cells Based on Graphene Nanoplatelets. *ACS Nano* 2010, 5, 165–172.

63. Das, S.; Sudhagar, P.; Verma, V.; Song, D.; Ito, E.; Lee, S. Y.; Kang, Y. S.; Choi, W., Amplifying Charge-Transfer Characteristics of Graphene for Triiodide Reduction in Dye-Sensitized Solar Cells. *Advanced Functional Materials* 2011, 21, 3729-3736.

64. Bard, A. J.; Faulkner, L. R., *Electrochemical methods : fundamentals and applications*. 2nd ed.; John Wiley: New York, 2000; p xxi, 833 p.

65. Kasry, A.; Kuroda, M. A.; Martyna, G. J.; Tulevski, G. S.; Bol, A. A., Chemical Doping of Large-Area Stacked Graphene Films for Use as Transparent, Conducting Electrodes. *ACS Nano* 2010, 4, 3839-3844.

66. Geng, H.-Z.; Kim, K. K.; Song, C.; Xuyen, N. T.; Kim, S. M.; Park, K. A.; Lee, D. S.; An, K. H.; Lee, Y. S.; Chang, Y.; Lee, Y. J.; Choi, J. Y.; Benayad, A.; Lee, Y. H., Doping and de-doping of carbon nanotube transparent conducting films by dispersant and chemical treatment. *Journal of Materials Chemistry* 2008, 18, 1261-1266.

67. Dresselhaus, M. S.; Dresselhaus, G., Intercalation compounds of graphite. *Advances in Physics* 2002, 51, 1-186.

68. Sorokina, N. E.; Maksimova, N. V.; Avdeev, V. V., Anodic Oxidation of Graphite in 10 to 98% $HNO_3$. *Inorganic Materials* 2001, 37, 360-365-365.

69. Sorokina, N. E.; Mudretsova, S. N.; Maiorova, A. F.; Avdeev, V. V.; Maksimova, N. V., Thermal Properties of Graphite Intercalation Compounds with $HNO_3$. *Inorganic Materials* 2001, 37, 153-156-156.

70. Dresselhaus, M. S.; Jorio, A.; Hofmann, M.; Dresselhaus, G.; Saito, R., Perspectives on Carbon Nanotubes and Graphene Raman Spectroscopy. *Nano Letters* 2010, 10, 751-758.

71. Kudin, K. N.; Ozbas, B.; Schniepp, H. C.; Prud'homme, R. K.; Aksay, I. A.; Car, R., Raman spectra of graphite oxide and functionalized graphene sheets. *Nano Letters* 2008, 8, 36-41.

72. Das, A.; Chakraborty, B.; Sood, A. K., Raman spectroscopy of graphene on different substrates and influence of defects. *Bulletin of Materials Science* 2008, 31, 579-584.

73. Ferrari, A. C.; Meyer, J. C.; Scardaci, V.; Casiraghi, C.; Lazzeri, M.; Mauri, F.; Piscanec, S.; Jiang, D.; Novoselov, K. S.; Roth, S.; Geim, A. K., Raman Spectrum of Graphene and Graphene Layers. *Physical Review Letters* 2006, 97, 187401.

74. Yang, D.; Velamakanni, A.; Bozoklu, G.; Park, S.; Stoller, M.; Piner, R. D.; Stankovich, S.; Jung, I.; Field, D. A.; Ventrice Jr, C. A.; Ruoff, R. S., Chemical analysis of graphene oxide films after heat and chemical treatments by X-ray photoelectron and Micro-Raman spectroscopy. *Carbon* 2009, 47, 145-152.

75. Fillaux, F.; Menu, S.; Conard, J.; Fuzellier, H.; Parker, S. W.; Hanon, A. C.; Tomkinson, J., Inelastic neutron scattering study of the proton dynamics in $HNO_3$ graphite intercalation compounds. *Chemical Physics* 1999, 242, 273-281.

76. Ishii, H.; Sugiyama, K.; Ito, E.; Seki, K., Energy Level Alignment and Interfacial Electronic Structures at Organic/Metal and Organic/Organic Interfaces. *Advanced Materials* 1999, 11, 605-625.

77. Park, J.; Lee, W. H.; Huh, S.; Sim, S. H.; Kim, S. B.; Cho, K.; Hong, B. H.; Kim, K. S., Work-Function Engineering of Graphene Electrodes by Self-Assembled Monolayers for High-Performance Organic Field-Effect Transistors. *The Journal of Physical Chemistry Letters* 2011, 2, 841-845.

78. Vivekanandan, K.; Selvasekarapandian, S.; Kolandaivel, P., Raman and FT-IR studies of Pb4(NO3)2(PO4)2·2H2O crystal. *Materials Chemistry and Physics* 1995, 39, 284-289.

79. Zistler, M.; Wachter, P.; Wasserscheid, P.; Gerhard, D.; Hinsch, A.; Sastrawan, R.; Gores, H. J., Comparison of electrochemical methods for triiodide diffusion coefficient measurements and observation of non-Stokesian diffusion behaviour in binary mixtures of two ionic liquids. *Electrochimica Acta* 2006, 52, 161-169.

80. Sudhagar, P.; Nagarajan, S.; Lee, Y.-G.; Song, D.; Son, T.; Cho, W.; Heo, M.; Lee, K.; Won, J.; Kang, Y. S., Synergistic Catalytic Effect of a Composite

(CoS/PEDOT:PSS) Counter Electrode on Triiodide Reduction in Dye-Sensitized Solar Cells. *ACS Applied Materials & Interfaces* 2011, 3, 1838-1843.

81. Sidik, R. A.; Anderson, A. B., Co9S8 as a Catalyst for Electroreduction of O2: Quantum Chemistry Predictions. *The Journal of Physical Chemistry B* 2005, 110, 936-941.

82. Y.F, N., Solution deposition of thin solid compound films by a successive ionic-layer adsorption and reaction process. *Applications of Surface Science* 1985, 22-23, Part 2, 1061-1074.

83. Englert, J. M. E. J. M.; Dotzer, C.; Yang, G. A.; Schmid, M.; Papp, C.; Gottfried, J. M.; Steinruck, H. P.; Spiecker, E.; Hauke, F.; Hirsch, A., Covalent bulk functionalization of graphene. *Nature Chemistry* 2011, 3, 279-286.

84. Zhang, J.; Yang, C.; Yang, W.; Feng, T.; Wang, X.; Liu, X., Appearance of a knee on the Fowler-Nordheim plot of carbon nanotubes on a substrate. *Solid State Communications* 2006, 138, 13-16.

CHAPETR 6

## SUMMARY

Large-area graphene and graphene-CNT hybrid structure synthesis are demonstrated by high temperature, thermal chemical vapor deposition (CVD) technique using different transition metals catalysts like Cu, Ni and Fe etc. Graphene growth on Cu and Ni surfaces has been carried out using CVD of methane ($CH_4$) at high temperature. We optimized graphene growth as large as 15 cm x 6 cm on Cu foil and transferred it to a transparent flexible polymer e.g. polyethylene tetrapthalate (PET). Different transfer process, like hot press lamination technique, chemical wet process has been developed to transfer graphene on several other surfaces like PET, parylene, $SiO_2$/Si, glass etc. Structural characterizations of graphene are carried out using Scanning electron microscopy, high resolution transmission electron microscopy (HRTEM), and Raman spectroscopy. From SEM observation, we found that graphene grown on Cu is overlapping multilayered structure which covered the Cu grain and grain boundaries. However, there were no systematic graphene growth pattern was found that can have a direct correlation with the Cu grain and grain boundaries. HRTEM and Raman spectroscopy revealed that there were 4-5 layers graphene growth on the Cu and Ni surface, with subsequent lattice mismatch with its substrates. Graphene surface topography is carried out using atomic force microscopy (AFM) and found that the surface is atomically smooth and the step height of the graphene film on cleaved mica is 2.7 nm which further testified the 4-5 layers graphene successfully transferred on the mica surface. We also observed that the free standing graphene's Raman response is quite

different than the graphene on different substrates which is due to the substantial phonon scattering at the graphene-substrate interface. Furthermore, we characterize graphene on different substrates and found that graphene on metals exhibits comparatively higher Raman intensity than the graphene on dielectrics.

Graphene on FTO glass was functionalized with $F^-$ ion by $CF_4$ plasma treatment for replacing platinum in cathode part of dye sensitized solar cells (DSSCs). $CF_4$ reactive-ion treated graphene shows promising electrocatalytic activity toward tri-iodide reduction while maintaining its conductivity and transparency. The electrochemical studies illustrate that charge-transfer resistance decreases and exchange-current density increases with controlled plasma treatment time for graphene-based electrodes. We believe that an increase in exchange-current density, as well as the decrease in charge-transfer resistance, may be attributed to the faster tri-iodide reduction kinetics occurring at the fluorinated graphene counter-electrode/electrolyte interface. Therefore, we suggest that the $CF_4$ plasma-treatment approach is suited for tailoring electron-transfer sites in graphene under controlled C–F covalent bond formation.

On the other hand, we explored the chemical doping of p-type donors ($HNO_3$) in graphene lattice. The structural and charge transfer characteristics of pristine graphene (PG) and $HNO_3$ doped graphene (HDG) were studied and discussed using X-ray photoelectron spectroscopy. It is affirm that different C-H, C(O)OH and $NO_3^-$ moieties were covalently attached with carbon atoms through $sp^2$-$sp^3$ hybridization which play an important role in the shift of graphenes' Fermi levels with doping concentration, from 4.52 to 5.31 eV. DSSC comprising of HDG counter electrodes exhibited three times higher photo-conversion efficiency than PG electrodes, which we believe is due to the

improvement of the in-plane charge transfer of basal planes and further fortifies the electro-catalytic activity of $HNO_3$ doped graphene.

Furthermore, large scale Graphene-CoS (G-CoS) hybrid electrode was synthesized using successive ionic layer absorption and reaction (SILAR) that is a simple and scalable process which can easily adapted for a large scale solar cells The CoS deposition onto graphene reduced charge transfer resistance and enhanced exchange current density at the electrode-electrolyte interfaces, results in 3 times higher efficiency than PG in DSSC cell. Deposition of CoS NPs on graphene film is an unambiguous evidence of enhancement of its higher electro-catalytic behavior towards iodine reduction which is attributed to creation of active electrode/electrolyte triple junction interfaces. In this context, control over the charge diffusivity of redox species at the graphene counter electrode, and surface charge transfer resistance by the different doping and composite electrodes offers enormous new insights of catalytic electrode development opportunities for electro catalytic devices.

Finally, we also synthesized in-situ self-organized graphene-CNT hybrid film by thermal CVD technique and its characterization. The structure is unique as it contains graphene top layer connecting to vertical CNT at the bottom. The hybrid film can easily be transferred to various polymer substrates, including PDMS, adhesive polymer tapes and flexible metal foils. The film exhibits excellent electro-mechanical properties demonstrating a distinguishable variation of electrical conductivity for both under tension and compression. Furthermore, controllable field emission currents with respect to

bending radius has been demonstrated and would be of great utility for future flexible field emission cathode.

CHAPETR 7

# SCOPE OF FUTURE WORKS

Graphene is a recently invented material which shows the distinctive electronics properties based on its unique band structures, density of states (DOS), number of layers and surface defects. In fact, graphene exhibit semi-metallic behavior due to its k and $k^{/}$ point touches each other at the brillouin zone; hence exhibit high charge carrier concentration and mobility which is highly beneficial for the ultrafast transistor application with high on and off ratio. However, the large scale graphene patterning and its applications for ultrafast transistors is still unexplored. On the other hand controlling charge carrier concentrations in graphene and their mobility is still a bigger challenge as there were surface atomic density is limited in the graphene.

When consecutive layer increases, graphene's semi-metallic property converts to semiconducting and then to metallic which strictly depends upon the number of graphene stacking layers on it. Graphene also shows its extraordinary conductivity, however due to the lower atomic density, the controlling resistivity is highly restrictive. Introducing doping in the graphene lattice and controlling its resistivity/conductivity is still a challenge at this moment and need to explore vigorously. On the other hand, graphenes' optical transparency is another layer dependent property which increases with decreasing graphene no of layers whereas resistivity decreases with increasing number of layers. In this context, high transparent graphene with low resistivity will need to optimize for future potential transparent conducting oxide for replacing toxic and fragile ITO and

FTO. It would highly in demand this type of graphene transparent conducting electrodes for potential future applications in flexible electronics and solar cells.

Due to their high surface area graphene also exhibit a potential transparent electro-catalytic material for different electro-catalytic devices, e.g. dye sensitized solar cells. To date Pt is the only highest performance electro-catalytic metal electrode possesses electro-catalytic redox reactions at its surface. Owing to its cost issue and potential scarcity researchers are still looking for a good alternative for platinum. Although graphene exhibit very low resistivity, electro-catalytic activities of graphene are not yet explored. In particular, these restrictions arise as graphene exhibits less number of electro-catalytic sites for charge transfer that could be controlled by different molecular doping and their concentrations. Controlling molecular doping concentrations, is still a challenge as doping causes some structural damages in the graphene lattice. Conversely, doping shifts the Fermi level and work function of graphene that is one of the prime focuses of this thesis. However, controlled doping and change in work function with high stability is needed to explore for future electronics and electro-catalytic devices.

Finally, graphene is a 2D structure; therefore when get contacted with 3D metals exhibit different electronics density of states and electronics transport at the interface. Uniform ohmic contact between graphene and metal has not been studied yet systematically in order to solve these existing critical issues. Therefore, electron transfer from graphene to metal is comparatively sluggish due to the mismatch of their 2D and 3D DOS respectively. Similarly, due to the anomalous interface there is a strong band bending at the vicinity of the metal–graphene junction which hampers the efficient photocurrent generation in graphene based optoelectronics devices. Therefore, graphene-

electrodes contact issues need to be solved in order to achieve low loss, energy efficient high performances electronics devices.

## APPENDIX

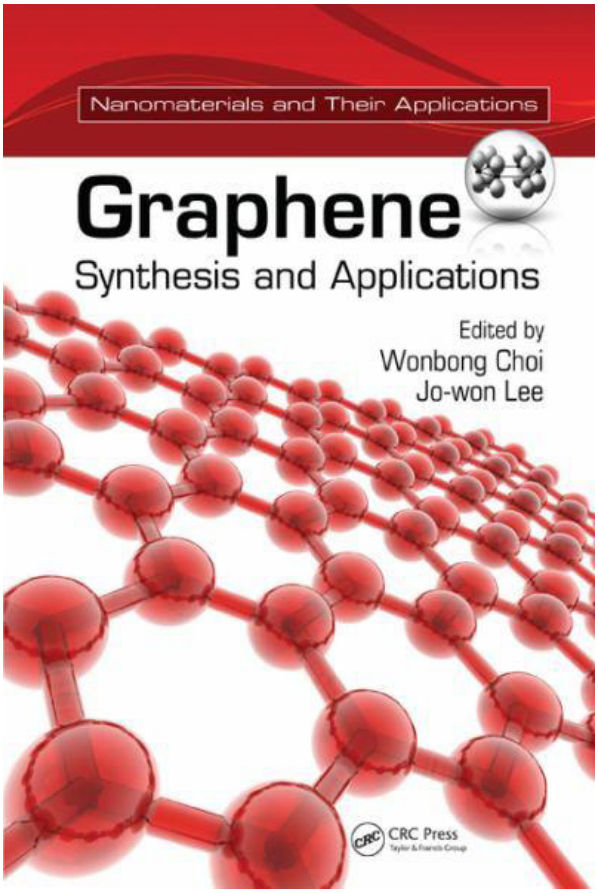


# 2 Graphene Synthesis

*Santanu Das and Wonbong Choi*

CONTENTS

ADVANCED FUNCTIONAL MATERIALS
www.afm-journal.de



# Amplifying Charge-Transfer Characteristics of Graphene for Triiodide Reduction in Dye-Sensitized Solar Cells

*Santanu Das, P. Sudhagar, Ved Verma, Donghoon Song, Eisuke Ito, Sang Yun Lee, Yong Soo Kang* and WonBong Choi**

**The fabrication and functionalization of large-area graphene and its electrocatalytic properties for iodine reduction in a dye-sensitized solar cell are reported. The graphene film, grown by thermal chemical vapor deposition, contains three to five layers of monolayer graphene, as confirmed by Raman spectroscopy and high-resolution transmission electron microscopy. Further, the graphene film is treated with $CF_4$ reactive-ion plasma and fluorine ions are successfully doped into graphene as confirmed by X-ray photoelectron spectroscopy and UV-photoemission spectroscopy. The fluorinated graphene shows no structural deformations compared to the pristine graphene except an increase in surface roughness. Electrochemical characterization reveals that the catalytic activity of graphene for iodine reduction increases with increasing plasma treatment time, which is attributed to an increase in catalytic sites. Further, the fluorinated graphene is characterized in use as a counter-electrode in a full dye-sensitized solar cell and shows ca. 2.56% photon to electron conversion efficiency with ca. 11 mA $cm^{-2}$ current density. The shift in work function in $F^-$ doped graphene is attributed to the shift in graphene redox potential which results in graphene's electrocatalytic-activity enhancement.**

## 1. Introduction

Graphene is a recently discovered 2D material exhibiting unique properties, such as high carrier mobility, good mechanical properties, high transparency, and excellent thermal conductivity.[1,2] To date, considerable research has been performed to demonstrate applications of graphene in transistors, transparent electrodes, optical devices, supercapacitors, solar cells, etc.[1,3,4] In particular, application in solar cells with enhanced efficiency is of great interest.[3,5–7] Graphene exhibits remarkable transparency in the entire solar spectrum from the infrared (IR) to the ultraviolet (UV) region, which is an added advantage for its application in high-efficiency solar cells.[3,8,9] In addition, graphene has been exploited to fabricate flexible electrodes by using several facile and scalable methods.[8,10] This versatile transformation remains promising for development of light-weight flexible electronics and solar cells.[8,10,11] In this context, applications of graphene are anticipated to offer enticing possibilities in flexible, conducting counter-electrodes for dye-sensitized solar cells (DSSCs), with enhanced triiodide reduction. In DSSCs, the counter-electrode (CE) is an indispensable component which injects electrons into the electrolyte to catalyze iodine reduction ($I_3^-$ to $I^-$) after charge injection from the photooxidized dye.[12,13] The electrocatalytic reduction of $I_3^-$ to $I^-$ at the CE dictates the cathodic activity of DSSCs and influences current generation at the photoanode counterpart through dye regeneration.[13–15] In this context, the high surface area of a 2D graphene sheet (2630 $m^2 g^{-1}$), in addition to its intrinsic high transmittance and charge mobility, provides great versatility as a counter-electrode in DSSCs.

Apart from these functionalities, enhanced chemical reactivity of graphene is indispensable for its use as a CE for DSSCs, and can proceed by surface-modification protocols, either via chemical modification or physical treatment of graphene.[7,16,17] It has often been reported that graphite intercalation compounds (GICs) have significantly improved conductivity and in-plane charge transfer, as compared to graphite.[18] However, the inert nature of the graphene basal plane often restricts charge transfer at the graphene/liquid interface despite the high in-plane charge mobility, so triiodide reduction occurs only at edge planes. Thus, surface modification of graphene is required to improve in-plane charge-transfer and enhance application as an efficient catalytic CE for triiodide reduction in DSSCs. Hasin et al. reported surface modification of graphene using water-soluble polymers (polyelectrolyte) whose ionic charge modified the surface-adsorption properties of graphene in $I/I_3^-$ reduction.[16] Roy-Mayhew et al. demonstrated enhancement of apparent electrocatalytic activity of graphene by functionalizing

S. Das, Dr. V. Verma, Prof. W. Choi
Department of Mechanical and Materials Engineering
Florida International University
Miami, Florida, 33174, USA
E-mail: choiw@fiu.edu
Dr. P. Sudhagar, D. H. Song, Prof. Y. S. Kang, Prof. W. Choi
WCU Program Department of Energy Engineering
Hanyang University
Seoul 133791, South Korea
E-Mail: kangys@hanyang.ac.kr
Dr. E. Ito, Dr. S. Y. Lee
Flucto-Order Functions Research Team
RIKEN-ASI, Saitama 351-0198, Japan

DOI: 10.1002/adfm.201101191

Journal of Materials Chemistry

Dynamic Article Links

Cite this: J. Mater. Chem., 2011, 21, 7289

www.rsc.org/materials

PAPER

# Synthesis and characterization of self-organized multilayered graphene–carbon nanotube hybrid films

Santanu Das,[a] Raghunandan Seelaboyina,[a] Ved Verma,[a] Indranil Lahiri,[a] Jun Yeon Hwang,[b] Rajarshi Banerjee[b] and Wonbong Choi*[a]

*Received 20th January 2011, Accepted 9th March 2011*
DOI: 10.1039/c1jm10316d

We report the synthesis and characterization of a self-organized graphene–carbon nanotube (CNT) hybrid film consisting of multilayer graphene (MLG) supported by vertical CNTs on a Si substrate. The hybrid film shows an interesting structure of graphene in connecting to vertical CNTs while maintaining ohmic contact at its junction. The *in situ* formation of a CNT–graphene heterojunction is confirmed by high resolution transmission electron microscopy (HRTEM). The as-obtained film shows a linear relationship for electrical conductance with significantly low resistance varying from 100–400 Ω on Si substrate. This hybrid film is inverted and transferred to flexible substrates for its application in flexible electronics, demonstrating an observable variation of electrical conductivity for both tension and compression. Furthermore, both turn-on field and total emission current were found to depend strongly on the bending radius of the film and were found to vary in ranges of 0.8–1.1 V μm$^{-1}$ and 4.2–0.4 mA, respectively.

## Introduction

Carbon nano-materials have been studied over the last 2 decades with great attention for their feasibility in future applications due to their exceptional properties like high current carrying capacity, ballistic charge transport, high thermal conductivity, chemical inertness, and high mechanical strength.[1–3] Fullerene (0D), carbon nanotube (CNT) (1D) and graphene (2D) are the carbon nanostructures most widely investigated in order to explore their novel properties. Apart from their individual properties, hybrid properties are also studied and applications have been proposed based on fullerenes–CNT, graphene–fullerene and graphene–CNT due to the significant technological importance of the hybrid structure.[11,22–25] The 1D form, carbon nanotube, has been studied rigorously for last 2 decades, but has limited applications due the difficulties in manufacturing it on-demand with uniform electrical and physical properties.[26–28]

Since the first report on isolation of single layer graphene sheet in 2004, scaling up of graphene is a major concern which is not only for its scientific interest but also for its impact on the feasibility of different technological applications.[4,29] So far graphene has been synthesized in either on SiC or metal substrates, and transferred to other flexible substrates afterwards to be used for flexible electronics and solar cell electrodes.[5–7] The results due to the exceptional properties of graphene, even in the device prototype stage, has led to demonstration of various devices in a wide range of areas including field emission (FE) cathode, sensors, electronics, solar cells, Li-ion batteries and so on.[5–8,30–33]

In addition to the applications based on either graphene or CNT, the graphene–CNT hybrid structure is highly beneficial for microelectronics applications as it can incorporate the advantages from properties of graphene and CNTs in the planar and axial directions, respectively. In particular, direct transfer of CNTs onto a polymer matrix suffers from lack of a homogeneous bottom contact for the CNT layers, as polymer substrates are high resistance in nature. In this context, the hybrid structure will be in high demand as it could provide a uniform conducting graphene layer which would be beneficial for applying on any type of polymer substrate. Furthermore, the thermal conductivity of a multiwall nanotube (MWCNT) is ~3000 W mK$^{-1}$ which reduces by several orders of magnitude even to 20 W mK$^{-1}$ or lower when MWCNTs are in the form of mat or forest structures.[11,23] The primary reason for the reduction in thermal conductivity is due to the discontinuities in the homogeneous bottom contacts in all the forest CNTs.[11] Similarly, electrical conductivity is also affected due to the non-uniform contact between all the CNTs in a mat or forest structure CNT film over any substrates.[3,15,17,26–28] Some of these shortcomings can be addressed by the unique graphene–carbon nanotube hybrid film, consisting of CNTs connected perpendicularly to graphene layers. Recently, Lee *et al.*[33] reported an interesting approach to grow vertically aligned MWCNTs on reduced graphene oxide platelets and proposed its applicability as a flexible field emission device. However, the reduced graphene oxide involves lot of issues like, low conductivity, less uniformity, and high

[a]Department of Mechanical and Materials Engineering, Florida International University, Miami, FL, 33174, (USA). E-mail: choiw@fiu.edu; Fax: +1 (305) 348 1932; Tel: +1 (305) 348 1975
[b]Department of Materials Science and Engineering, University of North Texas, Denton, TX, 76203, USA

VITA

SANTANU DAS

Education

| | |
|---|---|
| 2003 | B.Tech, Ceramic Technology, Calcutta University, INDIA. |
| 2005 | M.Tech, Ceramic Engineering, Institute of Technology, BHU, INDIA. |
| 2012 | Doctoral Candidate in Materials Science and Engineering Florida International University, USA. |

Awards and Achievements

1. Awarded Dissertation Year Fellowship (DYF) from Graduate School, Florida International University for the academic year 2011-2012.
2. Awarded Dissertation Evidence Acquisition (DEA) Fellowship from Graduate School, Florida International University for the academic year 2010-2011.
3. Awarded Honorary Membership offer for Sigma Xi, The Scientific Research Society, USA this year.
4. Awarded Second Prize for presentation in Florida International University, Graduate Scholarly Forum 2012.
5. Awarded third Prize for Materials Challenges in Alternative and Renewable Energy 2012 student poster contest.

**PUBLICATIONS**

**Book Chapter:**

1. Santanu Das and Wonbong Choi, Graphene Synthesis, **Graphene: Synthesis and Applications**; Series: Nanomaterials and their Applications CRC Press, Published October 2011.

**International Journals:**

**1.** Santanu Das, P. Sudhagar, Ved Verma, Donghoon Song, Eisuke Ito, Sang Yun Lee, Yong Soo Kang and WonBong Choi, Amplifying Charge Transfer Characteristic of Graphene for Triiodide Reduction in Dye-Sensitized Solar Cells, Submitted in **Advanced Functional Materials**, Volume 21, Issue 19, pages 3729–3736.

**2.** Santanu Das, Raghunandan Seelaboyina, Ved Verma, Indranil Lahiri, Jun Yeon Hwang, Rajarshi Banerjee and Wonbong Choi: Synthesis and characterization of self-organized multilayered graphene-carbon nanotube hybrid films: **Journal of Materials Chemistry**: 21 (2011) 7289-7295.

**3.** Santanu Das, P. Sudhagar, S Nagarajan, E Eto, S Y Lee, Yong Soo Kang and WonBong Choi: Synthesis of CoS decorated large scale graphene film for high efficiency solar energy conversion: Submitted to **Carbon, Accepted Manuscript, (2012) In Press**.

**4.** Santanu Das, P. Sudhagar, Eisuke Ito, Dong-yoon Lee, S.Nagarajan, Sang Yun Lee, Yong Soo Kang and WonBong Choi: Covalently functionalized catalytically active graphene for tri-iodide reduction in dye-sensitized solar cells: Submitted to **Journal of Materials Chemistry, Accepted Manuscript (2012) In Press**.

**5.** Debrupa Lahiri, Santanu Das, Arvind Agarwal and Wonbong Choi Unfolding the Damping Behavior of Multilayer Graphene Membrane in Low Frequency Regime: **ACS Nano, Accepted Manuscript (2012) In Press.**

**6.** Ved Prakash Verma, Santanu Das, Indranil Lahiri, and Wonbong Choi, Large-area graphene on polymer film for flexible and transparent anode in field emission device, **APPLIED PHYSICS LETTERS** 96, 203108 (2010).

**7.** Ved Prakash Verma, Santanu Das, Sookhyun Hwang, Hyonkwang Choi, Minhyon Jeon, Wonbong Choi: NO gas sensing at room temperature by functionalized single Zinc Oxide Nanowire: **Materials Science and Engineering B**: 171 (2010) 45–49.

**8.** Indranil Lahiri, Santanu Das, Chiwon Kang, Wonbong Choi: Application of carbon nanostructures – Energy to electronics, **Journal of Metals**, Volume 63 (2011), Issue 6, pp.70-76.

**9.** Santanu Das, Indranil Lahiri, Chiwon Kang, Wonbong Choi: Engineering Carbon Nanomaterials for Future Applications: Energy and Bio-sensor: Proceedings of The International Society for Optics and Photonics (SPIE) 25 - 29 April 2011, Orlando, Florida, USA.

**10.** Ved P. Verma, Santanu Das, Indranil Lahiri, Wonbong Choi, Large Area Graphene on Polymer Films for Transparent and Flexible Field Emission Device: MRS Symposium Proceedings, 29-3rd December 2010, Boston, MA, USA: MRS Proceedings 2011 1283 : mrsf10-1283-b08-03 (7 pages) DOI: 10.1557/opl.2011.801 .

**11.** Phani K. Vabbina, Santanu Das, Nezih Pala, Wonbong Choi, Synthesis of Crystalline ZnO Nanoflakes on Graphene and Other Substrates at Ambient Conditions, Materials Research Society Symposium Proceeding 2012 1449 : mrss12-1449-bb09-15.